THÈSE

En vue de l'obtention du

DOCTORAT DE L'UNIVERSITÉ DE TOULOUSE
Spécialité : Physique de la Matière

Présentée et soutenue par
Jakub JASIŃSKI

Control of the Excitonic Properties in Transition Metal Dichalcogenide based Structures

---

Ecole doctorale : Science de la Matière
Unité de recherche : Laboratoire National des Champs Magnétiques Intenses
Directeurs de Thèse : Paulina PŁOCHOCKA, Duncan MAUDE, Michał BARANOWSKI

Control of Excitonic Properties in Transition Metal Dichalcogenide based Structures

Abstract:

In recent years, atomically thin transition metal dichalcogenides (TMDs) have emerged as promising semiconducting materials. Their unique properties stem from their electronic band structure emerging from the broken inversion symmetry and strong spin-orbit coupling, as well the presence of strongly bound excitons. This endows them with additional degrees of freedom for charge carriers and excitons, which are promising for both studies of fundamental physical phenomena and applications in opto-electronic devices. Van der Waals nature of the interlayer bonding of TMDs and other emerging layered materials allows for fabrication of complex multi-layered structures, which add additional complexity and opportunity for achieving desired opto-electronic properties. Despite intense research, many mysteries regarding the fundamental physical phenomena governing properties of such structures remain to be solved.

The ongoing need for investigation of the intriguing characteristics of TMDs motivated the realization of this thesis. Here I present studies of several TMD-based structures, the focus of which was the possibility of controlling the excitonic properties via both intrinsic and extrinsic factors.

In monolayer MoS_2 deposited on a patterned substrate I demonstrate the unexpected effect of anisotropic strain on the fine structure and polarization properties of the charged exciton state.

In monolayer WSe_2 I show the importance of the Dexter-like coupling mechanism on the valley polarization and that it can be used for broad tunability of the degree of valley polarization by the choice of excitation energy.

In WSe_2/2D-perovskite heterostructure I reveal the successful spin injection from TMD into the 2D-perovskite and the formation of an interlayer exciton state, whose properties are closely related to those of the constituent WSe_2 monolayer.

Finally I explore the excitonic landscape of a natural bilayer of $MoSe_2$ and the tunability of the excitonic states via application of electric field, which revealed formation of new excitonic states and their complex interactions.

Overall, the results presented in this thesis constitute an important step towards understanding of fundamental properties of TMDs and TMD-based structures.

Keywords: Semiconductors, 2D materials, Transition metal dichalcogenides, Van der Waals structures, Excitons.

Contrôle des propriétés excitoniques dans les structures à base de dichalcogénures de métaux de transition

Abstract:

Ces dernières années, les dichalcogénures de métaux de transition (TMDs) atomiquement minces ont émergé comme des matériaux semi-conducteurs prometteurs. Leurs propriétés uniques découlent de leur structure de bandes électroniques résultant de la brisure de symétrie d'inversion et du fort couplage spin-orbite, ainsi que de la présence d'excitons fortement liés. Cela leur confère des degrés de liberté supplémentaires pour les porteurs de charge et les excitons, ce qui est prometteur à la fois pour l'étude des phénomènes physiques fondamentaux et pour les applications dans les dispositifs optoélectroniques. La nature van der Waals des liaisons intercouches des TMDs et d'autres matériaux stratifiés émergents permet la fabrication de structures complexes multicouches, ajoutant une complexité et des opportunités supplémentaires pour obtenir des propriétés optoélectroniques souhaitées.

Malgré une recherche intensive, de nombreux mystères concernant les phénomènes physiques fondamentaux régissant les propriétés de ces structures restent à élucider.

Le besoin continu d'explorer les caractéristiques intrigantes des TMDs a motivé la réalisation de cette thèse. Ici, je présente des études sur plusieurs structures à base de TMDs, dont l'objectif principal était d'examiner la possibilité de contrôler les propriétés excitoniques par des facteurs intrinsèques et extrinsèques.

Dans le cas de la monocouche de MoS_2 déposée sur un substrat structuré, je démontre l'effet inattendu de la contrainte anisotrope sur la structure fine et les propriétés de polarisation de l'état excitonique chargé.

Dans la monocouche de WSe_2, je montre l'importance du mécanisme de couplage de type Dexter sur la polarisation de vallée, et qu'il est possible d'ajuster largement le degré de polarisation de vallée en fonction de l'énergie d'excitation choisie.

De même, dans une hétérostructure WSe_2/pérovskite 2D, je révèle l'injection de spin réussie du TMD dans la pérovskite 2D et la formation d'un état excitonique inter-couche, dont les propriétés sont étroitement liées à celles de la monocouche WSe_2 constituante.

Enfin, j'explore le paysage excitonique d'une bicouche naturelle de $MoSe_2$ et la possibilité de moduler les états excitoniques via l'application d'un champ électrique, ce qui a révélé la formation de nouveaux états excitoniques et leurs interactions complexes.

Dans l'ensemble, les résultats présentés dans cette thèse constituent une étape importante vers la compréhension des propriétés fondamentales des TMDs et des structures à base de TMDs.

Mots-clés: Semi-conducteurs, Matériaux 2D, Dichalcogénures de métaux de transition, Structures de Van der Waals, Excitons.

Acknowledgements

I would like to express my wholehearted gratitude towards all the people that contributed and helped me during realization of this PhD thesis as well as enduring all the hardships along the way.

I would like to thank my supervisors: **Paulina Płochocka**, **Duncan Maude** and **Michał Baranowski** for their mentorship, guidance and the many enlightening conversations.

I would like to also thank other members of the research group, who helped me realize many tasks and in solving problems occurring along the way. Here I would like to especially acknowledge Alessandro Surrente for countless substantive discussions.

Additionally I would like to acknowledge the research groups of Ermin Malic, Alexey Chernikov and Anna Fontcuberta i Morral for succesful collaboration in the scientific projects which became a part of this dissertation.

I extend my gratitude towards the engineers at LNCMI, who were always there to assist in technical matters. Special thanks to Nicolas Bruyant and Franck Giquel for the help in optimising the design of the electrical adapter and to the Cryogenics team of Marc Nardone and Abdelaziz Zitouni.

I would like to deeply thank my family and friends for their constant support throughout this time. Here especially to my parents and parents in-law and most importantly to my wife Paulina Peksa-Jasińska, who was always there for me.

Finally, I acknowledge the NCN Preludium Bis-I project: ”Towards Deterministic Control of van der Waals Heterostructures Properties” as well as the French Government Scholarship for cotutelle PhD students for funding my research.

Contents

Chapter 1

Properties of transition metal dichalcogenides

1.1 Introduction

The discovery of graphene has shown how mundane materials like graphite can exhibit drastically different properties in the form of atomically thin layers in contrast to bulk crystals. Demonstration of its outstanding properties [Geim 2007], both mechanical and electronic has paved the way for a new class of atomically thin 2D materials. Graphite belongs to the family of van der Waals crystals, with weak van der Waals forces connecting the individual layers. This property allows for obtaining atomically thin layers even with simple mechanical methods [Frindt 1963]. Van der Waals materials include a variety of compounds with properties ranging from insulating, semiconducting, metallic, superconducting as well as magnetic and topological [Dean 2010, Mak 2010, Duan 2015, Mueller 2018, Grancini 2019, Chen 2018b, Straus 2018, Geim 2007, Samarth 2017, Klein 2018, Hu 2020, Kou 2017, Blatter 1996, Qiu 2021]. Among these, transition metal dichalcogenides (TMDs), such as MoS_2, $MoSe_2$, WS_2 and WSe_2, have emerged as extremely promising 2D semiconductors. Their fascinating properties arise from the unique electronic structure in the monolayer form. Similar to graphene they crystallize in a hexagonal lattice. The alternating metal and chalcogen atoms in the hexagon corners however lead to the broken inversion symmetry, which manifests in the emergence of non-equivalent K and K$'$ valleys in their Brillouin zone. Together with strong spin-orbit coupling stemming from the contribution of the heavy metal atoms, these effects lead to the robust valley physics [Chernikov 2014, He 2014, Ugeda 2014, Hanbicki 2015, Wang 2018a, Yao 2008, Zhu 2011, Xiao 2012, Xu 2014, Yu 2015, Stier 2016]. Moreover, their 2D nature in combination with the dielectric confinement [Chernikov 2014] lead to large exciton binding energies, making the excitonic particles stable even at room temperature. On top of that, the van der Waals nature TMDs and other layered materials allows for seamless stacking of virtually any combination of layers in order to construct complex heterostructures [Geim 2013] with novel opto-electronic properties. The pursuit for understanding the fundamental physical mechanisms governing the properties of TMDs and the TMD-based structures is an ongoing scientific endeavor. In particular, the control of their properties via both intrinsic and extrinsic factors is essential for future applications in opto-electronic devices.

1.2 Crystal structure

Transition metal dichalcogenides (TMDs) belong to the family of the 2D layered van der Waals (vdW) crystals characterized by strong covalent bonds within the plane of the layers and weak vdW forces connecting the layers in the out-of-plane direction. The weak vdW forces between the layers of a bulk crystal allow to relatively easily obtain very thin flakes, down to single monolayers via the process called mechanical exfoliation [Castellanos-Gomez 2014], which traditionally relies on the repeated tearing apart of a bulk crystal using an adhesive tape. Several derivatives of the mechanical exfoliation methods have been created over the years for improvement of the flake yield and quality [Li 2022]. Alternatively, atomically thin TMDs can be grown via Chemical Vapour Deposition (CVD) [Aras 2022]. Moreover, the nature of the interlayer vdW forces removes the lattice matching constraints present in the traditional epitaxial semiconductors, which allows for seamless stacking of virtually any combination of layers of TMDs and other 2D materials from the vdW crystals family. This opens the possibility for fabrication of almost any complex, multi-layer structure to achieve various desired properties. These can be tuned not only by the choice of materials, but also by the relative orientation (twist angle) of the layers [Geim 2013, Novoselov 2016, Ciarrocchi 2022, Huang 2022a].

The general formula of TMDs is MX_2, where M stands for a transition metal atom and X is the chalcogen atom. Similar to graphene [Geim 2007], TMDs crystallize in a hexagonal (honeycomb) lattice. However, in contrast to graphene, whose monolayer (*i.e.* a single stable layer of the material) lattice is composed of a single sheet of carbon atoms, a TMD monolayer comprises three atomic sheets, where the metal atoms are sandwiched in between two sheets of chalcogen atoms [Bromley 1972, Manzeli 2017]. A monolayer can form in two typical crystallographic phases characterized by different atomic configurations *i.e.* the octahedral and trigonal prismatic [Toh 2017, Coogan 2021], as can be seen in Fig. 1.1.

The octahedral coordination is characterized by an A-B-C sheet configuration, where the in-plane position of atoms in the three atomic planes are shifted relative to each other. The trigonal prismatic coordination exhibits A-B-A configuration, where the chalcogen atoms in the bottom and top atomic planes occupy the same in-plane position. For each chemical composition MX_2, the thermodynamically stable phase is either octahedral or trigonal prismatic. Consequently, the multi-layer crystals can exhibit different polymorphies (see Fig.1.1) depending on which monolayer coordination type they are composed of. Monolayers of octahedral coordination give rise to the so called 1T-phase (stacking) of tetragonal symmetry (Group D_{3d}), which exhibits metallic properties [Toh 2017] in case of the above mentioned materials. The trigonal prismatic coordination, on the other hand, can yield two polytypes: 2H-phase characterized by hexagonal symmetry (Group D_{3h}), corresponding to 60° twist angle between the consecutive layers, and 3R-phase characterized by rhombohedral symmetry (Group C_{3v}^{5}) corresponding to 0° twist angle between the consecutive layers.

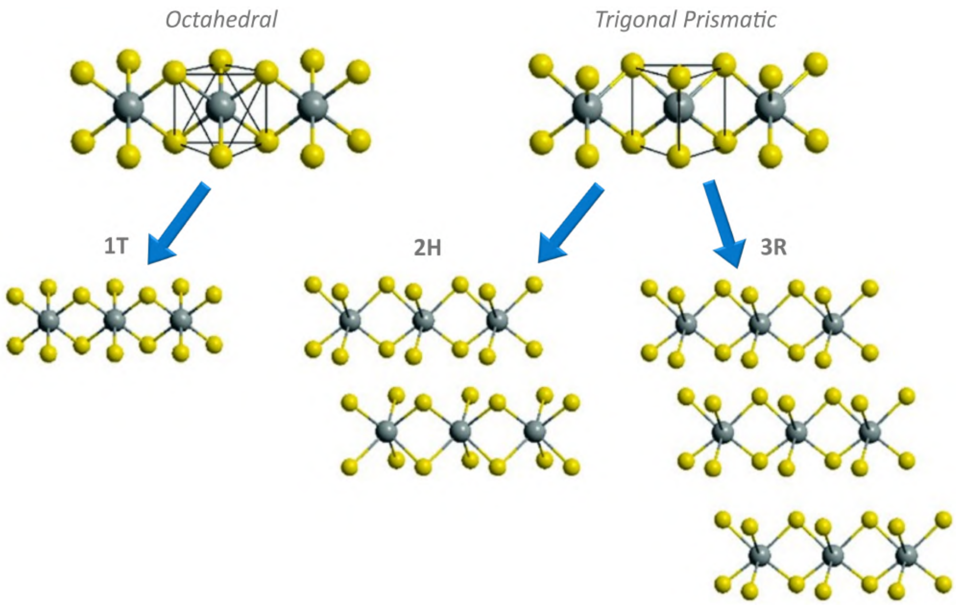

Figure 1.1: Octahedral and trigonal prismatic atomic coordination in TMD layers and the resulting crystallographic phases (polytypes): 1T, 2H and 3R. Adapted from Ref. [Coogan 2021].

The most important TMD materials for the field of opto-electronics are the group VI TMDs such as MoS_2, WS_2, $MoSe_2$, WSe_2 and $MoTe_2$, for which the trigonal prismatic coordination is thermodynamically preferred, although the octahedral coordination can be created in certain conditions as a metastable state [Manzeli 2017, Friedman 2017, Gan 2018]. Both polytypes originating from the trigonal prismatic coordination *i.e.* 2H and 3R, exhibit semiconducting properties. The 2H-stacking is energetically favourable and therefore most common and also found in naturally occurring crystals of MoS_2 and WS_2. The 3R-stacking can be however also easily obtained either in Chemical vapour deposition (CVD) growth [Li 2023b] or by artificial stacking of individual monolayers with the correct angle alignment.

Fig. 1.2 (a,b) presents the schematics of the atomic arrangement of the typical trigonal prismatic phase. Panel (a) shows the hexagonal lattice of a monolayer TMD as viewed from the top, while panel (b) shows the side view with a second monolayer added to show the 2H-stacking type (2H-stacked homobilayer), for which the interlayer distance d (typically $\simeq 0.6 - 0.65\,\text{nm}$) is marked. The yellow shaded area in panel (a) marks the trigonal prismatic coordination of the metal atom. The grey shaded area denotes the primitive unit cell constructed from the lattice vectors a_1 and a_2. The hexagonal lattice of a monolayer possesses a 3-fold in-plane rotational symmetry and at the same time it lacks the inversion center due to the atomic sites in the hexagon corners being occupied by the M and X atoms in alternating manner. Two crystallographic directions, referred to as zigzag (ZZ) and armchair (AC) can be distinguished, which alternate for every 30 ° of in-plane

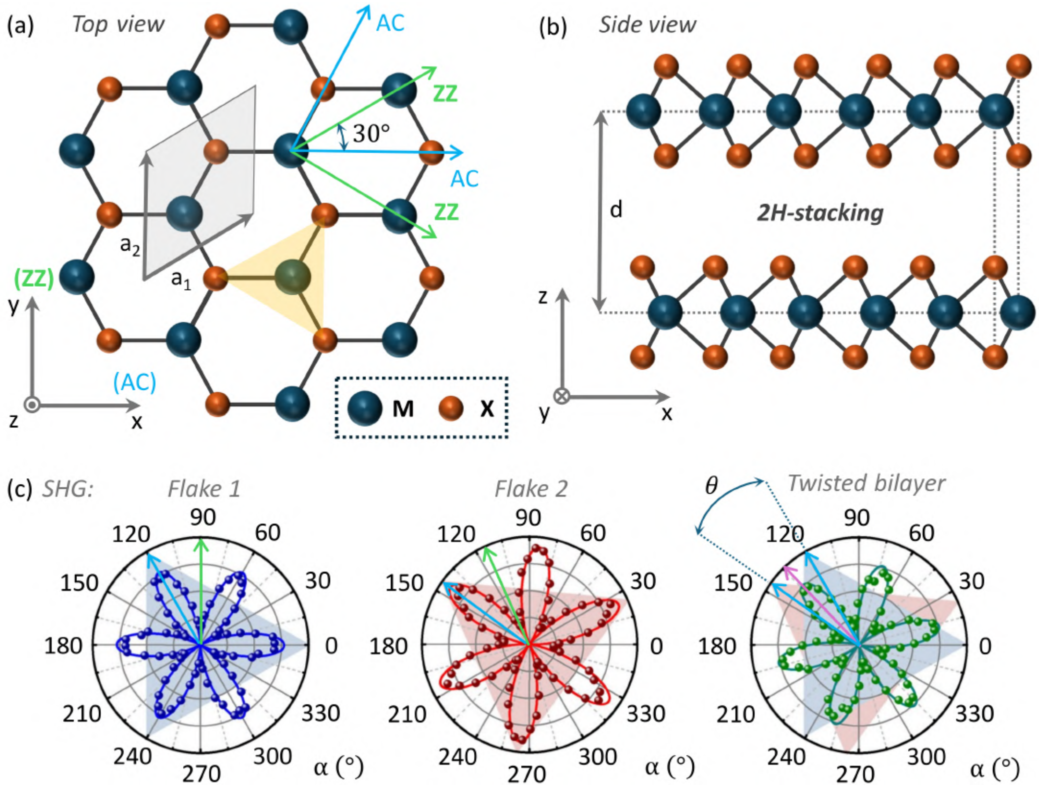

Figure 1.2: (a) Schematic drawing of the hexagonal crystal structure of a monolayer TMD with a trigonal prismatic coordination, as viewed from the top. The grey shaded area is the primitive unit cell and a_1 and a_2 are the real space vectors. The yellow shaded area emphasizes the trigonal prismatic coordination of the metal atom. Two important crystallographic directions, armchair (AC) and zigzag (ZZ) can be distinguished, marked by blue and green arrows, respectively. (b) Side view of a 2H-stacked bilayer. d corresponds to the interlayer distance, determined by the vdW forces between the monolayers (c) Results of the linear polarization resolved Second Harmonic Generation. The left (Flake 1) and middle (Flake 2) polar plots show results for two differently oriented MoS_2 monolayers (as depicted by the shaded triangles). The blue and green arrows mark the AC and ZZ directions, respectively. The right-most plot shows the result on an artificially stacked TMD bilayer with a non-zero twist angle. The purple arrow denotes the direction resulting from the superposition of the AC directions from the individual monolayers. θ is the relative twist angle between the monolayers composing the twisted bilayer. Panel (c) is adapted from Ref. [Hsu 2014].

rotation (6-fold rotational symmetry). The ZZ direction runs across the positions of the same atom type, while the AC direction crosses the alternating M/X pairs. This is an important distinction as the M/X pairs in the AC direction feature a dipole moment, which can interact with the electromagnetic field. This can be utilized to stimulate the Second Harmonic Generation (SHG). If the driving laser is linearly polarized, then the maximum of the SHG signal intensity is reached when the plane of polarization is parallel to the AC direction [Hsu 2014]. Thus, measurement of the SHG signal resolved in a linear polarization basis allows for determination of the crystallographic directions of the TMD monolayers [Hsu 2014]. Examples of such measurements are shown in the left and middle graphs of Fig. 1.2 (c), where two differently oriented monolayer flakes are compared. The same effect can be used to determine the relative twist angle (θ) between the constituent layers of a bilayer TMD. For the two extreme cases which are the 2H-stacking (see Fig. 1.2 (b)) and 3R-stacking characterized by 60° and 0° relative angles, respectively, the SHG signal undergoes a fully destructive (no SHG signal) or fully constructive (double intensity of SHG signal) interference, respectively [Hsu 2014]. This is due to the out-of-phase dipole orientation in the 2H case (due to mirror symmetry of the two monolayers) and in-phase orientation in the 3R case. For relative twist angles between 0° and 60°, the maximum of the SHG signal is projected onto the angle exactly in between the individual AC directions of the constituent monolayers, as depicted in the right-most graph of Fig. 1.2 (c). Hence the value of the twist angle can be determined either by knowing the angles of maximum SHG signal for the two constituent monolayers or in the bilayer region and one of the component monolayers.

1.3 Electronic structure

TMDs such as MoS_2, WS_2, $MoSe_2$, WSe_2 and $MoTe_2$ exhibit semiconducting properties with optical gaps in the visible and near infra red wavelength ranges [Kumar 2012]. Especially the monolayers of these materials have attracted a great interest in the opto-electronics field due to their optical gap transforming from an indirect one characterizing bulk and few layer crystals to a direct one in their monolayer form [Splendiani 2010]. The comparison of the calculated band structures for bulk and monolayer is presented in Fig. 1.3 (a) [Splendiani 2010]. The 2D hexagonal Brillouin zone is presented in Fig. 1.3 (b), with denoted high symmetry points (also referred to as valleys): Γ - zone center, K/K′ - hexagon corners and the intermediate points Q/Q′ and M/M′. The indirect band gap in a multi-layer crystals forms between Γ point in the valence band and the Q/Q′ point in the conduction band. Meanwhile, in monolayers, the direct optical gap opens at the K/K′ points (See Fig. 1.3 (a)). Such indirect to direct transition is directly related to the atomic orbital contribution to the band structure. The K/K′ band edges are mainly contributed by the d-orbitals of the heavy metal atom and are well confined within the individual layers. On the other hand, the Q/Q′ point is composed in much higher proportion by the p-orbitals of the chalcogen atoms and therefore is much more influenced by the interlayer coupling [Splendiani 2010] and hence by the number of layers. Such discrepancy explains the resulting thickness-dependent changes in the band structure.

The lack of inversion symmetry in monolayer TMDs leads to the presence of two degenerate but inequivalent types of points in their hexagonal Brillouin zone,

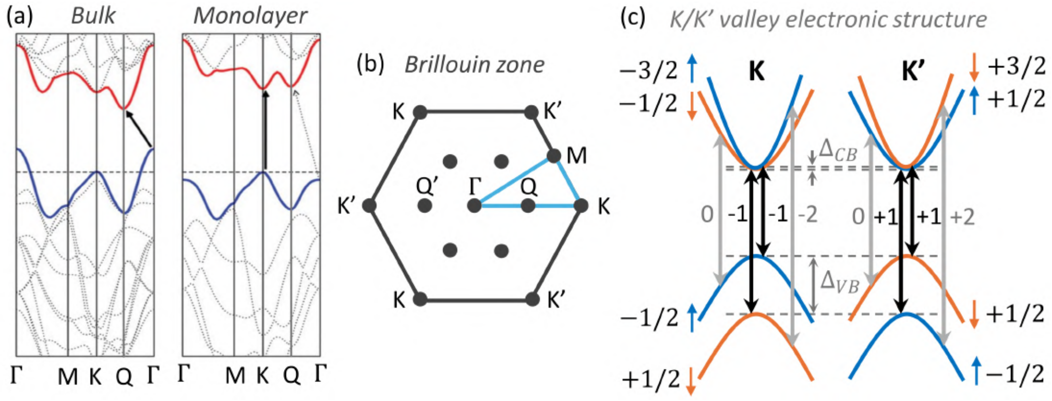

Figure 1.3: (a) Calculated electronic band structure of bulk and monolayer MoS_2. The black arrows denote the lowest energy transition between valence and conduction bands. (b) 2D hexagonal Brillouin zone of TMDs, with marked high symmetry points. The blue contour denotes the k-space cross-section for which the band structures in panel (a) are calculated. (c) Schematic of the electronic structure at the K/K′ valleys. $\Delta_{\mathrm{CB}}/\Delta_{\mathrm{VB}}$ denote the SOC splitting in conduction and valence band, respectively. The blue and orange arrows and values denote the electron spin orientation and projection of the total angular momentum J_z of the electronic bands, respectively. Black and grey arrows denote the inter-band transitions with corresponding values of the change of the total angular momentum ΔJ_z. The transitions with ΔJ_z of -1 in the K valley and +1 in the K′ valley (black) are spin-allowed, while those with ΔJ_z of 0 and ±2 (grey) are spin-forbidden. Panel (a) is adapted from Ref. [Splendiani 2010].

which are customarily denoted with *notprime* and *prime* (*e.g.* K and K′) as can be seen in Fig. 1.3 (b). Alternatively, "+" and "-" signs are used. Due to the 3-fold rotational symmetry, each point appears three times in a single Brillouin zone. The mirroring *notprime* (+) and *prime* (-) points are related to each other via the time reversal symmetry, imposing opposite spin of the corresponding electronic bands [Xiao 2012].

In addition, the strong spin-orbit coupling (SOC) present in TMDs, related to the contribution of the heavy metal atoms d-orbitals [Liu 2013] leads to substantial splitting of the spin-bands in the K and K′ valleys. The splitting in the valence band (Δ_{VB}) is on the order of 200 (in MoX_2) and 400 (in WX_2) meV [Zhu 2011]. The splitting of the conduction bands (Δ_{CB}) is much smaller, yet still significant, on the order of few to few tens of meV [Kośmider 2013].

The combination of both the broken inversion symmetry and strong SOC results in coupling of the spin and valley degrees of freedom, known as the spin-valley locking [Yao 2008, Zhu 2011, Xiao 2012, Xu 2014, Yu 2015, Stier 2016]. This can be seen in the contrast of the electronic structures of K and K′ points, schematically presented in Fig. 1.3 (c). The opposite color and arrow-mark direction of the corresponding degenerate bands between the K and K′ signify the opposite value of the electron in-plane total angular momentum projection (J_z). This picture leads to the valley-dependent optical selection rules [Chernikov 2014, He 2014, Ugeda 2014, Hanbicki 2015, Wang 2018a, Yao 2008, Zhu 2011, Xiao 2012, Xu 2014, Yu 2015, Stier 2016]. The "optically bright" electronic transitions, *i.e.* those that can couple to a photon, must satisfy the change in the total angular momentum of $\Delta J_z = \pm 1$ (transitions with ΔJ_z equal to 0 or ± 2 are "optically dark" in-plane). As depicted in Fig. 1.3 (c), two bright transitions, are possible in each valley. Both transitions in the same valley have the same change of the total angular momentum *i.e.* -1 in K and +1 in K$'$. Consequently, these transitions can couple to photons of right-handed (-1$\rightarrow \sigma^+$) and left-handed (+1$\rightarrow \sigma^-$) helicity. The consequences of this intricate electronic structure on the excitonic properties will be elaborated in more detail in section 1.4.2.

1.4 Excitons in TMDs

1.4.1 Bound electron-hole pair

In semiconducting materials, due to the presence of an optical band gap and strong Coulomb interactions, the dominating optical transitions stem from excitons rather than free electron-hole inter-band transitions, especially at low temperatures. Electron-hole pairs are created upon excitation of an electron to the conduction band, which leaves a positively charged hole in the valence band. The Coulomb interaction of the two charge carriers can lead to the formation of an excitonic particle, which is a bound state of a correlated electron-hole pair. Two types of excitons can be distinguished: Frenkel and Wannier-Mott excitons. Frenkel excitons, also called bound excitons, are highly localized around an atom or molecule and are characterized by very small size of their wave function, much smaller than the lattice parameter of the crystal. These usually appear in materials of relatively low value of dielectric constant such as insulators or molecular crystals, which aids very strong Coulomb interactions. On the other hand, Wannier-Mott excitons, also referred to as free excitons, are less localized with a wave function extending over several unit cells of the crystal lattice. These can move freely within the material. This type of exciton is usually present in relatively high dielectric constant materials, resulting in reduced Coulomb interaction. Semiconductors, including TMDs, predominantly host the Wannier-Mott type exciton.

Excitons can be thought of as analogous to hydrogen atom [Wannier 1937], *i.e.* the electron and hole exhibit a correlated motion and orbit a common center of mass. The two particles are correlated via Coulomb interaction which for a Wannier-Mott exciton can be expressed in an effective Hamiltonian, analogous to the hydrogen model [Peter 2010]:

$$H = -\frac{\hbar^2}{2m_e}\nabla_e^2 - \frac{\hbar^2}{2m_h}\nabla_h^2 - \frac{e^2}{4\pi\epsilon_0^2\epsilon_r^2|\boldsymbol{r_e} - \boldsymbol{r_h}|}, \tag{1.1}$$

where m_e and m_h are the effective masses of electron and hole, the ∇_e and ∇_h

are the nabla operators for the electron and hole coordinates, respectively, e is the elementary charge, ϵ_0 and ϵ_r are the dielectric constants of the vacuum and the material, respectively and the $\boldsymbol{r_e}/\boldsymbol{r_h}$ are the position vectors for the electron and hole, respectively. Due to the Coulomb attraction between the electron and hole, represented by the third term of the above equation, the exciton is characterized by a reduced total energy with respect to the sum of energies of the non-interacting electron and hole. This leads to appearance of excitonic states below the free particle band gap (E_g). This energy difference is denoted as the exciton binding energy E_B and expressed in the following equation:

$$E_B = E_e + E_h - E_X = E_g - E_X, \tag{1.2}$$

where the e, h and X subscripts denote the electron, hole, and exciton, respectively. Similar to the allowed energy levels of the hydrogen atom (Rydberg states), excitons can also exist in excited states. In a 3D system, the level (n) dependent binding energy can be modelled analogously to the 3D hydrogen model [Fox 2010] with a formula:

$$E_B(n) = \frac{R_X}{n^2}, \tag{1.3}$$

where R_X is the exciton Rydberg energy, which can be expanded to:

$$R_X = \frac{\mu}{m_0 \epsilon_r^2} R_H, \tag{1.4}$$

where $\mu = \frac{m_e m_h}{m_e + m_h}$ is the reduced electron and hole mass, m_0 is the free electron mass, r is the e-h separation distance and R_H is the hydrogen atom Rydberg energy ($R_H = 13.6\,\mathrm{eV}$).

Furthermore, the n-dependent wave function size *i.e.* the electron-hole orbit radius [Fox 2010] is described by equation

$$r_n = n^2 a_X, \tag{1.5}$$

where (a_X) is the exciton Bohr radius and is given by

$$a_X = \frac{m_0}{\mu} \epsilon_r a_H, \tag{1.6}$$

where a_H is the hydrogen atom Bohr radius ($5.29 \times 10^{-11}\,\mathrm{m}$).

From the above equations, one can note the inverse relation of the binding energy and radius *i.e.* the ground exciton state ($n = 1$) exhibits the highest binding energy, which translates to the lowest total energy as well as the smallest radius.

The binding energy of an excitonic particle is also the energy it takes to dissociate it into separate, non-interacting electron and hole (*i.e.* dissociation energy). Thus, the value of E_B determines the exciton stability, especially against interaction with thermally excited lattice vibrations. For example, in archetypical epitaxial semiconductors, such as GaAs, the binding energies are on the order of a few meV. At room temperature, the thermal phonon energies reach value of $k_B T \approx 25 meV$.

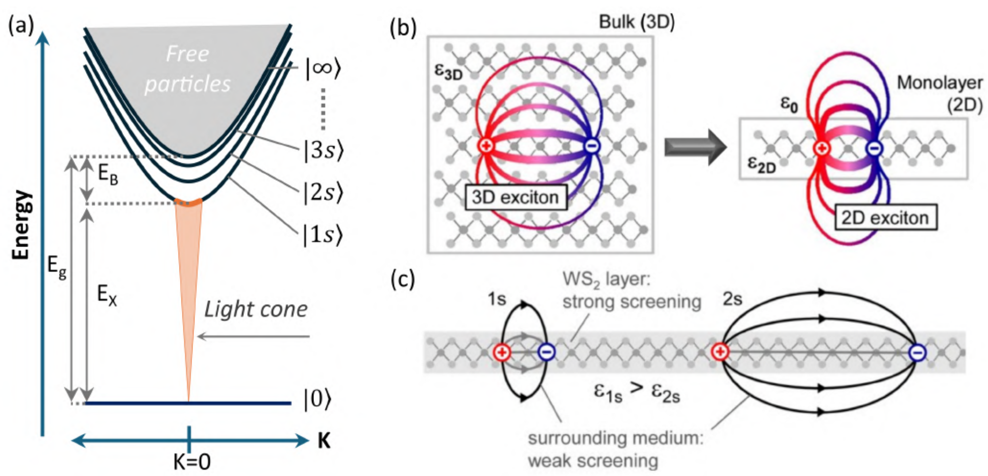

Figure 1.4: (a) Exciton dispersion relation $E(\boldsymbol{K})$, where $\boldsymbol{K}$ is the exciton center-of-mass momentum. E_X, E_g and E_B are the 1s exciton energy, band gap energy and binding energy, respectively. $|0>$ denotes the ground state, $|ns>$ is the exciton Rydberg progression, where s corresponds to the spherical symmetry in analogy to atomic orbitals, and $|\infty>$ is the free particle continuum. (b) Exciton wave function in a bulk TMD (left) and in a monolayer (right). Here, ϵ_{3D}, ϵ_{2D} and ϵ_0 represent the dielectric constant of the 3D, 2D semiconductor and the environment (*e.g.* vacuum or air), respectively. (c) 1s and 2s excitons wave functions in a TMD monolayer. The ϵ_{1s} and ϵ_{2s} denote the effective dielectric constants experienced by the 1s and 2s exciton states respectively. Panels (b) and (c) are adapted from Ref. [Chernikov 2014].

Hence in GaAs, the excitonic effects take precedence only at low, cryogenic temperatures, where the thermal energy $k_BT \sim T$ becomes lower than the binding energy.

Fig. 1.4 (a) presents the picture of the exciton Rydberg series dispersion relation. The excitonic energies of the n-th state can be expressed by the relation:

$$E_n(\boldsymbol{K}) = E_g - E_B(n) + \frac{\hbar^2 \boldsymbol{K}^2}{2(m_e + m_h)}, \tag{1.7}$$

where the last term corresponds to the kinetic energy of an exciton moving in the material lattice and $\boldsymbol{K}$ is the exciton center of mass momentum.

In systems of reduced dimensionality, *e.g.* 2D systems such as atomically thin TMDs, the additional quantum confinement along one of the directions yields a 2D form of a hydrogen model [Yang 1991]:

$$E_B(n) = \frac{R_X}{(n - \frac{1}{2})^2}. \tag{1.8}$$

This shows, that the quantum confinement in low-dimensional systems results in much larger exciton binding energies (four times larger for the ground excitonic state than in 3D system) and therefore enhanced excitonic effects. In real 2D systems such as TMD monolayers, the reduced dimensionality additionally leads the 2D excitons to experience reduced dielectric screening due to the dielectric contrast between the 2D semiconductor and the environment. This is due to the exciton wave function extending beyond the borders of atomically thin material, thus experiencing directly the dielectric effect of the surrounding environment, which is usually of much weaker value (*i.e.* vacuum or air), as presented in Fig. 1.4 (b), which compares the wave function of an exciton in a bulk and 2D semiconductor. This effect, called the dielectric confinement, leads to further enhancement of the of the electron-hole interaction and therefore binding energy [Chernikov 2014].

Moreover, as demonstrated experimentally and explained theoretically [Chernikov 2014], the exciton Rydberg series in 2D semiconductors does not follow the binding energy progression predicted by the 2D hydrogen model. This deviation stems from the above mentioned dielectric screening *i.e.* the effect of the contrast of the dielectric constants of the material and the environment on the electron-hole interaction, as depicted in Fig.1.4 (c) [Chernikov 2014]. This interaction can no longer be described via the simple Coulomb potential. The more appropriate model describing the electron-hole interaction in 2D systems, accounting for the non-hydrogenic binding energy scaling, is the Rytova-Keldysh potential [Rytova 2018, Keldysh 1979]:

$$V_{eh}(r) = -\frac{e^2}{8\epsilon_0 r_0}\left[H_0\left(\frac{\epsilon_{avg} r}{r_0}\right) - Y_0\left(\frac{\epsilon_{avg} r}{r_0}\right)\right], \tag{1.9}$$

where r is the exciton radius, r_0 is the screening length, H_0/Y_0 are the Struve/Bessel functions and the ϵ_0 and ϵ_{avg} are the vacuum permittivity and average dielectric constant of the top and bottom environment.

1.4.2 Excitonic species in TMDs

The complex electronic structure of TMDs stemming from the broken inversion symmetry and strong spin-orbit coupling [Chernikov 2014, He 2014, Hanbicki 2015, Wang 2018a, Mueller 2018, Xiao 2012, Perea-Causin 2022] provide additional degrees of freedom in the form of spin, valley, energy and layer. This allows for formation of plethora of excitonic species, which differ in energy, selection rules and spatial character. Among them we can distinguish a variety of neutral excitons, more complex excitonic particles *e.g.* trions or, in case of multi-layered structures, interlayer excitons.

1.4.2.1 Neutral excitons

TMD monolayers host several types of neutral (one electron, one hole) excitons which differ in energy and selection rules. Firstly, due to the strong-spin orbit coupling in the valence band as introduced in section 1.3, the excitons in the K/K$'$ valleys can form between different energy non-degenerate sub-bands of the CB and

VB. In each valley there are two spin-allowed optically bright ($\Delta J_z = \pm 1$) excitons, denoted as A exciton (lower energy) and B exciton (higher energy). Due to the spin-valley locking, both transitions in the same valley are characterized by the same change of the total angular momentum (-1 in K, +1 in K$'$), which results in the coupling to the same helicity of the circularly polarized photons *i.e.* right-handed σ^+ in K and left-handed σ^- in K$'$ as can be seen in Fig 1.5 (a). Such property allows for selective addressing or readout of signal from the opposite valleys via the use of circularly polarized light [Yao 2008, Xiao 2012, Xu 2014, Yu 2015, Stier 2016], which lead the scientific community to investigate the potential valleytronics applications [Xu 2014, Schaibley 2016, Liu 2019b, Ciarrocchi 2022]. The remaining two configurations of sub-bands yield spin-forbidden excitons, called dark excitons, with $\Delta J_z = 0$ and $\Delta J_z = \pm 2$. The $\Delta J_z = \pm 2$ excitons are optically inactive due to mismatch with the photon angular momentum of ±1. The $\Delta J_z = 0$ (denoted as D in Fig. 1.5 (a)) however is not entirely dark, as it does have a dipole moment in the out-of-plane direction (z) and thus is linearly polarized in this direction. Therefore, it is not observed in the standard experimental conditions (excitation and detection perpendicular to the TMD plane), however can be accessed by excitation and detection from the edge, parallel to the TMD plane [Wang 2017a].

Moreover, two types of TMD materials can be distinguished, *i.e.* "bright" TMDs and "dark" TMDs which are characterized by the opposite sign of the SOC in the conduction band, resulting in reversed band ordering, as shown in Fig. 1.5 (a) and (b). In "bright" TMDs ($MoSe_2$, $MoTe_2$), the lowest energy exciton is optically bright (A exciton). Conversely in "dark" TMDs (WSe_2, WS_2), the ground state is an optically dark exciton (D). The categorization of MoS_2 material is on the other hand slightly controversial as different theoretical calculations pointed to different band ordering [Qiu 2015, Echeverry 2016, Deilmann 2017, Malic 2018], however experimental studies suggested, that it may actually belong to the dark category [Robert 2020]. One of the consequences of the "bright" or "dark" band ordering is the impact on the ability to retain the injected valley-selective excitons *i.e.* valley polarization for time periods that allow its effective control. Despite the large separation of the K/K$'$ valleys in the momentum-space, the TMDs nevertheless are prone to several depolarization processes such as intervalley spin-flip scattering [Schmidt 2016a, Wang 2014, Song 2013, Ochoa 2013, Lu 2013, Dey 2017, Kim 2017] and intervalley exchange interaction [Xiao 2012, Zeng 2012, Zhu 2014b, Yu 2014a, Yu 2014b, Wang 2015c, Plechinger 2016, Dery 2016, Schmidt 2016b, Hao 2017, Yan 2015] which tend to quickly equalize the exciton populations between the two valleys and hence reduce the valley polarization. Studies on different TMDs have shown, that the "dark" TMDs such as WSe_2 and WS_2 are better at retaining the injected valley polarization in contrast to the "bright" $MoSe_2$ system in which the long-term polarization is hardly obtained. The mechanism responsible for this difference was identified to be precisely the presence of the lower energy long-lived dark exciton state, which acts as the reservoir for the higher lying bright excitons, thus limiting the effects of depolarization [Baranowski 2017, Tornatzky 2018].

In addition to the bright A and B excitons located in the K/K$'$ valleys, higher energy bright transitions, referred to as C excitons can also be found [Arora 2015, Hanbicki 2015, Frisenda 2017, Li 2018]. These are band-nesting excitons, which form along the $K-\Gamma$ direction in the Brillouin zone as depicted in Fig. 1.5 (c). All three transitions can be observed in absorption-type optical measurements such as differential reflectivity, as shown in Fig. 1.5 (d). In photoluminescence, usually only the lowest energy A exciton is visible due to the efficient energy relaxation.

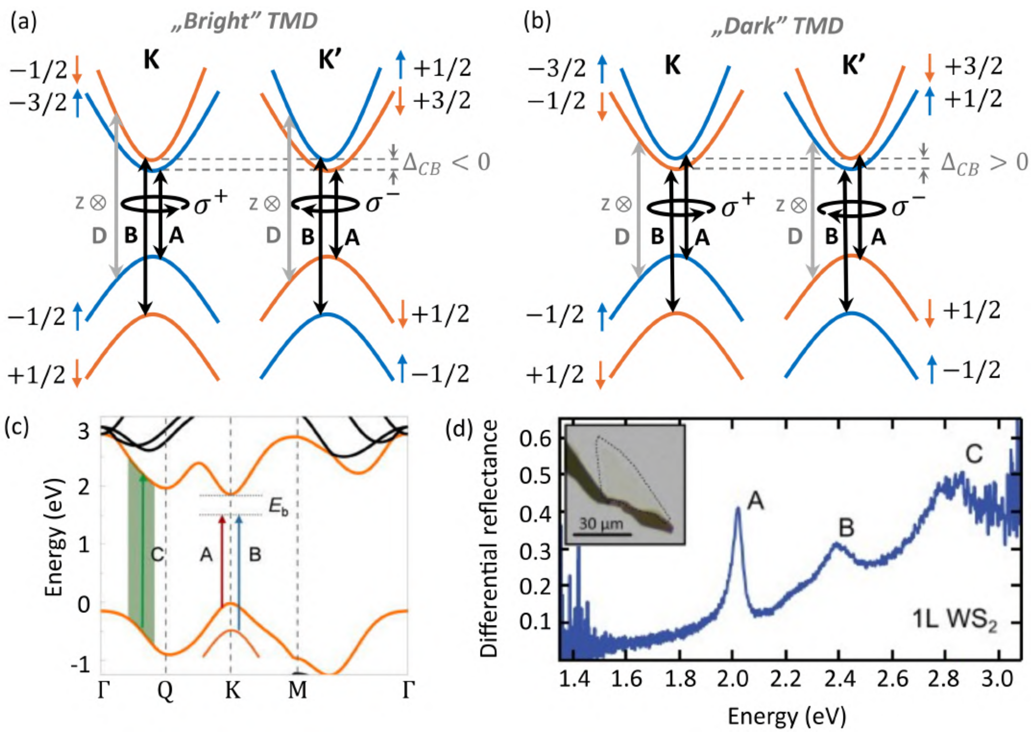

Figure 1.5: (a) and (b) Schematics of the electronic structure at the K/K′ valleys for the case of “bright” (a) and “dark” (b) TMDs characterized by reversed band ordering in the conduction band due to opposite sign of the SOC splitting (Δ_{CB}). The arrows and values denote the electron spin orientation and projection of the total angular momentum J_z of the electronic bands, respectively. A and B denote the spin-allowed bright excitons with the total angular momentum change of ΔJ_z of -1 in the K valley and +1 in the K′ valley. σ^+ and σ^- denote the polarization of the absorbed/emitted photon. D denotes the spin-forbidden dark exciton with $\Delta J_z = 0$, which is polarized in the out-of-plane (z) direction. (c) Calculated band structure of WS_2 monolayer with marked A, B and C excitonic transitions. (d) Differential reflectance spectrum of a monolayer WS_2 showing resonances at energies corresponding to transitions of A, B and C excitons. Panels (c) and (d) are adapted from Refs. [Li 2018] and [Frisenda 2017], respectively.

1.4.2.2 Complex excitonic particles

In addition to the neutral excitons, composed of one electron and one hole, more complex excitonic particles can form in semiconductors characterized by strong Coulomb interactions, such as TMDs. Three-particle complexes *i.e.* an exciton plus an additional charge carrier, either electron or hole, are referred to as charged excitons or trions. In suitable conditions, higher number of particles can bind together to form even more complex excitons such as 4-particle biexciton (bound state of two excitons), or five-particle charged biexciton. The binding of additional particles lowers the total energy of the excitonic complex due to the Coulomb interaction. The energy offset between the simplest neutral exciton and the more complex excitons is known as dissociation energy and it constitutes the energy necessary to remove the excess charge carriers from the exciton. Fig. 1.6 shows the schematic visualization of the several types of neutral and negatively charged excitonic complexes as well as the occupation of the constituent charge carriers in electronic bands in TMDs. Panels (a-d) show the general depiction of the different complexes as n-particle states. Panels (e-l) depict the configurations of charge carriers for the lowest energy versions of the excitonic complexes for the “dark” (e-h), and “bright” (i-l) band orderings. The “dark” band ordering offers multiple possible configurations which yield stable excitonic complexes. Panel (e) depicts a neutral exciton, which forms between an electron in the higher conduction band and the hole in the top valence band in one of the valleys. Charged excitons (trions), shown in panel (f) present an interesting case as the special electronic structure of TMDs allows for formation of different types of trions. The energetically lowest and optically bright trions can be either intravalley singlet (electron spins – ↑↓) $\mathrm{T_S^-}$ or intervalley triplet (electron spins – ↑↑) $\mathrm{T_T^-}$, which slightly differ in dissociation energy. The neutral biexciton, depicted in panel (g), is a bound state of a bright exciton (X) in one of the valleys and the low energy optically dark (D) exciton in the other valley, forming the so called XD complex. The photon emission from the XD complex results from recombination of the spin-allowed X transition, which leaves behind the dark exciton. Similarly, the charged biexciton, shown in panel (h), is the bound state of an intravalley singlet trion ($\mathrm{T_S}$) in one valley and the dark exciton in the opposite valley forming a TD complex. The described variety of excitonic complexes are commonly observed in materials like $\mathrm{WSe_2}$ [Ye 2018b, Barbone 2018, Lyons 2019] and $\mathrm{WS_2}$ [Plechinger 2016, Vaclavkova 2018, Conway 2022].

In case of the “bright” TMDs, in comparison, the spectrum of stable excitonic complexes is less diverse. Neutral exciton, shown in panel (i), similarly forms between the spin-adequate bands *i.e.* top of the VB and bottom of the CB. The lowest energy singlet and triplet trions, depicted in panel (j), on the other hand, are characterized by the opposite valley configuration with respect to the “dark” TMDs *i.e.* the singlet trion is an intervalley state, with the excess electron in the corresponding band of the other valley, while the intravalley triplet trion involves two electrons in the same lowest conduction band in a single valley. Consequently, the triplet trion T_T is an unbound state due to repulsive interactions between the electrons

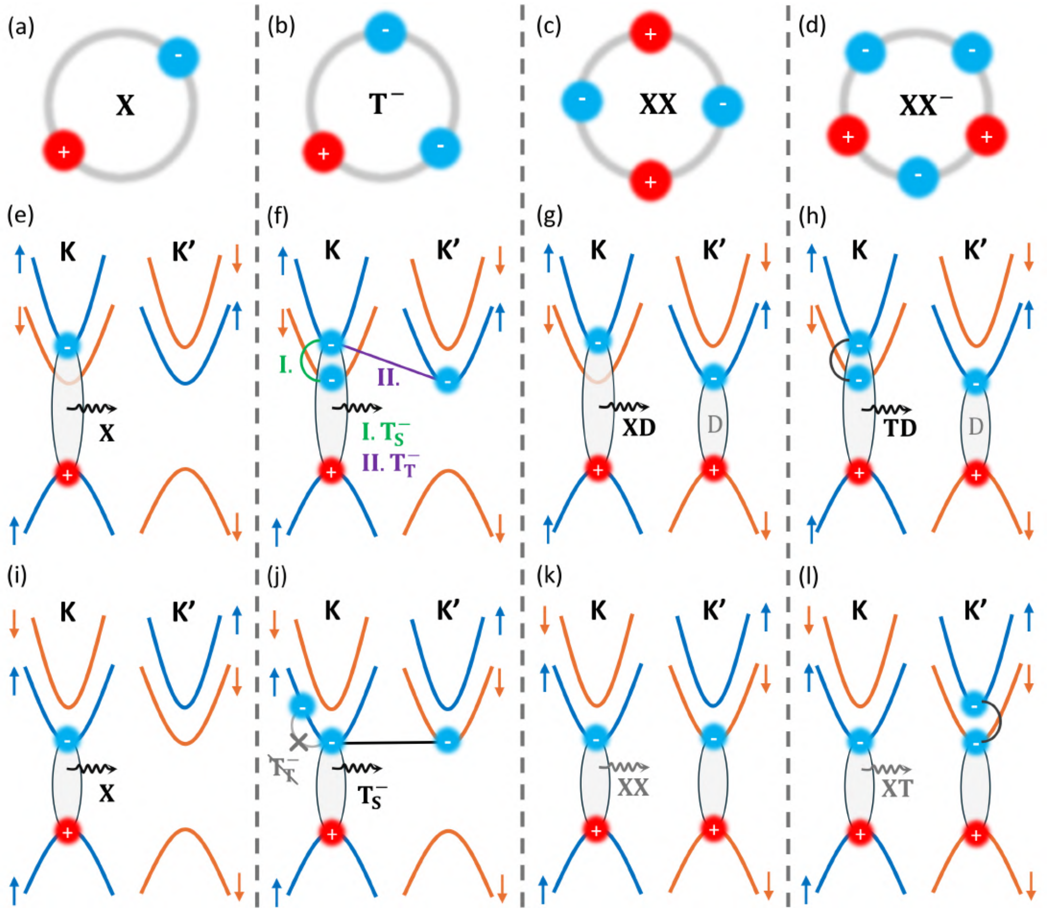

Figure 1.6: Schematic drawings of excitonic complexes: neutral exciton (a), negatively charged exciton (trion) (b), biexciton (c) and negatively charged biexciton (d). Schematic drawings of the lowest energy excitonic complexes within the electronic structure of "dark" TMDs: (e) neutral exciton in the K valley, (f) two optically active negatively charged excitons (trions) – 1. intravalley spin-singlet (↑↓) trion T_S and 2. intervalley spin-triplet (↑↑) trion T_T, (g) biexciton XD forms from an exciton in one valley (X) and dark exciton (D) in the opposite valley, (h) charged biexciton TD forms between a spin-singlet trion (T_S) in one valley and a dark exciton (D) in the opposite valley. The wavy arrow denotes the recombining e-h pair resulting in photon emission. Schematic drawings of the lowest energy excitonic complexes within the electronic structure of "bright" TMDs: (i) neutral exciton in the K valley, (j) Optically active intervalley spin-triplet (↑↑) trion T_T (intravalley spin-singlet (↑↑) trion T_S is unbound). (k) Biexciton XX (l) Charged biexciton XT. The wavy arrow denotes the recombining e-h pair resulting in photon emission.

[Tempelaar 2019] in the same valley and thus only the intervalley singlet exciton $\mathrm{T_S}$ contributes to the excitonic spectrum. The neutral and charged biexcitons, shown in panels can form simply between two excitons in the two valleys (XX) in case of neutral biexciton (panel (k)) and an exciton and trion in the two valleys (XT) in case of the charged exciton (panel (l)). However, these two states are not very stable, which is in contrast to the biexcitons in “dark” TMDs, which incorporate a long-lived low-energy dark state. They are therefore not observed in the photoluminescence spectra [Ross 2013, Shepard 2017, Ye 2018a]. On the other hand, they can be detected in other types of measurement such as photoluminescence upconversion [Jadczak 2023] or polarization-resolved two-dimensional coherent spectroscopy [Hao 2017].

The spectrum of positively charged excitons, in both “bright” and “dark” TMDs, is much simpler, which is related to the large valence band splitting in the range of hundreds of meV. Thus effectively only the top valence band edges contribute to trion formation so that only intervalley singlet trions (hole spins – $\uparrow\downarrow$) form.

1.4.2.3 Interlayer excitons

Layer degree of freedom in multi-layer homostructures (all layers of the same material) or heterostructures (layers of different material) provides the possibility for formation of spatially indirect, interlayer excitons (IXs). In homobilayer TMD structures (*e.g.* $MoSe_2/MoSe_2$), due to the energy degeneracy (same material of both layers), there is no preference for the accumulation of the electrons and holes in either layers, hence IXs of both configurations *i.e.* IX and IX′ can both exist simultaneously [Arora 2017, Gerber 2019, Hagel 2022, Feng 2024]. Fig. 1.7 (a) and (b) present the schematic drawing of a homobilayer TMD electronic structure (panel (a)) and real space (panel (b)) featuring both intralayer excitons (X, X′), confined within individual layers, and the two interlayer excitons (IX, IX′), where the charge carriers are separated between the two layers. Here the *notprime* and *prime* correspond to the layer degree of freedom. The spatial separation of the charge carriers results in a static dipole moment directed out-of-plane – opposite for IX and IX′. Heterobilayers (*e.g.* $WSe_2/MoSe_2$), on the other hand, usually exhibit a type II band alignment, which results in the charge transfer of the electrons and holes to the more energetically favourable layer, as depicted in panel (c) of Fig. 1.7. The preferential electron and hole occupation of the energy states of opposite layers imposes the specific orientation of the dipole moment [Jauregui 2019, Tran 2019, Choi 2021, Nayak 2017, Baek 2023, Sokolowski 2023, Luong 2017, Hagel 2021, Okada 2018, Tebyetekerwa 2021, Montblanch 2021, Yuan 2020, Li 2020a, Chen 2023, Yu 2020, Zhang 2020a, Ma 2021, Cho 2021, Khestanova 2023], as also shown in the real space schematic in Fig. 1.7 (d).

Additionally, in some structures of homo- and heterobilayers the Γ point tends to be strongly hybridized between the adjacent layers [Wilson 2017, Paradisanos 2020], which leads to delocalization of the hole between the layers. If the hybridized Γ point is higher in energy than the K/K′ a charge transfer of the holes to the favourable hybridized Γ point is enabled. Interlayer hybridized (IX_H/IX'_H) excitons, here K-Γ, can then form between the delocalized hole and the electron in one of the layers as depicted in Fig. 1.7 (e) and (f).

Moreover, IXs can be further categorized in relation to the relative position of the

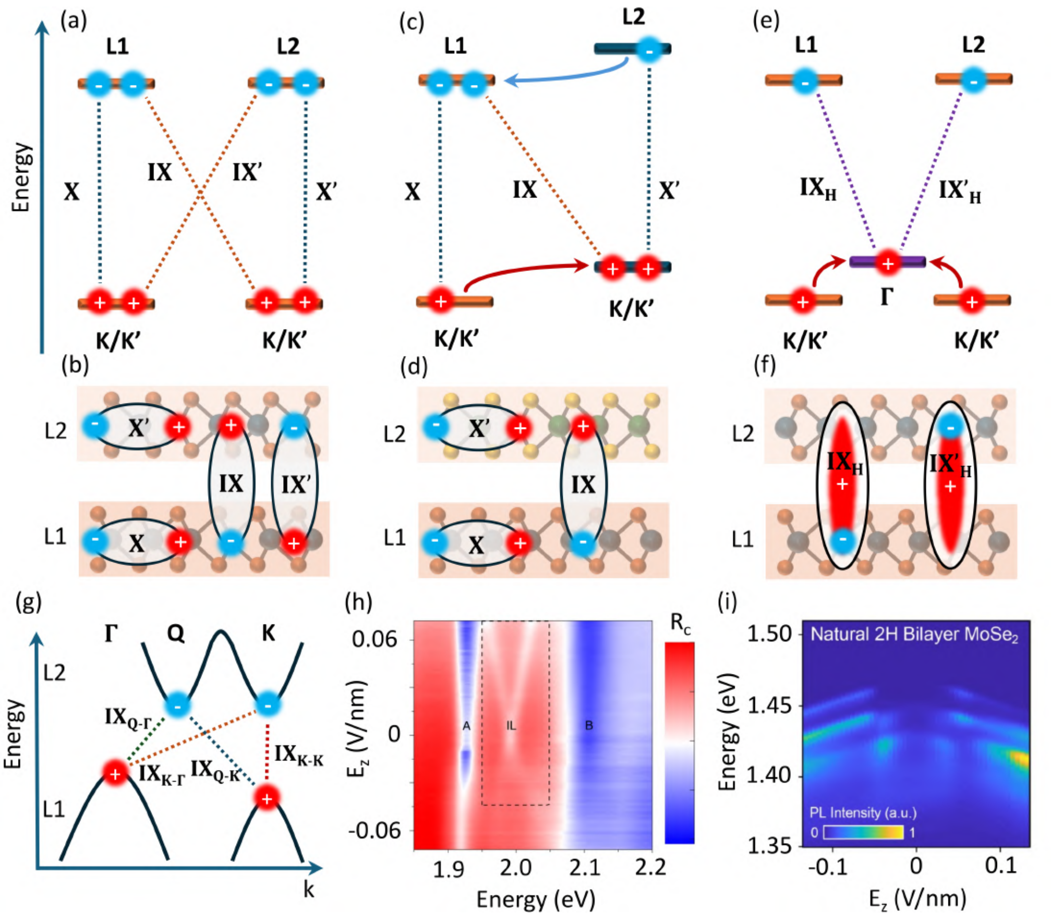

Figure 1.7: (a) Band alignment in a TMD homobilayer. X/X′ and IX/IX′ denote the intralayer and interlayer excitons. (b) Real space schematic of the intralayer (X/X′) and interlayer excitons (IX/IX′) in a TMD homobilayer. (c) Band alignment of a TMD heterobilayer (*e.g.* $WSe_2/MoSe_2$). Formation of only one IX is favoured due to the band alignment and the resulting charge transfer of electrons (blue arrow) and holes (red arrow). (d) Real space schematic of intralayer and interlayer excitons in a TMD heterobilayer. (e) Interlayer hybridized excitons (IX_H/IX'_H) in a TMD bilayer with the Γ point hybridized between the layers. (f) Real space schematic of interlayer hybridized excitons. The hole at the Γ point is delocalized between the layers. (g) Different possible interlayer excitons in a bilayer TMD: $IX_{K\text{-}K}$ – momentum-direct IX; $IX_{Q\text{-}K}$, $IX_{K\text{-}\Gamma}$, $IX_{Q\text{-}\Gamma}$ – momentum-indirect IXs. (h) Reflectivity contrast spectra as a function of out-of-plane electric field in a MoS_2 homobilayer. A, B and IL are the A exciton, B exciton and interlayer exciton resonances, respectively. (i) Photoluminescence spectra as a function of out-of-plane electric field of the interlayer hybridized exciton $IX_{K\text{-}\Gamma}$ and its phonon replicas in a homobilayer $MoSe_2$. Panel (h) and (i) are adapted from Refs. [Peimyoo 2021] and [Sung 2020], respectively.

charge carriers in the momentum space into the momentum-direct or momentum-indirect IXs. Fig. 1.7 (g) depicts the band edges that can be involved in formation of IXs: K and Q points for the electrons and K and Γ points for the holes. Which types are preferentially formed in a given structure depends on the TMD materials that compose it, specifically depending on the energy offsets of the band edges in the electronic structure. For example, homobilayers of $MoSe_2$ and MoS_2 feature both momentum-direct $IX_{K\text{-}K}$ and momentum-indirect (hybridized) $IX_{K\text{-}\Gamma}$ IXs [Sung 2020, Kovalchuk 2023, Feng 2024, Shimazaki 2020, Peimyoo 2021, Leisgang 2020, Lorchat 2021]. On the other hand, in WSe_2 and WS_2 homobilayers usually only the momentum-indirect $IX_{K\text{-}Q}$ or $IX_{Q\text{-}\Gamma}$ are experimentally observed [Wang 2018b, Huang 2022b, Brem 2020, Zhu 2014a, Tan 2019, Yan 2019].

Interlayer excitons endowed with a static out-of-plane dipole moments *i.e.* dipolar excitons respond to the application of the out-of-plane electric field with the field-induced energy shift due to the Quantum Confined Stark Effect (QCSE) [Miller 1984]. The dipolar states in TMDs are characterized by the first order Stark-shift [Jauregui 2019] which results in the linear dependence of the energy shift as a function of the applied electric field through the relation:

$$\Delta E = -ed_L E_z, \tag{1.10}$$

where $-ed_L$ is the dipole moment (e - elementary charge, d_L - dipole length). The sign of the energy shift (*i.e.* red shift or blue shift) depends on whether the dipole is parallel or anti-parallel to the E_z vector meanwhile the slope of the energy shift is proportional to the value of the dipole moment. The dipolar IXs in TMDs can be therefore easily tuned via the use of an external out-of-plane electric field [Wang 2018b, Peimyoo 2021, Liu 2020b, Tagarelli 2023, Tagarelli 2023]. Fig. 1.7 (h) presents an example of the electric field tuning of the interlayer exciton state (measured in reflectivity contrast) in a homobilayer MoS_2 [Peimyoo 2021]. For one direction of the electric field, due to presence of the IXs with both dipole moments orientation, the applied field splits them into a linearly red shifting (∼IX) and blue shifting (∼IX′) branch. For the opposite direction of the electric field, the energy shift sign of the IX and IX′ is reversed. Fig. 1.7 (i) shows an example of a momentum-indirect interlayer hybridized $IX_{K\text{-}\Gamma}$ in a homobilayer $MoSe_2$. The false color map shows the photoluminescence intensity as a function of electric field, on which several PL peaks related to phonon replicas of the $IX_{K\text{-}\Gamma}$ state can be observed. Here only the low energy red shifting branches for both field directions are optically active due to the nature of the photoluminescence experiment.

The dipole length, *i.e.* the separation of the charges, which determines the slope of the energy shift can be approximated by the interlayer distance of a bilayer structure [Jauregui 2019, Sung 2020], although in some cases the dipole length values are found to be below the value of interlayer distance [Peimyoo 2021]. The divergence is related to the not pure interlayer character stemming from the possible interlayer carrier tunneling, which hybridizes intralayer and interlayer states. This is especially prominent in the case of the earlier mentioned interlayer hybridized

$IX_{\text{K-}\Gamma}$ (delocalized hole), which *e.g.* in $MoSe_2$ homobilayer are found to exhibit an effective dipole length of around half the value of that of the $IX_{\text{K-K}}$ [Sung 2020].

1.4.3 Excitons and free carrier doping

Formation of the charged excitonic complexes introduced earlier requires the presence of excess free carriers that can bind with the excitons. If the sample exhibits an excess of free electrons in the conduction band (n-doping) then formation of negatively charged complexes is enabled whereas the excess of free holes (p-doping) allows for formation of positively charged complexes. The amount of the excess carriers can be expressed in terms of the density of free carriers or by the Fermi energy – E_F. In case of excess electrons, E_F corresponds to the energy of an electron at the Fermi level μ relative to the lowest level in the conduction band (E_{c0}):

$$E_F = \mu - E_{c0}. \tag{1.11}$$

At the absolute zero temperature, the Fermi energy corresponds exactly to the highest lying electron which at the same time is the kinetic energy $\frac{\hbar^2 k^2}{m_e}$ (see Eq. 1.1) of that electron as can be seen in Fig. 1.8 (a). Due to fermionic nature of electrons, all states below μ are occupied. At non-zero temperatures, a part of the electrons lie above μ, due to thermal excitation and their distribution is described by the Fermi-Dirac statistics [Zannoni 1999, Dirac 1926]

Fig. 1.8 (b) and (c) show the doping dependence (induced via application of gate voltage) of the excitonic spectrum (photoluminescence) of a monolayer WSe_2 and monolayer $MoSe_2$ [Lin 2022], respectively. For positive/negative gate voltages, the samples are tuned into n-doping/p-doping regimes. In the n-doping regime, monolayer WSe_2 exhibits two negatively charged exciton features related to singlet and triplet trions, meanwhile $MoSe_2$ shows only one feature related to spin singlet trion as expected for the “dark” and “bright” TMDs (see section 1.4.2.2). In the p-doping regime, both materials show only one positively charged trion feature as only one valence band of the opposite valley can contribute the excess holes. Fig. 1.8 (d) and (e) present the doping dependent energies of the exciton and trion features (panel (d)) as well as the relative energy distance between the two (panel (e)) in a monolayer MoS_2 [Mak 2013]. The data show that increasing of the Fermi energy results in the red shift of the trion and blue shift of the exciton (panel (d)). The synchronous energy shift of X and T energies, aside from their splitting described below, can be attributed to doping-related effects such as exciton energy renormalization due to screening of Coulomb interaction by the excess carriers [Chernikov 2015, Lundt 2018, Zhao 2020]. At the same time, the energy separation between the two transitions maintains a linear dependence on the Fermi energy (panel (e)). The simple explanation for this effect stems from the phase space filling effect *i.e.* occupation of the available energy states by the excess electrons as depicted in Fig. 1.8 (a), which defines the Fermi energy. In the few-particle picture of the exciton and trion, the neutral exciton can be treated as an ionized trion. The ionization *i.e.* removal of the extra electron (which happens during recombination of the "exciton part" of the trion) requires the left behind electron to be moved into the surface of the Fermi sea (*i.e.* the lowest available energy state in the conduction band). The Fermi energy denotes the lowest available state for the electron and hence the separation of the exciton and trion energy should scale linearly with the Fermi energy [Huard 2000, Mak 2013]:

$$E_X - E_T = E_B^T + \alpha E_F, \tag{1.12}$$

where E_B^T is the dissociation energy of trion (at infinitesimally small doping – $E_F \approx 0$) and α is the proportionality factor.

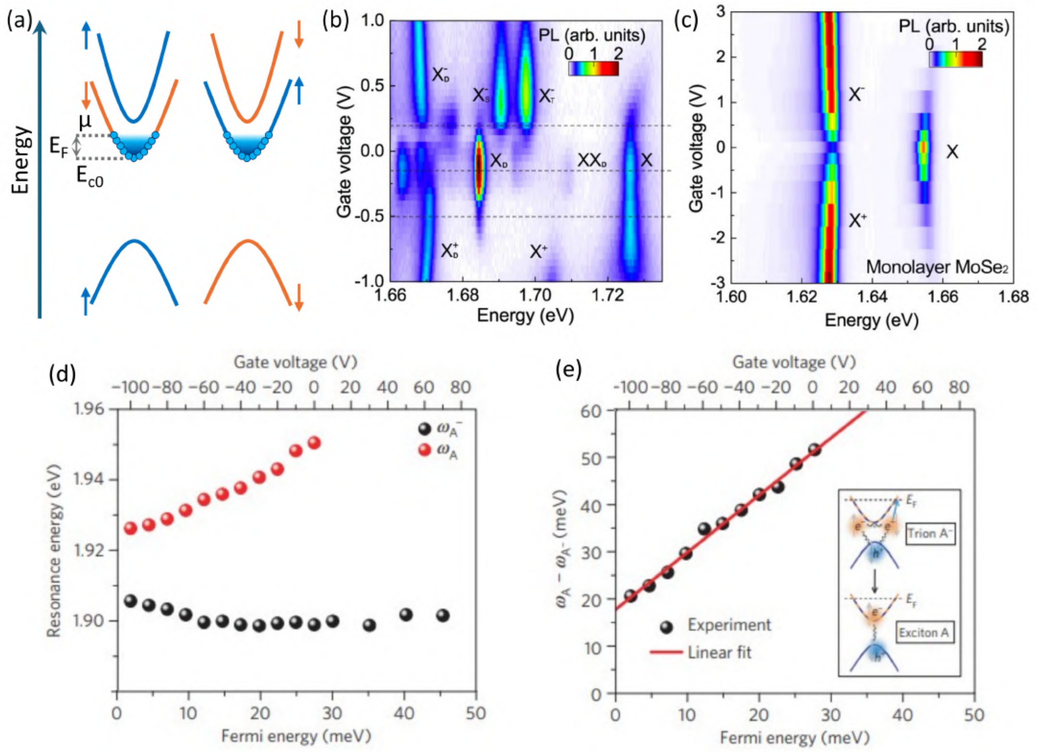

Figure 1.8: (a) Schematic depiction of the free electron gas in the conduction bands of the K/K′ valleys (blue shaded area) and the electrons (blue circles) occupying the states up to the Fermi level μ. The Fermi energy (E$_F$) corresponds to the kinetic energy of the highest energy electron in the electron gas and the energy between the bottom of the conduction band (E$_{c0}$ to the Fermi level. (b) and (c) Doping dependence of photoluminescence of monolayer WSe$_2$ (b) and MoSe$_2$ induced via application of gate voltage. (d) and (e) Exciton and trion energies shift (d) and the their energy separation (e) for monolayer MoS$_2$ as a function of Fermi energy. The linear fit in panel (e) has a slope of $\alpha = 1.2$. Panels (b) and (c) are adapted from Ref. [Lin 2022] and panels (d) and (e) from Ref. [Mak 2013].

1.4.3.1 Fermi polarons

An alternative approach to the standard description of excitonic quasiparticles as few-particle states, is the many-body description of excitons as Fermi polarons [Sidler 2017, Efimkin 2017, Glazov 2020, Wagner 2020, Liu 2021, Muir 2022, Huang 2023]. This approach takes into account the direct interaction of the excitons and the 2D electron or hole gases, which are present in TMD systems and is therefore important for thorough understanding of excitonic physics in the presence of Fermi gases. In this view, the excitons are treated as mobile impurities within the Fermi sea, which interact with it via attractive and repulsive interaction, which gives rise to the attractive polaron (AP) and repulsive polaron (RP) branches – counterparts to the trion and exciton in the low doping limit, respectively, as depicted in Fig. 1.9 (a) [Sidler 2017].

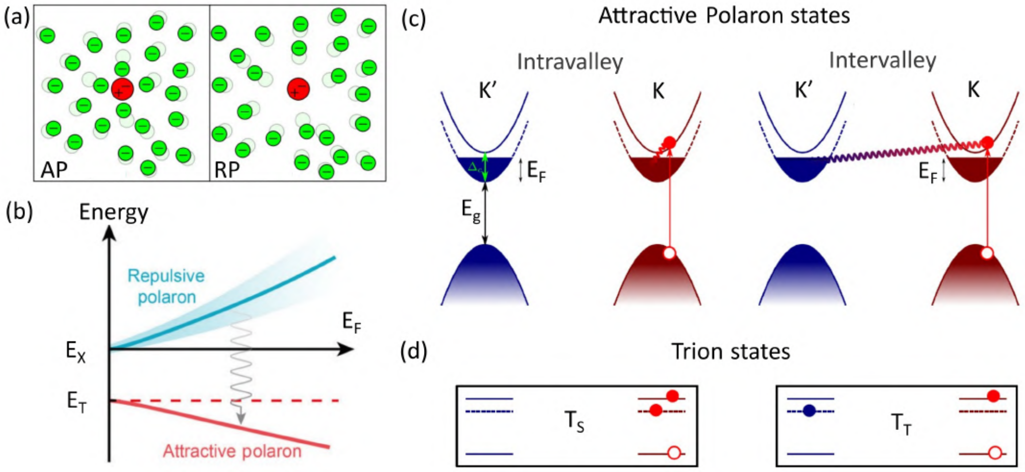

Figure 1.9: (a) Schematic depiction of attractive polarons – AP (left) and repulsive polarons –RP (right) and their interaction with the electrons in the Fermi sea. (b) Energy of the exciton/RP (E_X) and trion/AP (E_T) as a function of Fermi energy. (c) Fermi-polaron picture of attractive polarons in "dark" TMDs. Intravalley/intervalley interaction of excitons with Fermi sea in the same/opposite valley corresponding to two attractive polarons. (d) Few-particle picture of the intravalley singlet and intervalley triplet trions. Trion states in (d) correspond to the AP states in (c) in the low doping limit. Panels (a) and (b) are adapted from Refs. [Sidler 2017, Huang 2023], respectively, and panels (c,d) from Ref. [Glazov 2020].

The red shift of the AP (trion) and blue shift of the RP (exciton), depicted in Fig. 1.9 (b) [Huang 2023] and their relative splitting, (as well as oscillator strengths and line widths) as a function of the Fermi energy can be explained by the sum of effects of renormalization of exciton and the polaronic dressing [Sidler 2017] accounted for in the Fermi polaron picture. The exciton renormalization accounts for the modification of exciton energy and oscillator strength, meanwhile the polaronic dressing leads to the relative behaviour, including the linear splitting as a function of Fermi energy [Huang 2023]. The predicted proportionality factor α in Eq. 1.12 takes the value of 3/2, related to the inverse reduced mass of exciton-electron [Efimkin 2017], which corresponds also to the trion/exciton mass ratio ($\frac{2m_e+m_h}{m_e+m_h} \approx 3/2$, due to comparable effective masses of electron and hole in TMDs $m_e \approx m_h$ [Kormányos 2015]).

It was argued however, that many effects, even up to moderate doping levels regarding the properties of the attractive polarons (trions) can actually be explained equally well within both Fermi-polaron (Fig. 1.9 (c)) and trion (Fig. 1.9 (d)) frameworks [Glazov 2020]. On the other hand, some properties such as the exchange interaction and its influence on the fine structure of excitons and trions substantially differ for the two approaches. Namely, in the few-particle picture, the trion does not exhibit fine structure splitting (*e.g.* in the presence of the symmetry modifying factors such as anisotropic strain fields) due to effectively nullified exchange interaction. Conversely, in the Fermi polaron description, the attractive polaron retains the exchange interaction characteristic for the neutral exciton [Iakovlev 2023]. Results presented in chapter 3 of this thesis, required taking into account the more advanced Fermi-polaron description to understand the observed phenomenon of the strain induced lifting of the degeneracy of a charged exciton state.

Chapter 2

Experimental Techniques

2.1 Optical spectroscopy

Optical spectroscopy is a powerful tool that allows to gain insight into the optical and vibronic properties of the solid materials. It relies on the analysis of the spectrum of light either transformed due to interaction with the material or emitted by the material itself. It usually requires initial illumination with a light source, the interaction of which with the medium can be described in several general steps [Fox 2010]. Firstly, at the interface of the material, part of the illuminated light can be reflected from the surface. This depends on the reflectivity coefficient (R), which is generally defined as the ratio of the reflected to initial intensity of the light. Passing the interface, during propagation through the medium, the light undergoes refraction *i.e.* decrease of the velocity and bending, which is defined by the refractive index (n). Light can also be scattered *i.e.* redirected due to interaction with local inhomogeneity in the refractive index caused *e.g.* impurities (Rayleigh scattering) or the vibrations of lattice *i.e.* phonons (Raman scattering). Moreover, if the wavelength of light is resonant with electronic transitions of the material (such as atomic, vibronic or electronic transitions), the light can be absorbed, which can be quantified by the absorption coefficient (α). Finally, in the case of sufficiently thin or transparent samples, part of the light can be transmitted (described by transmitivity T), leaving the material from the opposite side. All these interactions are governed by the intrinsic optical properties of the investigated material, that can be described, in particular, by the wavelength-dependent complex dielectric permittivity $\tilde{\epsilon} = \epsilon_1 + i\epsilon_2$, which is determined by the electronic band structure of the material.

Analysis of the spectrum of light transformed by the interaction with the material can therefore be utilized to obtain information about the energetic structure of the material [Fox 2010]. Furthermore, in the aforementioned process of light absorption, the absorbed energy is subsequently released, usually in the form of lattice vibration *i.e.* heat or re-emitted via the process of luminescence, which is a general term for the spontaneous photon emission due to energy relaxation from an excited state. Analysis of the emission spectrum provides further information about the opto-electronic structure of the investigated material. Similarly, the interaction of the light with phonons in Raman scattering event can provide information about the phonon spectrum of the investigated system, which can be utilized for example as a probe for strain in strain engineering applications.

2.1.1 Reflectivity

Reflectivity is one of the most commonly used absorption-type spectroscopy techniques providing insight into the opto-electronic properties of semiconductors. It relies on the analysis of the spectrum of light reflected from the surface of the measured material. It depends on the complex refractive index of the material $\tilde{n} = n + i\kappa$, where n is the refractive index of the medium and κ is the extinction coefficient. These coefficients are related to the complex dielectric permittivity via relations:

$$\begin{aligned} \epsilon_1 &= n^2 - \kappa^2, \\ \epsilon_2 &= 2n\kappa. \end{aligned} \tag{2.1}$$

The general formula for the reflectivity (R), in the simplest form (assuming perpendicular incidence on the sample and disregarding polarization of light), can be written as

$$R = \left| \frac{\tilde{n} - 1}{\tilde{n} + 1} \right|^2 = \frac{(n-1)^2 + \kappa^2}{(n+1)^2 + \kappa^2}. \tag{2.2}$$

The extinction coefficient, which describes the attenuation of light propagating in the medium is directly related to the absorption coefficient (α) via relation

$$\alpha = \frac{4\pi\kappa}{\lambda}, \tag{2.3}$$

where λ is the free space light wavelength. This shows that optical response of the material in the form of both reflection and absorption are governed by the same set of material parameters. In this case, the absorption spectrum can be indirectly probed by reflectivity, which is often the easiest measurement to realize experimentally as it does not require the sample to be sufficiently thin and/or transparent.

It is possible to calculate the absorption spectrum based on measured reflectivity by first deducing $\kappa(\omega)$ based on Eq. 2.2 and then applying the relation from Eq. 2.3. The dependence on both n and κ can be untangled by using the Kramers-Kronig relations, which describe the inter-dependence of the two parameters [Fox 2010]:

$$n(\omega) = 1 + \frac{1}{\pi} P \int_{-\infty}^{\infty} \frac{\kappa(\omega')}{\omega' - \omega} d\omega', \tag{2.4}$$

$$\kappa(\omega) = -\frac{1}{\pi} P \int_{-\infty}^{\infty} \frac{n(\omega') - 1}{\omega' - \omega} d\omega', \tag{2.5}$$

where P is the Cauchy principal value.

At the energies corresponding to electronic or excitonic transitions, the complex refractive index changes abruptly when incident photons are absorbed. This leads to the appearance of characteristic resonances in the reflectivity spectrum, which can be modeled by dipole oscillators characterized by certain natural frequencies [Fox 2010]. Since the reflected spectrum is essentially a transformed spectrum of the initial illuminating light, it is most often useful to analyse relative reflectivity instead of raw reflectivity spectra, to avoid source-related artifacts. Relative reflectivity is created relative to the spectrum of the initial illuminating spectrum *i.e.* reference R_0 and analysed in the form of either reflectivity divided by reference R/R_0 or reflectivity contrast $(R-R_0)/R_0$. The latter is especially useful for analysis in case of thin ($d << \lambda$) and layered structures such as TMD flakes deposited on substrates in order to calculate the absorption coefficient. Analysing the experimentally obtained reflectivity in the $(R-R_0)/R_0$ form allow for valid approximations that reduce the complexity of the expression for multi-layered structures related to their thicknesses and reflections at the interfaces influencing the shape of the reflectivity spectrum [McIntyre 1971]. A detailed calculation of the parameters of such samples can be performed *e.g.* by the transfer matrix method [Hecht 2012, Robert 2018]. In some cases, it is useful to calculate a 1^{st}, or higher order derivative of the relative reflectivity to identify or accentuate weak spectral features.

In the semiconductor systems, concerned in this thesis, the optical response is dominated by the excitonic effects, described in more detail in section 1.4. Fig. 2.1 shows exemplary reflectivity spectra of a monolayer MoS_2 deposited on Si substrate in the form of R/R_0 and 1^{st} derivative of R/R_0 with three observable resonant features originating from excitonic transitions in MoS_2, namely the charged exciton (X_T), neutral A exciton (X_0) and B exciton (X_B).

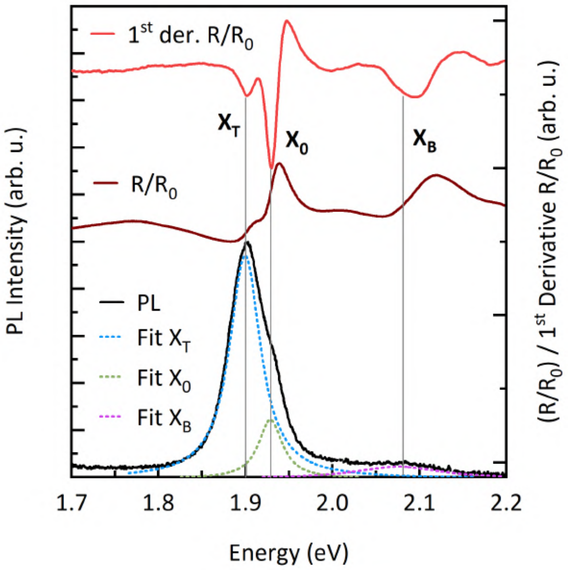

Figure 2.1: Exemplary photoluminescence and reflectivity spectra of MoS_2 on Si substrate: the reflectivity in the form of R/R_0 (brown curve) and its 1^{st} derivative (red curve) are shown. The PL spectrum (black curve) was fitted with 3-peak Lorentz function to the three visible peaks assigned to charged exciton (X_T), neutral A exciton (X_0) and B exciton (X_B), with the individual fitted peaks plotted in dotted lines. The resonances in the reflectivity spectrum match the peak positions of the photoluminescence spectrum.

2.1.2 Photoluminescence

Photoluminescence (PL) refers to the event of luminescence, which was initiated by optical excitation (photo-excitation), while luminescence is a general term for spontaneous radiation of emission. The first step for realization of PL is the excitation of the emitting material, *e.g.* semiconductor, from the ground state into an excited state. The excitation - here via absorption of the incident photon energy - generates a pair of charge carriers - electron and hole. The electron is elevated to higher energy level, which leaves behind an empty state - the hole. This event is also referred to as the creation of an electron-hole pair. After excitation, the carriers (both electron and holes) undergo thermal relaxation to the lowest energy available states. In semiconductors, this is usually bottom of the conduction band for the electrons and top of the valence band for the holes. The thermal relaxation processes *i.e.* scattering with phonons, are very efficient and happen on very short timescales on the order of 100 fs [Fox 2010]. After a while, the electron-hole pairs can recombine, *i.e.* return to the ground state, which is also referred to as the annihilation of an electron-hole pair. The recombination can be divided into two types *i.e.* radiative and non-radiative. (i) In radiative recombination, the energy of the electronic transition is released by emission of a photon - luminescence. The characteristic mean time after which the event of emission takes place is the radiative lifetime τ_r. The values of τ_r tend to be much longer as compared to the relaxation processes, on the order of nanoseconds [Fox 2010] in epitaxial semiconductors or picoseconds in the case of TMDs at low temperature [Palummo 2015, Robert 2016]. This leaves sufficient time window for the carriers to thermalize, hence the observable luminescence predominantly originates from the fundamental (lowest energy) transitions in the material. (ii) In non-radiative recombination, the energy is released usually in the form of heat *i.e.* emission of phonons. Alternatively the non-radiative recombination can result in energy transfer to the so called trap states (defects, impurities) or to excite a neighbouring carrier to a higher energy level (Auger recombination [Li 2012]). The mean time for non-radiative recombination, not taking into account the specific origin, can be described by an analogous parameter of non-radiative recombination lifetime τ_{nr}.

The dynamics of the system returning to the ground state via radiative and non-radiative events can be described via the general relation:

$$\frac{1}{\tau} = \frac{1}{\tau_r} + \frac{1}{\tau_{nr}}, \tag{2.6}$$

where $\frac{1}{\tau}$ is the rate of the transition from the excited to ground state.

The different emission origins can be additionally divided into monomolecular and bimolecular processes [Pelant 2012]. The monomolecular recombination involves a single particle or quasi-particle. It is characteristic of the emission from localized centers such as local defects/impurities or excitons in which the electron and hole are correlated via Coulomb attraction and hence cannot be treated as independent particles (see section 1.4.1). The dynamics of monomolecular process is determined by concentration (N) of the recombination centers (or population in case of excitons) which can be described via the relation:

$$\frac{dN(t)}{dt} = G - \frac{N}{\tau_r} - \frac{N}{\tau_{nr}} = G - \frac{N}{\tau}, \tag{2.7}$$

where G is the generation term, which can be approximated as the product of excitation intensity and absorption coefficient $G = \alpha I_{exc}$, where I_{exc} denotes the number of photons per unit of area and time. The decay of the monomolecular luminescence (*i.e.* after switching off the excitation – $G = 0$ at time $t = 0$) can be then written as:

$$\frac{dN(t)}{dt} = -\frac{N}{\tau}, \tag{2.8}$$

with solution in the form of $N(t) = N(0)e^{-t/\tau}$. The resulting time dependence of luminescence decay takes form of a mono-exponential decay:

$$I(t) = \frac{N(t)}{\tau_r} = \frac{N(0)}{\tau_r}e^{-t/\tau} = I(0)e^{-t/\tau}. \tag{2.9}$$

In the steady state conditions (usually acquired by using a continuous wave (cw) excitation source) *i.e.* when the generation and recombination reaches an equilibrium ($\frac{dN(t)}{dt} = 0$) resulting in constant luminescence intensity, the Eq. 2.7 then reads:

$$G = \frac{N(0)}{\tau_r} + \frac{N(0)}{\tau_{nr}} = I(0) + \frac{N(0)}{\tau_{nr}}. \tag{2.10}$$

Relating the generation term directly to the excitation intensity via $G = \alpha I_{exc}$, we can obtain the luminescence intensity as a function of the excitation in the form:

$$I(0) = G - \frac{N(0)}{\tau_{nr}} = \alpha I_{exc} - \frac{\tau_r}{\tau_{nr}} I(0). \tag{2.11}$$

From the above equation we can obtain the proportionality $I(0) \propto I_{exc}$, which shows that the monomolecular luminescence intensity is a linear function of the excitation intensity.

The bimolecular recombination involves two independent particles. An example of the bimolecular process in semiconductors is the recombination of the free electron-hole pairs *i.e.* the direct band-to-band transitions. For such an event to take place, a free electron in CB and a free hole in VB must randomly encounter each other so that their wave functions overlap considerably. The recombination is thus proportional to the product of free electron (n) and free hole concentrations (p) as described in the relation:

$$\frac{dn(t)}{dt} = G - \beta np. \tag{2.12}$$

The β parameter is the bimolecular recombination coefficient, which includes both the radiative and nonradiative terms – $\beta = \beta_r + \beta_{nr}$. In the simple case of an intrinsic semiconductor (where $n = p$), the above equation reads:

$$\frac{dn(t)}{dt} = G - \beta_r n^2 - \beta_{nr} n^2 = G - \beta n^2, \tag{2.13}$$

where the $\beta_r n^2$ and $\beta_{nr} n^2$ denote the radiative (luminescence) and nonradiative recombination terms. The decay of a bimolecular process ($G = 0$ at $t = 0$) can be obtained from the above equation as:

$$\frac{dn(t)}{dt} = -\beta n^2. \tag{2.14}$$

The solution of this equation, following the substitution of $\frac{1}{n} = x$ and boundary conditions of $n(t = 0) = n(0)$, reads:

$$n(t) = \frac{n(0)}{\beta n(0)t + 1}. \tag{2.15}$$

The time dependence of the the luminescence intensity $I(t)$ taken as $I(t) = \beta_r n^2(t)$ can be then deduced as:

$$I(t) = \frac{\beta_r n^2(0)}{(\beta n(0)t + 1)^2} = \frac{I(0)}{(\beta n(0)t + 1)^2} = \frac{I(0)}{(\frac{\beta}{\sqrt{\beta_r}}\sqrt{I(0)}t + 1)^2}. \tag{2.16}$$

As can be seen from the above equation, in contrast to the monomolecular process whose decay is a monoexponential function, here the decay is a power-law function – approximately proportional to t^{-2} at longer times.

In the the steady state conditions ($\frac{dn(t)}{dt} = 0$), the Eq. 2.13 gives:

$$I(0) = \beta_r n^2(0) = G - \beta_{nr} n^2(0) = G - \beta_{nr}\frac{I(0)}{\beta_r}. \tag{2.17}$$

By assuming that the generation term $G = \alpha I_{exc}$ and transforming the above equation into:

$$I(0) = \left(\frac{\beta_r}{\beta_r + \beta_{nr}}\right) G = \left(\frac{\beta_r}{\beta_r + \beta_{nr}}\right) \alpha I_{exc}, \tag{2.18}$$

we obtain the linear dependence of the luminescence intensity on the excitation intensity, similar as in the monomolecular process. It is worth noting however, that in excitation conditions which do not result in obtaining of the steady state, *e.g.* when using excitation with very short pulses, the dependence may become quadratic instead of linear [Pelant 2012]. This is due to the bimolecular recombination probability being proportional to the square of the electron-hole pair density.

Focusing specifically on the radiative recombination, there are several possible (both monomolecular and bimolecular) channels which can result in the photon emission such as: recombination of free electron-hole pairs, free excitons, free excitons with emission of LO phonons, bound excitons (*e.g.* bound to donor or acceptor states), excitonic complexes (*e.g.* trions, biexcitons) or defect-related such as donor-acceptor pairs or free electrons/holes with neutral acceptor/donor [Pelant 2012]. Among them, the most illustrative for the overall picture in semiconductor systems are the free electron-hole pair, excitonic and defect emission, which are schematically presented in Fig. 2.2.

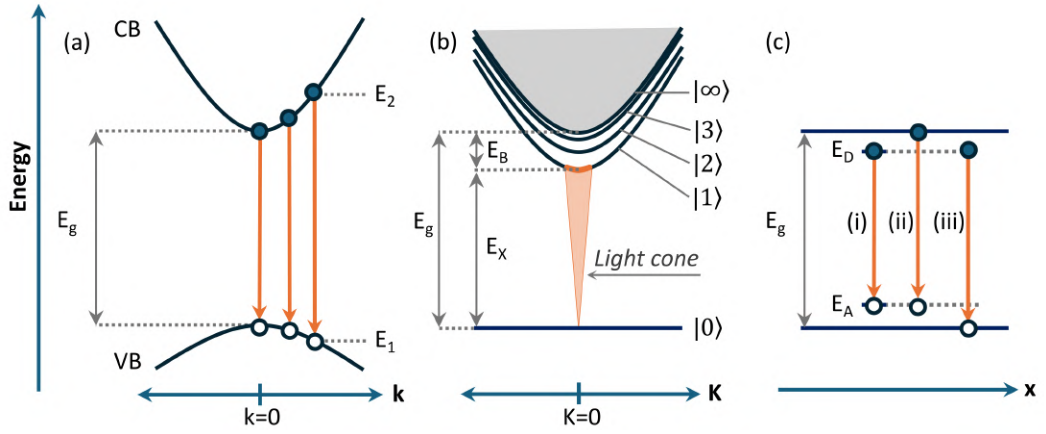

Figure 2.2: Typical radiative recombination types in semiconductors. (a) Band to band recombination in direct band gap semiconductors, (b) Excitonic recombination. Here the |n⟩ denotes the number in the exciton Rydberg series (|0⟩ being the ground state) and |∞⟩ corresponds to the free-particle limit continuum. (c) defect-related emission: (i) donor-acceptor, (ii) band-acceptor, (iii) donor-band. Here x (horizontal axis) denotes the spatial coordinate.

The free electron-hole pair (direct band to band) recombination emission (see Fig. 2.2 (a)) entails the recombination between the free electrons in CB and free holes in VB. As mentioned, this type of recombination belongs to the bimolecular process category since it requires interaction of two independent particles. The energy of the emitted photon is equal to the energy difference between the electron state in CB (E_2) and hole in the VB (E_1), satisfying the law of conservation of energy:

$$E_{photon} = E_2 - E_1. \tag{2.19}$$

In direct band gap semiconductors, the lower limit of the photon energy is thus naturally the value of the electronic band gap - E_g. Additionally, the radiative transition must meet the condition of conservation of the quasi-momentum $\hbar k$. Since the photon momentum $\hbar k_{photon}$ is very small ($k_{photon} \approx 10^{-3} a_0^{-1}$, where a_0 is the crystal lattice parameter) compared to the range of electronic band structure dispersion $E(k)$, the optical transitions can take place only if the wave vectors of the electron and hole have practically the same value *i.e.* $k_e = k_h$. Such transition between the two bands can be drawn as a vertical arrow, as depicted in Fig. 2.2 (a). The PL spectrum resulting from the combination of transitions at different k-values is the convolution of the density of states and thermal distribution of the carriers. At low temperatures, due to the efficient thermal relaxation of the free carriers, most free electrons and holes will predominantly recombine in the vicinity of the band edges at $k = 0$.

The excitonic (see more details on excitons in section 1.4) recombination, presented schematically in Fig. 2.2 (b), is a monomolecular process since the electron and hole constituting an exciton are correlated and act as a single quasi-particle.

Since the movement of the electron and the hole are correlated in an excitonic particle, the momentum is expressed in terms of the exciton wave vector ($\boldsymbol{K}$) giving the center of mass momentum $\hbar K$. The conservation of the momentum dictates that the excitonic transition can occur only within the photon momentum dispersion *i.e.* light cone, which is a region defined in the E($\mathbf{K}$) space by:

$$E \geq \frac{\hbar c|\boldsymbol{K}|}{\sqrt{\epsilon}}, \tag{2.20}$$

where the ϵ is the dielectric constant of the material. As the excitonic state is annihilated upon recombination, its momentum must vanish completely. Therefore the exciton can recombine only at the bottom of the exciton dispersion curve (see Eq. 1.7) at $K \approx 0$, as drawn in Fig. 2.2 (b). The energy of the exciton (E_X) is lower than the band gap energy E_g due to the binding energy E_B resulting from the Coulomb interaction between the correlated electron and hole. Taking into account the momentum conservation condition ($K \approx 0$) for the radiative recombination, the energy of the emitted photon E_{photon} is then simply:

$$E_{photon} = E_X = E_g - E_B. \tag{2.21}$$

Another type of emission present in semiconductors is the defect-related emission, such as for example the donor-acceptor, band-acceptor or donor-band transition, depicted in Fig. 2.2 (c) which involves electronic excitations localized in the crystal structure. The defect states are energetically located within the band gap of the material ($E_D < E_g$) and therefore are usually preferentially occupied by the thermally relaxing carriers (carrier trapping), which is often detrimental to the performance of devices. The radiative recombination originating from such states is also a monomolecular process with similar recombination dynamics as the excitonic one. Importantly however, the density of the defects in a given material is fixed. At low excitation powers, the luminescence intensity is a linear function of the excitation intensity as per Eq. 2.11, same as as for the excitonic emission. At very high excitation powers, in contrast to excitonic emission, the luminescence intenstity of defects becomes saturated when all recombination centers are already excited, and becomes constant, independent from the excitation intensity.

In the atomically thin TMD systems which are the subject of this thesis, the most important type of emission originates from the excitonic states. This is due to the very strong Coulomb interaction enhanced by their natural 2-dimensionality (spatial confinement) and the dielectric confinement, leading to large binding energies, making the excitons stable and primary features even at room temperature [Chernikov 2014].

2.1.3 Photoluminescence excitation

Photoluminescence excitation (PLE) is another absorption-type experiment in which a series of PL measurements is taken at varying excitation energies (E_{exc}). A PLE spectrum is constructed by plotting the PL intensity (I_{PL}) at a fixed emission energy (E_{PL}) or integrated intensity of specific emission peak as a function of the excitation energy. If we assume that the PL yield efficiency is independent on the E_{exc} and keep the excitation intensity constant (number of photons per unit of time and area) at all E_{exc}, then the PLE spectrum essentially recreates the absorption spectrum ($\alpha(E)$) of the material [Pelant 2012]:

$$I_{PL}(E_{PL}) \sim \alpha(E_{exc}), \tag{2.22}$$

which at the same time means that the higher the excitation power *i.e.* more photons absorbed, the more light is subsequently emitted. This simple picture does not take into account the possible non-linear effects or efficiencies of different processes such as carrier relaxation or transfer, nevertheless demonstrates the utility of PLE measurements as a simple technique for study of the opto-electronic properties of the material. It is a useful tool to complement the reflectivity measurement as it additionally provides practical information on the optimal excitation parameters for obtaining the best PL signal. An exemplary PLE spectrum of encapsulated monolayer WSe_2 together with reflectivity spectrum for comparison are presented in Fig. 2.3 Furthermore, since PLE is more sensitive to the intermediate processes happening between the absorption and emission, it can be used

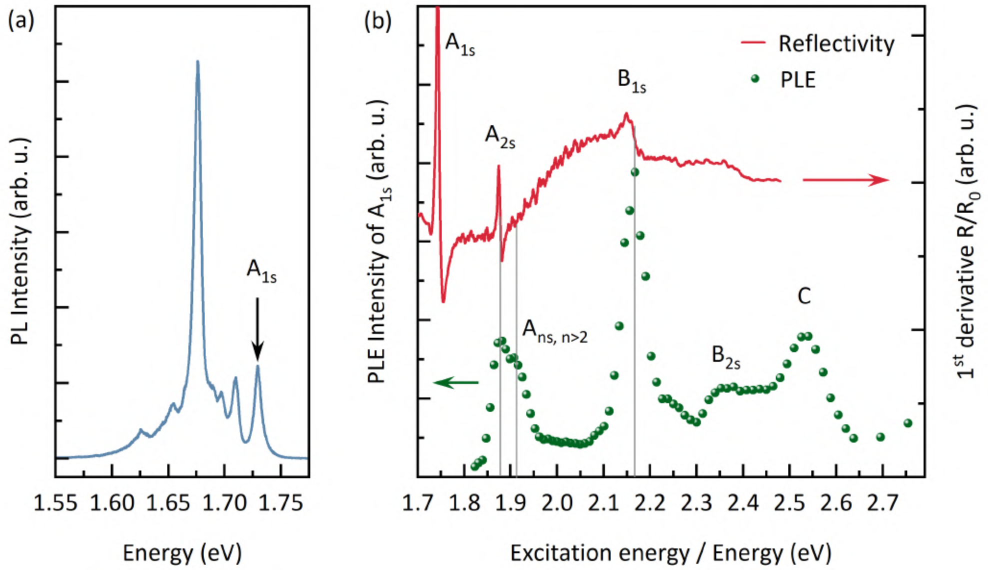

Figure 2.3: Exemplary PLE measurement and comparison with reflectivity on 1L-WSe_2: (a) PL spectrum of 1L-WSe_2 excited at the energy of B_{1s} resonance (~2.167 eV). Emission peak assigned to the A_{1s} exciton is marked. (b) Excitation energy-dependent (PLE) intensity of A_{1s} exciton and reflectivity in the form of the 1^{st} derivative of R/R_0. Both PLE show clear resonances at A_{2s} and B_{1s} transition energies. Additional features are visible in the PLE spectrum *i.e.* the high energy shoulder of the A_{2s} exciton, most likely originating from higher Rydberg states ($A_{ns,n>2}$), weak enhancement at B_{2s} transition energy and at C exciton.

for example to obtain information on energy or charge transfer processes, especially in more complex devices composed of more than one semiconductor material [Karpinska 2021, Karpińska 2022, Tanoh 2020, Zhang 2019, Kozawa 2016], which can occur due to the specific band/excitonic structures of constituent materials. Moreover, by employing additional techniques *e.g.* in the form of resolving of the PL polarization (described in section 2.1.4), one can study the dynamics of spin/polarization transfer. An example of such study will be presented in detail in this thesis in chapter 4, where the excitation energy dependent valley polarization properties of monolayer WSe_2 and $(BA)_2PbI_4/WSe_2$ heterostructure are studied.

2.1.4 Polarization-resolved measurements

Every optical transition, aside from conserving the energy and momentum, (as described earlier in section 2.1.2) must also conserve the total angular momentum $\vec{J}$, which is the sum of spin ($\vec{S}$) and orbital angular ($\vec{L}$) momentum ($\vec{J} = \vec{S} + \vec{L}$). The total angular momentum of a photon is ±1 in the units of reduced Planck constant $\hbar$. The transition must then satisfy a total angular momentum change of

$$\Delta J = \pm 1, \tag{2.23}$$

which is transferred to the emitted photon (or from an absorbed photon). This means that the transitions with the $\Delta J \neq \pm 1$ can not couple to photons, thus they are optically dark.

The total angular momentum at the same time defines the helicity of the photon polarization *i.e.* $J = -1 \rightarrow \sigma^+$ and $J = +1 \rightarrow \sigma^-$, which correspond to right-handed and left-handed circular polarization, respectively. On the other hand, a superposition of the left- and right-handed circularly polarized light results in the linear polarization. By resolving the polarization of the photon one can obtain additional information about the band structure properties and optical selection rules of the investigated material.

The circular polarization usually reflects the rotational symmetry of the investigated system. In this case, the helicity of the polarization corresponds directly to the total angular momentum of the emitting state *e.g.* an exciton. The study of circular optical polarization is especially important in TMD systems, which exhibit unusual polarization properties. These are related to the spin-valley locking effect [Yao 2008, Zhu 2011, Xiao 2012, Xu 2014, Yu 2015, Stier 2016], due to which the excitons localized in the opposite valleys K/K′ in their Brillouin zone only couple to the σ^+/σ^- polarized photons. This feature gives the possibility to selectively address or detect signal originating from the two valleys. (see details in sections 1.3 and 1.4.2). On the other hand, the linearly polarized emission usually indicates some form of anisotropy of the structure either intrinsic (*e.g.* low symmetry crystallographic structure) or extrinsic (*e.g.* anisotropic strain field), which is especially prominent in semiconductor nanostructures such as quantum dots or nanowires [Hu 2001, Kumar 2006, Lundskog 2014, Thomas 2021] and distorted 2D crystals such as 2D perovskites [Posmyk 2024b, Posmyk 2024a]. In TMDs, which nominally emit circularly polarized light, the linear optical polarization can be induced via application of anisotropic strain [Mitioglu 2018, Glazov 2022, Jasiński 2022], which breakes the rotational symmetry of the system. Alternatively, the linear optical polarization can arise via the valley coherence effect, through which, upon excitation with a linearly polarized source, which coherently excites both K and K′ valleys, the PL emission keeps the same linear polarization as that of the source [Jones 2013, Zhu 2014a, Hao 2016, Yu 2015, Wang 2015a, Dufferwiel 2018, Li 2024].

2.1.5 Raman scattering

Raman spectroscopy is a technique that utilizes the phenomenon of Raman (inelastic) scattering to probe the phonon spectrum of the measured material.

The scattering of light can be put in two main categories [Toporski 2018, Larkin 2017]: First, elastic scattering *i.e.* conserving the scattered photon energy. This is referred to as Rayleigh scattering. It results in the change of the direction of light without changing the photon energy. In solids, the Rayleigh scattering is usually the result of scattering on material impurities or irregularities (roughness) of the surface. Second type is the inelastic scattering *i.e.* Raman scattering. In this case both the direction and the energy of the photon are changed. In a solid material, the Raman scattering is related to scattering on the vibrational motion of the lattice *i.e.* phonons. The energy of the Raman scattered photon (E_{Raman}) will be increased or decreased with respect to the initial photon (E_0), depending whether an already existing phonon energy (E_{phonon}) was transferred to the photon or whether part of the photon energy was transferred to excite a new phonon in the lattice.

$$E_{Raman} = E_0 \pm E_{phonon}. \tag{2.24}$$

The scattered Raman light spectra can be separated into two parts, appearing on the low and high energy side of the initial excitation, and are referred to as Stokes and anti-Stokes Raman, respectively. The Stokes part of the spectrum is usually characterized by higher intensity, especially at low temperatures, than anti-Stokes, which due to the probability of encountering an already excited phonon being lower than that of the ground, unexcited vibrational state. For this reason, the analysis of the Raman spectrum usually focuses on the low energy, Stokes part. The three scattering types, *i.e.* Rayleigh, Stokes Raman and anti-Stokes Raman, are schematically drawn in Fig. 2.4 (a).

The phonon structure in semiconductors follows similar dispersion relation $E(k)$ as the electronic bands for electrons and holes [Peter 2010]. Two main categories of phonons are distinguished, namely acoustic (A) and optical (O) phonons. The acoustic phonons are characterized by a coordinated in-phase oscillation (atom displacement) which travels throughout the crystal lattice constituting a sound wave. Their energy (or frequency) is 0 at the center of the Brillouin zone ($k = 0$) and their dispersion ($E(k)$) is linear in the vicinity of that momentum space point. These do not interact with light because their dispersion falls outside of the light cone (as defined in Eq. 2.20). Additionally, along the high-symmetry directions of the crystal lattice, the longitudinal (LA) and transverse (TA) phonons can be distinguished which relates the direction of the atom displacement and the wave vector $\boldsymbol{k}$, *i.e.* parallel for LA and perpendicular for TA. The optical phonons on the other hand are the characterized by an out-of-phase motion of molecules and therefore require the correlated motion of at least two atoms. Their energy is non-zero at k=0 and therefore they meet the light cone requirement for coupling to photons. Similarly to acoustic phonons, the two types *i.e.* longitudinal (LO) and transverse (TO) can be distinguished.

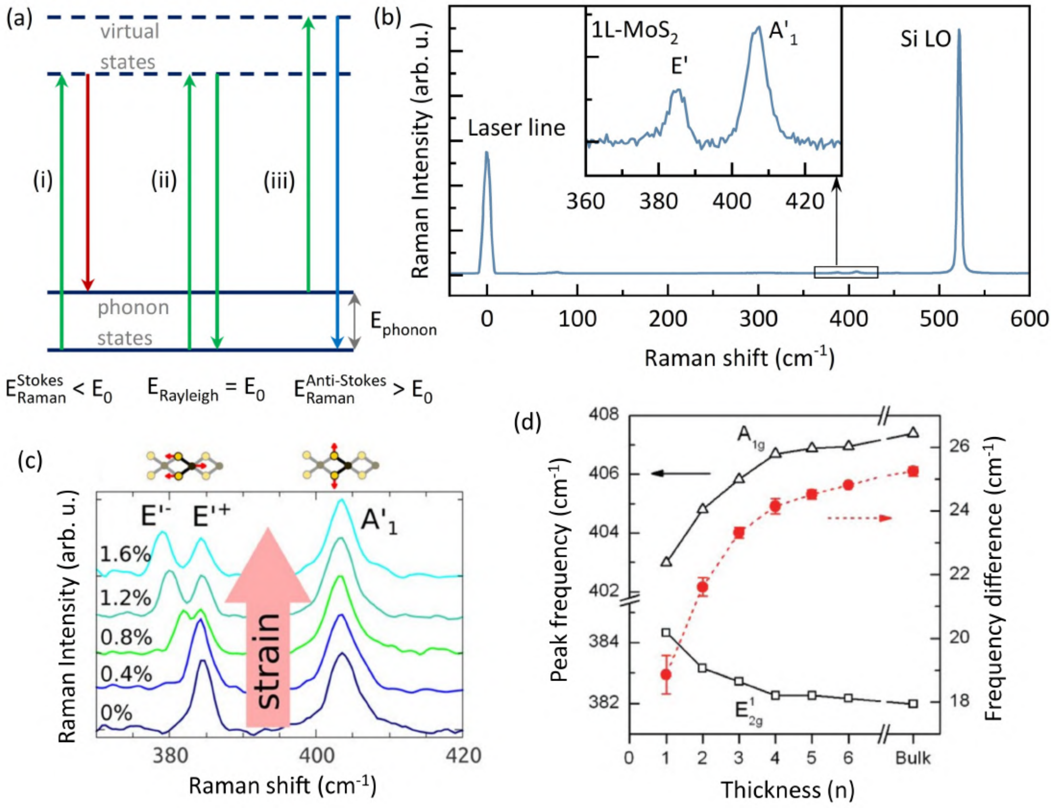

Figure 2.4: (a) Schematic representation of the Stokes Raman (i), Rayleigh (ii) and Anti-stokes Raman (iii) scattering events. (b) Exemplary Stokes Raman spectrum of monolayer MoS_2 deposited on Silicon (Si) substrate. Prominent longitudinal optical mode of the Si substrate (Si LO) and the characteristic monolayer MoS_2 in-plane (E') and out-of-plane (A_1') modes can be observed. (c) Evolution of Raman spectra for increasing level of uniaxial strain in MoS_2. At higher strain fields, the in-plane E' mode splits into E'^- and E'^+ due to breaking of the rotational symmetry. (d) Thickness (number of layers) dependence of the frequency of Raman modes E^1_{2g} and A_{1g} (multilayer counterparts to E' and A_1' in monolayer) as well as their frequency difference in MoS_2. Panels (c) and (d) are adapted from Refs. [Conley 2013] and [Lee 2010], respectively.

Typical Raman-active phonons energies present in TMDs, which are the subject of this thesis have energies in the range of few to few tens of meV, which is a very small detuning with respect to the incident laser. Therefore, use of a high quality laser with sufficiently low energy linewidth is required for proper spectral resolution of the Raman signal.

In this work, Raman scattering experiment was used as a probe to to detect and quantify the strain fields by tracking the change in the relevant Raman-active phonon mode energy and intensity. In particular, for atomically thin layers of TMDs, the frequency shift of E' mode (see exemplary Raman spectrum of monolayer $\mathrm{MoS_2}$ in Fig. 2.4 (b)) can be directly recalculated to strain using experimentally obtained gauges. For example, under biaxial tensile strain, the Raman mode frequency red shifts [Lloyd 2016, Michail 2023, Shin 2024] and the opposite is the case under compression [Hui 2013]. In the case of uniaxial tensile strain, due to breaking of the rotational symmetry, the degeneracy of the in-plane E'_1 mode is lifted at higher strain fields into a doublet – E'^{-} and E'^{+}, which are polarized along the major strain axes [Conley 2013, Dadgar 2018] as can be seen in Fig. 2.4 (c). Furthermore, the frequency separation $\Delta F = F_{\mathrm{A}'_1} - F_{\mathrm{E}'}$ depends on the thickness (number of layers) of a TMD flake which can be used to define the number of layers of the studied TMD sample as can be seen in Fig. 2.4 (d) [Lee 2010]. Similarly, the intensity of Raman modes also primarily depends on the sample thickness [Lee 2010].

2.2 Optical spectroscopy setup

The setup I used to realize the experiments presented in this thesis allows to perform a variety of optical experiments such as PL, PLE, reflectivity and Raman scattering as well as their more complex derivatives. The simplified schematic drawing of the setup is shown in Fig. 2.5.

The setup can be divided into three fundamental parts *i.e.* excitation, sample and detection. For PL, PLE and Raman scattering, a monochromatic excitation source such as a laser is used to photoexcite (PL, PLE) or scatter from (Raman) the sample. For measurements of reflectivity, a broadband white light source such as a Tungsten-halogen lamp is used instead. The light beam path is created by a series of mechanical and optical elements, such as mirrors, lenses, beam splitter cube. The light is focused on the sample by a x50 microscope objective with high numerical aperture (NA=0.55 or NA=0.75) providing high spatial resolution limited by the wavelength diffraction limit of around 1 μm. This corresponds to the size of the laser/white light spot. For example, using Rayleigh resolution criterion for typically used wavelength of 532 nm and objective of numerical aperture NA=0.55, we obtain $R.R. = 0.61\lambda/\mathrm{NA} \approx 0.59\,\mu$m. The signal from the sample is collected by the same objective and directed into the detection part where the signal is focused by a lens onto the entrance slit of a spectrometer (Teledyne Princeton Instruments HRS-500 or Acton SP-2300) coupled with a liquid nitrogen cooled CCD camera (Teledyne Princeton Instruments PyLoN) allowing for the spectral analysis of the

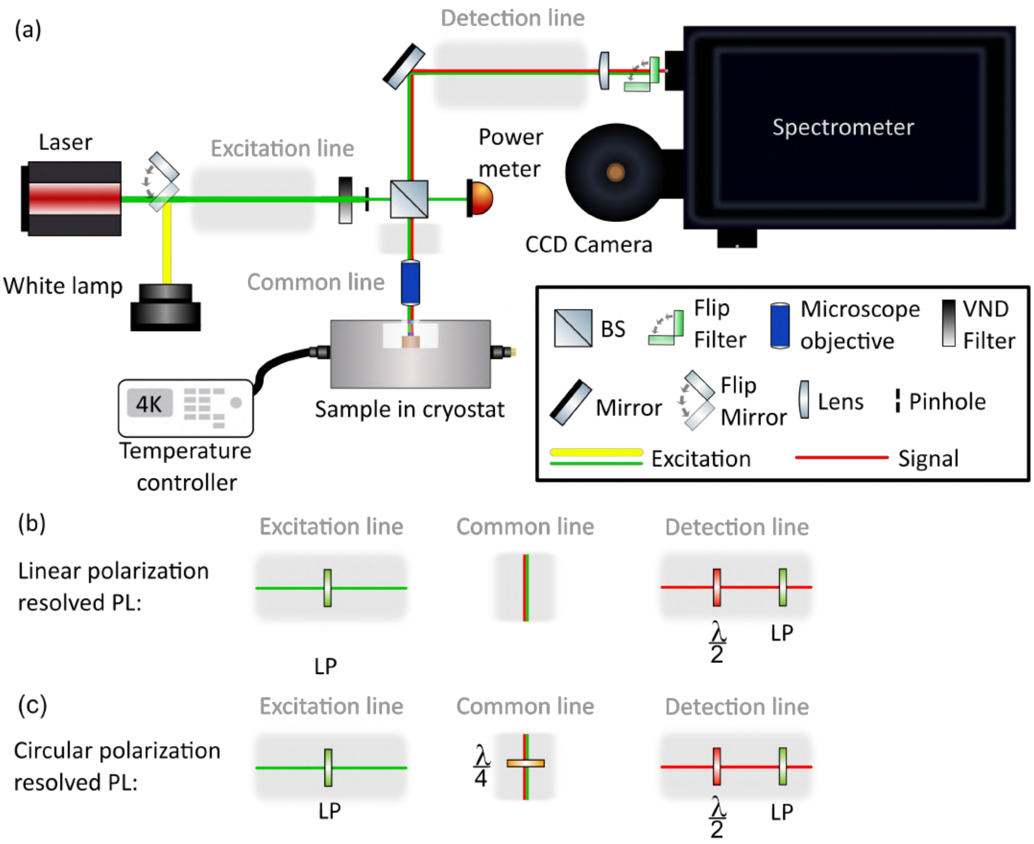

Figure 2.5: (a) Simplified schematic drawing of the optical spectroscopy setup. (b,c) Schemes of additional elements necessary to perform linear and circular polarization resolved measurements, respectively.

sample's optical response. Additional edgepass filter, adequate for the excitation laser protects the CCD camera from the high power laser beam reflected or Rayleigh scattered from the sample. In order to control the temperature of the sample, it is mounted on a cold finger inside the vacuum chamber of a helium flow cryostat (MicrostatHires Mk2). The combination of the cryogenic gas flow stimulated by an external pump and with regulated flux along with an in-built heater allows for stabilization of the temperature in the range of 3.4 K to 500 K.

The requirements of various experiment types necessitate either exchange of or addition of optical elements or switching of the light source, which is described below. Table 2.1 contains the list and parameters of the light sources used in experiments shown in this work.

Reflectivity measurements were performed with a broad-band source in the form of a halogen white lamp (Ocean Optics HL-2000) In this case, no elements perturbing the white light spectrum *i.e.* edge-pass filters were used.

For standard PL measurements a monochromatic, continuous wave excitation laser source was used, either 532 nm or 405 nm. During experiment, it is vital

Table 2.1: Light sources

Short name	**532 nm cw laser**	**405 nm laser**	**Ti:Saph + OPO**	**White lamp**
Name	MGL-III-532	Omicron Quixx® PS120	Coherent Chameleon	Ocean Optics HL-2000
Type	DPSS laser	Diode laser	Ti:Saph + OPO	Tungsten -Halogen lamp
Wavelength (nm)	532	405	Ti:Saph 680-1080, Ti:Saph SHG 340-540, OPO 1000-1600 OPO SHG 500-1000	360-2400
Operation mode	cw	cw/pulsed	pulsed	-
Repetition rate (MHz)	-	0-100	80	-
Pulse length (ps)	-	70/500	Ti:Saph ~0.15 OPO ~0.3-0.4	-

to filter out the part of excitation light that was reflected from the surface of the sample in order to protect the CCD camera as well as remove the features from the spectrum unrelated to the investigated structure. For that, edge-pass filters are used in front of the spectrometer slit with edge wavelength adequate for the used excitation source. Additionally, when necessary, additional filters, edge-pass or laser line filters are used in the excitation part of the setup for additional cleaning of the excitation spectrum.

The PLE measurements have been performed with a tunable Ti:Saph laser in conjunction with optical parametric oscillator (OPO) allowing for tuning of the excitation wavelength in a wide range.

In polarization-resolved measurements, in order to resolve the photon polarization, optical elements such as linear polarizers (LP) and retardation plates *i.e.* half-wave plate ($\lambda/2$) and quarter-wave plate ($\lambda/4$) must be implemented. For linear polarization, necessary additions to the setup are shown in Fig. 2.5 (b). On the excitation part a linear polarizer is used to properly clean the initial linear laser polarization. Optionally, a half-wave plate is used to rotate the angle of the exciting linear polarization *e.g.* to match the structural axes of the investigated structure. On the detection line, a $\lambda/2$ together with another LP form the analyser. The LP fixes the polarization angle incoming into the spectrometer in order to avoid the influence of the spectrometer grating efficiency dependence on the light polarization.

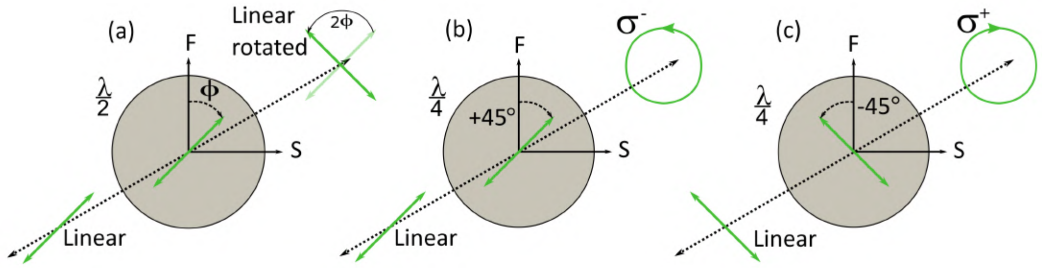

Figure 2.6: Scheme of the effects of retardation plates on light polarization. (a) Half-wave plate ($\lambda/2$) rotates the linearly polarized light by the angle $2 \times \Phi$, where the Φ is the angle between the initial light polarization and the fast axis (F) of the half-wave plate. (b,c) Linearly polarized light passing through a quarter-wave plate ($\lambda/2$) can be transformed into circularly polarized light provided the angle between the incoming light and the fast axis is 45° for left-handed (σ^-) or $-45°$ for right-handed (σ^-) helicity. Initial light polarization angle matching either fast or slow (S) axis results in no change to the polarization. For angles in between the aforementioned extreme cases, the resulting light polarization is elliptical. In the reversed scenario, when circularly polarized light passes through a quarter-wave plate, it is transformed to a linearly polarized light with angles defined by the light helicity and the orientation of quarter-wave plate axes. The opposite helicities of light are always projected into two orthogonal linearly polarized states.

The angle selection is made by rotating the $\lambda/2$ which projects the linearly polarized light onto the LP according to the working principle shown in Fig. 2.6 (a). In the case of analysis in circular polarization basis, an additional $\lambda/4$ is implemented which allows to transforms the linearly polarized into circularly polarized light (and vice versa), provided that a 45° angle between the light linear polarization and the slow axis of $\lambda/4$ is kept (see Fig. 2.6 (b,c)). In this work, a single $\lambda/4$ plate is used as shown in Fig. 2.5 (c), that serves a double role due to its placement in the common path of the excitation and detection beams. Initially linearly polarized laser light is transformed into either left-handed or right-handed circularly polarized light passing through the $\lambda/4$. The circularly polarized signal from the sample is transformed by the same $\lambda/4$ into linearly polarized light (see Fig. 2.6b,c). The previously left-handed and right-handed components of emission are transformed respectively into two orthogonal linearly polarized states. This way, the analyser composed of $\lambda/2$ and LP can be used in a similar manner to resolve the two helicity components of emission.

To realize a Raman scattering measurement, two important requirements have to be met: Firstly, the excitation laser line width has to be sufficiently narrow, which is achieved by the use of a cw laser (532 nm) with an additional laser line filter. Secondly, due to close energetic proximity of the excitation laser and the Raman features, the laser beam has to be sufficiently filtered out before entering the spectrometer and the CCD camera. To realize that, instead of a beam splitter cube, an adequate dichroic mirror (cut-off wavelength 532 nm) is installed which does not let the laser beam pass through into the detection line.

2.3 Electrical measurements

Part of the experiments realized in this work (chapter 5) rely on the controlled application of the electric field and free carrier doping in gated devices. To realize that, substrates with gated samples (details further below) are installed in 20 I/O pin chip carriers (Kyocera® ceramic package), shown in Fig. 2.7 (a), which are then placed in a custom-made adapter for the cryostat (depicted in Fig. 2.7 (b)). The adapter consists of several elements depicted in Fig. 2.7 (c). The copper mount comprises a thin base for mounting and a 5mm x 5mm column in the center extending vertically. The PCB (printed circuit board) mounted on the base of the copper mount (around the central column) features twenty gold-plated pads, five on each side, matching the arrangement of the gold pads of the chip carrier (see Fig. 2.7 (a) and (d)). The oppositely located pairs of pads are electrically shorted. Each pair is connected to an output pin, giving 10 output pins in total. These pins are subsequently connected separately to the ten cryostat pins inside the vacuum chamber via insulated silver-plated copper wires (ÖLFLEX® HEAT 260). The insulating plastic positioner, placed on top of the PCB, features 20 vertical bores matching the arrangement of the PCB and chip carrier pads. These contain spring-loaded pins which make physical contact with the PCB pads on the bottom side and protrude out of the positioner on the top. The chip carrier is positioned on top of the spacer so that the chip carrier pads (located on the ridges of the bottom surface) make contact with the spring-loaded pins. At the same time, the middle part of the bottom surface of the chip carrier makes physical contact with the protruding copper column providing thermal contact. Top securing plate is installed with two screws (see top view of the adapter in Fig. 2.7 (d)), which allows to slightly press the chip carrier down onto the pins engaging the springs and improving physical contact with the copper column. A small amount of silver paste (alternatively rubber cement glue - Fixogum®) is put between the copper and chip carrier to improve the thermal contact. This design guarantees good electrical connection between the sample and the rest of the electrical connections without the need for soldering, at the same time providing an easy way of exchanging samples. To selectively apply voltage to a given contact, an electrical cord is used to connect the 10-pin electrical output of the cryostat and a break-out box with ten numbered BNC sockets each corresponding to a specific contact reaching the sample. Two single-channel voltage sources, VS1 (Keithley series 2400 Sourcemeter) and VS2 (Yokagawa GS200 DC Voltage/Current source), can be connected simultaneously to desired contacts for voltage application, as depicted in Fig. 2.7 (e). On the other hand, in order to ground a given contact, a BNC terminator is plugged into a corresponding socket. It serves to short the electrical path with the metal casing of the break-out box, which itself is grounded by securing it to the grounded surface of the optical table.

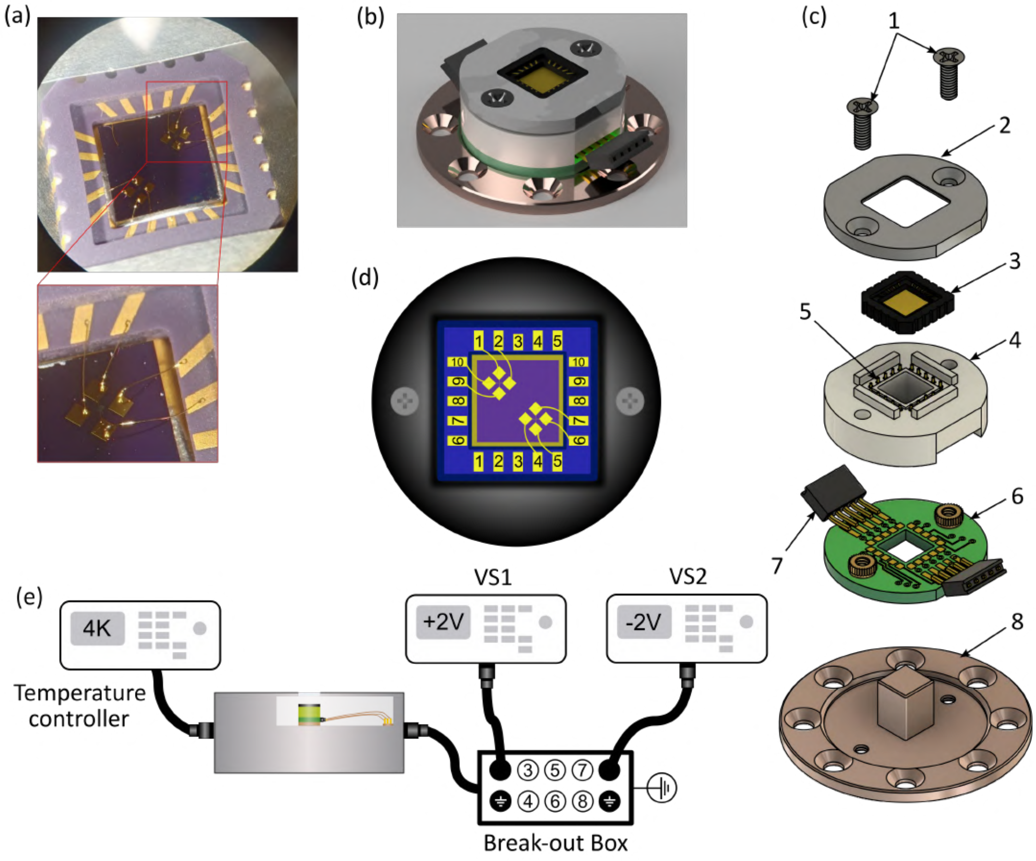

Figure 2.7: Electrical measurement setup. (a) Microscope image of a real sample, bonded and installed in a chip carrier. (b) 3D visualization of the electrical measurements sample adapter. (c) Schematics of the adapter elements: 1 - M2 screws, 2 - securing top plate, 3 - chip carrier, 4 - insulating plastic positioner, 5 - spring-loaded pin, 6 - PCB, 7- 5 wire-pin connector, 8 - modified copper mount. (d) Schematic top view of the adapter with installed sample in a chip carrier. (e) Schematic drawing of the setup for electrical measurements. First electrical output of the cryostat is connected to the temperature controller, while the second (output of the pins inside the cryostat) is connected to a break-out box with BNC sockets, which allows to externally connect to the 10 available electrical paths inside the cryostat. The metal casing of the break-out box is grounded. An exemplary connection is shown: voltage sources connected to sockets 1 and 9, terminators (path grounding) plugged in sockets 2 and 10.

2.3.0.1 Fabrication of double-gated devices

The electrically contacted devices presented in chapter 5 are designed in a parallel plate capacitor like structure. They feature two electrical gates *i.e.* the bottom gate (BG) and the top gate (TG), which are the bottom-most and top-most layers of the structure, respectively. The active TMD layer is positioned in the center of the device. The insulating spacers in the form of hBN are used between the TMD and the two gates to isolate them electrically. Additional electrodes (at least one) are in direct contact with the TMD layer providing electrical grounding (grounding contacts). All electrodes are made of few layer graphite (FLG) flakes, which is a conductive, semi-transparent material. The scheme of the device structure is presented in Fig. 2.8 (a).

The substrates (chips) used for fabrication of the devices are pre-patterned with evaporated gold pads to provide electrical connections. These are made by first evaporating a thin layer of adhesion-improving metal layer (here, 11 nm of titanium) followed by evaporation of 100 nm of gold (see Fig. 2.8 (b)). Two areas, each featuring four gold pads ($\sim$ 350 μm^2), are located in the opposite corners of the substrate, arranged as depicted in Fig. 2.7 (b) and (e). Narrow gold paths ($\sim$ 5μm) extend from the gold pads into the central space *i.e.* the sample area, in which the devices are assembled flake by flake via the all-dry transfer method [Castellanos-Gomez 2014] (see section 2.4). All FLG electrodes are deposited so that they overlap the nearby gold paths providing electrical connection with the larger gold pads. Schematics of the top view of the sample area together with an exemplary arrangement of the flakes is shown in Fig. 2.8 (c).

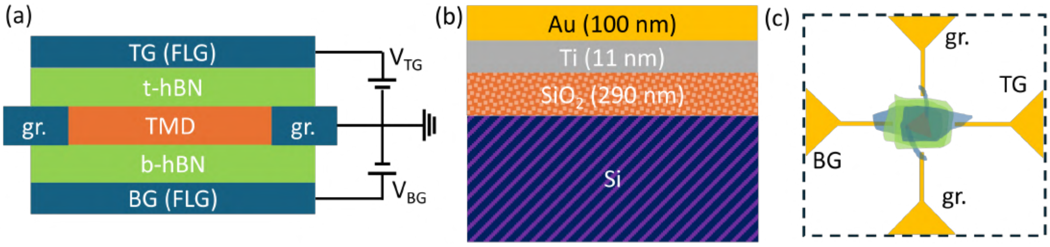

Figure 2.8: (a) Schematics of the double-gated device with marked electrical connections. “gr.” denotes the grounding FLG electrodes. (b) Schematical top view of the sample area between the gold pads. The shaded shapes correspond to flakes constituting the device shown in (a), with corresponding colors. (c) Schematical cross-section of the evaporated gold pads on the Si/SiO$_2$ substrate. On top of the natural Si/SiO$_2$ surface, a thin layer of titanium followed by 100 nm of gold layer is deposited.

With the structure assembled, the substrate is subsequently installed in a chip carrier using a two-ingredient epoxy glue (EPO-TEK® H20E). The gold evaporated contacts on the substrate are then wire bonded (with a 25 μm gold wire) to the contacts on the chip carrier as depicted in Fig. 2.7 (b) and (e). The completed chip carrier is then ready for installation within the custom made electrical adapter for the helium flow cryostat as described in the previous subsection.

2.3.0.2 Application of electric field and free carrier doping

In the complete device, the individual electrical connections to bottom and top gates as well as the grounding contacts can be connected to voltage sources or grounded.

The typical connection scheme entails grounding of all the grounding contacts, while the voltage is actively applied independently to the bottom (V_{BG}) and top (V_{TG}) gates.

The two gates are characterized by their geometric capacitance per unit of area:

$$\begin{aligned} C_{TG} &= \frac{\epsilon_0 \epsilon_{hBN}}{d_{t-hBN}}, \\ C_{BG} &= \frac{\epsilon_0 \epsilon_{hBN}}{d_{b-hBN}}, \end{aligned} \tag{2.25}$$

which depend on the out-of-plane dielectric constant of the insulating hBN spacer (ϵ_{hBN}) and its thickness d_{b-hBN}/d_{t-hBN}, for the bottom and top hBN respectively. Based on the parallel plate capacitor model [Leisgang 2020], application of voltage to each gate controls independently displacement field to the active material (TMD) inside the device:

$$\begin{aligned} D_{TG} &= C_{TG}(V_{TG} - V_{TG}^0), \\ D_{BG} &= -C_{BG}(V_{BG} - V_{BG}^0), \end{aligned} \tag{2.26}$$

where the $V_{BG/TG}^0$ are the offset voltages, related to the presence of intrinsic unintentional doping. The displacement field induces both the free carrier doping (*i.e.* shifting of the Fermi energy) and the uniform out-of-plane electric field (E_z). The contribution to the induced carrier doping from the each gate as a function of applied gate voltage can be formulated as:

$$\begin{aligned} n_{TG} &= \frac{1}{e} C_{TG}(V_{TG} - V_{TG}^0), \\ n_{BG} &= \frac{1}{e} C_{BG}(V_{BG} - V_{BG}^0), \end{aligned} \tag{2.27}$$

where e is the elementary charge.

The total free carrier doping is the sum of the induced carrier density related to the bottom and top gates [Leisgang 2020]:

$$n = n_{TG} + n_{BG} = \frac{\epsilon_0 \epsilon_{hBN}}{e} \left(\frac{(V_{TG} - V_{TG}^0)}{d_{t-hBN}} + \frac{(V_{BG} - V_{BG}^0)}{d_{b-hBN}} \right) \propto \frac{V_{TG}}{d_{t-hBN}} + \frac{V_{BG}}{d_{b-hBN}}, \tag{2.28}$$

Meanwhile, the effective out-of-plane electric field E_z within the TMD can be calculated from the effective displacement field via $D = \epsilon_0 \epsilon_{TMD} E_z$, which gives [Leisgang 2020]:

$$E_z = \frac{\epsilon_{hBN}}{2\epsilon_{TMD}} \left(\frac{(V_{TG} - V_{TG}^0)}{d_{t-hBN}} - \frac{(V_{BG} - V_{BG}^0)}{d_{b-hBN}} \right) \propto \frac{V_{TG}}{d_{t-hBN}} - \frac{V_{BG}}{d_{b-hBN}}, \tag{2.29}$$

where ϵ_{TMD} is the out-of-plane dielectric constant of the TMD sample within the device.

By analysing the above equations for n and E_z, it is clear that a double gated device allows for independent control of the two effects. The free carrier doping scales with the sum of the gate voltages divided by their respective hBN layer thickness (Eq. 2.28), while the electric field scales with their difference (Eq. 2.29). Therefore, applying the gate voltages (V_{TG} and V_{BG}) of the same polarity with a ratio that accounts for unequal hBN thicknesses (*e.g.* $\frac{d_{t-hBN}}{d_{b-hBN}} = \frac{1}{2} \rightarrow \frac{V_{TG}}{V_{BG}} = \frac{1}{2}$) induces free carrier doping while the E_z is invariant. If the gate voltages polarities are opposite (*e.g.* $\frac{V_{TG}}{V_{BG}} = -\frac{1}{2}$), then the E_z can be tuned while the induced carrier concentration n is set. Diverging from the optimal voltage ratio in either of the two modes leads to both effects being present simultaneously.

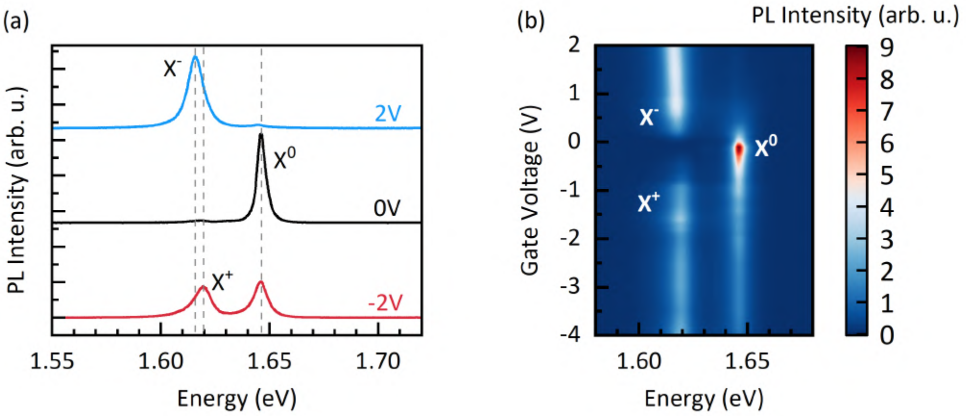

Figure 2.9: 1L-MoSe$_2$: (a) PL spectra at different gate voltages. X^0, X$^-$ and X$^+$ denote the neutral, negatively charged and positively charged exciton, respectively. (b) False-color map of PL intensity as a function of gate voltage.

An example of the effect of a single gate control is shown in Fig. 2.9, where PL spectra of 1L-MoSe$_2$ are plotted a function of the gate voltage. Application of the voltage to a single gate generates both the uniform electric field as well as induces carrier doping. The monolayer MoSe$_2$ spectrum shows a clear change between the doping regimes, consistent with prior reports [Shepard 2017], meanwhile the effect of the out-of-plane electric field is negligible as expected for monolayers where excitons are strongly confined in-plane. A double-gated device based on a natural homobilayer of MoSe$_2$ is studied in chapter 5, where the independent doping and out-of-plane electric field measurements, utilizing a double-gated control, are presented.

2.4 Fabrication by all-dry transfer method

The all-dry flake transfer method [Castellanos-Gomez 2014] is a well established and relatively simple method for fabrication of van der Waals structures composed of virtually limitless number of constituent layers. The process is based on exfoliation of atomically thin flakes of a given material from the bulk crystal and subsequent deposition by visco-elastic transfer as described in the following steps:

1. Bulk crystal of the material (TMD, hBN or graphite) is cleaved to uncover clean and smooth surface.

2. An adhesive tape is subsequently placed on the smooth surface and then slowly ripped off, so that thin flakes of the material remain on the tape, which is referred to as exfoliation.

3. Another tape is then placed on the first tape. The two are then slowly taken apart, which results in further thinning of the material flakes, which divide between the two tapes. This process is repeated several times, also with fresh tapes in order to obtain tape pieces containing reasonably thin flakes of the material.

4. From the selection of available tapes, a chosen one is placed on a square sheet of PDMS (Polydimethylsiloxane) gel of approximately $1\,\mathrm{cm}^2$ in size, which is pre-mounted on a microscope glass slide. The tape is then slowly ripped off from the PDMS sheet, which leaves the exfoliated flakes on the PDMS.

5. Microscope glass slide containing PDMS with exfoliated flakes is placed under the microscope. The flake with desired properties (number of layers, size, shape, smoothness) is found by manual search under the microscope via optical contrast. Fluorescent microscopy can also be used to detect the emission originating from TMD monolayers, by illuminating the PDMS with an ultraviolet instead of the white light.

6. Once the appropriate flake has been found, the glass slide containing it is installed upside down in a holder mounted on stages, which allow for fine movement in all three directions.

7. A substrate, usually silicon, is mounted on the heater stage under the microscope.

8. The glass slide containing the flake and the substrate are aligned under the microscope, so that the flake can be deposited in a desired spot. Additionally a manual rotation of the substrate is used when angle-aligning is required *e.g.* with another, already deposited flake or with structures such as evaporated gold pads.

9. Substrate is heated to moderate temperatures of 60-90° Celsius, which aids in adhesion between the flake and the substrate.

10. Flake is deposited by slowly coming in contact of the PDMS and the substrate. After a short period of $\sim$ 2 minutes. The PDMS is very slowly lifted off the substrate. The viscoelastic properties of PDMS result in the flake remaining on the substrate.

11. After successful deposition, the substrate is annealed for $\sim$ 15 minutes at higher temperatures of $\sim$ 150° in order to improve adhesion of the flake to

the substrate and at the same time to remove air bubbles, which tend to form during the deposition.

12. For multi-layered devices, the process described in points (1-11) is repeated and subsequent flakes are stacked on top of each other to form the desired device structure.

Chapter 3

Anisotropic strain effects in MoS_2 monolayer

Monolayer flakes of TMDs have been shown to exhibit robust durability against applied external strain reaching up to 10 % [Bertolazzi 2011]. This fact paves the way for effective straintronics applications in TMD devices. Stress in TMDs can be applied using two approaches. First, on the "macro" level either by mechanical bending on a flexible substrate, piezoelectric substrates or other mechanical systems [Rice 2013, Hui 2013, Zhu 2013, Dadgar 2018, Christopher 2019, Martín-Sánchez 2017]. The stress level can be tuned continuously, but it affects the whole sample uniformly. Secondly, on a "micro" level by deposition on patterned substrates or nanostructures *e.g.* nanopillars, the morphology of which deterministically induces local stress in the deposited flake [Palacios-Berraquero 2017, Branny 2017, Wang 2021b, Ji 2023, Kumar 2015]. Usually, the patterning is done in dielectric SiO_2 on SiO_2/Si substrate. The SiO_2, however, suffers due to high surface roughness and dangling bonds, which may be suboptimal for the device performance [Koperski 2015]. Thus, development of alternative high quality materials for deterministic patterning is required. One such attractive material system is the III-V epitaxial semiconductors, technology of which is highly developed. The advanced state of epitaxial growth and processing of III-V crystals allows for a vast playground with plethora of varying in shape nanostructures of high quality, which can be grown deterministically.

In this chapter, I show the results of the investigation of the optical properties of monolayer MoS_2 deposited on deterministically grown nanostructures in the form of GaAs nanomembranes. The studies comprised the determination of how the nanostructured pattern affects the strain distribution and excitonic properties. This is probed by spatially resolved optical spectroscopy measurements such as Raman scattering, PL, and reflectivity. Furthermore, by resolving PL in linear polarization basis I tested whether the imposed strain impacts the excitonic fine structure via changes to the symmetry of the system.

3.1 Sample structure

The samples on which I performed the optical measurements have been fabricated and characterized by AFM (Atomic Force Microscopy) and SEM (Scanning Electron Microscopy) in École Polytechnique Fédérale de Lausanne (EPFL) in the group lead by Anna Fontcuberta i Morral. Their expertise in MBE (Molecular Beam Epitaxy) growth of nanostructures [Tutuncuoglu 2015] presented a possibility to study TMDs deposited on high quality GaAs patterned substrates.

3.1.1 Fabrication of GaAs nanomembranes

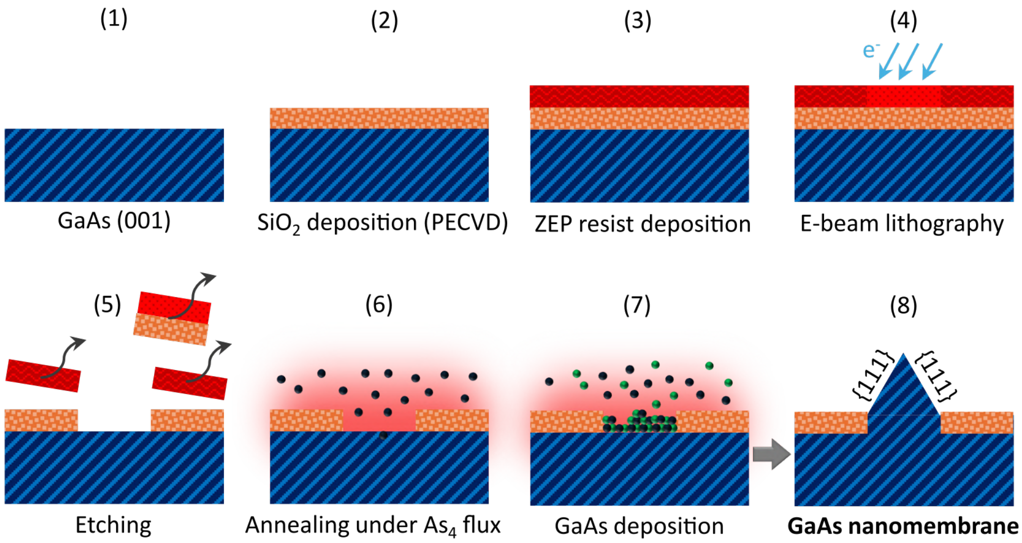

Figure 3.1: Nanomembrane growth procedure starts with a prepared, clean substrate of undoped (001) GaAs (1) on which 25 nm of SiO_2 mask is deposited by PECVD (2). Next, a layer of ZEP resist is deposited (3). Electron beam lithography is then performed to deterministically define the pattern in the resist (4), followed by development in n-amyl acetate. Next, the pattern in SiO_2 mask is etched in a two step etching (5). First, fluorine chemistry dry etching, followed by wet etching in HF solution. Afterwards, the substrates are placed in the MBE system. Before the growth, the substrates are annealed at 630° under As_4 flux (6). Further, at 610° Ga deposition together with As_4 flux allows for GaAs growth in the SiO_2 mask openings (7). The defined patterns of the SiO_2 mask and the crystallographic properties result in the growth of GaAs in the form of nanomembranes (8).

For the pattern of nanostructures acting as the stressor for TMD flake, we have chosen GaAs nanomembranes (NMs). These are essentially horizontally grown nanowires of triangular cross-sections defined by the crystallographic directions of GaAs. As depicted and detailed in Fig. 3.1, the growth of the NMs starts with deposition of an SiO_2 mask on a clean, undoped GaAs substrate. Then, via E-beam lithography and etching, an appropriate pattern of openings is created. Subsequently, during MBE deposition of GaAs, the material grows only within the pattern-defined slits, forming the NMs. Their size is determined by the size of the etched openings. Fig. 3.2 shows the SEM images of an exemplary substrate with the pattern of NMs. In panel (a), three adjacent NMs, part of an array, are presented showcasing high precision of the growth process. In a close-up view of a single NM (panel (b)) we can see the triangular shape of the NM cross-section and part of the surrounding flat surface with thin 25 nm layer of SiO_2 mask. Panel (c) presents the top SEM view of the NMs with marked crystallographic directions. The NMs are elongated along the <0-11> direction.

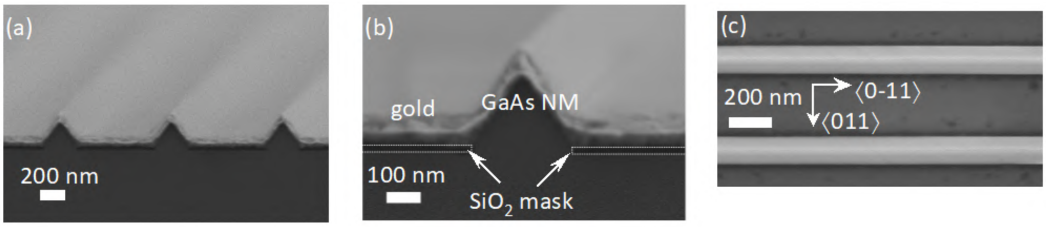

Figure 3.2: SEM images of an exemplary substrate with nanomembranes. Here, gold is evaporated on the surface to provide contrast for SEM imaging. These images present a different substrate to the one used in the experiments presented chapter. (a) View from the side of a cleaved substrate (b) Zoom-in side view of a single NM. (c) Top view of the nanomembranes with marked crystallographic directions.

In the investigated sample, the NMs are arranged in arrays with a separation of 1 μm between adjacent NMs. Their width is nominally $\sim$ 50 nm, and length is 20 μm. Such design aims to impose periodic, uniaxial stress on the deposited TMD flake.

3.1.2 MoS_2 flake deposition and AFM characterization

For the TMD material, we chose an MoS_2 monolayer. This material is relatively easiest technically in terms of achieving large flake sizes and at the same time the most studied among other TMD materials. In particular, MoS_2 monolayer was the one demonstrated to withstand the highest stress of $\sim$ 10 % before breaking, [Bertolazzi 2011] making it optimal for the strain engineering. The flake was obtained via exfoliation of MoS_2 crystal by a scotch tape and subsequent deposition on viscoelastic material (PDMS). The flake was then stamped on top of the nanomembrane array using the established all-dry transfer method [Castellanos-Gomez 2014]. The results of the stamping are presented in the optical images shown in Fig. 3.3. Large monolayer (1L) part and smaller bilayer (2L) part can be distinguished by the optical contrast. Additionally, local morphological features such as wrinkles and fractures in the flake can be observed (Fig. 3.3 (a)). The sample includes also a small 1L located outside of the NM arrays on the flat part of the substrate (Fig. 3.3 (b)), thus being nominally unstrained and therefore suitable as a reference in further optical characterization.

To characterize the flake morphology after deposition we performed the AFM measurements. Fig. 3.4 shows an AFM map (Fig. 3.4 (a)) of a region at the edge of the deposited flake and bare, uncovered NMs, to compare the height profiles from the two areas (Fig. 3.4 (b)). As can be seen from the comparison of the AFM

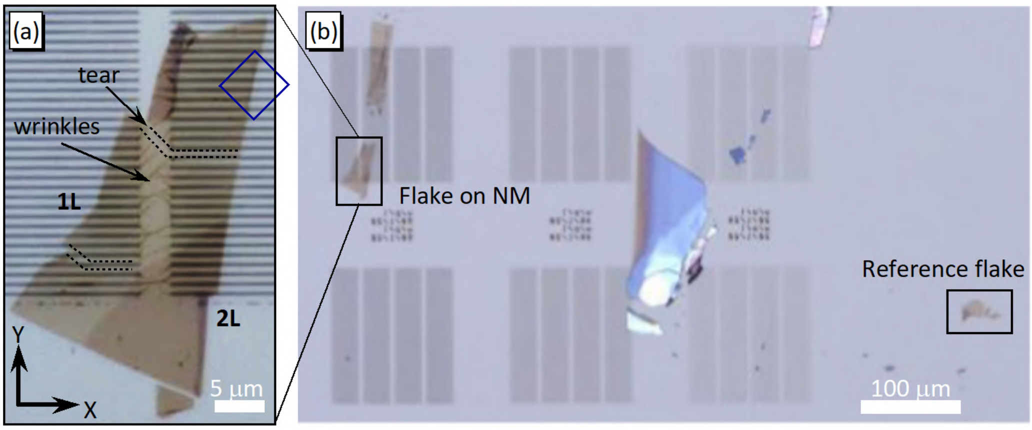

Figure 3.3: (a) Microscope image of the MoS_2 flake deposited on GaAs nanomembranes. The blue rectangle denotes the AFM scan area presented in Fig. 3.4 (b) Wider area view showing both the investigated flake on nanomembranes as well as a small monolayer flake (Reference flake) located outside of the NM arrays.

cross-sections across the bare NMs and NMs covered by the MoS_2 flake we can see a very good conformity of the monolayer to the nanostructures. The flake does not adhere completely to the nanomembranes, forming a tent-like structure across, and seems to be slightly elevated (a few nm) above the in between flat surface. Nevertheless, the observed morphology of the deposited flake points to the presence of the uniaxial tensile strain, particularly around the tips of the NMs, with the major axis (stretching direction) across the NMs.

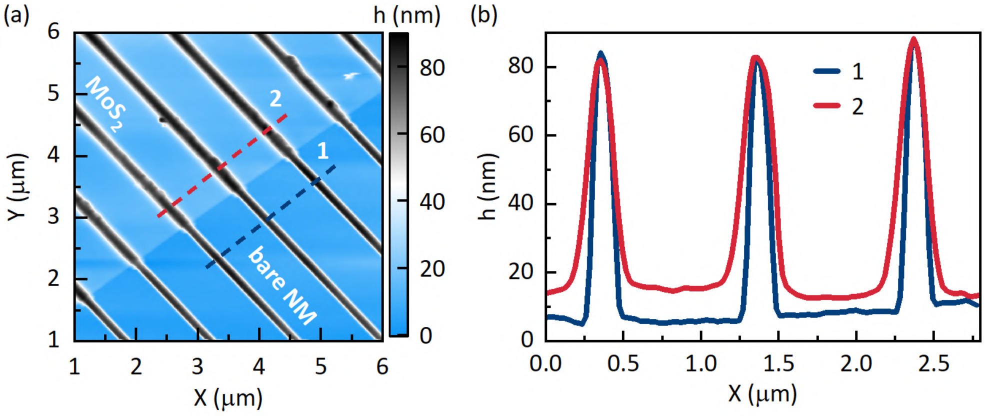

Figure 3.4: (a) AFM scan of a 6x6 μm^2 area at the edge of the flake and bare exposed NMs. The false-color map corresponds to the height - h. (b) Comparison of cross-sections taken across bare NMs (1) and across NMs covered with the deposited MoS_2 flake (2).

Additional AFM measurements from different parts of the flake are shown in

Fig. 3.5. Inside the the middle parts of the NMs, the flake conforms quite well keeping a reasonable homogeneity although some local fractures can be observed in the form of tears in the flake, an example of which is shown in Fig. 3.5 (a,d). At the ends of the NMs on the other hand, the flake tends to form wrinkles extending out, (see Fig. 3.5 (b,e)), which includes the few micrometer gap between adjacent NM arrays. There, plethora of wrinkles have formed, connecting the neighbouring NMs. Such dense formations of wrinkles might perturb the uniformity of the distribution of strain across the deposited flake.

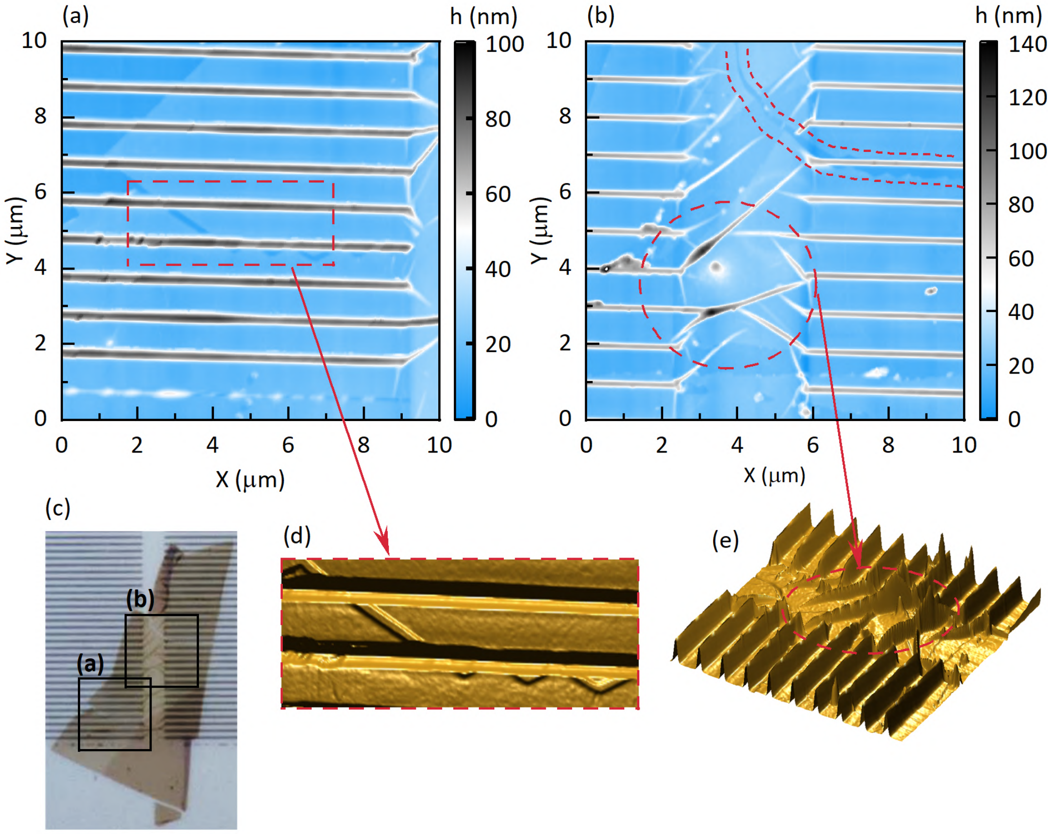

Figure 3.5: (a) False-color map of AFM height in the area of the flake located inside the NM array. The dashed red rectangle marks a fracture in the flake. (b) False-color map of AFM height centered at the gap between two adjacent NM arrays. Additional fractures and formations of wrinkles can be observed. (c) Micrograph of the sample with marked areas of AFM mapping corresponding to graph (a) and (b). (d) and (e) 3D AFM visualizations from the marked (red dashed lines) areas in panel (a) and (b), respectively.

The AFM characterization shows that although the process of fabrication is in principle deterministic, many factors influencing the deposition and details of design ultimately decide the structure homogeneity. The result overall is successful and allows to make a step in the direction of deterministic and repeatable structure engineering.

3.2 Optical characterization

In this section, I present the results of the optical characterization performed on the MoS_2/Nanomembranes structure. The goal of the measurements was the study of the impact of nanomembranes on the optical properties of monolayer MoS_2. These experiments included spatially resolved Raman scattering, photoluminescence, and reflectivity, which can be used to estimate the character and spatial distribution of strain. Finally, I measured photoluminescence resolved in the linear polarization basis in order to determine the effect of strain on the excitonic fine structure.

3.2.1 Probing strain by Raman modes

To obtain information about the distribution of strain I performed the Raman scattering experiment as the first step in the optical characterization of the sample. Raman modes depend directly on the crystallographic structure and the lattice parameters. Application of strain changes the lattice parameters, therefore its effects can be observed and estimated by measuring the change in the frequency (energy) of the Raman modes. In TMDs, the characteristic in-plane E' and out-of-plane A_1' Raman-active vibration modes [Molina-Sanchez 2011] are commonly used to estimate the level of strain [Rice 2013, Hui 2013, Zhu 2013, Dadgar 2018, Christopher 2019]. Here I measured the spatially resolved Raman response from the sample, from which I determined the position-dependent intensities and frequencies of the Raman-active modes *i.e.* the GaAs LO mode and the E' and A_1' Raman modes of MoS_2. The intensities of MoS_2 Raman modes along with the frequency separation between them, give information about the thickness (number of layers) of the measured flake. The shift in frequencies, especially the in-plane E' mode, on the other hand, allows for estimation of the level and character (*i.e.* tensile or compressive) of strain. The effectiveness of the nanomembranes in deterministic imposition of strain can be determined by spatially correlating the Raman frequency shift with the morphology of the structure.

Raman scattering measurements were performed at cryogenic temperature ($\simeq 5\,\mathrm{K}$) with 532 nm cw laser at $P = 2\,\mathrm{mW}$ power. First, in Fig. 3.6 (a) I compare the Raman spectra taken from the bare NMs, NMs with 1L-MoS_2 and 2L-MoS_2. At $\simeq 295\,\mathrm{cm}^{-1}$ a strong characteristic longitudinal optical (LO) mode of GaAs can be observed, which is the only resonance in the spectrum of bare NMs in the presented frequency range. In spectra taken at spots with deposited MoS_2 at $\simeq 386\,\mathrm{cm}^{-1}$ and $\simeq 407\,\mathrm{cm}^{-1}$ appear the characteristic MoS_2 modes E' and A_1', respectively. As can be seen the frequency separation $\Delta F = F_{\mathrm{A}_1'} - F_{\mathrm{E}'}$ between the two modes and their intensities increase for the spectrum taken at 2L-MoS_2/NM as compared 1L-MoS_2/NM to confirming the 1L and 2L assignment. Next, in Fig. 3.6 (b,c,d) I show the intensities of the three Raman modes: GaAs LO and MoS_2 E' and A_1', respectively. For the GaAs LO we can distinguish the areas of NM arrays and the

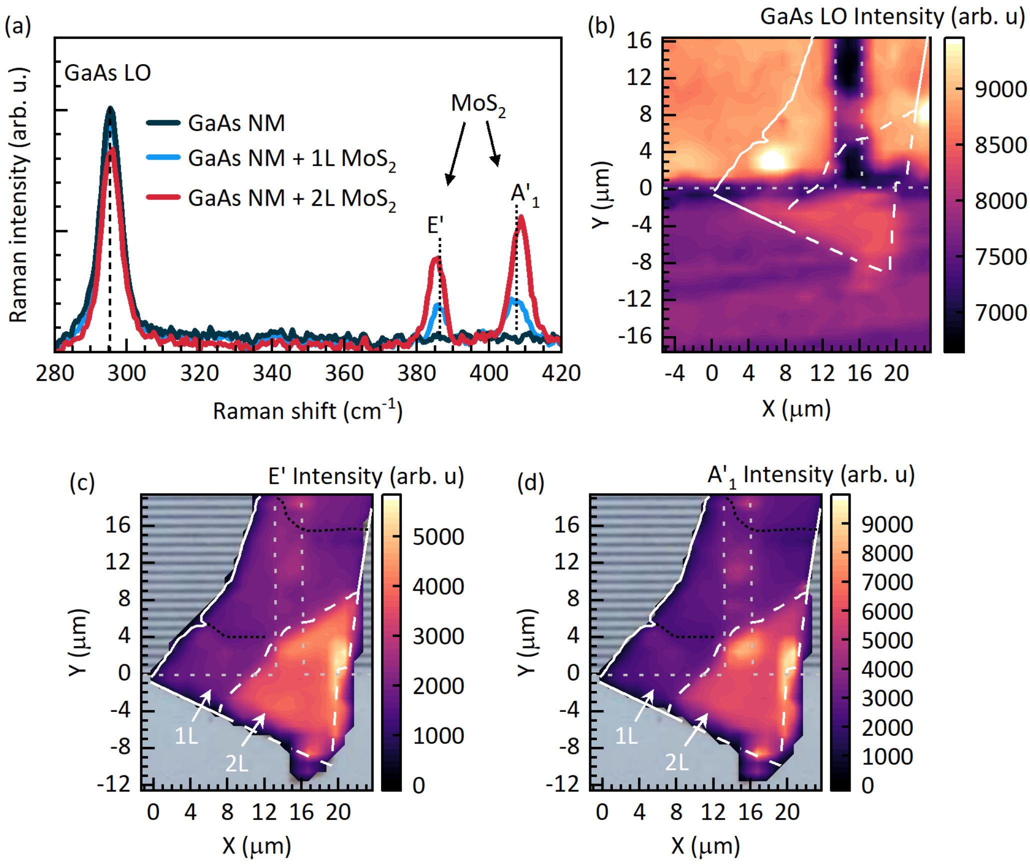

Figure 3.6: (a) Raman spectra for bare GaAs NM, NM with 1L-MoS$_2$ and NM with 2L-MoS$_2$ on top. (b,c,d) Spatially resolved intensity of GaAs LO Raman mode (a), in-plane E$'$ mode (b) and out-of-plane A$'_1$. (c).

flat substrate. The NM arrays exhibit increased intensity of the GaAs LO mode as compared to the rest of the substrate. This can be attributed most probably to the lack of SiO$_2$ capping the GaAs NMs. The intensity of MoS$_2$ Raman modes E$'$ (Fig. 3.6 (c)) and A$'_1$ (Fig. 3.6 (d) both show similar response being mostly dependent on the thickness of the flake, where the 2L-MoS$_2$ part of the flake is much brighter than the 1L-MoS$_2$ [Lee 2010].

Looking at the modes' frequencies presented in Fig. 3.7 (a,b) again the largest difference in frequency can be seen between the 1L and 2L parts of the flake. In particular, the frequency separation map (Fig. 3.7 (c)) clearly shows the distinction between 1L and 2L, where the separation is $\simeq 21\,\mathrm{cm}^{-1}$ and $\simeq 23\,\mathrm{cm}^{-1}$, respectively.

Having obtained the general picture, next I analyze in detail the Raman shift of the in-plane E$'$ mode, which is the most sensitive to the in-plane strain fields and will allow to quantify the strain imparted by the NMs. For clarity I focus only on the 1L-MoS$_2$ part of the flake. In Fig. 3.8 (a) I compare the Raman spectra from two different regions of the flake showing red shift of the E$'$ mode on the order of $0.5\,\mathrm{cm}^{-1}$. The spectra marked 1 and 2 are taken from the spots marked in the

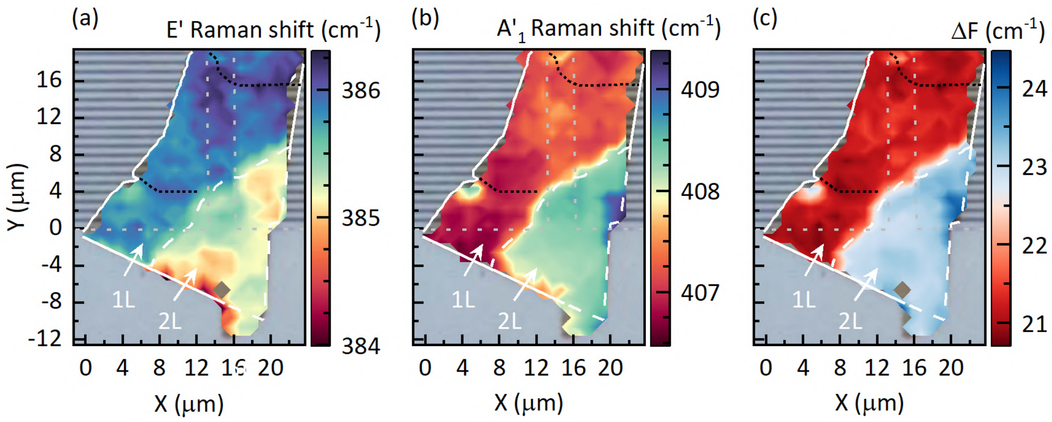

Figure 3.7: (a) and (b) Spatially resolved Raman frequency shift for modes E′ and A'_1, respectively. The frequencies were obtained by Lorentzian fitting of the Raman peaks. (c) Spatial map of frequency difference $\Delta F = F_{A'_1} - F_{E'}$.

E′ frequency map in Fig. 3.8 (b), where the color-axis is rescaled to exclude the bilayer region. We can distinguish regions of the flake lying on NMs with higher (1) and lower (2) E′ frequency signifying low and high level of tensile strain, respectively. Using the experimentally obtained strain gauge from ref [Christopher 2019] of 2.1 $\mathrm{cm}^{-1}/\%$ the variation in Raman frequency can be recalculated into the variation of strain, which is presented on the secondary color-axis in Fig. 3.8 (b). The variation of strain across the sample is found to be around 0.35 %.

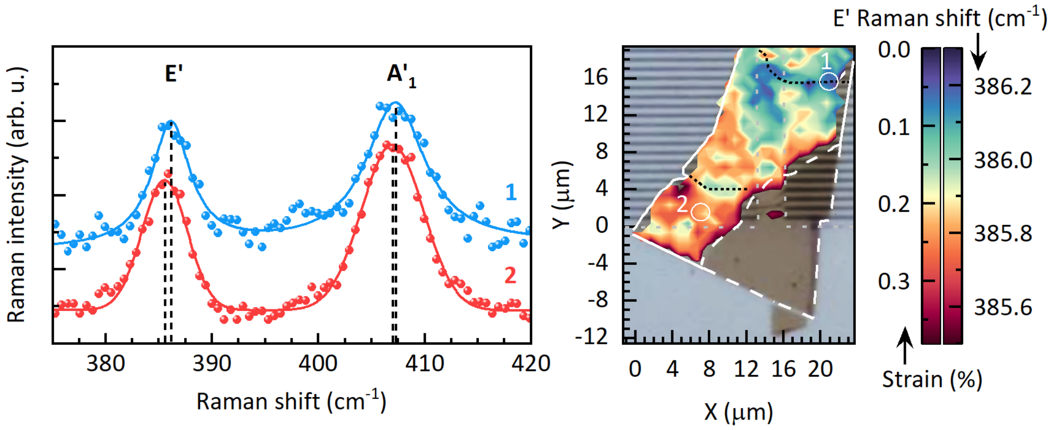

Figure 3.8: (a) Representative Raman spectra of the E′ and A'_1 modes taken from areas denoted 1 and 2. The solid lines correspond to double Lorentzian fitting to the datapoints (scatter points). (b) Position-dependent E′ Raman frequency. White circles corresponds to the areas from which spectra 1 and 2 in graph (a) were taken. The black dotted lines correspond to the fractures in the MoS_2 flake.

As a general observation we can note an increase in the tensile strain in the regions of the flake on NMs, especially on the left-side NM array (Fig. 3.8 (b)). All deviations from the general trend, resulting in not full uniformity can be traced back to the local morphology of the flake observed in optical imaging (3.3 (a)) and AFM (3.3 (a)). Several unintentional features such as wrinkles and fractures in the flake correlate very well with the Raman response. For example, the two prominent tears in the flake seen in the AFM map (Fig. 3.5), also marked with black dotted lines on the Raman response maps, would relax the strain in the flake in their vicinity, thus resulting in lower or no red shift of E′ mode frequency, which is exactly what can be observed. Similarly, in the micrograph in Fig. 3.3 one can see nonuniform color (brighter and darker areas) within the monolayer part of the flake. These correlate as well with the spatial strain distribution and signify that the flake conforms to the substrate to a varying degree. Despite those imperfections, the presence of tensile strain is confirmed and demonstrates the possibility of utilizing GaAs nanostructures as deterministic stressors.

3.2.2 Probing strain by excitonic transitions

As a second characterization tool I performed the position-dependent PL studies using 405 nm cw laser of $P = 500\,\mu$W power complemented by position-dependent reflectivity in order to determine the exciton energies. Similar to the Raman response, the strain-induced changes in the crystal structure will affect the band structure of the material. In MoS_2, the tensile (compressive) strain will result in red shift (blue shift) of the energy of excitonic transition [Christopher 2019]. Based on the exciton energy shift, the level of strain can be estimated, making it a complementary experiment to Raman scattering.

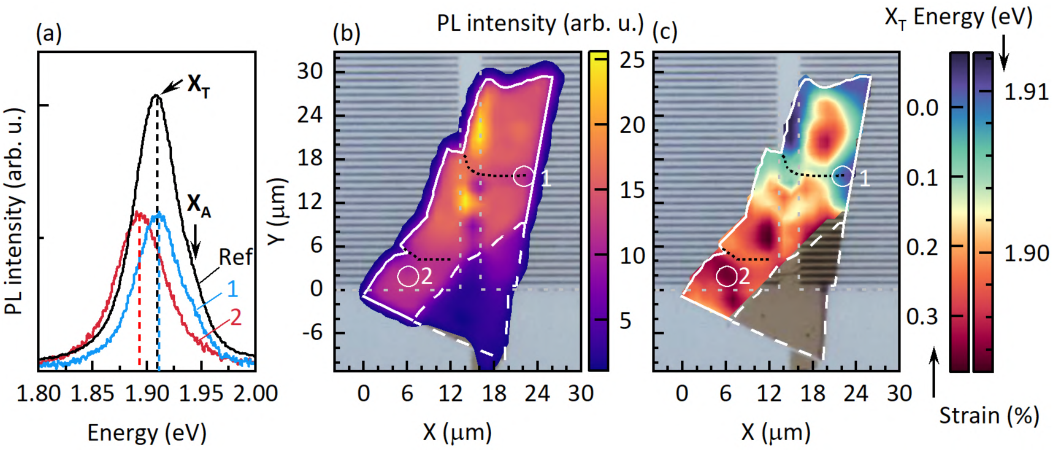

Figure 3.9: (a) PL spectra taken from regions (1) and (2) as well as PL spectrum of a reference flake ("Ref"). X_A and X_T denote the neutral and charged exciton, respectively. (b) Spatially resolved map of PL intensity. (c) Spatially resolved map of X_T peak energy. The secondary color-bar corresponds to the level of uniaxial tensile strain calculated based on the X_T energy with a 0 % set for the peak energy of the reference flake.

The results of the PL experiment are shown in Fig. 3.9. In panel (a) I compare PL spectra from the same regions of the sample (1 and 2) as previously in Raman experiment. The third spectrum (denoted “Ref”) was taken from the reference flake located on the flat substrate away from the NMs (see Fig. 3.3 (b)). The spectra show an asymmetric peak structure with a high energy shoulder. The reflectivity spectra (Fig. 3.10 (a)) show more clearly the presence of two resonances at ~1.91 eV and ~1.94 eV matching the main peak and the high energy shoulder position in PL, respectively. Due to their energy position and relative energy distance, the two peaks/resonances are assigned as the charged exciton (X_T) and neutral A exciton (X_A) [Mak 2013]. The high ratio of charged to neutral exciton PL emission intensity signifies strong unintentional doping in the structure. Though non encapsulated MoS_2 is known to usually exhibit unintentional n-doping, here additional effect of GaAs as the substrate might contribute due to type-II band alignment between GaAs and MoS_2 [Iff 2017, Rojas-Lopez 2021]. In that case, I focus the analysis on the charged exciton emission. From the compared spectra, we can notice that energy of X_T in spectrum 1 matches closely that of the “Ref” spectrum, which is from a nominally unstrained flake. This shows that the region 1, located around a fracture in the flake exhibits relaxed strain and can be therefore treated as mostly unstrained. The X_T in spectrum 2 is red shifted by $\simeq 16\,\text{meV}$, which based on the strain gauge for charged exciton from ref. [Christopher 2019] (43 meV/%) amounts to almost $\simeq 0.4\,\%$ of strain, very close to the value obtained in Raman measurement.

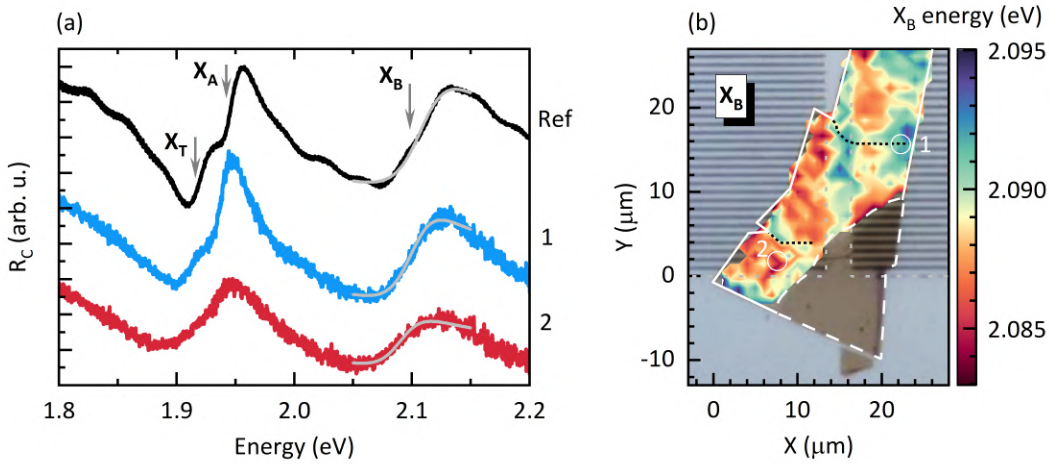

Figure 3.10: (a) Normalized reflectivity contrast $\frac{R-R_0}{R_0}$ taken from the regions (1) and (2) and from the reference flake (“Ref”). The grey lines correspond to the transfer-matrix fitting curves in the range of the X_B resonance. (b) Spatially resolved X_B resonance energy. Energy values were obtained from the transfer-matrix fitting.

Very similar picture can be obtained by tracking the excitonic resonance energies in the reflectivity (Fig. 3.10). Panel (a) again shows the exciton red shift on the strained MoS_2 areas with respect to the reference. Panel (b) shows the position-dependent B exciton (X_B) energy obtained by fitting the reflectivity spectra using the transfer-matrix method [Robert 2018]. Here the X_B energy is shown instead of the X_T or X_A due to broadening related energy overlap of these two making it difficult to perform a reliable fitting. Nevertheless, the position dependent map of X_B energy shows the same spatial distribution as the PL and Raman presented earlier.

3.2.3 Charged exciton fine structure

Having determined the strain imposed by GaAs nanomembranes on the MoS_2 monolayer I have performed linear polarization resolved PL measurements on the strained areas of the sample in order to determine the effects of the uniaxial strain on the excitonic fine structure due to lowering of the system symmetry. In other typical semiconductor systems, especially prevalent in epitaxial quantum dots [Bayer 2002, Gong 2011, Höfer 2019], the low symmetry of the structure, either intrinsic (*e.g.* low crystal symmetry or anisotropic confinement) or externally imposed by anisotropic strain leads to the lifting of the degeneracy of excitonic states causing energy splitting of its fine structure and changing the polarization to linear along the main anisotropy axes. Similar, low-symmetry effect can be found in some other semiconductors, *e.g.* 2D perovskites [Posmyk 2024b], but also in TMDs [Mitioglu 2018]. In work [Mitioglu 2018], the authors observed experimentally the fine structure splitting and linearly polarized emission. There however, uniaxial strain causing the effect had random, fabrication-related direction. Here, on the other hand, the major axes of uniaxial strain are expected to be defined by the morphology of the stressor, *i.e.* the NMs.

Fig. 3.11 (a) shows the results obtained at four different spots on the sample: three from the strained MoS_2 on NMs and one on the reference flake. The top panel of Fig. 3.11 (a) shows the PL intensity as a function of the polarization angle, while the bottom panel shows the PL peak energy corresponding to the X_T energy. Both the intensity and peak energy of photons emitted from the reference flake ("Ref") remain constant regardless of the polarization angle, indicating either complete circular polarization or unpolarized light. This outcome aligns with the anticipated behavior stemming from the three-fold rotational symmetry inherent in an unstrained TMD monolayers *i.e.* circularly polarized photon emission [Yu 2015]. Conversely, all series measured on the NMs show a sinusoidal dependence on the polarization angle with the extreme angles corresponding to the two characteristic directions in the structure *i.e.* along the length of NMs (denoted as X) and across the NMs (denoted as Y). We observe that for the X direction, the peak energy is highest and the intensity lowest, while the opposite is true for the Y direction. The estimated energy splitting (ΔE) between the two orthogonal polarizations is between 1-1.5 meV while the degree of linear polarization (P_l) reaches 12-15 %, depending on the measured spot (Fig. 3.11 (b,c)). Furthermore, a correlation between ΔE and P_l and the average PL energy, which corresponds to the level of strain (Fig. 3.11 (c)) corroborates the interpretation that the strain in the monolayer is the determining factor for the observed charged exciton fine structure splitting.

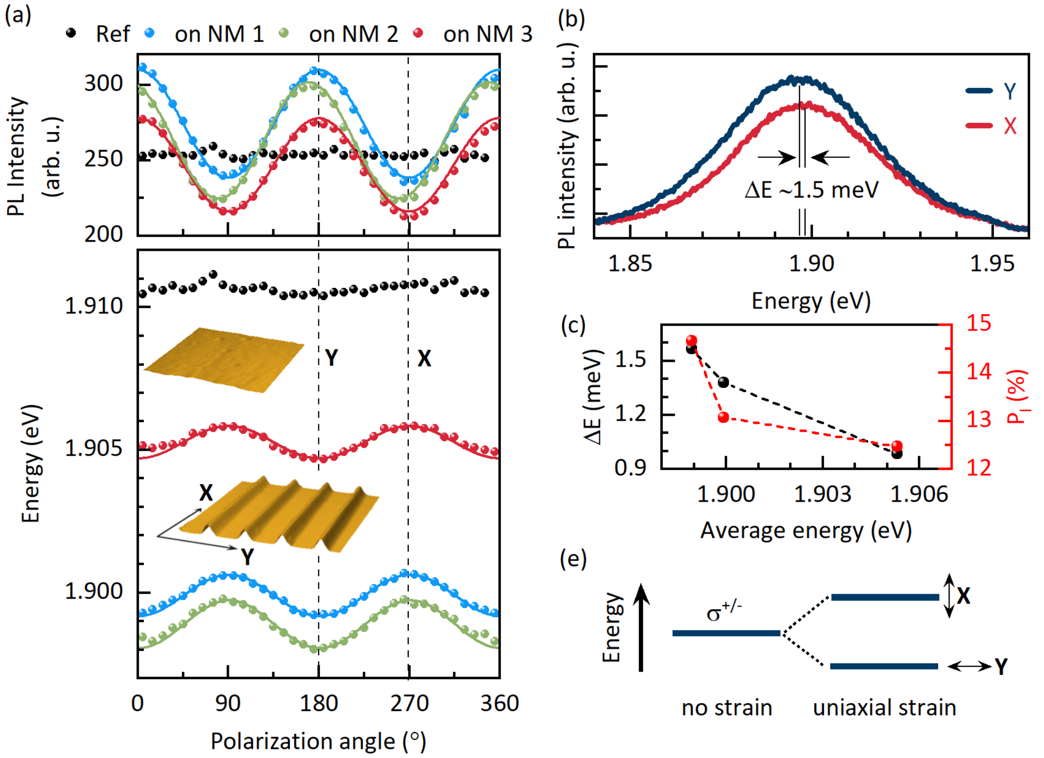

Figure 3.11: (a) Linear polarization angle dependent PL intensity (top panel) and peak energy corresponding to the X$_T$ energy (bottom panel) measured on the reference flake ("Ref") and 3 spots on the nanomembrane-strained flake (on NM 1,2,3). The extreme angles denoted X and Y correspond to the directions along the length of NMs and across NMs, respectively, as shown in the inset. (b) Two orthogonal spectra at X and Y angles for the spot on NM 2. (c) Energy splitting (ΔE) and degree of linear polarization (P_l) as a function of the average PL energy. (d) Schematic depiction of uniaxial strain induced lifting of the X$_T$ state degeneracy and linearization of photon polarization.

These results paint a picture of the lifted degeneracy of the excitonic states due to the anisotropy induced by uniaxial strain as schematically depicted in Fig. 3.11d, similar to other systems such as the aforementioned quantum dots [Bayer 2002]. It is worth noting however, that the origin of the splitting is the electron-hole exchange interaction [Bayer 2002]. Due to that fact, at least in tightly confined systems like quantum dots or for localized excitons, only the neutral excitons are expected to undergo the splitting and linearization of the polarization. This is because in the case of charged excitons, the additional electron with an antiparallel spin occupies practically the same space as the primary electron causing the local spin density to be zero (together forming a spin singlet state), thus nullifying the exchange interaction [Bayer 2002]. In experimental observations presented here however, the charged exciton clearly shows the strain-induced splitting and linearly polarized emission, defying the initial expectations. Experimentally, in uniaxially strained TMD systems, both the neutral excitons [Glazov 2022, Mitioglu 2018] and charged excitons [Mitioglu 2018] have been shown to undergo the splitting under uniaxial strain. This clearly shows, that the simple, few-particle picture of a charged exciton, like the one appropriate in quantum dots, here is not sufficient to explain the observed phenomenon. It is then necessary to take a different approach to the description of excitonic complexes and include the many body effects arising from interactions of excitons and their environment. Since TMD systems host 2D free electron gases, it is vital to consider the interaction of excitons and the Fermi sea. In this picture, the excitonic particles should be thought of as excitons dressed in electron-hole excitations within the Fermi sea *i.e.* Fermi polarons [Sidler 2017] (see section 1.4.3. This approach gives an exciton-like repulsive polaron and trion-like attractive polaron. The attractive polaron can be described as an exciton correlated with a Fermi sea electron-hole excitation of zero total spin, thus such complex essentially has the same total angular momentum of ±1 characteristic of the neutral exciton. This picture indeed predicts that both neutral and charged excitons in TMD systems experience the anisotropic strain induced fine structure splitting which has been theoretically demonstrated in Ref. [Iakovlev 2023].

3.3 Summary

In summary of the results presented in this chapter, I have studied the possibility of imposing a deterministic strain on a monolayer MoS_2 via deposition on III-V nanostructures in the form of GaAs nanomembranes. The samples and the structural characterization (AFM and SEM) were provided by the group of Anna Fontcuberta i Morral (EPFL, Lausanne). By means of optical spectroscopy I characterized the spatial strain distribution of an MoS_2 monolayer deposited on the nanomembranes. The results of Raman scattering, PL and reflectivity consistently show a picture of uniaxial tensile strain on the order of $\simeq 0.3 - 0.4\,\%$. Though the spatial distribution is not perfectly uniform due to uncontrolled effects such as formation of wrinkles and fractures of the flake, it shows that the strain can be succesfully applied by utilising the high quality III-V substrate patterning paving the way for further development of deterministic straintronics in TMDs. Finally, I investigated the effect of the strain on the fine structure of the charged exciton. Remarkably, the charged exciton displays similar effect of lifting of the fine structure degeneracy as the neutral exciton under the influence of an anisotropic strain field. Such behaviour can be explained by turning to the Fermi polaron picture of excitonic particles, in which the electron-hole exchange interaction is not zero for the trion-like attractive polaron. These findings demonstrate an additional control knob of the excitonic properties using strain engineering *e.g.* for applications in devices utilizing the linearly polarized signal. The results of these studies were published in 2D Materials 9.4 (2022), p. 045006 - Jakub Jasiński et al. "Strain induced lifting of the charged exciton degeneracy in monolayer MoS_2 on a GaAs nanomembrane” [Jasiński 2022].

CHAPTER 4

Control of the valley polarization by Dexter-like coupling effect

---

TMDs are known for their robust valley physics [Chernikov 2014, He 2014, Ugeda 2014, Hanbicki 2015, Wang 2018a, Yao 2008, Zhu 2011, Xiao 2012, Xu 2014, Yu 2015, Stier 2016] due to the spin-valley locking effect [Yao 2008, Zhu 2011, Xiao 2012, Xu 2014, Yu 2015, Stier 2016] (as described in detail in sections 1.4 and 1.4.2.1). The direct band gap in their band structure appears at points (valleys) named K^- and K^+. Six valleys in total (three of each type) appear at opposite corners of their hexagonal Brillouin zone and are related via time-reversal symmetry, yielding exactly opposite spin values in the corresponding bands of the neighbouring valleys, which in turn translates to contrasting polarization selection rules. This, together with sizeable spin orbit coupling, which splits the conduction band ($\Delta_{\mathrm{CB}} \simeq$ tens of meV) and valence band ($\Delta_{\mathrm{VB}} \simeq$ few hundred meV) [Zhu 2011, Kośmider 2013], endows TMDs with additional degrees of freedom for carriers or excitons in the form of spin and valley (pseudospin) indices [Xu 2014]. From the spin and energy separation, the robust polarization properties were expected to arise, which allow for selective initiation and readout of the valley excitons via circularly polarized light. The imbalance of the exciton population between the two valleys in TMDs is known as the valley polarization [Yao 2008, Xiao 2012, Xu 2014, Yu 2015, Stier 2016]. The valley excitons are however prone to some depolarizing processes such as spin-flip intervalley scattering [Schmidt 2016a, Wang 2014, Song 2013, Ochoa 2013, Lu 2013, Dey 2017, Kim 2017] and, the most prominent, intervalley exchange interaction [Xiao 2012, Zeng 2012, Zhu 2014b, Yu 2014a, Yu 2014b, Wang 2015c, Plechinger 2016, Dery 2016, Schmidt 2016b, Hao 2017, Yan 2015], which limit the long-term persistence of the valley polarization.

In this section I present results of investigation of the effects of another, extremely important, and not yet very emphasized in the literature, intervalley coupling mechanism. The mechanism is the Dexter-like coupling, which couples the same-spin states of the opposite valleys in k-space as presented in Fig. 4.1 [Berghäuser 2018]. In resonant excitation conditions, the coherent exciton population in the excited state in one of the valleys can be effectively transferred to the corresponding same-spin states of the opposite valley, which results in the inversion of the valley polarization. The initial theoretical and experimental investigation of this effect has been conducted by the group of Ermin Malic (Marburg Technical University) [Berghäuser 2018]. These results demonstrated the impor-

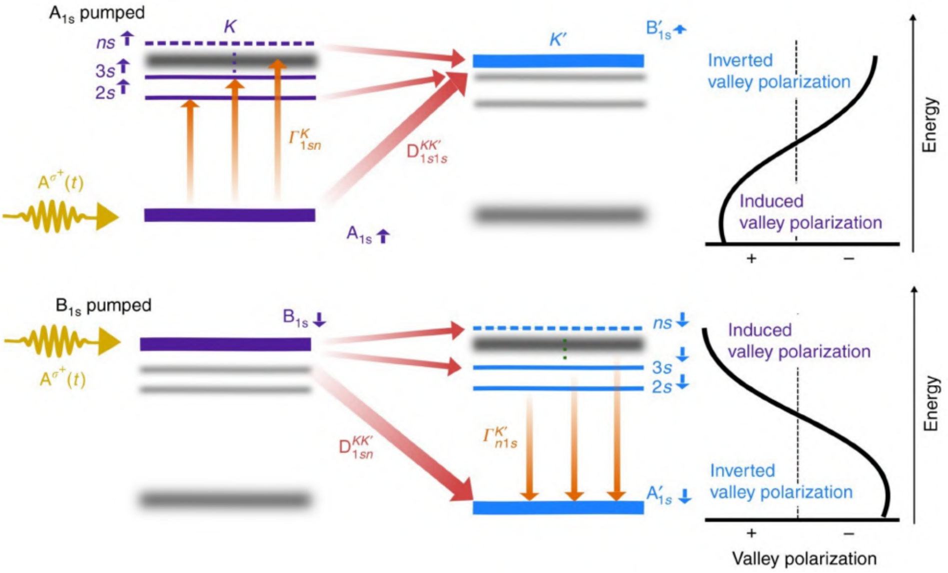

Figure 4.1: Schematic of Dexter-like coupling mechanism. The effect of the induced exciton population transfer on the valley polarization for polarized excitation resonant with A_{1s} state in K valley (top) and B_{1s} in K valley (bottom) are shown. Figure adapted from Ref. [Berghäuser 2018].

tance of Dexter-like coupling at very short timescales ($\simeq$ 100 fs) and allowed to explain the previous observation of upconversion characterized by inverted optical polarization [Manca 2017]. My studies extended the existing research to the static, time-integrated regime in which, as it turns out, the effects of Dexter-like coupling profoundly influence the valley polarization properties. This chapter is divided in two sections containing results on two different TMD-based systems:

The first section (4.1) concerns the investigation on encapsulated monolayer WSe_2, on which I performed optical spectroscopy measurements in the form of PL, reflectivity and PLE, additionally resolved in circular polarization basis. The sample was fabricated and provided by Maciej Śmiertka (Wrocław University of Science and Technology). The theoretical calculations complementing the experimental results were provided by the collaborators from the group of Ermin Malic, most notably, by Joshua J. Thompson.

The second section (4.2) entails similar optical studies on a heterostructure composed of a monolayer WSe_2 and a thin multi-layer of buthylammonium lead iodide (BA_2PbI_4), which is a member of 2D Ruddlesden Popper hybrid organic-inorganic perovskite [Stoumpos 2016]. The sample was provided by the collaborators from the group of Alexey Chernikov (Dresden Technical University), specifically, fabricated by Jonas D. Ziegler. The TMD/2D-perovskite heterostructures have been heavily investigated in recent years [Yang 2019, Fu 2019, Zhang 2020b, Wang 2020a, Erkılıc 2019, Chen 2020a, Chen 2020b, Wang 2021c, Wang 2021a, Zhou 2022, Karpinska 2021, Karpińska 2022, Baranowski 2022b, Yao 2022, Singh 2023] and have been shown to exhibit interesting features such as charge transfer, which can result in formation of an interlayer exciton [Chen 2020a, Chen 2020b, Karpińska 2022, Yao 2022] or energy transfer [Zhang 2020b, Wang 2021a, Karpinska 2021, Karpińska 2022, Baranowski 2022b], which occurs for heterostructures characterized by energy resonance between excitonic states of TMD and 2D-perovskite. Additionally, by utilizing chiral spacers in the 2D-perovskite, selective spin injection from TMD into 2D-perovskite were shown [Chen 2020a, Chen 2020b, Wang 2021a, Baranowski 2022b]. For standard, achiral perovskites, signs of spin-conserving transfer of the valley polarized carriers from TMD to 2D-perovskite have been observed [Singh 2023]. The studies I present in this section expand on the aspects of charge transfer and spin injection and demonstrate that the interlayer exciton found in these heterostructures inherits the valley properties of the constituent TMD, which is evidence of successful spin injection. This is shown clearly by observation of the same Dexter-like coupling effect influencing the interlayer exciton, which is found for excitonic transitions in bare WSe$_2$ monolayer, presented in the first section.

4.1 Dexter-like coupling in WSe$_2$ monolayer

4.1.1 Sample characterization

The investigated sample is a fully hBN-encapsulated WSe$_2$ monolayer, deposited on a Silicon substrate. The optical image, presented in Fig. 4.2 shows the structure of the sample with the constituent layers of bottom hBN, 1L-WSe$_2$ and top hBN outlined. The sample was fabricated by Maciej Śmiertka, layer by layer using an all-dry transfer method, which is described in section 2.4 in more detail.

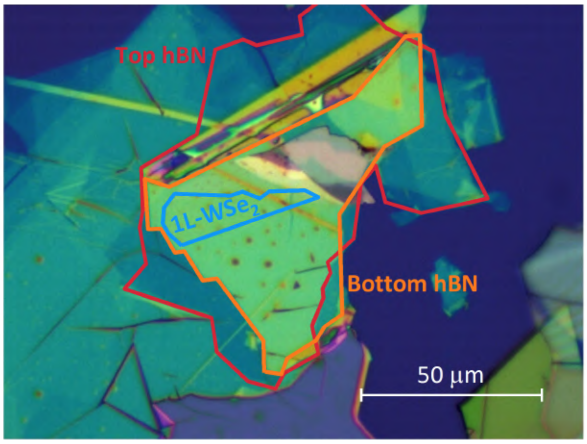

Figure 4.2: Optical microscope image of the investigated encapsulated 1L-WSe$_2$ sample. The 1-L WSe$_2$ and the top and bottom hBN flakes are outlined with blue, red and orange lines, respectively.

In the optical image (Fig. 4.2) we can observe the presence of unintentional bubbles, which are notorious in van der Waals stacks obtained via the all-dry transfer method. To avoid the disorder in the optical response created by those locally strained areas, the measurement spots for all the experiments was always chosen in the flat part of the 1L-WSe$_2$ flake. To achieve that, firstly the spot was chosen by looking at the preview microscope image of the sample and, secondly, by the energy position and shape of the PL response. For each measurement, the sample position was chosen so that in similar excitation conditions, the PL spectrum shape and energy position were consistent.

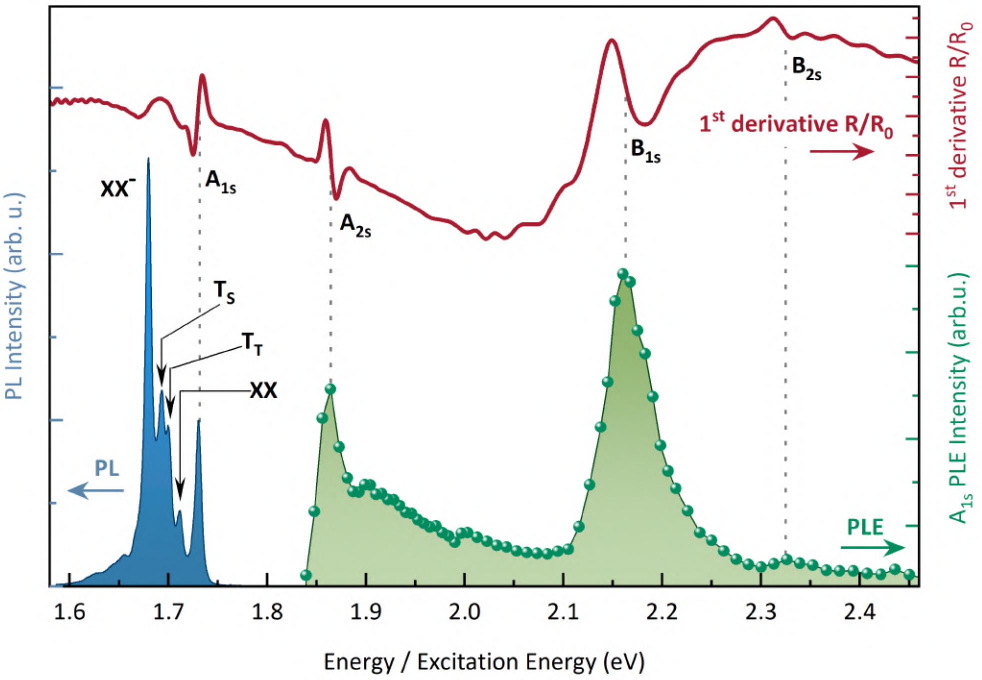

Figure 4.3: Optical characterization of encapsulated 1L-WSe$_2$: reflectivity in the form of 1^{st} derivative of R/R_0 (red curve), PLE intensity of A$_{1s}$ exciton state (green curve), PL spectrum excited at B$_{2s}$ resonance (blue curve) with laser power $P = 50$ μW. The PLE intensity data points were obtained by Lorentzian fit to the A$_{1s}$ peak.

To characterize the basic optical response and determine the excitonic transitions in the sample I conducted reflectivity, PL and PLE experiments. The results of all three combined are presented in Fig. 4.3. The PL spectrum (blue curve) shows a multi-peak structure, common in the encapsulated 1L-WSe$_2$, where the different PL peaks correspond to different excitonic complexes. The most prominent of which are marked in the spectrum as the neutral A exciton (A$_{1s}$), triplet and singlet charged excitons (T$_T$ and T$_S$) and the neutral and charged biexcitons (XX and XX$^-$). The assignment was based on their energy position and relative energy separation from the neutral A$_{1s}$ exciton *i.e.* the dissociation energy [Ye 2018b, Chen 2018a, Gupta 2019, Li 2018, Li 2020b] as well as the, discussed further, power dependence of the PL intensity shown in Fig. 4.4.

Reflectivity (red curve) shows four prominent resonances, which are assigned based on their energy position and separation to the A_{1s}, A_{2s}, B_{1s} and B_{2s} excitonic transitions, in agreement with previous reports [Zhu 2023, Wang 2020b, Liu 2019a, Chen 2019]. Additional small features just below the A_{1s} resonance might belong to the direct absorption of the more complex excitonic particles - charged excitons and biexcitons, due to matching of the resonance and PL emission energy. The PLE measurement (green curve), with monitored intensity of the A_{1s} exciton, corroborates the results of reflectivity, showing, in the scanned excitation energy range, three resonances belonging to the A_{2s}, B_{1s} and B_{2s} transitions.

The excitation power dependent PL measurement is presented in Fig. 4.4. Panel (a) shows a stack of PL spectra at different excitation powers using a 405 nm laser in cw mode. The spectra are normalized to the A_{1s} PL peak intensity to emphasize the change in the intensity ratio between different excitonic complexes. At low powers, the neutral A_{1s} exciton dominates the spectrum. By increasing the excitation power we can observe that the intensity of the PL peaks assigned to XX and XX^- increase faster than the A_{1s}. This is clearly shown by the dependence of PL intensity (extracted from the fitting of the PL peaks by 5-peak Lorentz function) on the excitation power shown in panel (b). The excitons and charged excitons exhibit a lower power coefficient (parameter b in the $y = ax^b$ fitting function), close to 1 *i.e.* linear. The biexcitons are characterized by higher, superlinear power coefficient of $b \simeq 1.5$, characteristic of higher order excitonic particles. Panel (c) and (d) show similar power dependence as in (a) and (b), but for the pulsed excitation mode. In this case we can observe that the XX^- peak dominates starting at low powers. This is due to the pulsed excitation mode, in which, the average measured power does not correspond directly to the power affecting the sample. The high amount of excitation energy is accumulated in short pulses with long breaks in between consecutive pulses. Effectively the sample is excited on a short time scale with a much higher power than the measured average, explaining the discrepancy between the two excitation modes. The power coefficients deduced for the observed transitions, however exhibit comparable values to those obtained in cw mode. The parameters of the observed excitonic transitions combined from all experiments are summarized in Table. 4.1.

Table 4.1: Encapsulated 1L-WSe$_2$ - Parameters of excitonic transitions.

Exciton	$\mathbf{XX^-}$	$\mathbf{T_S}$	$\mathbf{T_T}$	**XX**	$\mathbf{A_{1s}}$	$\mathbf{A_{2s}}$	$\mathbf{B_{1s}}$	$\mathbf{B_{2s}}$
Energy (eV)	1.676	1.690	1.697	1.709	1.727	1.864	2.164	2.324
Dissociation energy (meV)	51	37	30	18				
1s-2s separation (meV)					137		160	
Power coefficient - cw	1.35	1.04	1.28	1.56	1.15			
Power coefficient - pulsed	1.39	1.01	1.28	1.46	1.21			

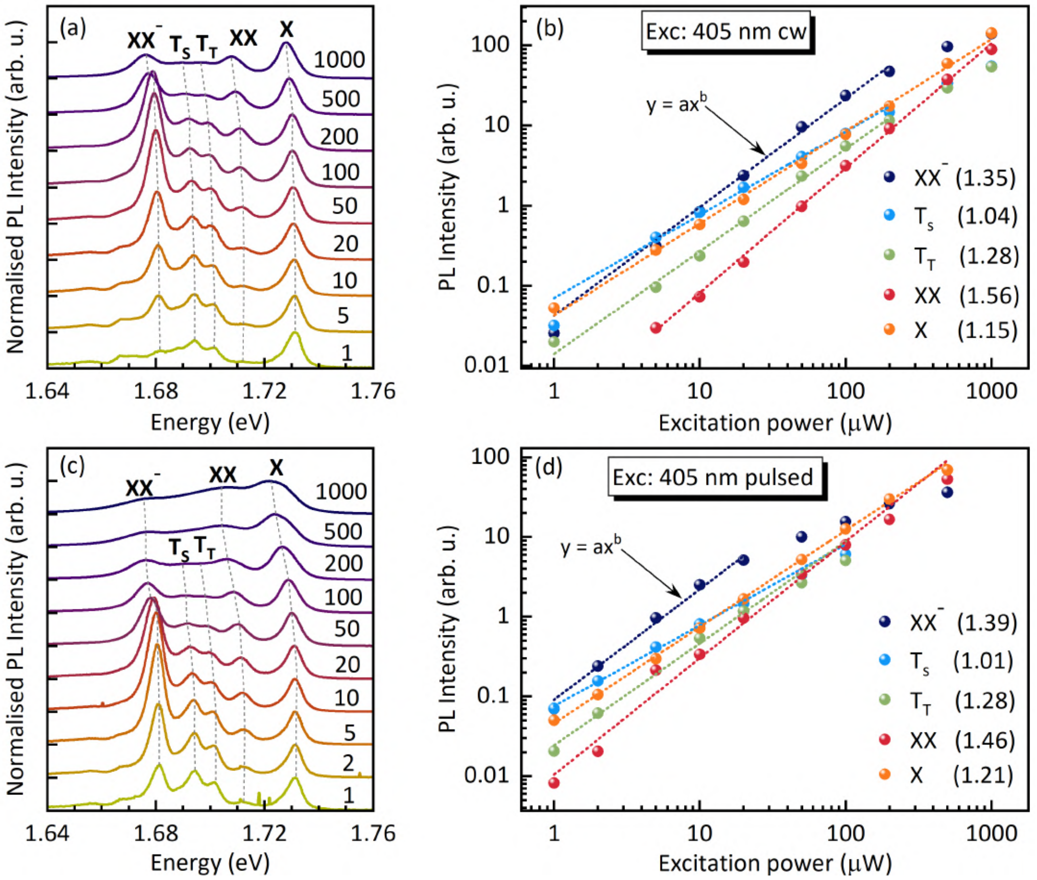

Figure 4.4: 1L-WSe$_2$ Excitation power dependence of PL. (a,c) PL spectra at different excitation powers (numbers next to curves correspond to the average power in [μW] measured by power detector) for cw excitation and pulsed excitation. (b,d) PL intensity as a function of excitation power (double logarithmic scale) of the five identified excitonic transitions denoted XX$^-$ (charged biexciton), T$_\mathrm{S}$ (singlet charged exciton), T$_\mathrm{T}$ (triplet charged exciton), XX (biexciton) and X (neutral exciton), for cw and pulsed excitation, respectively. The dotted lines correspond to fitting with a function $y = ax^b$, where b is the power coefficient. Both modes of excitation have been performed with the same 405 nm laser, by switching of the lasing mode. The PL intensities were obtained by fitting of the 5-peak Lorentz function to the PL spectra.

4.1.2 Valley polarization

To gain insight into the valley polarization properties and detect the fingerprints of the Dexter-like coupling I conducted the PLE experiment with additional resolution in circular polarization basis. For broad range wavelength tuning, the Ti:Saph+OPO source was used, which produces pulsed signal (80MHz repetition rate) of $\simeq 150$ (bare Ti:Saph) or $\simeq 300 - 400$ (OPO) fs temporal line width (Table 2.1). Circular polarization is resolved by polarizing the excitation light into one of the circular states (σ^+ or σ^+) and detection of the same polarized (co-polarized) and orthogonally polarized (cross-polarized) optical response. In TMDs, since the photon polarization is coupled to the valley from which the excitonic recombination takes effect *i.e.* $\sigma^{+(-)}$ for the $K^{+(-)}$ valley (as described in section 1.4.2.1), we can then assume that the calculated degree of circular polarization (P_c) defined as:

$$P_c = \frac{I_{co} - I_{cross}}{I_{co} + I_{cross}}, \tag{4.1}$$

where $I_{co/cross}$ denote the intensity of the co- and cross-polarized emission component, respectively, directly corresponds to the valley polarization.

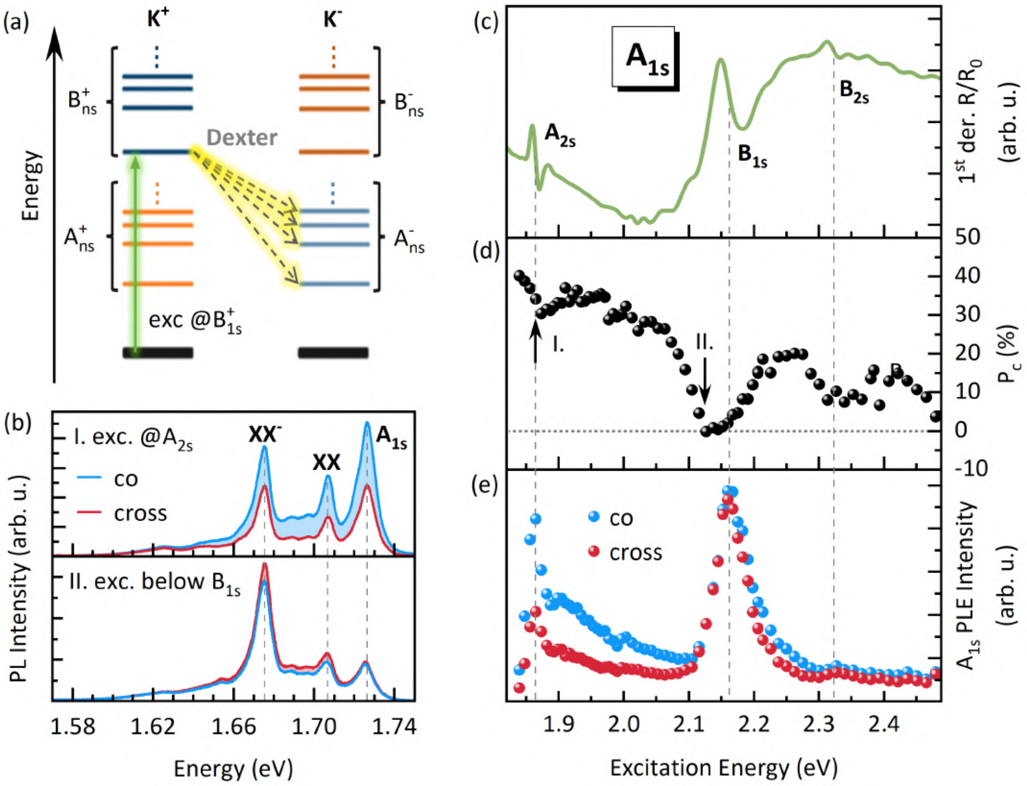

Figure 4.5: (a) Schematic of Dexter-like exciton transfer. Here is shown an example of the Dexter-like transfer of excitons from the resonantly pumped B^+_{1s} state into the A^- states in the opposite valley. The "ns" subscript denotes the Rydberg series of the given exciton type. (b) Comparison of the co-polarized and cross-polarized spectra for excitation energy matching the A_{2s} resonance (top panel) and slightly below B_{1s} resonance (bottom panel), which corresponds to the most cross-polarized emission. (c) Reflectivity spectrum with marked A_{2s}, B_{1s} and B_{2s} resonances (d) Degree of circular polarization (P_c) calculated from the co- and cross-polarized component of A_{1s} emission intensity shown in (e). The PL intensity values were obtained by Lorentzian fit to the A_{1s} peak.

Time-integrated PL measurements allow to examine the optical response from the fundamental *i.e.* lowest lying states from which PL emission predominantly originates. Hence I focus the study of the Dexter-like coupling related effect by probing the polarization of the PL emission, while tuning the excitation energy in the higher energy range *i.e.* at the energies corresponding to the higher lying states and in between them. An exemplary experimental condition of excitation resonant with the B_{1s} state in the K^+ valley (selection of the valley via circularly polarized excitation light - σ^+) is depicted in Fig 4.5 (a). The Dexter-like coupling [Berghäuser 2018] couples the same-spin states of the opposite valleys in k-space (see Fig. 1.5 (a,b) in section 1.4.2.1) *i.e.* the $A^+_{ns} \leftrightarrow B^-_{ns}$ and $A^-_{ns} \leftrightarrow B^+_{ns}$. Consequently, such excitation conditions are expected to result in a transfer of the coherent exciton population, into the A states (all Rydberg states) in the opposite valley [Berghäuser 2018]. Due to the efficiency of the exciton transfer, a significant part of the initially created excitons, after transferring, will eventually recombine with the opposite circular polarization with respect to excitation. This results in the inversion of the valley polarization of the A states of the TMD system on very short time scales, during and shortly after the excitation pulse [Berghäuser 2018]. Here I probe, whether the static, time-integrated optical response shows any fingerprints, and therefore evidence for Dexter-like exciton transfer.

First, looking at the co- and cross-polarization components of the PL response when the excitation is resonant with the A_{2s} state, as shown in the top part of Fig. 4.5 (b), we can observe that the emission is strongly co-polarized as emphasized by the blue shadowed area corresponding to the difference in intensity in favour of the co-polarized response. The P_c value of the whole PL spectrum is approximately 30 %, which agrees with the expectation that, normally, resonant excitation helps partially preserve the induced valley polarization by minimizing the number of relaxation processes and time for depolarizing processes to take effect. Bottom part of the same figure, on the other hand, shows the PL response when the excitation is just below ($\sim 20\,\text{meV}$) the B_{1s} resonance. We observe the strong reduction in the P_c of the whole spectrum reaching 0 % or slightly below 0 % for the lower energy part of the spectrum corresponding to the emission from more complex excitonic particles, which is emphasized by the more intense red shadowed area.

Focusing now on the neutral A_{1s} exciton, its broad-range excitation energy dependent polarization properties are presented in Fig. 4.5 (c-e). Panel (c) shows the reflectivity spectrum with marked energy positions of the A_{2s}, B_{1s} and B_{2s} excitons which serves as comparison for the PLE experiment. Panel (d) shows the value of P_c as a function of the excitation energy, which was calculated using the formula 4.1 from the co-polarized and cross-polarized intensity components shown in panel (e). The P_c exhibits a clearly non-monotonic dependence on the excitation energy. The observed trend can be broken down into two main factors. Firstly, there is an overall tendency for the increase of the P_c as the excitation energy decreases. At the highest measured excitation energy of $\simeq 2.48\,\text{eV}$ the P_c is around 10 %, while in the low energy range, around A_{2s} resonance and between the A_{2s}-B_{1s} resonances, P_c reaches approximately 35 %. This behaviour is expected as the electron-hole exchange, the most prominent valley depolarization mechanism depends on the excess energy of the pump (*i.e.* relative energy distance from the emission) and is more efficient, the higher the excess energy [Yu 2014b, Baranowski 2017]. Secondly, when the pump energy crosses the B$_{2s}$ and B$_{1s}$ resonances, the P_c value deviates from the above mentioned trend in the form of a strong decrease, within the broadening of these resonances. This effect is especially prominent around the B$_{1s}$ resonance, where the P_c reaches the lowest value of $\simeq 0\,\%$. This observation is a clear signature of the Dexter-like coupling and its profound influence, even at long timescales, as clearly seen in the time-integrated results presented here. The final result of vanishing ($\sim 0\%$) valley polarization is the product of all the intervalley processes which take place between the excitation pulse and the radiative exciton recombination, which for this sample was found to be around 25 ps [Jasiński 2024b]. In addition to the Dexter-like transfer, which inverts the valley polarization, there are also other depolarization mechanisms. The most prominent are the efficient electron-hole exchange intervalley coupling [Xiao 2012, Zeng 2012, Zhu 2014b, Yu 2014a, Yu 2014b, Wang 2015c, Plechinger 2016, Dery 2016, Schmidt 2016b, Hao 2017, Yan 2015] and the low efficiency phonon-mediated intervalley scattering [Schmidt 2016a,

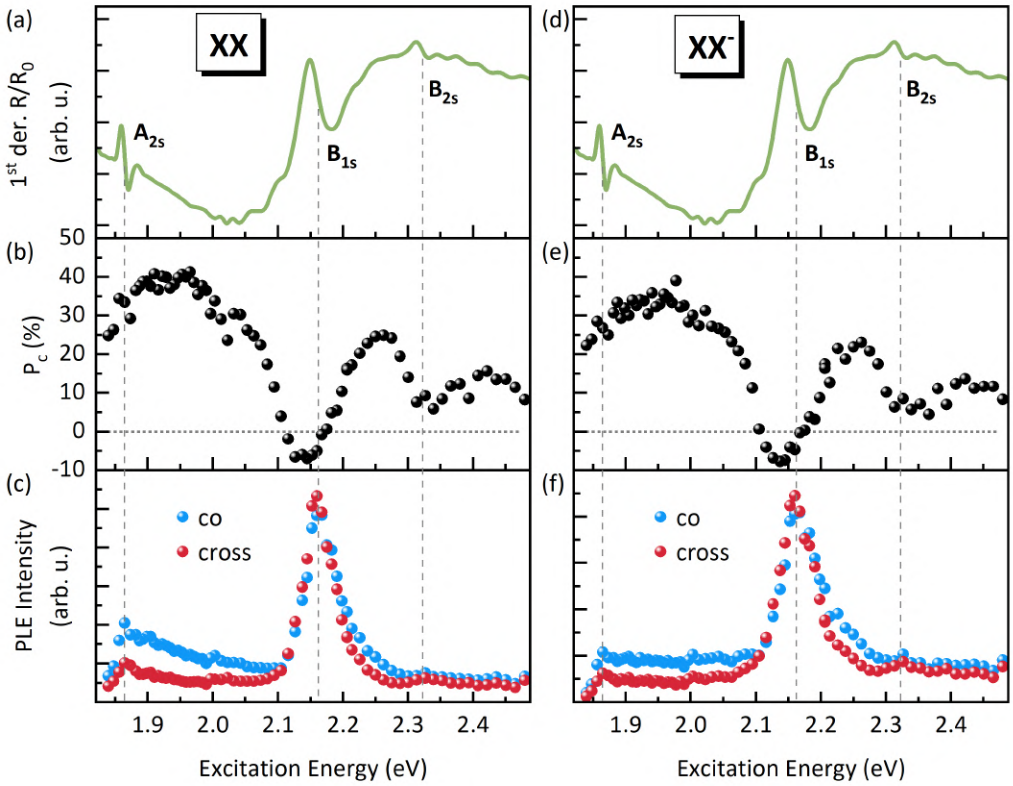

Figure 4.6: (a) Reflectivity spectrum with marked resonances of A$_{2s}$, B$_{1s}$ and B$_{2s}$ states. (b) Degree of circular polarization (P_c) calculated from the co- and cross-polarized component of XX emission intensity shown in (c). (d-f) same as (a-c), but for the XX$^-$ transition.

Wang 2014, Song 2013, Ochoa 2013, Lu 2013, Dey 2017, Kim 2017], both of which act to equalize (bring to 0 %) the valley polarization. It is worth adding, that a similar experiment, showing practically the same result for the excitation energy dependent P_c of the $\mathrm{A_{1s}}$ exciton, has been conducted before [Wang 2015b], however, the authors of the cited paper did not comment on the peculiar observation.

Similar analysis on the XX and $\mathrm{XX^-}$ complexes is presented in Fig. 4.6. The excitation energy dependent P_c shown in panel (b) and (e), for XX and $\mathrm{XX^-}$, respectively, show the same general trend as the neutral $\mathrm{A_{1s}}$ exciton. One difference, however, is visible in the absolute values of P_c. At low excitation energies the the P_c reaches higher values of around 40 %. At the same time, around the $\mathrm{B_{1s}}$ resonance, the P_c becomes clearly negative with lowest value of around -7 %. This shows that the effect of the Dexter-like coupling is more pronounced for the more complex excitonic particles. A probable explanation of such a behaviour might be related to the fact that due to larger number of component particles involved in formation of the more complex excitons such as trions and biexcitons. This in turn would make them more robust against other depolarization mechanisms [Singh 2016] that equalize the valley polarization following the Dexter-like transfer.

4.1.3 Theoretical model

To corroborate the experimental observations, we employed the theoretical simulation performed by our collaborators from the group of Ermin Malic (Marburg Technical University). The calculations are based on a fully microscopic model, which tracks the time evolution of the both coherent (pump-driven) and incoherent exciton populations [Berghäuser 2018, Bernal-Villamil 2018, Jasiński 2024b]. This framework allows to simulate the evolution of the valley polarization of the neutral exciton as a function of excitation energy.

Fig. 4.7 shows the results of the simulation of the time evolution of the $\mathrm{A_{1s}}$ exciton state following a single excitation pulse, which is centered at $t = 200\,\mathrm{fs}$ with $FWHM = 400\,\mathrm{fs}$ (pulse onset at $t = 0\,\mathrm{ps}$). Panel (a) and (b) present the PL decay of the co- and cross-polarized component for an off-resonant excitation energy between the $\mathrm{A_{2s}}$ and $\mathrm{B_{1s}}$ resonances (a) and resonant with the $\mathrm{B_{1s}}$ exciton state (b). The initial strong co-polarized signal in Fig. 4.7 (a) is due to quick relaxation to the emissive $\mathrm{A_{1s}}$ state. The cross-polarized signal rises slowly due to intervalley exchange and phonon-scattering processes which transfer excitons to the opposite valley. For excitation resonant with the $\mathrm{B_{1s}}$ exciton in Fig. 4.7 (b), the state is initially populated, however, the excitons are quickly transferred via Dexter-like coupling to the opposite valley, leading to an initial strong cross-polarized signal. Then, the intervalley exchange repopulates the originally pumped valley. The interplay between the excitons relaxing from the directly excited B state and the intervalley exchange and scattering processes of both the still occupied B states and A states produces a complex picture of the ratio of the co- and cross-polarized signal. After initial domination of the Dexter-mediated transfer of coherent population to the opposite valley, the co-polarized signal briefly rises above the cross-polarized signal before

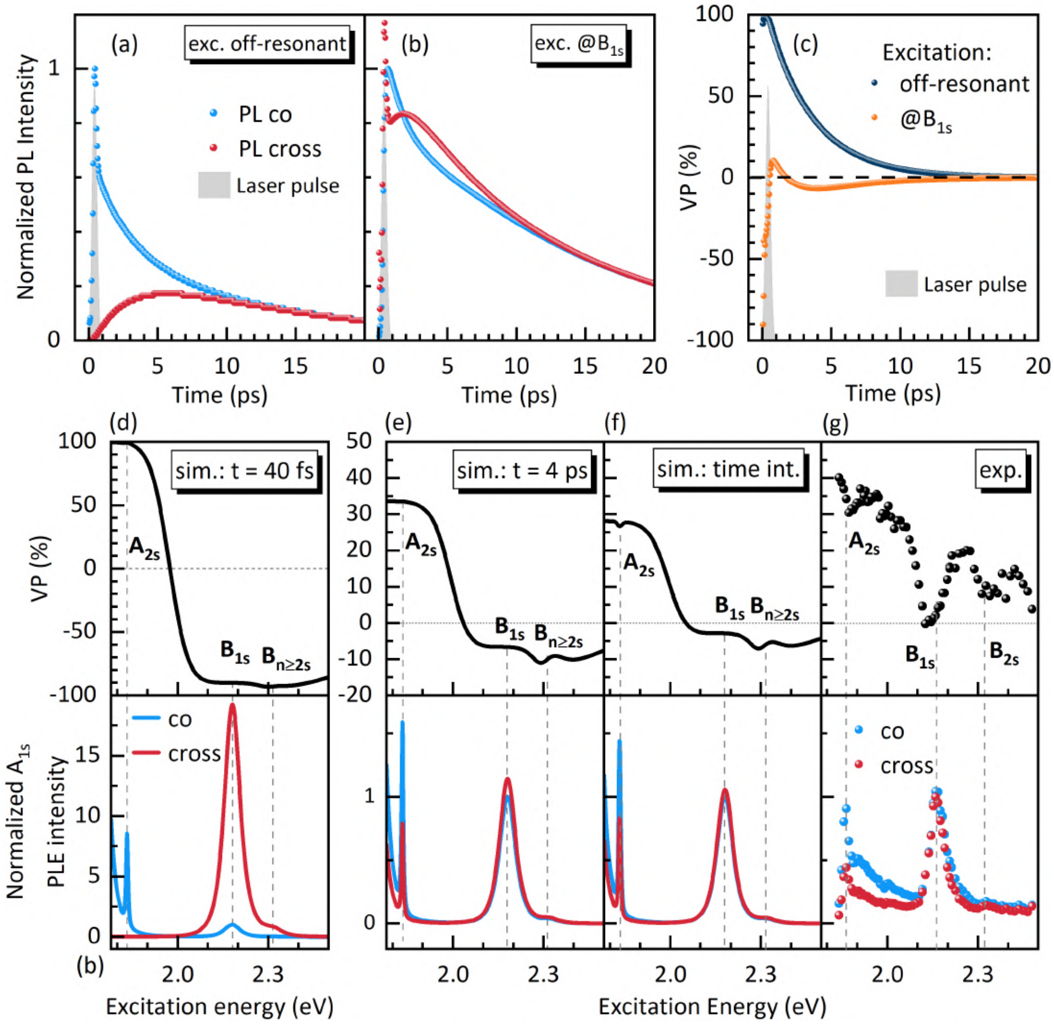

Figure 4.7: Simulation of time evolution of the valley polarization of A_{1s} exciton. (a) and (b) Simulated PL decay curves of the co-polarized and cross-polarized signal after a single excitation pulse modeled as a gaussian of $FWHM = 400\,\text{fs}$, centered at 200 fs (grey shadowed curve) for off-resonant excitation energy (a) and resonant with the B_{1s} state (b). (c) Comparison of the time evolution of the valley polarization (VP) for the two excitation energies presented in (a) and (b). (d-f) Simulation of the A_{1s} PLE spectrum with resolved co-polarized and cross-polarized components (bottom panels) and calculated valley polarization (top panels) at $t = 40\,\text{s}$ (d), $t = 4\,\text{ps}$ (e) and time-integrated (f). (g) Experimentally obtained PLE intensity (bottom) and P_c (top) as a function of excitation energy.

then switching again due to decrease of the influence of the B state population due to exchange. At longer times, when the incoherent populations are established, the further decay are mediated by the exchange and scattering processes which in the end equalize the contributions of the two polarization components. Panel (c) of

Fig. 4.7 shows the evolution of the valley polarization for the two excitation conditions calculated from the intensity values shown in panel (a) and (b). Panels (d-g) compare the simulated PLE intensity spectrum at time points of $t = 40\,\text{fs}$ *i.e.* onset of the pump pulse (d), at 4 ps, when the pump pulse is mostly over thus suppressing Dexter-like transfer (e), time-integrated result of the simulation (e) and the experimentally obtained data in (f). Comparing the time-integrated simulation in (e) and experimental time-integrated PLE we observe a good qualitative agreement of the valley polarization dependence on the excitation energy. At low excitation energies in the vicinity of A_{2s} resonance, the valley polarization shows similar value of around 30 %. Within the line widths of all the B_{ns} states there is a strong, flat decrease in the valley polarization reaching small negative values of minus few %. The absolute minimum of valley polarization in the simulation coincides at the energy between the B_{1s} and B_{2s} resonances which is related to the overlap of the Dexter-mediated inversion arising in both states. In contrast, the experimental curve shows much narrower dips in P_c around the B_{1s} and B_{2s} resonances, despite nominally the same transition line width. For example, a substantially positive P_c is recovered in between the resonances. This discrepancy might stem from the differences between the parameters of the simulation and those present in the real sample, which can not be experimentally deduced for perfect matching between the theoretical model and experiment, such as *e.g.* the speed of coherent to incoherent population transfer at A and B states.

Furthermore, the experimental curves of P_c for all analysed excitonic complexes (Fig. 4.5 (d) and Fig. 4.6 (b,e)) and shows the minimum value is actually slightly below, $\sim 20\,\text{meV}$, the B_{1s} resonance. This is consistent with the prior observations presented in reference [Wang 2015b]. The probable explanation for this behaviour might be related to the fact that the Dexter-like transfer is equally efficient within the full line width of the resonance as is evident from the simulation, which leads to early onset of the decrease in P_c. At the same time, other scattering processes, likely underestimated in the simulation, lead to the fast increase of the time-integrated P_c with rising excitation energy within a given resonance, which ultimately results in the observed experimental picture. Another point suggesting an underestimation of the scattering or exchange processes in the simulation is the fact, that in the experiment, the P_c vanishes, while in time-integrated simulation it remains slightly inverted. Despite the discrepancies, a very good qualitative and reasonable quantitative agreement between the theoretical model and experimental results demonstrate the profound importance of the Dexter-like intervalley coupling.

4.1.4 Exciton renormalization

Another prediction of the theory behind the Dexter-like transfer, is the Dexter-mediated broadening and energy renormalization of excitonic resonances as shown in one of the earlier publications [Bernal-Villamil 2018] on the topic. To investigate these effects, I extracted the PL energy positions and line widths of the A_{1s}, XX and XX^- from the circular polarization resolved PLE experiment presented earlier. The

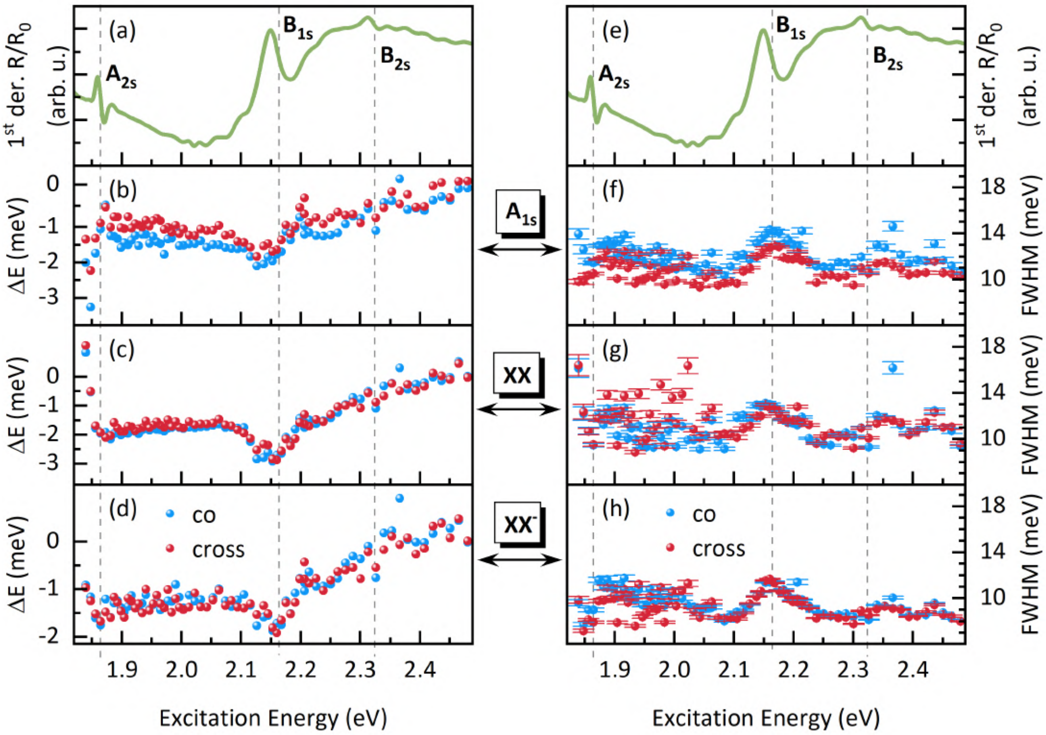

Figure 4.8: 1L-WSe$_2$ Dexter-like coupling induced renormalization. (a-d) Reflectivity (a) and exciton energy dependent energy shift ΔE for A_{1s} (b), XX (c) and XX^- (d) transition. (e-h). Reflectivity (e), same as in (a), and excitation energy dependent FWHM of A_{1s} (f), XX (g) and XX^- (h) transition. Dashed lines mark the positions of A_{2s}, B_{1s} and B_{2s} resonances.

results are presented in Fig. 4.8. For all of the analysed excitonic complexes, there is a small, clear red shift of the emission energy by approximately 2 meV (see panels (b-d)), as well as increase in the line width in the form of FWHM from $\simeq 10$ meV to $\simeq 13$ meV (see panels (f-h)), when the excitation energy coincides with the B_{1s} exciton resonance at $\simeq 2.16$ eV. The observed shift in energy is in fact larger, than predicted for the similar material of WS$_2$ [Bernal-Villamil 2018], which again shows the profound influence of this intervalley coupling mechanism.

4.2 Dexter-like transfer in WSe_2/BA_2PbI_4 heterostructure

4.2.1 2D hybrid metal-halide perovskites

The 2D hybrid metal-halide perovskites are a class of layered semiconducting materials, which are of great interest to the scientific community due to their wide tunability of opto-electronic properties [Chen 2018b, Mao 2018, Smith 2018] and high optical yield, which make them especially promising in light emission and photovoltaic applications [Cao 2015, Tsai 2016, Blancon 2017, Chen 2018b, Gong 2018, Straus 2018]. Their intriguing properties arising from their electronic properties and a soft, ionic lattice resulting in strong electron-phonon coupling render them interesting for studying of the nature of the fundamental excitations and polaronic effects [Straus 2018, Hurtado Parra 2022, Dyksik 2024].

2D-perovskite crystals are composed of alternating inorganic and organic sheets. The inorganic "inner" sheet consists of metal-halide octahedral slabs, which exhibit semiconducting properties. The organic "outer" sheet, often referred to as spacer, is an insulator with a drastically lower dielectric constant. Such structure resembles that of a quantum well, as depicted in Fig. 4.9 (a). The organic spacer acts as a high energy barrier forcing the charge carriers to locate in the inorganic, semiconducting layer. Due to the very high spatial and dielectric confinement and a smooth interface (due to natural atomic arrangement), the 2D-perovskites are regarded as the natural quantum wells. The coupled effect of spatial and dielectric confinements, similar to TMDs, results in greatly enhanced electron-hole interaction, resulting in binding energies reaching few hundred meV [Cao 2015, Tsai 2016, Blancon 2017, Chen 2018b, Gong 2018, Straus 2018, Baranowski 2022a]. The same as in quantum wells, the thickness of the the semiconducting layer, which can be controlled by the number of octahedral slabs n (see Fig. 4.9 (a)), impacts the optical band gap energy (Fig. 4.9 (b)) and modifies the exciton binding energy and radius (Fig. 4.9 (c)). On the other hand, the properties of the 2D-perovskites depend very weakly on the crystal thickness *i.e.* the total number of individual layers, which can be considered as electronically decoupled [Takeoka 2006, Dou 2015].

Moreover, the different members of 2D-perovskites crystallize in one of the two distinct phases, Dion-Jacobson (DJ) [Mao 2018] or Ruddlesden-Popper (RP) [Chen 2018b]. The two phases differ in their interlayer binding. In DJ perovskites the organic spacer is shared between the consecutive inorganic sheets (layer order: -*O*-*I*-*O*-*I*-). On the other hand, in RP perovskites, each inorganic sheet is individually surrounded by the organic spacers on both sides, while the consecutive layers are connected via van der Waals forces (layer order: $\cdots O\text{-}I\text{-}O\cdots O\text{-}I\text{-}O\cdots$). The latter 2D RP perovskites, due to their weak van der Waals bonding between the layers allows to relatively easy obtain very thin or even single layers of the material via mechanical exfoliation. This feature is especially interesting in terms of constructing complex heterostructures with other 2D layered materials such as TMD/2D-perovskite heterostructures [Baranowski 2022b], which are the subject of this chapter.

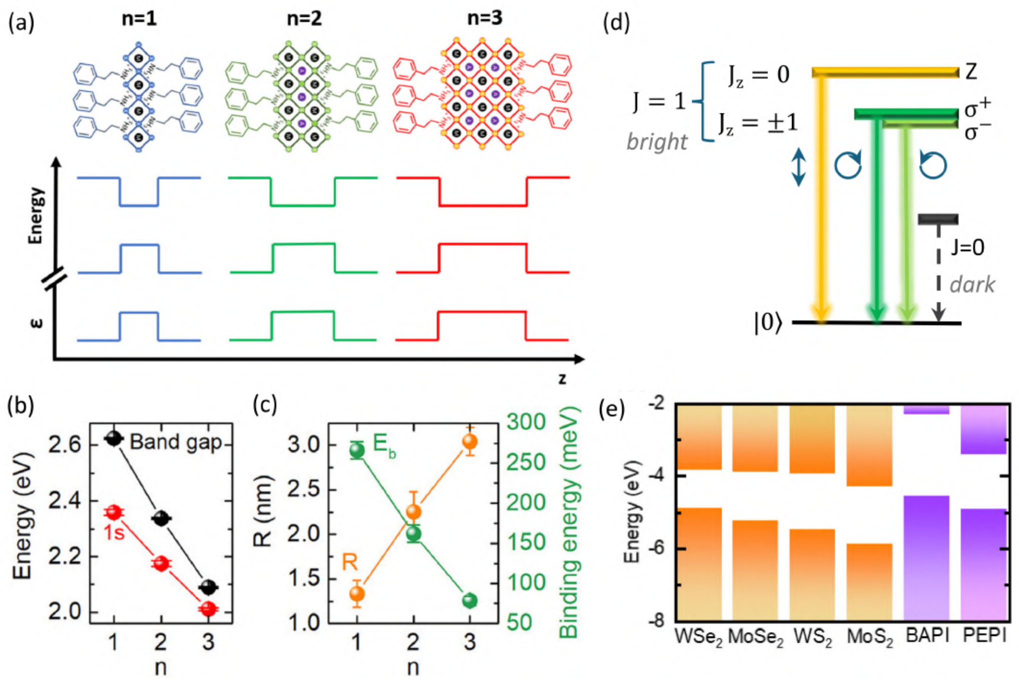

Figure 4.9: (a) Top: schematic drawings of 2D-perovskites single sheet structures for different number of octahedral slabs (n). Bottom: schematics of band alignment of the conduction and valence band energies as well as dielectric constands (ϵ) of the inner inorganic layer and outer organic spacer. (b) Dependence of the band gap and 1s exciton energies on the number of octahedral layers for PEA$'_2$MA$_{n-1}$Pb$_n$I$_{3n-1}$. (c) Dependence of exciton binding energy and radius on the number of octahedral layers for PEA$'_2$MA$_{n-1}$Pb$_n$I$_{3n-1}$. (d) Schematic of a general exciton fine structure due to exchange interaction in 2D-perovskites. J and J_z are the total angular momentum and in-plane projection of the total angular momentum, respectively. (e) Comparison of conduction and valence band offsets for several TMDs and 2D Ruddlesden-Popper perovskites: PEPI ((PEA)$_2$PbI$_4$) and BAPI ((BA)$_2$PbI$_4$). Panels (a-c) and (e) are adapted from Ref. [Baranowski 2022b].

The chemical formula for the RP 2D-perovskites is A'_2A_{n-1}M$_n$X$_{3n-1}$, where A' is the 1$^+$ large organic cation (*e.g.* BA$^+$ - buthylammonium or PEA$^+$ - phenylethylammonium), A is a small 1$^+$ cation (*e.g.* MA$^+$, FA$^+$, Cs$^+$), M is the metal atom (*e.g.* Pb^{2+}, Sn^{2+}, Cd^{2+}) and X is the halide anion (I$^-$, Cl$^-$, Br$^-$), meanwhile n denotes the number of octahedral slabs within the inorganic sheet [Tang 2021, Baranowski 2022b, Baranowski 2022a].

2D-perovskites exhibit a direct optical gap at Γ point in the Brillouin zone [Baranowski 2019, DeCrescent 2020]. A characteristic feature of their band structure is that, in contrast to the traditional III-V semiconductors, the strong spin orbit coupling affects the conduction band instead of the valence band [Even 2013]. This is due to the VB being composed mainly from the s-like orbitals, while the CB is mainly composed of p-like orbitals [DeCrescent 2020, Baranowski 2022a]. Consequently, the lowest CB is the spin-orbit coupling split band with electron angular momenta of $\pm\frac{1}{2}$, which is the same as the top of the VB. The excitons are composed of the electrons and holes from the CB and VB edges, both characterized by the total angular momenta of $\pm\frac{1}{2}$, which yields 4 possible excitonic states: one with the total angular momentum of $J = 0$, which is optically dark, and the remaining three with $J = 1$ *i.e.* optically bright, with the in-plane projections $J_z = -1, 0, 1$. Due to the exchange interaction, the degeneracy of the bright states and the dark state is lifted [Baranowski 2022a], yielding the dark exciton as the ground state of the system [Dyksik 2021, Posmyk 2024b, Posmyk 2024a]. Furthermore, the spatial confinement due to the 2D nature results in the splitting off of the exciton with J_z=0. Due to its out of plane dipole orientation it is coupled to photons with an out-of plane linear polarization [Posmyk 2024b, Posmyk 2024a]. The remaining J_z=±1 are degenerate and couple to the left-handed (σ^-) and right-handed (σ^+) circularly polarized photons. The resulting exciton fine structure is shown in Fig. 4.9 (d). The degeneracy of the two in-plane excitons can be further lifted in 2D-perovskites characterized by in-plane anisotropy, the example of which can be found in the archetypical $\mathrm{PEA_2PbI_4}$ [Dyksik 2021, Posmyk 2024b, Posmyk 2024a]. On the other hand, in the $\mathrm{BA_2PbI_4}$ (BAPI), which is the component of the TMD/2D-perovskite heterostructure studied in this chapter, no evidence of a substantial in-plane excitons splitting has been observed so far.

Heterostructures composed of RP 2D-perovskites and TMDs are expected to exhibit type II band alignment as shown in Fig. 4.9 (e) [Baranowski 2022b]. This opens the possibility of charge transfer leading to formation of interlayer excitons [Chen 2020a, Chen 2020b, Karpińska 2022, Yao 2022], which is of interest in the studies presented in the following sections of this chapter.

4.2.2 Sample characterization

The investigated TMD/2D-perovskite heterostructure (HS) sample was prepared using an all-dry transfer method by Jonas D. Ziegler from the group of Alexey Chernikov (Dresden Technical University). The microscope image and schematic drawing of the HS are presented in Fig. 4.10. In the microscope image in panel (a) the lines marking the positions of the constituent flakes show that areas of bare $\mathrm{WSe_2}$, bare perovskite and HS regions can be distinguished. The HS is encapsulated from bottom and top side with insulating hBN layers. The HS itself consists of monolayer $\mathrm{WSe_2}$ flakes (bilayer $\mathrm{WSe_2}$ in part of the HS) on the bottom and the thicker, multi-layer $\mathrm{(BA)_2PbI_4}$ on the top. The individual $\mathrm{(BA)_2PbI_4}$ layers have the octahedral sheet thickness of $n = 1$ *i.e.* a single octahedral $\mathrm{PbI_4}$ sheet between organic BA cations (see Fig. 4.9 (a) in section 4.2.1) as schematically drawn in panel (b).

To determine basic optical properties of the HS I performed spatially resolved PL measurements complemented with reflectivity at several representative spots on the sample. The results are shown in Fig. 4.11. Panel (a) shows PL and re-

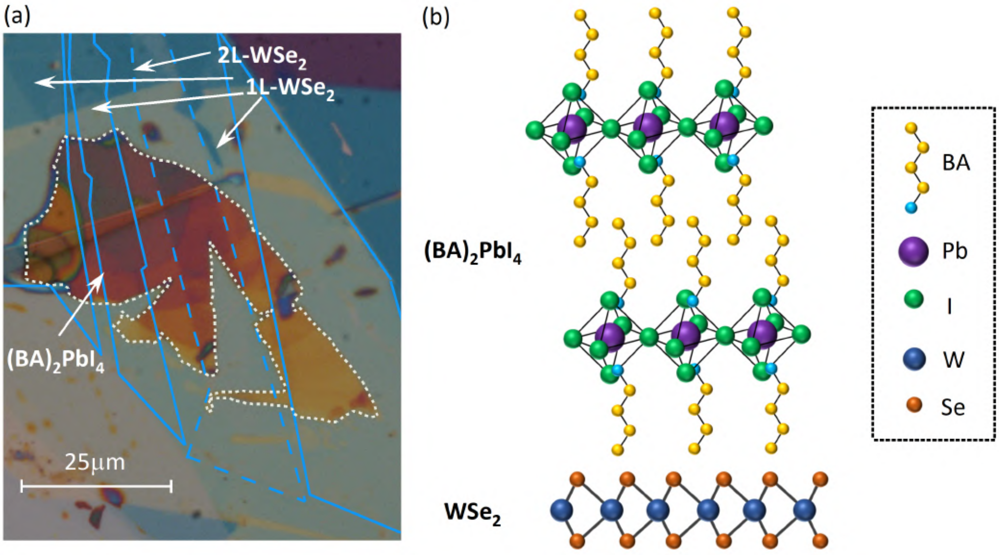

Figure 4.10: (a) Microscope image of the investigated WSe$_2$/(BA)$_2$PbI$_4$ heterostructure. The WSe$_2$ and perovskite flakes are outlined. (b) Schematic drawing of the heterostructure with 1L-WSe$_2$ on the bottom and multi-layer (BA)$_2$PbI$_4$ $n = 1$ on top.

flectivity spectra from regions of HS, bare 1L-WSe$_2$ and bare perovskite. Bare 1L-WSe$_2$ spectra exhibit very similar structure to those presented in previous section in Fig. 4.3, in which emission of several excitonic complexes and reflectivity resonances of higher excitonic states can be observed. Bare perovskite spectra show excitonic emission and absorption in two energy ranges around 2.53 eV and 2.4 eV, which correspond to the low temperature (LT) and high temperature (HT) phases of (BA)$_2$PbI$_4$ [Baranowski 2019, Ziegler 2022]. Despite the cryogenic temperatures at which, the optical spectra were taken it is possible for the HT phase to partially persist [Baranowski 2019] as seen here. The same absorption features are present in the reflectivity spectrum of the HS. There, aside from the perovskite features we can observe that the features related to the WSe$_2$ are practically absent. This is likely related to the appearance of additional electronic interactions with the perovskite and non-radiative charge or energy transfer [Wu 2019, Zhou 2020] from WSe$_2$ to the perovskite layer. On the other hand, the reflectivity of HS exhibits an additional feature at $\simeq 2.08$ eV, denoted as X_B^{HS}, which is around $\simeq$80 meV lower in energy from the B$_{1s}$ exciton in bare 1L-WSe$_2$. The PL spectrum of HS, similar to reflectivity, shows suppressed emission of the WSe$_2$ excitonic complexes, *e.g.* A$_{1s}$ as evident by its much weaker emission as compared to bare 1L-WSe$_2$.

In the PL spectrum of the HS, the typical excitonic transitions of the WSe$_2$ are strongly suppressed, similar as in the reflectivity spectrum. Furthermore, a new feature can be spotted in form of a broad PL emission peak at $\simeq 1.55$ eV. This PL peak is assigned to the interlayer exciton (IX), which is expected to form due to the

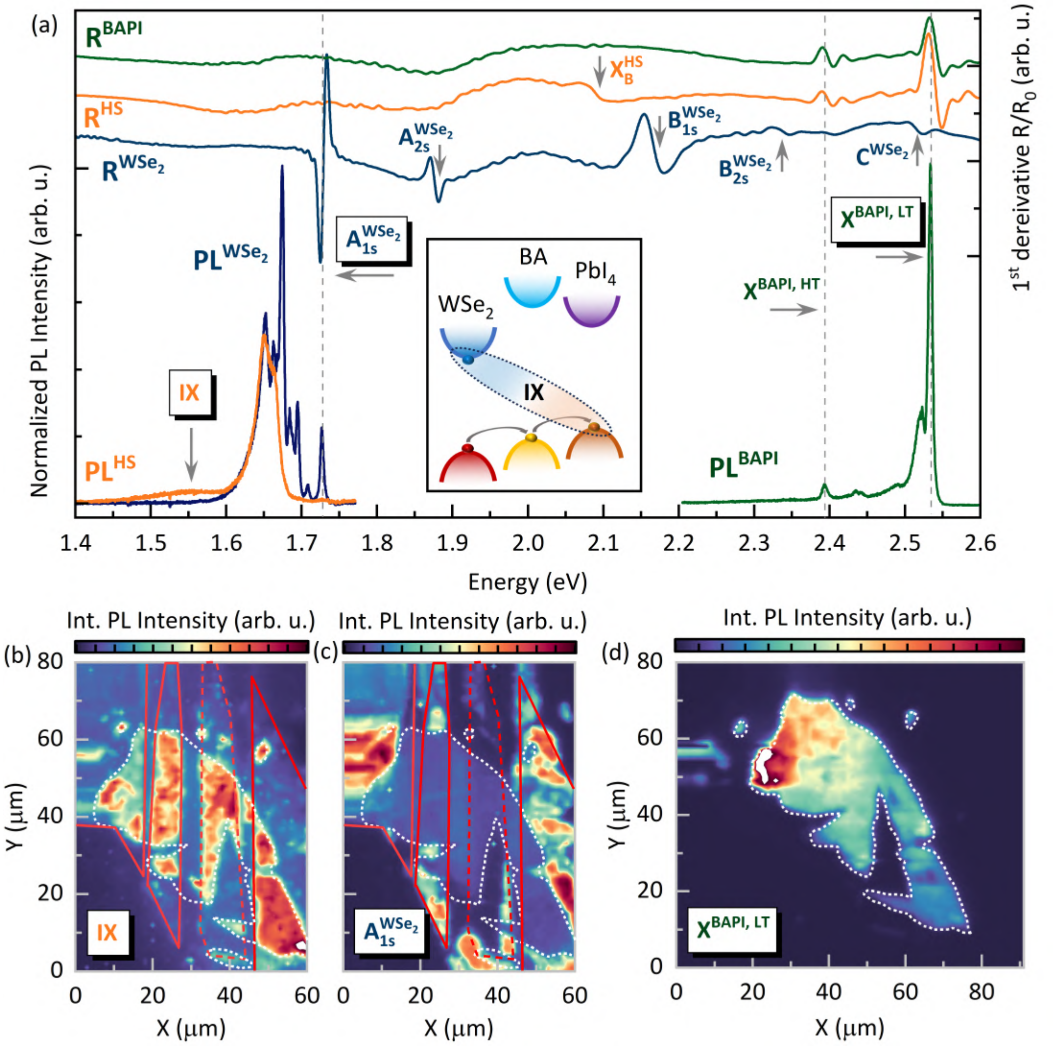

Figure 4.11: Optical characterization of the heterostructure. (a) Bottom of the graph: PL spectra from different regions of the sample: heterostructure (HS) region (orange PL curve), bare 1L-WSe_2 (blue PL curve) and bare BA_2PbI_4 (BAPI) perovskite green PL curve). HS and 1L-WSe_2. Top of the graph shows corresponding in color reflectivity spectra of bare 1L-WSe_2, bare BA_2PbI_4 and the heterostructure, for comparison. Inset shows the band alignment of the heterostructure and schematic drawing of the origin of the interlayer exciton (IX). (b-d) False-color maps of spatially resolved PL Intensity integrated in the regions corresponding to the new IX peak (b), the neutral WSe2 A_{1s} exciton (c) and the exciton of the BA_2PbI_4 (d). Red lines mark the positions of the WSe_2 flakes (solid for 1L and dashed for 2L), while the white dotted line outlines the perovskite flake. PL Maps in (b) and (c) were obtained with excitation wavelength of 532 nm (2.33 eV), (*i.e.* below the band gap of the perovskite) and perovskite PL map (d) with 430 nm (2.883 eV).

type II band alignment in TMD/2D-perovskite heterostructures (see Fig. 4.9 (e)). As in the earlier reported comparable heterostructures of $MoSe_2/PEA_2PbI_4$ and $MoSe_2/BA_2PbI_4$, the expected band alignment is shown in the inset of panel (a). The included band offsets of the organic spacer suggest the blocking of the electron transfer between the WSe_2 and PbI_4 layers and at the same time a cascaded charge transfer of the hole from the WSe_2, through BA to PbI_4. Consequently, the IX state should form between the electron in the conduction band of the WSe_2 and the hole in the valence band of the perovskite, precisely in the inorganic PbI_4 slab. It is worth noting, that the PL spectra in Fig. 4.11 (a) for the 1L-WSe_2 and the HS were acquired with excitation energy below the band gap of the perovskite (as noted in the caption of Fig. 4.11), so that the electron-hole pairs are created nominally only in the WSe_2. The detection of the WSe_2 or HS emission for excitations above the perovskite band gap was not reliable due to strong overlap of the tail of the intense low energy below-band gap PL emission from the perovskite of uncertain origin (likely self-trapped or defect related). The realized below-band gap excitation condition additionally strengthens the interpretation of the new PL feature in the HS as the IX. Upon excitation of the WSe_2, the electron is blocked in the WSe_2 layer due high potential barrier of the organic spacer of the perovskite (BA), meanwhile the hole transfer to the inorganic PbI_4 layer of the perovskite is allowed due to the step-like structure of the valence band alignment (see inset of Fig. 4.11 (a)). The observed formation of the IX state is in agreement with theoretical predictions and observations in other TMD/2D-perovskite heterostructures [Chen 2020a, Chen 2020b, Karpinska 2021, Karpińska 2022].

The spatially resolved PL measurements are presented in panels (b-d) of Fig. 4.11. Panel (b) shows the PL intensity integrated in the energy range corresponding to the IX peak. From the map we note that it is present only in the regions, where the WSe_2 (red lines) and perovskite (white dotted line) overlap *i.e.* in the HS. This further corroborates the assignment of the peak as an interlayer exciton. Panel (c) shows the PL intensity of the neutral A_{1s} exciton of WSe_2. Its emission is clearly observed on the bare monolayer WSe_2 flakes and much weaker one the bare bilayer part. It is also strongly suppressed in the HS region as was visible on the exemplary PL and reflectivity spectra in panel (a). Panel (c) shows the PL intensity of the LT phase exciton of BA_2PbI_4. The different intensity levels correspond to the thickness of the the perovskite flake matching the color contrast seen in the microscope image (Fig. 4.10 (a)).

To further confirm the origin of the IX peak as an interlayer transition I performed the PL measurement on the HS as a function of excitation power and temperature.

The power dependence is depicted in Fig. 4.12. Panel (a) shows PL spectra at powers ranging from 1 to 50 μW. Four emissions are marked as IX, L (localized states), T (charged exciton) and A_{1s} states. The PL intensity of these as a function of excitation power is shown in panel (b). All four emissions show a power coefficient close to 1, which suggests the free excitonic character. An exception for the L states is visible due to saturation of emission at highest excitation powers, which in turn

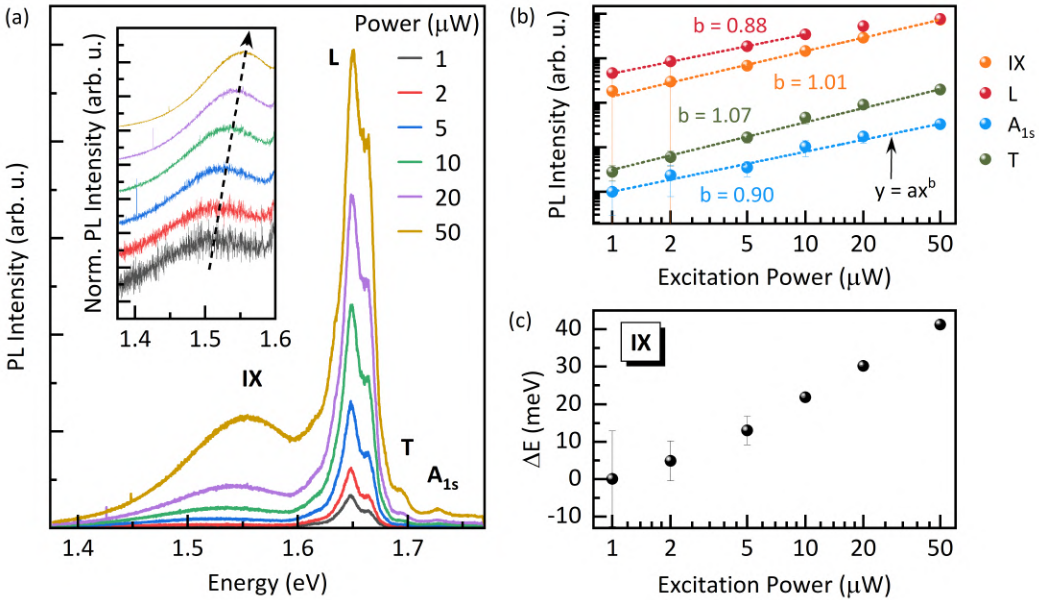

Figure 4.12: Power dependence of PL emission on the heterostructure: (a) Stacked PL spectra at different excitation powers. Inset shows the zoom-in on the IX peak evolution on stacked normalized PL spectra. (b) Double logarithmic scale of PL Intensity of the four emissions marked in (a) as a function of excitation power. (c) Energy shift and FWHM of the IX peak as a function of excitation power in logarithmic scale.

rather suggests localized state as the origin. The inset of panel (a) shows vertically stacked PL spectra normalized to the intensity of the IX peak, which emphasizes its strong energy blue shift with increasing excitation power. The energy shift is plotted in panel (c). The high value of the blue shift slope *i.e.* $\simeq 30\,\text{meV}$ per only one order of magnitude change in excitation power is a characteristic feature for interlayer excitons of dipolar nature due to strong dipolar repulsion [Butov 1999, Laikhtman 2009, Rivera 2015] and is in agreement with results in similar TMD/2D-perovskite heterostructures [Chen 2020a, Yao 2022].

Fig. 4.13 shows the temperature dependence of the PL emission from the HS. Panel (a) shows the stacked PL spectra at different temperatures, which show the evolution of both IX and the A_{1s} neutral exciton of WSe_2. Both transitions exhibit an energy red shift and a non-monotonic intensity change with increasing temperature, which are analysed in detail in panels (b) and (c), respectively. Panel (b) shows the emission energy of IX and A_{1s} as a function of temperature. The energy shift as a function of the temperature for both transitions was fitted using a modified Varshni formula [Huang 2016] given by:

$$E(T) = E(0) - S\langle\hbar\omega\rangle \cdot \left(\coth\frac{\langle\hbar\omega\rangle}{2K_BT} - 1\right), \tag{4.2}$$

where the $E(0)$ is the energy at $T = 0\,\text{K}$, S is the dimensionless parameter describing the strength of the electron-phonon coupling and $\langle \hbar\omega \rangle$ is the average acoustic phonon energy. The A_{1s} transition red shifts with increasing temperature as expected in TMDs [Liu 2020a]. The fit with Eq. 4.2 gives the parameter values of $S \approx 2.15$ and $\langle \hbar\omega \rangle \approx 17.5\,\text{meV}$, similar to what was obtained in earlier studies on monolayer WSe_2 [Huang 2016]. The IX state red shifts in similar manner to A_{1s} with increasing temperature albeit more strongly. The obtained fitting parameters are $S \approx 7.7$ and $\langle \hbar\omega \rangle \approx 29.4\,\text{meV}$. The $(BA)_2PbI_4$ also exhibits a red shift of the band gap with increasing temperature [Gong 2024]. The faster energy shift is hence likely related to the IX state energy being dependent on the bands shifts in both of the constituent materials, specifically CB shift of WSe_2 and VB shift in 2D-perovskite, the effects of which sum up. Panel (c) shows the extracted from

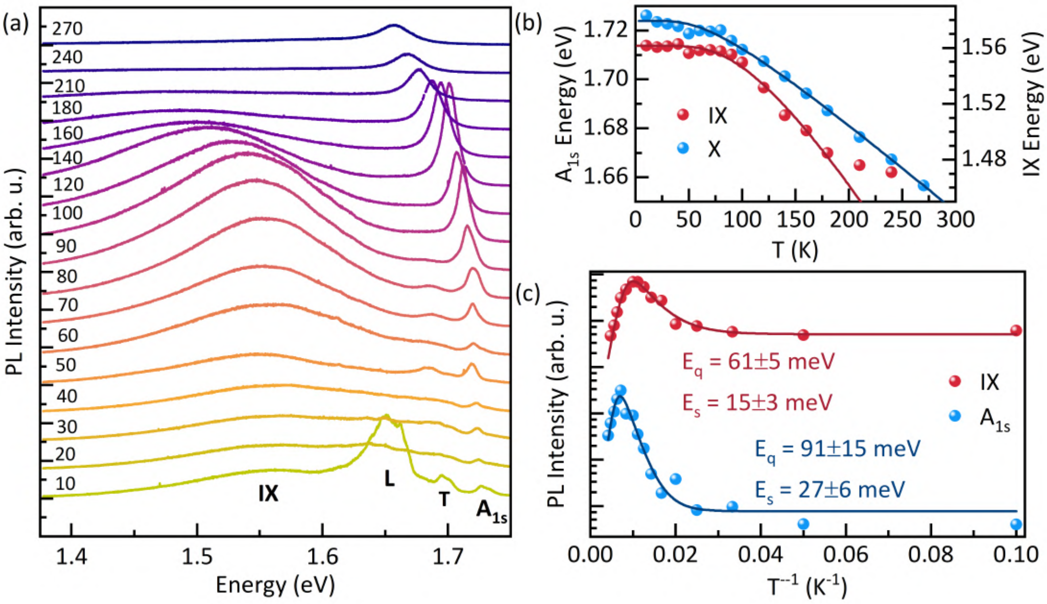

Figure 4.13: Temperature dependence of PL emission of the heterostructure. (a) Stacked PL spectra at different temperatures. The number above each spectrum corresponds to the temperature $T(K)$. (b) Peak energies of IX and A_{1s} as a function of temperature. The lines represent the fit to the data with modified Varshni formula (Eq. 4.2). For the IX state the last two temperature data points were purposefully omitted from the fitting procedure due clearly diverging from the linear behaviour expected from the Eq. 4.3. This might be related to additional mechanisms affecting the excitonic energy, which are not considered, or to the uncertainty of the energy position obtained from Gaussian fitting due to very low IX intensity at high temperatures. (c) Plots of PL intensities of IX and A_{1s} peak (in logarithmic scale) as a function of inverse temperature. The lines represent the Arrhenius fits to the data (Eq. 4.3) with two activation energies E_q (quench) and E_s (supply) as parameters, which account for the temperature induced decrease and increase of intensity, respectively.

fitting PL intensities of the IX and A_{1s} peaks plotted as a function of inverse temperature. We can clearly observe the temperature-induced brightening of both IX and A_{1s} peaks. This effect is expected for the so called "dark" TMDs due to the band ordering, which yields the spin-dark exciton state as the lowest energy state [Kapuściński 2021] (see Fig. 1.5 (a,b) in section 1.4.2). In that case, increasing the temperature promotes the excitons from the lower energy dark state to the higher energy bright state resulting in increase of the emission intensity. To extract the activation energies of the involved processes I fit the data in panel (c) with a modified Arrhenius formula [Huang 2016]:

$$I(T) = I_0 \cdot \frac{1 + B_s \cdot \exp\left(\frac{-E_s}{k_B \cdot T}\right)}{1 + B_q \cdot \exp\left(\frac{-E_q}{k_B \cdot T}\right)}, \tag{4.3}$$

which includes the standard quenching term $\exp(\frac{-E_q}{T \cdot k_B})$ with related activation energy E_q, which corresponds to a non-radiative recombination process and an additional supply term $\exp(\frac{-E_s}{T \cdot k_B})$ with activation energy E_s, which corresponds to a process supplying excitons to the emitting state. The I_0 is the PL intensity at $T = 0\,\mathrm{K}$, k_B is the Boltzmann constant and the $B_{q(s)}$ corresponds to the magnitude of the quenching (supply) process.

The E_s of the A_{1s} state value of $\approx 27\,\mathrm{meV}$ falls in between the calculated value of the conduction band splitting calculated for a free standing monolayer [Kośmider 2013, Liu 2013, Kormányos 2015] of $\approx 36\,\mathrm{meV}$ and obtained experimentally for a fully encapsulated monolayer $\approx 14\,\mathrm{meV}$ [Kapuściński 2021]. The determined activation energy however does not correspond directly to the energy splitting between the dark and bright states. The obtained value based on Arrhenius analysis is convoluted with competing non-radiative processes. It also does not account for the temperature dependence of the radiative lifetime as well as the thermal equilibrium between the populations of the two states [Zhang 2015]. One of the possible processes responsible for the quenching of emission is the dissociation of excitons *i.e.* overcoming of the binding energy. The binding energy of the exciton in 1L-WSe_2 is expected to be on the order of 400 meV (based on the A_{1s}-B_{1s} energy separation in the studied sample), thus not matching the fitted value of $\approx 91\,\mathrm{meV}$. However, previous studies also reported much lower values than the expected binding energy [Huang 2016, Davila 2024] and related this effect to the presence of defects, impurities as well as interaction with the substrate, which create additional quenching channels. The IX emission shows comparable values of $E_s \approx 15$ meV and $E_q \approx 61$ meV. The smaller values likely stem from additional non-radiative channels available for this state (shared between WSe_2 and BA_2PbI_4), due to more complex environment posed by the HS, as well as probably lower binding energy of the IX complex. The similarity of the temperature-dependent behaviour of the A_{1s} and IX state suggests nevertheless that the IX properties are in large proportion inherited from the TMD layer.

4.2.3 Valley polarization

The optical characterization of the IX state shown in the previous subsection strongly suggests the substantial similarity of its properties to the excitons in the TMD layer. In the next step I performed the circular polarization resolved PLE on the IX state, similar to that presented for excitons in bare WSe_2 in section 4.1.2. This experiment allows to acquire information whether the IX also inherits the valley polarization properties of the TMD.

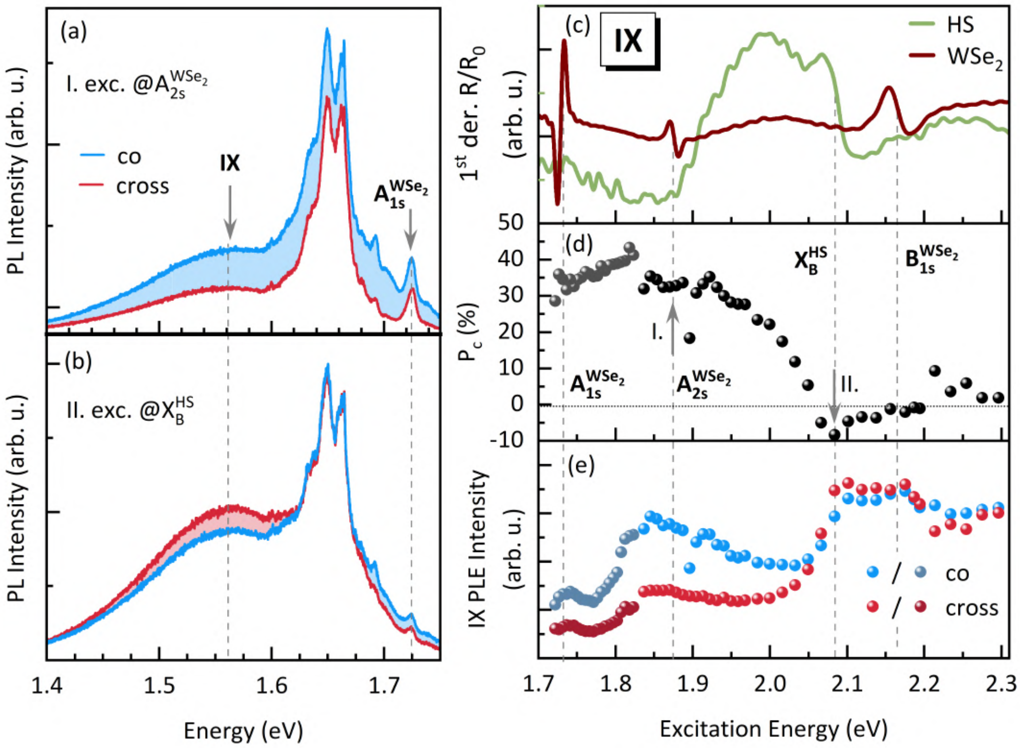

Figure 4.14: Valley polarization of IX state. (a,b) Co- and cross-polarized PL spectra of the heterostructure (HS) excited at the energy corresponding to the A_{2s} resonance of 1L-WSe_2 (a) and to the X_B^{HS} resonance present in the HS. The blue and red shaded areas in (a,b) denote the intensity difference in favour of the co- or cross-polarized emission, respectively. (c-e) Circular polarization resolved PLE of IX state. (c) Reflectivity spectrum of the HS (green curve) and of the bare 1L-WSe_2 for comparison (brown curve). (d) P_c as a function of excitation energy, calculated from the co- and cross-polarized PLE intensity shown in (e).

Fig. 4.14 shows the results of the PLE experiment. Panels (a) and (b) compare the co- and cross-polarized PL spectra of the HS at two different excitation energies corresponding to the A_{2s} state of WSe_2 (a) and the new feature present on the HS at $\simeq 2.08$ eV named X_B^{HS}. We can observe that the whole spectrum *i.e.* both the WSe_2 excitons and the IX are strongly polarized in the (a) case with $P_c \approx 30\,\%$, which is a similar result to that on the bare WSe_2 presented earlier. In the case of (b), on the other hand, there is a clear difference between the low energy side of the spectrum (dominated by IX), which shows more cross-polarized intensity, and the high energy side of the spectrum (dominated by WSe_2 excitons), which is more co-polarized. The entire PLE series of the IX state is presented in panels (c-e). Panel (c) shows the reflectivity spectra for the HS and bare 1L-WSe_2 for comparison of the energy position of excitonic resonances. Panel (d) shows the excitation energy dependent P_c calculated from the co- and cross-polarized PLE intensities shown in panel (e). The PLE intensity shows comparable shape to that of bare WSe_2 shown earlier in Fig. 4.5 (e). There are however two important distinctions. Firstly, the extrema around the WSe_2 related resonances are much more broadened, which might be related to disorder and more available coupling channels. Secondly, there seems to be two PLE intensity maxima in the vicinity of WSe_2 B exciton. The higher energy one at $\simeq$2.16 eV corresponds well to the B_{1s} resonance of bare WSe_2, while the lower energy one at $\simeq 2.18\,\mathrm{eV}$ is a new feature with respect to the bare WSe_2 and matches energetically the resonance, which appears only on the HS, denoted as X_B^{HS}. The P_c also shows a comparable response to that of bare WSe_2. At low excitation energies, including both excitation around the A_{1s} and A_{2s} states of WSe_2, the P_c of IX is strongly positive at around $\simeq 30\,\%$. However, when the excitation energy falls in the vicinity of the B_{1s} exciton and the new X_B^{HS} feature, the P_c decreases strongly to around $\simeq 0\,\%$ and even slightly below into the negative values. This is a clear indication that the Dexter-like coupling exciton transfer affects the IX state in a similar manner as excitons in bare WSe_2. This observation demonstrates that the charge transfer of the hole from the valence band of TMD to the PbI_4 layer of the perovskite is a spin conserving process, which allows for the preservation of the valley polarization originated in the TMD layer, thus facilitating a successful spin-injection.

Interestingly, the absolute minimum of $\simeq -8\%$ corresponds to excitation at the X_B^{HS} resonance. The origin of this new feature present only on the HS is not fully understood. On the one hand, it is clearly characterized by the same Dexter-like effect as the excitation at B_{1s} for the A_{1s}. One possibility would then be that the X_B^{HS} is a renormalized B_{1s} state of WSe_2 due to the dielectric environment of the HS. However, the 80 meV difference is too large to be the result of the change in the dielectric environment. At the same time, the PLE intensity of the IX and accordingly P_c seems to react at both of these energies.

Moreover, I compare the P_c and PLE intensity of the IX and the A_{1s} exciton from the very same PLE spectra on HS, which are shown in Fig. 4.15. There, it is clear that the A_{1s} exciton response is very similar to that of the bare WSe_2 *i.e.* the Dexter-like effect of decrease of the valley polarization is present only around the B_{1s} exciton and not at the energy corresponding to the X_B^{HS}. This observation suggests that two separate entities simultaneously exist within the HS. The fact that only the IX state responds to the resonance of the X_B^{HS} indicates that this might be another form of an interlayer exciton state, related to the B state, presence of which was not initially predicted. In that case, its presence in the reflectivity spectrum would suggest the momentum-direct nature of this transition. On the

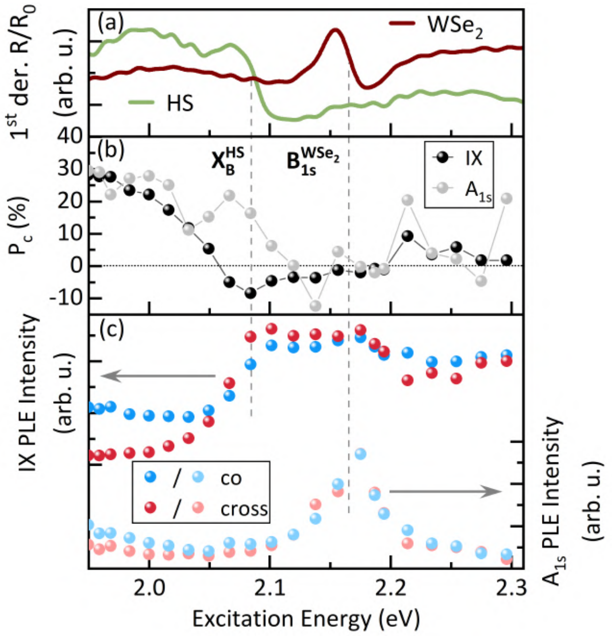

Figure 4.15: Comparison of Dexter-like coupling effect for IX and A_{1s}. (a) Reflectivity spectra of heterostructure (HS) and bare WSe$_2$ for comparison. (b) P_c of IX and A_{1s} calculated from the PLE intensity data points from panel (c). The PLE data for the IX and A_{1s} excitons is taken from the same PLE measurement.

other hand, the clear resonance of X_B^{HS} visible in reflectivity stands as a counter argument to that interpretation as the interlayer states are usually characterized by very low absorption probability and therefore are rarely visible in reflectivity spectra. Another probable explanation might be that the X_B^{HS} originates from a form of a TMD-perovskite hybridized state with a momentum-direct nature of its transition. To fully understand the origin of the new state present on the HS, further experimental and theoretical investigations are necessary.

Overall, the observed excitation energy dependence of the valley polarization of an interlayer state in TMD/2D-perovskite heterostructure demonstrates the possibility of controllable spin injection from TMD into the 2D-perovskite. The observed Dexter-like coupling effect, which impacts the interlayer exciton in a similar fashion as the intralayer TMD excitons shows that its properties are largely dependent on the choice of the TMD and at the same time provides an additional control knob for tuning of the optical polarization in such systems.

4.3 Summary

The results presented in this chapter provide insight into the profound effects that Dexter-like intervalley coupling has on the polarization properties of TMDs and TMD-based structures such as the presented TMD/2D-perovskite heterostructure.

I have studied this effect by characterizing the excitation energy dependent PL intensity resolved in the circular polarization basis. This allowed for quantification of the valley polarization in the time-integrated regime. I studied two samples, one consisting of an encapsulated monolayer WSe_2 (section 4.1) and second consisting of a heterostructure of 1L-WSe_2/$(BA)_2PbI_4$ (section 4.2). In the bare 1L-WSe_2 I investigated the polarization properties of several excitonic complexes such as the neutral exciton, biexciton and charged biexciton. In the TMD/2D-perovskite heterostructure I studied the response of an interlayer exciton, which emerges as a consequence of type II band alignment at the interface of TMD and 2D-perovskite. In both cases, the PL emission of WSe_2 intralayer excitons as well as in the interlayer exciton in the heterostructure exhibit strong decrease or even inversion of the valley polarization, when the polarized excitation is energetically resonant with higher lying B exciton states of WSe_2 and, uniquely in the heterostructure, the new state (X_B^{HS}), which appears below the B_{1s} resonance of WSe_2. The same effect experienced by both intralayer (WSe_2) and interlayer exciton (HS) demonstrated that the charge transfer of the hole from the TMD to 2D-perovskite is a spin-conserving process, which opens the possibilities for applications utilizing spin-injection. Overall, the demonstrated Dexter-like coupling gives an additional control knob in tuning of the excitonic properties, in the form of optical polarization, which can be switched, simply by choosing an appropriate excitation energy. The results presented in chapter 4.1 were published in 2D Materials 11.2 (2024), p. 10110 - Jakub Jasiński et al. “Control of the Valley Polarization of monolayer WSe_2 by Dexter-like Coupling”[Jasiński 2024b]. The results shown in 4.2 are the topic of a currently prepared manuscript to be submitted for review.

Chapter 5

Electric field tuning of excitons in natural $MoSe_2$ homobilayer

TMD structures can be regarded as ideal platforms for engineering of excitonic properties and light matter interactions. Firstly, due to the fascinating excitonic physics related to strong electron-hole interactions enhanced by their 2D nature and dielectric screening with the additional control opportunities provided by the spin-valley physics [Chernikov 2014, He 2014, Hanbicki 2015, Wang 2018a, Mueller 2018, Xiao 2012, Perea-Causin 2022] (see sections 1.3 and 1.4). Secondly, the lack of stacking constraints due to van der Waals nature of interlayer binding of TMDs and other emerging 2D materials allow for seamless stacking of virtually any combination of layers to form complex devices, properties of which are additionally tunable by the interlayer relative orientation (twist angle) and choice of materials [Geim 2013, Novoselov 2016, Ciarrocchi 2022, Huang 2022a]. One of the prominent properties of the multilayer structures is the emergence of the long-lived interlayer excitons (IXs), in which the constituent electrons and holes are separated into different layers of the structure [Rivera 2015, Rivera 2018, Lee 2014, Gerber 2019, Jiang 2021, Arora 2017, Merkl 2019, Sung 2020, Kovalchuk 2023, Villafañe 2023, Feng 2024, Shimazaki 2020, Peimyoo 2021, Leisgang 2020, Lorchat 2021, Van Der Zande 2014, Liu 2014, Arora 2018, Wang 2018b, Huang 2022b, Brem 2020, Zhu 2014a, Tan 2019, Yan 2019, Jauregui 2019, Tran 2019, Choi 2021, Nayak 2017, Baek 2023, Sokolowski 2023, Luong 2017, Hagel 2021, Okada 2018, Tebyetekerwa 2021, Montblanch 2021, Yuan 2020, Li 2020a, Chen 2023, Yu 2020, Zhang 2020a, Ma 2021, Cho 2021, Khestanova 2023] (see section 1.4.2.3). Such spatial arrangement of the charge carriers endows these excitonic states with a static, out-of-plane dipole moment. Such interlayer, dipolar excitons can be easily tuned via the application of an out-of-plane electric field [Wang 2018b, Peimyoo 2021, Liu 2020b, Tagarelli 2023, Tagarelli 2023]. In the widely studied TMD heterobilayers [Jauregui 2019, Tran 2019, Choi 2021, Nayak 2017, Baek 2023, Sokolowski 2023, Luong 2017, Hagel 2021, Okada 2018, Tebyetekerwa 2021, Montblanch 2021, Yuan 2020, Li 2020a, Chen 2023, Yu 2020, Zhang 2020a, Ma 2021, Cho 2021, Khestanova 2023], the band alignment of the constituent materials results in the interlayer exciton being the lowest energy state of the system and, at the same time, enforces the singular orientation of the dipole moment. In homobilayers, the energy degeneracy allows for simultaneous existence of dipolar excitons with opposite dipole moments [Arora 2017, Gerber 2019, Hagel 2022, Feng 2024].

The dipole-dipole interactions are highly tunable via extrinsic factors such as tuning of charge and exciton density or electric field and are also heavily influenced by intrinsic factors such as material composition and relative twist of layers composing the TMD structure. In particular, the interactions of dipolar state system are strongly influenced by the presence of the periodic moiré potential, which emerges in twisted or lattice-mismatched TMD bilayers [Yu 2017, Wu 2017]. The moiré superlattice leads to the formation of flat minibands [Zhang 2020c, Li 2021, Kundu 2022], which decreases the kinetic energy of the states trapped in the moiré sites. The relative decrease of the kinetic energy with respect to the Coulomb interaction energy enhances the correlations between the charges or excitons. The dipolar interactions can lead to emergence of exciting many-body physics phenomena such as superfluidity, Mott insulators and Bose-Einstein condensates [Eisenstein 2004, Wang 2019, Fogler 2014, Regan 2020, Tang 2020, Huang 2021, Gu 2022, Zhou 2021, Xu 2020, Xiong 2023, Brem 2024]. Fig. 5.1 shows examples of correlated states realized in TMD heterobilayers in the form of excitonic insulator consisting of moiré trapped interlayer excitons, realized in a heterobilayer of WSe_2/WS_2 (panel (a)) and interlayer exciton condensation in $MoSe_2/WSe_2$ (panel (b)).

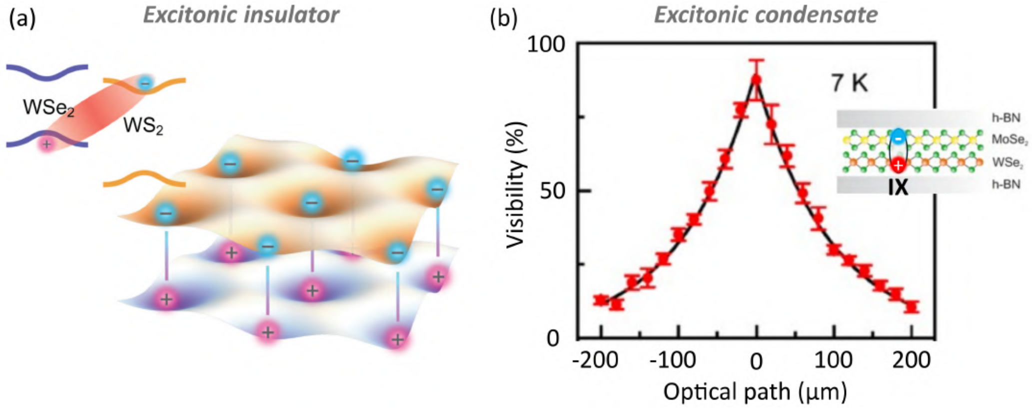

Figure 5.1: (a) Bosonic correlated insulator state in WS_2/WSe_2 moiré heterobilayer consisting of moiré trapped dipolar interlayer excitons (IXs). (b) Temporal coherence visibility as a function of optical path for the IX state pointing to a coherent IX condensation in $MoSe_2/WSe_2$ heterobilayer. Panels (a) and (b) are adapted from Refs. [Xiong 2023] and [Sigl 2020], respectively.

Additionally, strong interactions between dipoles of opposite orientation of their dipole moment can lead to the formation of higher order states, namely, the quadrupolar excitons. The quadrupole-quadrupole interactions open the path for even more exciting physics in the form of rotonization, Bose-Einstein condensates with new properties with respect to the dipole-based ones, topological superfluids and charge-density waves [Weber 2003, Lahrz 2014, Lahrz 2015, Bhongale 2013, Slobodkin 2020]. The quadrupolar systems are especially promising for the quantum simulations and revealing novel many-body phenomena [Slobodkin 2020, Astrakharchik 2021]. In recent years, the emergence of quadrupolar excitons have been theoretically predicted and observed experimentally in TMD heterotrilayers [Yu 2023, Li 2023a, Lian 2023, Bai 2023, Xie 2023, Slobodkin 2020, Astrakharchik 2021, Deilmann 2024]. Such trilayer structures (*e.g.* $WSe_2/WS_2/WSe_2$) pose the adequate symmetry for formation of two dipolar excitons with anti-aligned dipole moments. One is formed between the bottom and middle layer, while the other - between the middle and top layer. Through superposition of these two dipolar states via charge carrier tunneling between the outer layers, the formation of the linear electric quadrupole has been realized, as depicted in Fig. 5.2 (a). A characteristic feature of quadrupolar excitons is their nonlinear energy shift in the out-of-plane electric field, shown in 5.2 (b), which is due to acquisition of non-zero dipole moment as the electric field increases [Barré 2023].

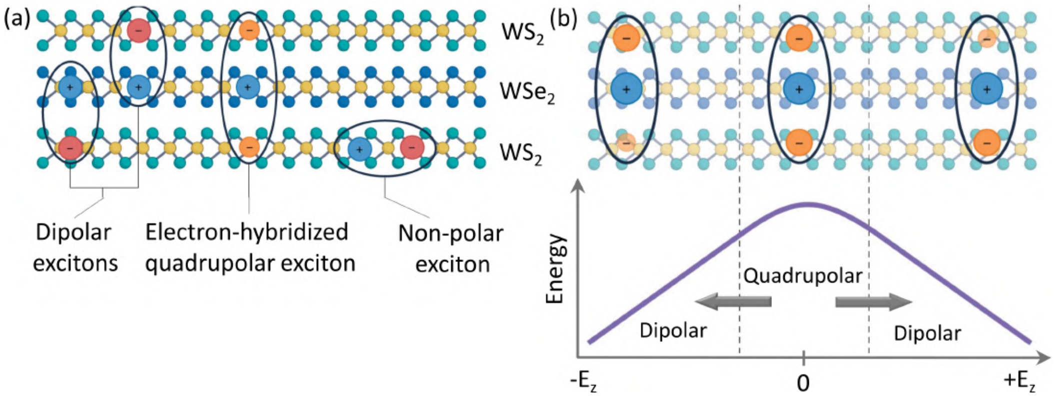

Figure 5.2: (a) Schematic of a TMD hetero-trilayer structure ($WS_2/WSe_2/WS_2$) with depicted intralayer non-polar excitons, interlayer dipolar excitons and quadrupolar excitons (superposition of two anti-aligned dipolar excitons due to electron tunneling between the outer WS_2 monolayers). (b) Dependence of the quadrupolar exciton energy on the applied out-of-plane electric field E_z. For high E_z, the quadrupolar state transitions into a dipolar state. Panels (a) and (b) are adapted from Ref. [Barré 2023].

On the other hand, the TMD homobilayers also allow for simultaneous existence of anti-aligned dipolar excitons [Arora 2017, Gerber 2019, Hagel 2022, Feng 2024]. This suggests that, at least in principle, quadrupolar formation could be possible also in those systems, although no clear observation of quadrupolar features has been made so far. Additionally, the homobilayers, especially the natural (H_h^h-stacked) homobilayers provide a platform with the additional advantage of simplicity for both practical device realization as well as the experimental and theoretical investigation due to clean, moiré- and reconstruction-free interface, strong interlayer hybridization and smooth potential landscapes [Hsu 2019].

In this chapter I present the experimental and theoretical studies on the properties of a fully encapsulated natural homobilayer of $MoSe_2$ under the influence of the out-of-plane electric field. In particular, I focused on the tunability of various interactions between excitonic particles and observation of novel states, such as the quadrupolar excitons. This project was realized in collaboration with the group of Ermin Malic (Marburg Technical University), which provided the microscopic many-body theoretical simulations and with the group of Alexey Chernikov (Dresden Technical University), which provided the know-how in the fabrication of gated devices and technical realization of measurements utilizing electric field. To carry out the studies I constructed a gated device in a design resembling a parallel plate capacitor, which allows for independent control of electric field and free carrier doping (see details of fabrication and realization of electrical measurements in sections 2.3, 2.4 and 5.1. To characterize the intricate excitonic landscape of the MoSe$_2$ homobilayer I performed reflectivity and PL measurements as a function of the out-of-plane electric field and free carrier doping. The experimentally obtained complex picture of the excitonic landscape was complemented by the microscopic model provided by the group of Ermin Malic (Marburg Technical University), which aided the interpretation of the observed phenomena.

5.1 Double-gated MoSe$_2$ homobilayer device

The controlled application of an electric field in a TMD-based structure requires fabrication of a device with electrical contacts and gates, to which voltage can be applied. For the purpose of investigation of excitonic properties in electric field, presented in this chapter, I fabricated double-gated, capacitor-like devices containing natural MoSe$_2$ homobilayers using a well established all-dry transfer method [Castellanos-Gomez 2014], which is a relatively simple method for fabrication of multilayer structures (see the general scheme of the fabrication process in section 2.4).

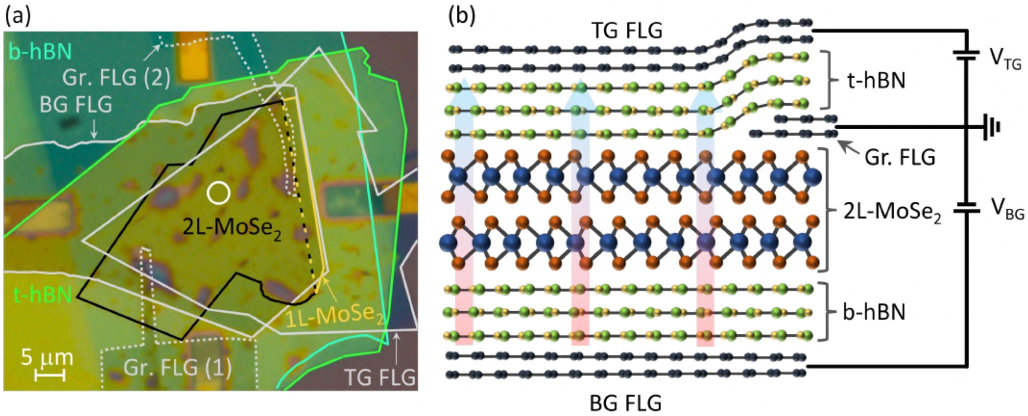

Figure 5.3: (a) Optical microscope image of the natural 2L-MoSe$_2$ device with constituent layers outlined. The white circle marks the position of the signal collection in optical measurements. (b) Scheme of the device. Vertical arrows illustrate the application of an out-of-plane electric field.

The parallel plate capacitor-like design of the device allows for independent tuning of the out-of-plane electric field and free carrier doping, as described in section 2.3. To function properly, the device requires at least three electrical contacts. Two of them serve the role of bottom and top gates. These are isolated from the main sample material via insulating spacer layers of hexagonal boron nitride (hBN). Additionally, at least one lateral contact, which physically touches the active material (*i.e.* the $MoSe_2$ homobilayer) serves as the grounding contact to the sample. The conductive material used to construct electrical contacts in this case is the few layer graphene (FLG). Each of the FLG electrodes are connected separately between the device and the nearby evaporated gold pads on a prepared Si/SiO_2 substrate (see section 2.3 for details). The individual layers composing the device were stacked in the space between the evaporated gold pads (see Fig.2.8 (b) in section 2.3) using the aforementioned all-dry transfer deposition method, in the following order:

1. Bottom gate – FLG
2. Bottom insulating spacer – hBN
3. Sample – $MoSe_2$ homobilayer
4. Grounding contact – FLG (at least one).
5. Top insulating spacer – hBN
6. Top Gate – FLG

Additional FLG flakes were used in step 4. and 5. as a bridge between the primary FLG electrodes and the evaporated gold pads, to ensure the electrical connection.

The results of the fabrication are presented in Fig. 5.3. Panel (a) shows the microscope image of the double-gated $MoSe_2$ homobilayer device, where the constituent layers are outlined. Panel (b) shows the schematic of the device with marked electrical connections. The vertical arrows illustrate the application of the out-of-plane electric field (E_z).

As described in section 2.3, in a double-gated device, the effective out-of-plane electric field (Eq. 2.29) and the free carrier doping (Eq. 2.28) can be tuned independently. To achieve that, the possible inequivalence of the thicknesses of the insulating hBN spacers, which results in difference in the displacement field experienced by the TMD sample, has to be accounted for. Therefore, the ratio of the voltages applied to the bottom and top gates should be kept close to the ratio of the hbn thicknesses *i.e.*: $|\frac{V_{BG}}{V_{TG}}| = \frac{d_{b-hBN}}{d_{t-hBN}}$, where $d_{b-hBN/t-hBN}$ is the thickness of the bottom/top hBN spacer. By keeping that ratio and applying the voltages of the same polarity, the effect of the electric field inside the device cancels out (see Eq. 2.29), which leaves the free carrier doping as the only applied effect. Conversely, applying the voltages of the same ratio, but with opposite polarity induces out-of-plane electric field without doping. For the device investigated in this chapter, the experimentally obtained voltage ratio (opposite polarity), which accounts for the difference in the hBN thicknesses was found to be approximately $|\frac{V_{BG}}{V_{TG}}| \approx \frac{1}{2}$.

5.2 Optical response without the electric field

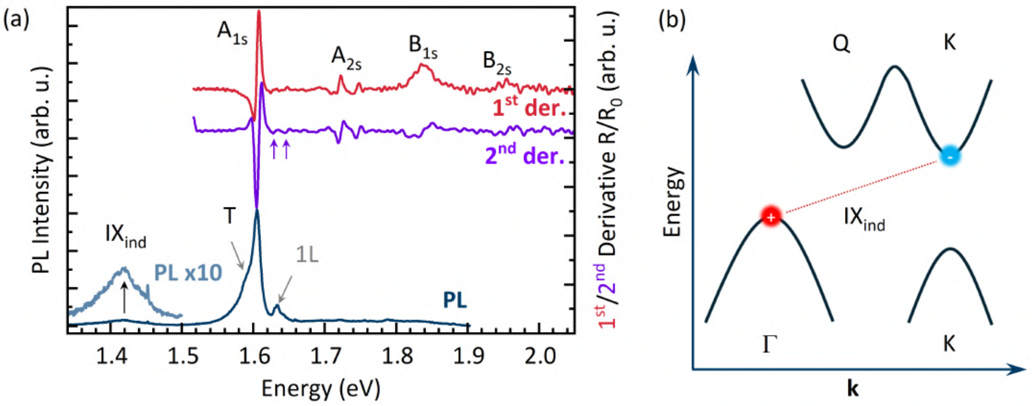

Figure 5.4: (a) Optical response of the MoSe$_2$ homobilayer without electric field in PL and reflectivity in the form of 1^{st} and 2^{nd} derivative of R/R_0. The PL spectrum was acquired using 532 nm cw laser at $\simeq$ 1 mW power. (b) Schematic of the momentum-indirect (IX$_{\text{ind}}$) exciton originating from the K-Γ transition, where the electron is localized in one of the layers, while the hole is delocalized over both layers due to strong hybridization of the Γ point present in homobilayers.

The initial optical characterization of the MoSe$_2$ homobilayer without application of E_z is presented in Fig. 5.4 (a), which shows PL and reflectivity in the form of 1^{st} and 2^{st} derivatives of R/R$_0$. The differential reflectivity spectra (red and purple curves) show a typical optical response of a bilayer MoSe$_2$, with the strongest resonance associated with the neutral A$_{1s}$ excitons at ~1.606 eV. On the higher energy side, other intralayer transitions of A$_{2s}$, B$_{1s}$ and B$_{2s}$ can be observed. The PL (blue curve) is similarly dominated by the transition originating from the A$_{1s}$ exciton at the same energy as the corresponding absorption feature in reflectivity. On the low energy shoulder of the main peak, a weaker emission of the trion (T) can be observed. This suggests the presence of some unintentional doping. However, the fact that the neutral exciton remains much stronger and the simultaneous lack of trion (or attractive Fermi polaron [Sidler 2017]) related feature in reflectivity shows that the amount of doping in the sample is relatively low. Furthermore, at much lower energies, around 1.42 eV, a broad, weak emission, denoted as IX$_{\text{ind}}$ can be observed. This feature matches prior observations in similar homobilayer structures of MoSe$_2$ [Sung 2020, Kovalchuk 2023, Villafañe 2023], and is ascribed to the momentum-indirect IX, which stems from transition between the electron localized in the K/K′ valley in one of the layers and the hole delocalized over both layers at the strongly hybridized Γ point (see schematic in Fig. 5.4 (b)). The additional small PL peak denoted as 1L on the high energy side of the A_{1s} exciton is most probably related to the stray emission from a nearby (few μm away) monolayer part of the flake. This is likely due to the large excitation power necessary to observe emission in bilayers (here used $\simeq 1\,\text{mW}$). As opposed to monolayers, the bilayer TMDs become indirect bandgap semiconductors [Splendiani 2010], which substantially lowers PL efficiency. Thus, despite spatial separation, the much stronger PL of the nearby monolayer might contribute to the PL spectrum.

The signatures of the momentum direct IXs cannot be immediately observed in the optical response, which is likely related to their very low oscillator strength as compared to the intralayer transitions, as well as them not being the ground energy states of the system favoured by relaxation processes. On the other hand, some very weak features seem to emerge in the 2^{nd} derivative reflectivity spectrum such as the two marked by purple arrows in 5.4 (a). Such features are however barely distinguishable from the background noise. Thus, for further investigation, the application of the out-of-plane electric field is required, which should reveal the presence of IXs due to their electric field-dependent energy shift.

5.3 Electrostatic doping

Before applying the electric field I have performed free carrier doping measurements of PL and reflectivity, which are presented in Fig. 5.5. The goal of this experiment was to find the most neutral regime of doping as an optimal starting point for the electric field sweep, in order to avoid additional complexity posed by the presence of charged excitonic states. Panel (a) of Fig. 5.5 of shows the false color map of PL as a function of the applied gate voltages of the same polarity (with pre-determined ratio of $V_{BG} = \frac{1}{2}V_{TG}$). In the vicinity of 0 V of gate voltages, the spectrum shows emission from the neutral A_{1s} as well as the neutral A_{2s} and B_{1s} excitons. A weak IX_{ind} emission is located $\simeq 190\,\text{meV}$ below the A_{1s}. For positive gate voltages ($V_{BG} = \frac{1}{2}V_{TG} > 0.5\,\text{V}$) we can observe a stark change of the emission due to appearance of the now dominating negatively charged exciton A^-_{1s}, which continues to red shift with increasing gate voltages, consistent with an increasing Fermi energy [Huang 2023]. The charged B^-_{1s} exciton similarly shows a consistent red shift. The charged A_{2s} exciton is observed briefly for very low positive gate voltages ($V_{BG} = \frac{1}{2}V_{TG} < 1V$), however, the emission quickly quenches at higher doping levels. The emission of the IX_{ind} is quenched in a similar manner, howeve,r a weak red shifting trace can be observed, likely related to the emission from the charged version of the state. For negative gate voltages, in the hole doping regime, the neutral A_{1s} emission remains as the dominant peak and no clear energy shift is observed for all emission peaks. The IX_{ind}, on the other hand gains intensity, which may be related to more holes being localized in the hybridized Γ point, available for formation of the IX_{ind} complex. The complementary false color map of reflectivity is shown in Fig. 5.5 (c).

For positive gate voltage, the absorption features related to intralayer transitions follow exactly the same evolution as in the PL emission. For the negative voltages on the other hand, clear emergence of positively charged A^{+}_{1s} state (or attractive Fermi polaron [Sidler 2017]) on the low energy side of the neutral A_{1s} can be observed, which is not the case in the PL spectra. This can be potentially due to the relaxation of the holes to the energetically favourable Γ point in the band structure, which limits the PL emission. Compared individual spectra of PL and reflectivity at several gate voltages are shown in Fig. 5.5 (b) Based on the characterization of doping regimes as a function of the gate voltages it is clear that the most neutral regime falls in the vicinity of $V_{BG} = \frac{1}{2}V_{TG} = 0\,\mathrm{V}$. which shows that the investigated sample nominally exhibits minimal unintentional doping. Thus, the $V_{BG} = \frac{1}{2}V_{TG} = 0\,\mathrm{V}$ conditions are appropriate as the starting conditions for the electric field sweep.

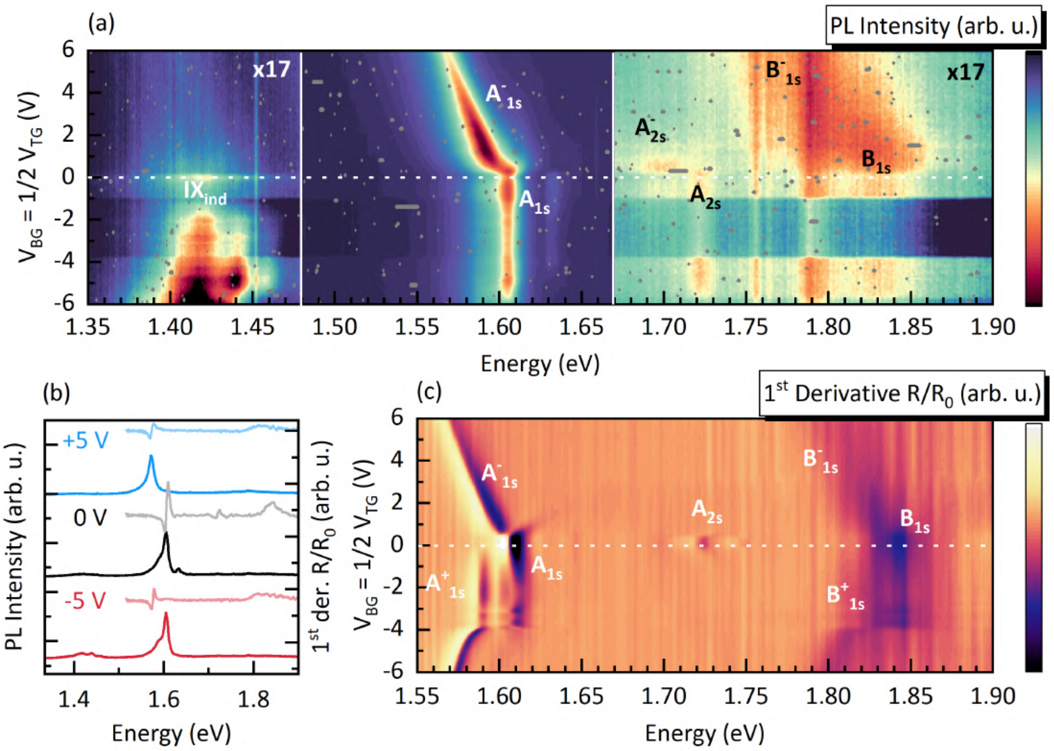

Figure 5.5: 2L-MoSe$_2$ - Doping regimes: (a) False-color map of PL intensity (excited with 532 nm cw laser at ∼1 mW power) as a function of the applied gate voltages of the same polarity (applied with constant ratio of: $V_{BG} = \frac{1}{2}V_{TG}$). The low ($< -125\,\mathrm{meV}$) and high ($> 62\,\mathrm{meV}$) energy range are multiplied (x17) with respect to the middle range in order to emphasize the weak PL features. (b) Comparison of PL and 1^{st} derivative of reflectivity (R/R_0) spectra at $V_{BG} = \frac{1}{2}V_{TG}$ of -5 V, 0 V and +5 V, *i.e.* in the n-doped, neutral and p-doped regimes. The spectra are shifted vertically for clarity. (c) False-color map of 1^{st} derivative of reflectivity (R/R_0) as a function of the applied gate voltages (same voltage range as in (a)).

5.4 Excitonic landscape in electric field

5.4.1 Reflectivity in electric field

To detect the presence of interlayer excitons and characterize their properties I performed the reflectivity measurement as a function of electric field. Fig. 5.6 presents the results of electric field sweep via application of the gate voltages, swept with a constant ratio of $V_{BG} = -\frac{1}{2}V_{TG}$, which minimizes the contribution of free carrier doping. In order to emphasize the very weak spectral features the reflectivity spectra are shown firstly in the form of 1^{st} (top graph) and then 2^{nd} (bottom graph) derivatives of relative reflectivity R/R_0. The obtained reflectivity spectra reveal a very rich excitonic landscape and its evolution in the presence of the electric field.

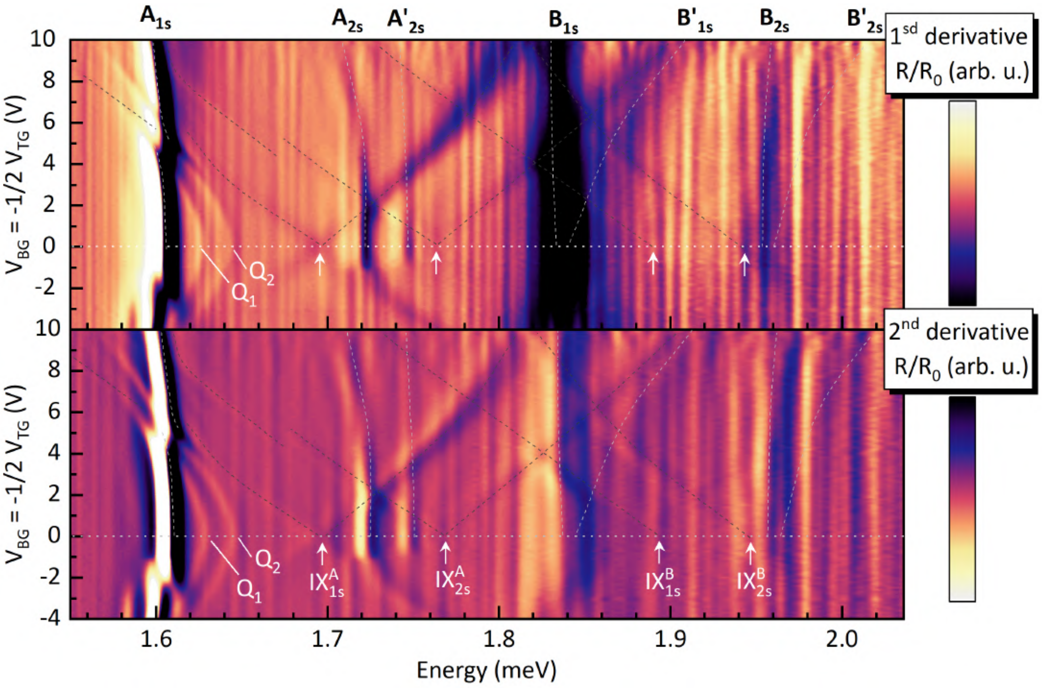

Figure 5.6: False-color maps of reflectivity in the form of 1^{st} (top graph) and 2^{nd} (bottom graph) derivatives of R/R_0 as a function of the electric field via application of gate voltage. The dashed lines track the evolution of the visible intralayer (grey) and interlayer (black) excitons. The energy onset (at 0 field) of the dipolar interlayer excitons is marked by white arrows. In both graphs, the dominating A_{1s} exciton is intentionally over-saturated in order to emphasize the weaker features in the spectra. Note here that for the downward E_z direction, below $V_{BG} = \frac{1}{2}V_{TG} = -1.5\,\mathrm{V}$ there is a considerable unintentional doping in the sample, thus only the positive E_z direction is considered.

Firstly, the initially identified in the 0 field spectra (Fig. 5.4 (a)) intralayer transitions (A_{1s}, A_{2s}, A_{2s} B_{2s}) do not exhibit any significant change in their energy as expected for excitons confined within one layer (no out-of-plane dipole moment).

Notably however, some of these states exhibit splitting into two branches (denoted as *notprime* and *prime*), value of which increases with the electric field.

Secondly, four states (marked by arrows in Fig. 5.6) split into red shifting and blue shifting branches which shift linearly with increasing E_z. The linear shift in the presence of electric field confirms the dipolar nature of these states. The two oppositely shifting branches originate from the oppositely aligned IX dipoles. Their energy position and comparable Stark shift indicate that they originate from the different species of lower and higher energy momentum-direct IXs (see Fig. 5.7 in the following section 5.5) and their excited Rydberg states. At higher electric fields however, their energy shifts slightly deviate from the linear behaviour. Interestingly, this is correlated with the earlier mentioned splittings and energy shifts of some of the intralayer states.

Thirdly, two additional features on the high energy side of the A_{1s} exciton, named Q_1 and Q_2 (same weak features spotted in the 0 field spectra Fig. 5.4 (a)), show a clear quadratic Stark shift. This matches the expected behaviour of quadrupolar excitons, similarly to those observed in TMD heterotrilayers (see Fig. 5.2).

As can be seen, the observed spectrum and the correlated behaviour of the various intralayer and interlayer states is very complex. In order to explain these observations, a thorough analysis, aided by a theoretical model, has been performed, which is presented in the following section.

5.5 Many-body microscopic model

In order to construct a thorough theoretical model, let us first consider the excitonic species which are expected to form in natural $MoSe_2$ bilayer. Natural TMD homobilayers exhibit the H_h^h stacking configuration, equivalent to 60° (or 180°) twist angle between the two layers. In such configuration, the K/K′ valleys of the bottom layer overlap in momentum space with the opposite K′/K valleys of the top layer. To simplify the notation of the excitonic species, the momentum-aligned valley of the top layer (layer 2) will inherit the name (K or K′) of the bottom layer (layer 1) valley, while being characterized by reversed spin configuration of the bands as depicted in Fig. 5.7. Furthermore, the TMD homobilayers host a fourfold degeneracy of excitonic states which stems from the combination of layer and valley degrees of freedom. Thus, among each exciton species type, intralayer and interlayer alike, four sub-species can be distinguished, characterized by their spin configuration and spatial position of the constituent carriers (layer 1 or layer 2). In addition, the spin degree of freedom results in the presence of the spin-singlet (↑↑/↓↓) and spin-triplet (↑↓/↓↑) states.

On the example of the neutral spin-singlet intralayer A exciton schematically depicted in Fig. 5.7 (a) we can distinguish two opposite spin configurations ↑↑ (localized in K valley) and ↓↓ (localized in K′ valley) for the two excitons localized in layer 1. The first arrow denotes the spin of the electron and the second of the hole.

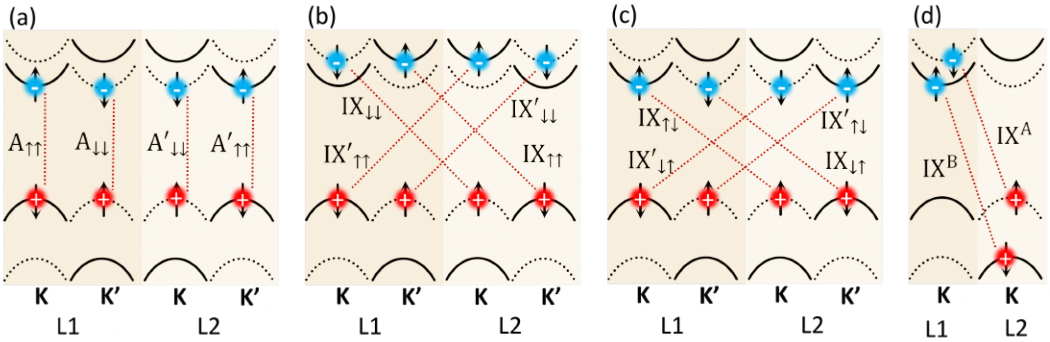

Figure 5.7: Exciton species in $MoSe_2$ homobilayer. Schematic representation of the (a) 4-fold degenerate intralayer A_{1s} excitons, (b) spin-singlet IXs and (c) spin-triplet IXs. (d) Example of the (spin-singlet) lower energy A-like and higher energy B-like IXs denoted with superscript "^{A}" and "^{B}", respectively.

Note here that in the electron-hole picture, the spin of the hole is reversed. The two counterpart A excitons localized in layer 2 are denoted with *prime* and have the opposite valley/spin relation.

In the case of spatially-indirect interlayer excitons (IXs), the constituent carriers are separated between the two layers as schematically depicted in Fig. 5.7 (b,c), which shows the spin-singlet and spin-triplet IXs, respectively. Here the spatial position of the carriers is better thought of in terms of the static dipole moment orientation, which emerges as a result of charge separation. In this case the *not-prime* and *prime* denote the excitons with opposite dipole moment *i.e.* exchanged positions of the electron and hole. Moreover, similar to the intralayer A and B excitons, the IXs can also exist in the lower energy (A-like) and higher energy (B-like) states as schematically presented in Fig. 5.7 (d).

All the complexity posed by the degrees of freedom present in the natural $MoSe_2$ homobilayers can be implemented in the effective many-body microscopic model, developed by the collaborating group of Ermin Malic (Marburg Technical University). The model is used to simulate the evolution of the excitonic energy landscape in the presence of external electric field making it complementary to the experimentally obtained spectra. The effective Hamiltonian in this model includes three terms that account for various interactions present in a TMD homobilayer structure. In the simple form, it can be written as:

$$H = H_0 + H_T + H_{QC}. \tag{5.1}$$

The H_0 accounts for the electron-hole Coulomb interaction via the generalized Wannier equation [Ovesen 2019]. This term also describes the response of the excitonic state to the applied external electric field. The H_T is the charge carrier tunneling term. The last term H_{QC} is derived from a generic Coulomb Hamiltonian, through which different dipoles can be mixed. It is attributed to the dipolar exchange interaction, which couples anti-aligned dipoles, as required to form the quadrupolar states.

5.5.1 Quadrupolar excitons

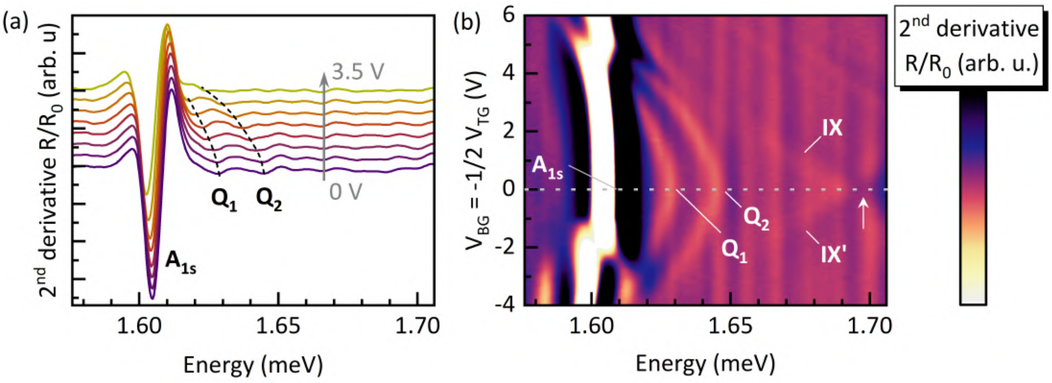

Figure 5.8: 2L-MoSe$_2$ in electric field. (a) Several selected spectra at various gate voltages of opposite polarity ($V_{BG} = -\frac{1}{2}V_{TG}$) between 0–3.5 V, which translates to application of an out-of-plane electric field. (b) False-color map of 2^{nd} derivative of reflectivity (R/R_0) as a function of applied gate voltages (with constant ratio of $V_{BG} = -\frac{1}{2}V_{TG}$). The A$_{1s}$ exciton feature is intentionally over-saturated in order to emphasize the weaker features in the spectrum. The horizontal dashed line marks the zero E_z. The arrow points to the energy position ($\simeq$ 90 meV) of degenerate IXs at 0 electric field. Note here that for downward direction, below $V_{BG} = \frac{1}{2}V_{TG} = -1.5$ V there is a considerable unintentional doping in the sample, thus for simplicity only the upward direction is analysed.

At first, I focus on the origin of the formation of quadrupolar excitons. Fig. 5.8 shows the 2^{nd} derivative reflectivity spectra focused in the range of the quadratically shifting Q$_1$ and Q$_2$ features. Panel (a) of Fig. 5.8 shows several reflectivity spectra obtained for different values of gate voltages ($V_{BG} = -\frac{1}{2}V_{TG}$) between 0–3.5 V, where 0 V corresponds to the spectrum without electric field. Panel (b) contains the false color map of reflectivity from which the spectra shown in panel (a) were extracted. The Q$_1$ and Q$_2$ states exhibit a quadratic energy red shift at low E_z, which becomes more linear at higher E_z. This behaviour is a clear evidence of the quadrupolar nature of these states [Yu 2023, Li 2023a, Xie 2023]. Quadrupolar excitons form as a result of superposition of a pair of anti-aligned dipolar excitons. As per definition, the dipole moment of an electric quadrupole is zero due to symmetric arrangement of the four constituent charges. The application of an external electric field displaces the charge carriers breaking the symmetrical arrangement. This way, the quadrupoles gradually acquire a non-zero dipole moment with rising strength of the electric field, giving rise to the quadratic Stark shift. At sufficiently high electric fields, the electrons and holes become separated into the opposite layers so that the quadrupolar state effectively transitions into a dipolar state with linear Stark shift proportional to its dipole moment. Additionally, on the higher energy side ($\simeq$ 1.696 meV at 0 V), we can observe transitions related to interlayer dipolar

IX/IX′ states, which follow a linear dependence on the applied electric field.

In order to obtain quadrupolar states, a coupling between two oppositely aligned dipolar states, as schematically shown in Fig. 5.9 (a), is required. Such coupling, in the simplest form, can be expressed via a Hamiltonian:

$$H = \begin{pmatrix} E_{IX} + d_L E_z & J \\ J^* & E_{IX'} - d_L E_z \end{pmatrix}, \tag{5.2}$$

where E$_{IX}$/E$_{IX'}$ are energies of the oppositely oriented dipolar IXs. The $d_L E_z$ describes the linear Stark shift in electric field, where d_L is the dipole length. The J is the coupling between the two anti-aligned dipoles. The diagonalization of this simple Hamiltonian yields two quadrupolar branches: low energy red shifting (symmetric) Q and high energy blue shifting (anti-symmetric) Q′, separated by the value of $2J$. Transformation of the spectrum due to coupling J is schematically drawn in Fig. 5.9 (b) and (c). Additionally, upon inclusion of the coupling J (panel (c)), the dipolar IXs, which formed the quadrupoles are no longer the eigenvalues of the system and hence disappear from the spectrum.

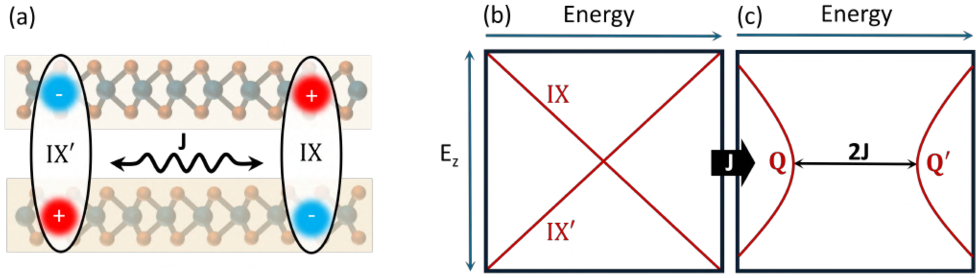

Figure 5.9: (a) Schematic representation of coupling between two anti-aligned dipolar IXs via coupling J. (b) Schematic drawings of the IX spectrum in the presence of electric field without J coupling. (c) Transformation of the IX spectrum from panel (b) upon including coupling J, which results in formation of two quadrupoalar branches Q and Q' of opposite curvature.

As we can see, this simple form of the dipole coupling is not sufficient to explain the experimentally obtained picture as seen in Fig. 5.8. The reflectivity spectra show not one, but two (Q$_1$/Q$_2$) red shifting quadrupoalar branches. At the same time the dipolar state is still present in the spectrum.

In order to obtain a proper picture, it is necessary to increase the complexity of the model by including all the possible spin-valley configurations of the excitons stemming from the spin, valley and layer degrees of freedom (Fig. 5.7). These are incorporated in the $\tilde{J}$ coupling term, which is included in the Hamiltonian:

$$H_{QC} = \sum_{\tilde{s}\tilde{s}'\xi\xi'LL'\mathbf{Q}} \tilde{J}^{\tilde{s}\xi L}_{\tilde{s}'\xi'L'}(\mathbf{Q}) X^{\xi\tilde{s}\dagger}_{L\mathbf{Q}} X^{\xi'\tilde{s}'}_{L',\mathbf{Q}}, \tag{5.3}$$

where the summation runs over the valley index $\xi(\xi') = (\xi_e, \xi_h)$, spin index $\tilde{s}(\tilde{s}') = (\uparrow\uparrow, \downarrow\downarrow, \uparrow\downarrow, \downarrow\uparrow)$, layer index for hole and electron $L(L') = (l_e, l_h)$, and the center-of-mass momentum $\mathbf{Q}$. The $X(X^\dagger)$ is the exciton annihilation(creation) operator. For the dipolar exchange coupling $\tilde{J}$ it is assumed that the coupling for the 2s excitonic states is weak and therefore only the 1s states are taken into account. Noteworthy, the $\tilde{J}$ only couples the spin-singlet IXs ($\uparrow\uparrow/\downarrow\downarrow$) as the spin-triplet states ($\uparrow\downarrow/\downarrow\uparrow$) are not spin conserving.

Due to the four-fold state degeneracy, there are four degenerate spin-singlet IXs, two of them having an opposite dipole moment ($\mathrm{IX}_{\uparrow\uparrow}, \mathrm{IX}_{\downarrow\downarrow}$) with respect to the remaining two ($\mathrm{IX}'_{\uparrow\uparrow}$,$\mathrm{IX}'_{\downarrow\downarrow}$) as shown in Fig. 5.7 (b). This yields two possible pathways for the dipolar exchange coupling ($\tilde{J} = J + J'$): First one, denoted as J, is the coupling between two anti-aligned spin-singlet IXs which reside in the same valley, but have the opposite spin configuration *i.e.*: $\mathrm{IX}_{\uparrow\uparrow}+\mathrm{IX}'_{\downarrow\downarrow}$ and $\mathrm{IX}_{\downarrow\downarrow}+\mathrm{IX}'_{\uparrow\uparrow}$. The second pathway, denoted as J', is the coupling between two anti-aligned spin-singlet IXs which reside in the opposite valleys but have the same spin configuration *i.e.*: $\mathrm{IX}_{\uparrow\uparrow}+\mathrm{IX}'_{\uparrow\uparrow}$ and $\mathrm{IX}_{\downarrow\downarrow}+\mathrm{IX}'_{\downarrow\downarrow}$. The two types of couplings are schematically presented in Fig. 5.10 (a) and (b). The extended Hamiltonian, which explicitly includes the two coupling pathways can be written as:

$$H_{QC} = \sum_{\tilde{s}\tilde{s}'\xi\xi'LL'\mathbf{Q}} \left(J^{\tilde{s}\xi L}_{\tilde{s}'\xi L'}(\mathbf{Q})\delta_{\xi\xi'} + J'^{\tilde{s}\xi L}_{\tilde{s}\xi' L'}(\mathbf{Q})\delta_{\tilde{s}\tilde{s}'} \right) X^{\xi\tilde{s}\dagger}_{L\mathbf{Q}} X^{\xi'\tilde{s}'}_{L',\mathbf{Q}}. \tag{5.4}$$

As can be seen from the above equation, the J' term entails mixing of IXs between different valleys, and therefore exhibits only the long-range interaction (short-range interaction is symmetry forbidden [Yu 2014a]), as opposed to J which has both long-range and short-range interactions. Therefore the strength of the J coupling is expected to be larger than that of the J'.

The effects of the dipolar exchange couplings J/J' on the spectrum of interlayer excitons is schematically presented in Fig. 5.10 (d-f). Panel (d) shows the evolution of the spin-singlet and spin-triplet IX excitons in the presence of the electric field without including the J/J' coupling. There we can see that both spin-singlet and spin-triplet states, which at $E_z = 0$ are separated energetically by the value of spin orbit coupling (SOC), split and shift linearly with increasing electric field as expected for dipolar excitons. Panel (e) shows the picture with J coupling included. Now the spin-singlet IXs hybridize which yields two, quadratically shifting (red shifting symmetric and blue shifting anti-symmetric) branches of quadrupolar excitons - Q and Q$'$. Each of two branches are separated by the coupling value of J from the energy position of spin-singlet IXs from which they originate (separated by 2J from each other). By further including the second coupling channel - J' (panel (f)), the two quadrupolar branches experience an additional splitting into the Q$_1$, Q$_2$ and Q$'_1$, Q$'_2$, respectively. The doublets are separated by the value of $2J'$. The spin-triplet IX states, since they do not interact via dipolar exchange, retain their dipolar character and linear Stark shift.

The obtained theoretical picture matches the experimental observations in reflectivity (Fig. 5.8). The two quadratically shifting branches can then be assigned to the double red shifting symmetric branch of the quadrupolar excitons, which formed from the combinations of pairs of spin-singlet IXs, precisely: $\mathrm{Q}_1 \sim \mathrm{IX}'_{\uparrow\uparrow} + \mathrm{IX}_{\downarrow\downarrow}$ and

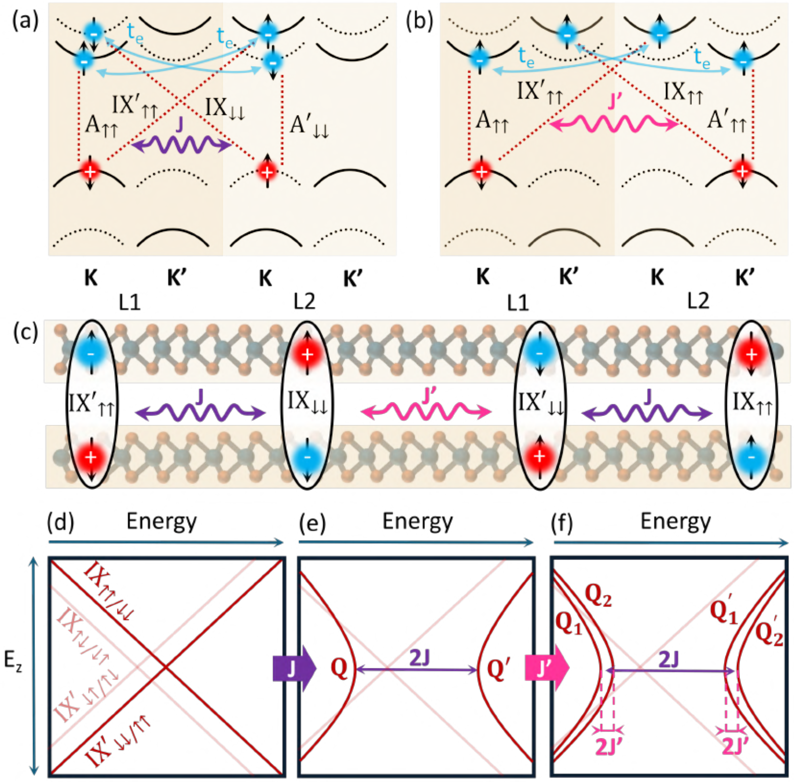

Figure 5.10: Dipolar exchange coupling in 2L-MoSe$_2$ homobilayer. (a) Schematic drawing of the two possible paths of dipolar interaction between the anti-aligned spin-singlet dipolar excitons residing in the same valley but having different spins, denoted as J, and anti-aligned spin-singlet dipolar excitons from opposite valleys but with the same spin, denoted as J'. (b) Schematic drawing of the real space interaction via J and J' between the spin-singlet dipolar excitons. (c) Schematic evolution of exciton energy landscape in electric field without dipolar exchange (d), including the J term (e) and including J' term (f).

Q$_2$ $\sim$ $IX'_{\downarrow\downarrow}+IX_{\uparrow\uparrow}$. Simultaneously, the higher energy linearly shifting states (IX and IX$'$) are attributed to the spin-triplet IXs, which do not mix through the dipolar exchange interaction $\tilde{J}$ and retain their dipolar character. Although spin-triplet states are usually optically dark, in the case of interlayer excitons they can become bright [Yu 2018], which could explain their weak presence in the reflectivity spectrum.

The coupling values of J and J' can be estimated based on the energy positions of the Q$_1$, Q$_2$, and IX features in the experiment. By estimating the energy separation (at zero electric field) between the two quadrupolar branches of $\simeq 16$ meV as equal to $2J'$ we obtain $J'= \simeq 8$ meV. The energy separation between the middle point of the Q$_1$, Q$_2$ and the spin-triplet IX (at 0 field) + the value of SOC (in the simulation assumed to be 22 meV [Kormányos 2015]), yields the value of J of $\simeq 90$ meV. The obtained values match the aforementioned expectation that $J > J'$ due to lack of short-range interactions in the J'. The absolute values are however much larger than expected for dipolar exchange interactions in TMDs. In the case of intralayer excitons, the exchange coupling value was calculated to be around 20 meV [Qiu 2015]. For interlayer excitons it should hence be even smaller due to reduced wave function overlap of the constituent electron and hole with respect to an intralayer exciton. On the one hand, it suggests that the coupling strength might have been underestimated, and that TMD homobilayers host much stronger exchange interactions than previously considered. On the other hand, likely other effects such as, for instance, the density dependent dipole-dipole attractive interaction, which are not taken into account in the model might contribute to the effective coupling strength. Additionally, the inherent variability of TMD-based devices properties which depends on the technical details of each fabrication process might play a role in determining the performance of a given device. Overall, the very good qualitative agreement of the simulated and measured spectra with regards to formation of quadrupoles shows that they can emerge from the dipolar exchange interaction. The understanding of the difference between the expected and measured coupling strength, however, requires further investigation.

5.5.2 Carrier tunneling

Having understood the probable origin of the emergence of two quadrupolar excitons Q_1 and Q_2, now I focus on the complex interactions between various intralayer and interlayer states.

Firstly, as can be observed in Fig. 5.11 (a), the dipolar interlayer IXs repulse with intralayer states as they are tuned closer into energy resonance by the applied electric field. This additionally leads to the splitting of the intralayer states at higher electric fields, accompanied by the exchange of the oscillator strengths. These interactions are marked with black arrows in 5.11 (a). Fig. 5.11 (b) presents the simulated excitonic landscape in the presence of electric field with included only the hole tunneling (t_h) term. As can be observed, the marked interactions can be very well recreated by the model and attributed to the effect of states mixing via hole tunneling.

Secondly, at intermediate electric fields we can observe a small but clear avoided crossing when the interlayer states pass through the A_{1s} resonance (see dashed oval Fig. 5.11 (a)). This phenomenon cannot be explained by the hole tunneling as in Fig. 5.11 (b) no such avoided crossing can be observed. In order to understand the emergence of this feature we include also the electron tunneling term (t_e). It leads to mixing of the interlayer states to their respective A_{1s} exciton sub-states as shown in Fig. 5.10 (a) and (b). Fig. 5.11 (c) shows the results of the simulation with both hole and electron tunnelings included. As marked by the dashed oval, the same avoided crossing as observed in the experiment (panel (a)) emerges and hence can be attributed to the effect of electron tunneling. Surprisingly however, for naturally stacked H_h^h homobilayers, the electron tunneling is expected to be symmetry forbidden [Wang 2017b]. Nevertheless, the experimental results clearly show that some limited electron tunneling is allowed and its inclusion is necessary

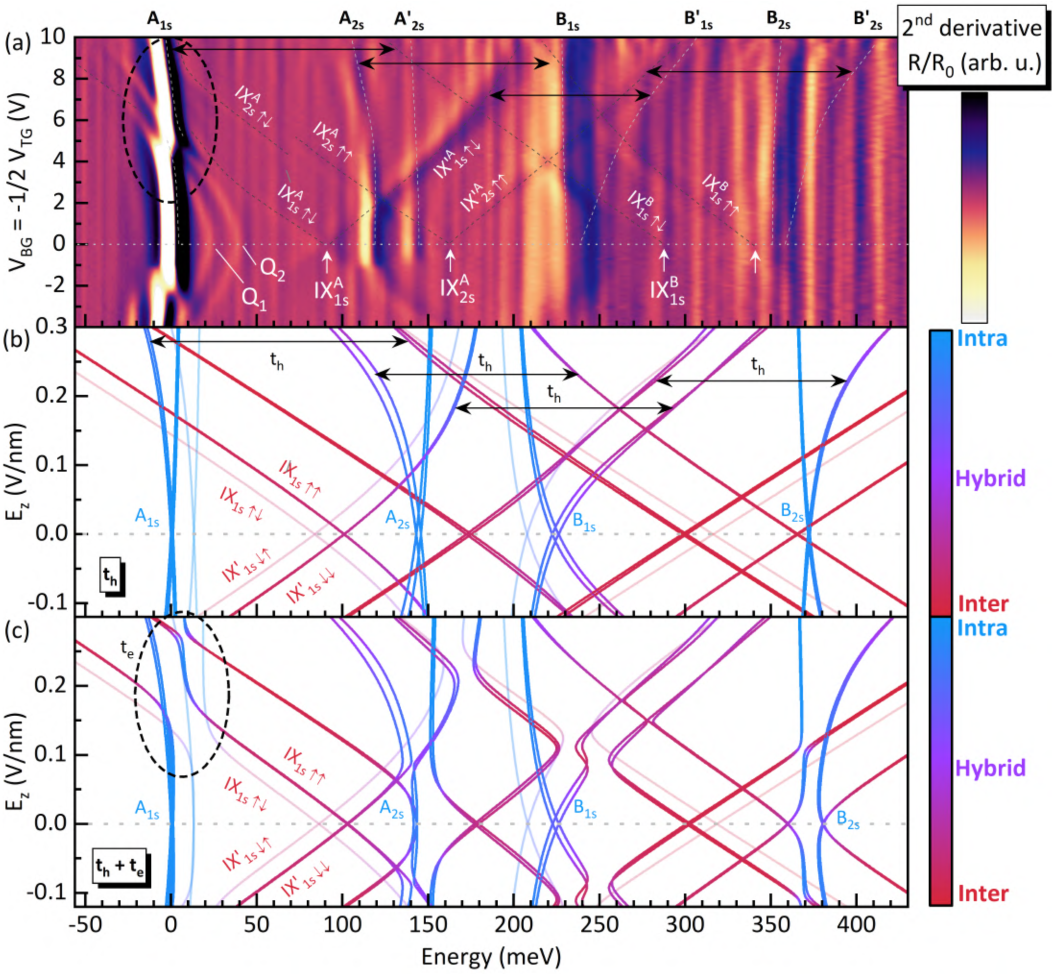

Figure 5.11: (a) False-color map of 2^{nd} derivative of R/R_0. The black arrows mark the interactions between the various intralayer and interlayer states. The dashed oval marks the avoided crossing region between the interlayer dipolar and quadrupolar states with the A_{1s} excitons. (b) and (c) Simulated exciton energy landscape in the presence of electric field with included only the hole tunneling t_h (b) and both hole and electron tunneling $t_h + t_e$ (c). The color coding corresponds to the degree of intra-inter layer spatial character of the transitions, where blue, purple and red correspond to intralayer, hybrid and interlayer character, respectively. The carrier tunneling values used in the simulation are $t_h = 56.3\,\text{meV}$ [Hagel 2021] and $t_e = 11.9\,\text{meV}$. Here, the assumed value of t_e is the value calculated for a similar H_h^X stacking [Hagel 2021].

to explain the observed avoided crossing.

The mixing of the states due to both hole and electron tunnelings result in the change in the spatial character of the transitions as can be seen in the color coding of the simulated states in Fig 5.11 (b) and (c). The states can be effectively tuned between the intralayer, hybrid and interlayer characters by tuning the value of the applied electric field. This can be utilized as an additional control knob in tuning of the many-body interactions in TMD homobilayer systems.

5.5.3 Comparison of the experimental and theoretical pictures

Finally, I compare the experimental picture and the simulation which includes all the discussed couplings in the form of dipolar exchange, hole and electron tunneling. The full Hamiltonian can be written as:

$$\begin{aligned} H = \sum_{\xi\xi'\tilde{s}\tilde{s}'\mathbf{Q}LL'\mu\nu} \Bigg(& \Big(E^{\tilde{s}\xi\mu}_{L\mathbf{Q}} + d_L E_z\Big) X^{\mu\tilde{s}\xi\dagger}_{L\mathbf{Q}} X^{\mu\tilde{s}\xi}_{L\mathbf{Q}} \delta_{LL'}\delta_{\tilde{s}\tilde{s}'}\delta_{\xi\xi'}\delta_{\mu\nu} \\ & + T^{\mu\nu\xi}_{LL'} X^{\mu\tilde{s}\xi\dagger}_{L\mathbf{Q}} X^{\nu\tilde{s}\xi}_{L'\mathbf{Q}} \delta_{\tilde{s}\tilde{s}'}\delta_{\xi\xi'} + \Big(J^{\tilde{s}\xi L}_{\tilde{s}'\xi L'}(\mathbf{Q})\delta_{\xi\xi'} + J'^{\tilde{s}\xi L}_{\tilde{s}\xi' L'}(\mathbf{Q})\delta_{\tilde{s}\tilde{s}'}\Big) X^{\xi\tilde{s}\dagger}_{L\mathbf{Q}} X^{\xi'\tilde{s}'}_{L',\mathbf{Q}} \Bigg), \end{aligned} \tag{5.5}$$

where $E^{\tilde{s}\xi\mu}_{L\mathbf{Q}}$ is the bare exciton dispersion and $d_L E_z$ is the Stark shift in electric field. In the model, the nominal value of $d_L = 0.65e\cdot$ nm was used [Laturia 2018]. The $T^{\mu\nu\xi}_{LL'}$ is the tunneling matrix element which includes both the hole and electron tunneling. The indices μ and ν are the exciton Rydberg progression number, which correspond to 1s and 2s states, respectively. The simulation was performed separately for the spin-singlet and spin-triplet states. For the spin-triplet configuration, only the 1s states where taken into account.

The comparison is presented in Fig. 5.12 (a,b) in which we can see a very good qualitative agreement. The interactions between the intralayer and interlayer states, as well as formation of quadrupolar states are reproduced well by the theoretical model.

An additional prediction of the microscopic model is that the intralayer states can exhibit a non-zero splitting even at zero electric field (Fig. 5.12 (b)), This can be explained by the fact, that even at zero electric field, the various states exhibit a not pure intra- or inter-layer character related to the mixing due to carrier tunneling. In turn, the dipolar exchange coupling $\tilde{J}$ can affect all states which exhibit non-zero interlayer character in an attempt to form quadrupolar states. This would result in splitting of the four degenerate states into two pairs *prime* and *notprime*. In the measured spectra (Fig. 5.12 (b)) this is clearly visible for the A$_{2s}$/A$'_{2s}$ states, in line with the theoretical picture. For other interlayer states, the splitting at zero field is much less visible, probably due to broadening of the features, which obscures the visibility of the effect. The more prominent splitting of the A$_{2s}$/A$'_{2s}$ states, might be caused by the close energy proximity to the predicted anti-symmetric branch of the quadrupolar states (Q$'_1$/Q$'_2$) with which they heavily mix. This, at the same time, is also the probable explanation as to why, the anti-symmetric quadrupoles are not directly observed in the reflectivity spectra (5.12 (a)). These results signify the importance of carrier tunneling, both electron and hole, as well as dipolar exchange in understanding of the complex excitonic landscape present in natural MoSe$_2$ homobilayers. The carrier tunneling explain the mutual interactions of the intralayer and interlayer states accompanied by exchange of their spatial character.

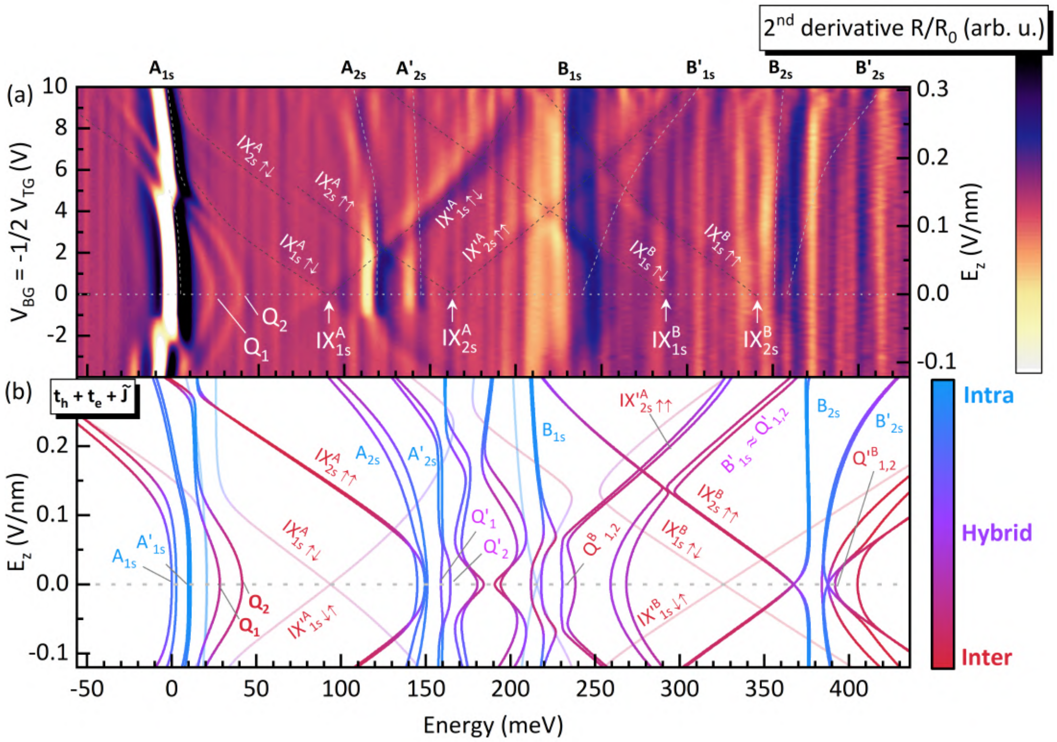

Figure 5.12: (a) False-color map of 2^{nd} derivative of reflectivity (R/R_0) as a function of applied gate voltages (constant ratio of $V_{BG} = -\frac{1}{2}V_{TG}$). The horizontal dashed line marks the zero E_z. The remaining dashed lines mark the evolution of several of the observed states with increasing E_z. The right axis shows the calculated E_z strength based on matching the slope of the $\mathrm{IX}^{\mathrm{A}}_{1\mathrm{s},\uparrow\downarrow}$ state to the simulated slope in (b). (b) Simulated exciton energy landscape in the presence of electric field. The simulation contains three types of interactions *i.e.* hole tunneling, electron tunneling and dipolar exchange. The energy is measured relative to the energy position of $\mathrm{A}_{1\mathrm{s}}$ exciton at zero field (1.606 eV).

The dipolar exchange coupling constitutes the probable explanation for the origin of the formation of quadrupolar excitons.

5.6 Photoluminescence

To complement the experimental data obtained in reflectivity I performed additional PL measurements as a function of the electric field. Fig. 5.13 shows the PL measurement in the presence of the out-of-plane electric field. Panel (a) of Fig. 5.13 shows the false color map of PL intensity as a function of electric field. Panel (b) of Fig. 5.13 shows selected PL spectra from the positive E_z direction from 0 to 0.24 V/nm. At zero field, the PL emission is dominated by the $\mathrm{A}_{1\mathrm{s}}$ exciton and a weaker low energy shoulder related to the trion (T) emission. The energy position of the $\mathrm{A}_{1\mathrm{s}}$ follows the same trend with increasing E_z as its absorption feature in the reflec-

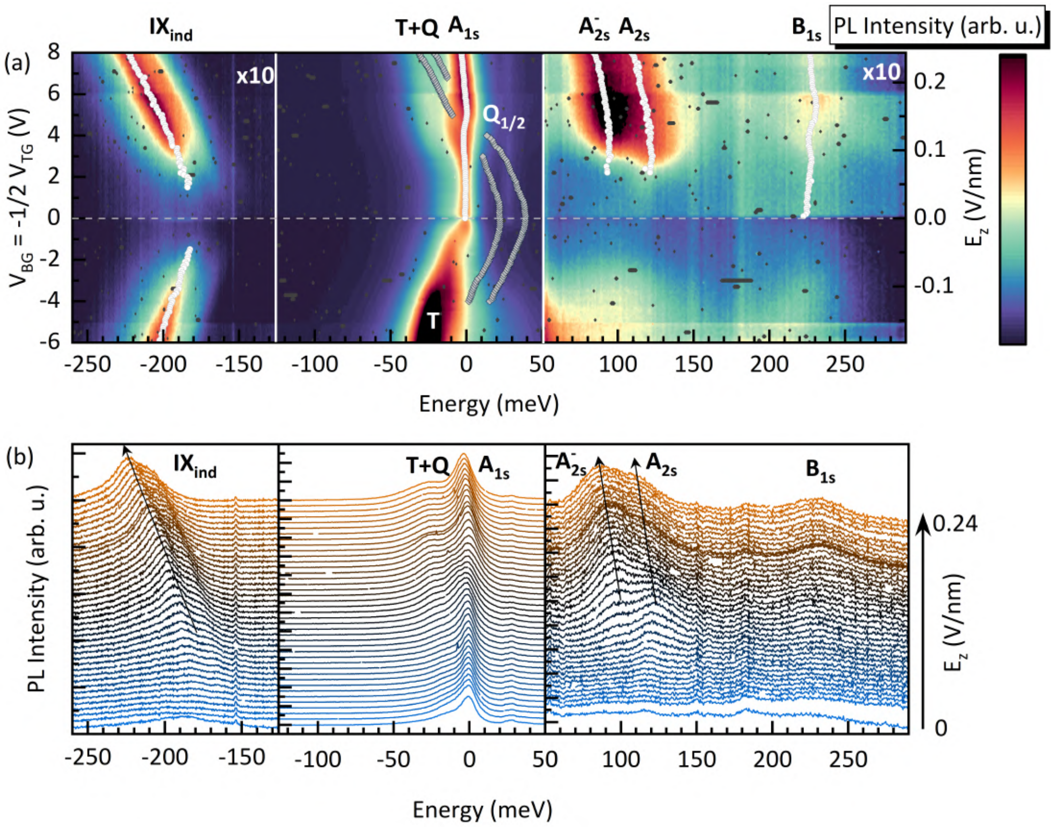

Figure 5.13: (a) False-color map of PL intensity (excited with 532 nm cw laser at $\simeq 1$ mW power) as a function of electric field. The overlaid white points correspond to the transitions energies extracted from the PL spectra. The grey overlaid points correspond to the quadrupolar Q$_1$ and Q$_2$ branches extracted from the reflectivity spectra. (b) Selected individual spectra taken from the positive E_z direction between $E_z = 0 - 0.24$ V/nm. The spectra are vertically shifted for clarity. In both (a) and (b) the low (< -128 meV) and high (> 50 meV) energy ranges are multiplied (x10) with respect to the middle range in order to emphasize the weak PL features. For the negative E_z direction, below $\simeq -0.03$ V/nm, the sample becomes unintentionally doped, similarly as was observed in the reflectivity measurement, therefore only the positive E_z direction is analysed.

tivity (Fig. 5.12 (a)). At $E_z \approx 0.10 - 0.15$ V/nm, the PL energy of A$_{1s}$ is modulated between lower then higher energy, which coincides exactly with the avoided crossing with the approaching quadrupolar states Q$_1$, Q$_2$ (see the overlaid black points in Fig. 5.13 (a)). At higher E_z, the low energy shoulder of the A$_{1s}$ (attributed to weak trion emission at low E_z), brightens and broadens, as a result of energy overlap with the red shifting quadrupolar states which have passed the avoided crossing region with the A$_{1s}$. At this point the low energy shoulder of A$_{1s}$ is likely related to the convoluted emission of the trion and the quadrupolar excitons (T+Q). Similar crossing-related energy modulation can be found around $E_z \approx 0.08 - 0.18\,\mathrm{V/nm}$ range for the $\mathrm{B_{1s}}$ states. Furthermore, the A_{2s} emission shows a doublet of peaks, separated by around 25 meV. The higher energy peak matches, with energy position and the same small red shift with increasing E_z, the A_{2s} absorption feature in the reflectivity. The lower energy PL peak follows the same red shift as the higher energy PL peak. Its origin is probably related to the charged $\mathrm{A_{2s}^{-}}$ (similar to what was observed for monolayer TMDs [Sell 2022]) due to unintentional doping in the sample. Moreover, at the low energy side of the spectrum, around -180 meV of energy detuning we can observe a weak emission from the momentum-indirect $\mathrm{IX_{ind}}$. It is exhibits a linear red shift and brightening with increasing E_z. The energy shift slope is approximately 50% of that observed for the momentum direct IXs in the reflectivity spectra (Fig. 5.12 (b)), Similar to what was observed in other $\mathrm{MoSe_2}$ bilayer systems [Sung 2020, Kovalchuk 2023, Villafañe 2023]. This corroborates the interpretation of its origin as the momentum-indirect interlayer exciton which is composed of an electron in the K valley in one of the layers and the hole delocalized over both layers at the hybridized Γ point (as schematically depicted in Fig 5.4 (b)), thereby lowering its effective dipole moment.

Overall, the presented studies of reflectivity and PL under the out-of-plane electric field, complemented with many-body microscopic simulations allowed to uncover the very rich excitonic interactions present in natural $\mathrm{MoSe_2}$ homobilayers. Utilization of the coupling effects stemming from the hole and electron tunneling, allows for high tunability of not only the energies but also the spatial characters of the excitonic transitions by tuning the value of applied electric field. The surprising emergence of the quadrupolar states has been attributed to the dipolar exchange coupling, which hybridizes spin-singlet interlayer excitons of opposite static dipole orientation.

5.7 Summary

The investigation of the properties of natural homobilayer $\mathrm{MoSe_2}$ device under electric field presented in this chapter provided a fascinating picture of a rich and complex exciton energy landscape. Combining optical spectroscopy in the form of electric field-resolved reflectivity and photoluminescence with microscopic simulations helped reveal and explain the observation of several different kind of exciton types and their mutual interactions. The emergence of the two quadrupolar states, characterized by a quadratic Stark shift, can be attributed to the mixing of anti-aligned spin-singlet dipolar excitons via the dipolar exchange interaction. The large coupling value obtained from the experiment suggests that natural TMD homobilayers harbour much stronger dipole-dipole interactions than the previously studied TMD heterotrilayers. Besides the quadrupolar excitons, four highly tunable dipolar exciton states were observed, found to be originating from the 1s spin-triplet states and 2s spin-singlet states, which are not affected by the dipolar exchange coupling and thus retaining their dipolar character. On top of that, the spatial character of the excitons can be effectively tuned between the interlayer and intralayer character depending on the value of applied electric field. The mixing between intralayer and interlayer states is primarily driven by a strong hole tunneling, as evidenced by the avoided crossings and exchange of the oscillator strength between the involved states. In addition, the observed avoided crossing between the A$_{1s}$ neutral exciton and some of the interlayer states could be explained by inclusion of the electron tunneling. For natural TMD bilayers, the electron tunneling was thought to be symmetry-forbidden, however the clear experimental results indicate that some limited electron tunneling is actually possible and necessary to account for the abovementioned effect.

These results show that devices based on natural TMD bilayers are an excellent platform for electric field tuning of excitonic properties and light matter interactions. Moreover, such devices provide the additional simplicity, due to lack of requirement for twist-angle engineering and resulting from that inherent immunity to either moiré or reconstruction effects. The surprising emergence of quadrupolar excitons, attributed to the effect of dipolar exchange coupling paves the way for realization of advanced correlated states utilizing quadrupole-quadrupole interactions. The results presented in this chapter are the topic of a scientific manuscript: J. Jasiński et al "Quadrupolar Excitons in natural MoSe$_2$ Bilayers" [Jasiński 2024a], currently under review.

Chapter 6

Conclusions

In this thesis I explored the optical properties of several structures based on transition metal dichalcogenides, which are currently intensively researched by the scientific community due to their outstanding opto-electronic properties. In particular, I focused on the possibilities of control of the excitonic features utilizing both intrinsic characteristics of TMDs as well as external tuning parameters such as strain and electric field.

In Chapter 3 I investigated the effects of uniaxial stress on the polarization properties of trions in MoS_2 monolayers. The strain was imposed via deposition of MoS_2 on a patterned substrate in the form of GaAs nanomembranes. I estimated the strain distribution imposed by the nanomembranes and correlated the optical properties with the morphological features of the structure. Using linear polarization resolved photoluminescence I observed a strain induced lifting of the charged exciton degeneracy, resulting in a fine structure splitting and linearly polarized emission. The unexpected emergence of this phenomenon was attributed to the Fermi polaron nature of excitons in TMDs.

In Chapter 4 I investigated the valley polarization properties in monolayer WSe_2 (chapter 4.1) and a TMD/2D-perovskite heterostructure 4.2, precisely $WSe_2/(BA)_2PbI_4$. In both structures I studied the possibility of controlling the value and sign of the valley polarization by utilizing an intrinsic feature of TMDs in the form of Dexter-like intervalley coupling. This mechanism enables for efficient transfer of coherent exciton populations from one, resonantly pumped valley, into the same-spin states of the opposite valley. The valley polarization was found to be strongly dependent on the energy of the circularly polarized excitation. In monolayer WSe_2, the valley polarization of the ground A exciton state reaches above 30% for excitation energies resonant with the excited A exciton Rydberg states and between the excitonic resonances. On the other hand, for excitation energies in the vicinity of the B exciton states, the valley polarization vanishes for the neutral exciton and even changes sign to around -8% in the case of biexciton and charged biexciton. In the TMD/2D-perovskite heterostructure I demonstrated similar excitation energy dependent valley polarization in the interlayer excitons, which form between an electron in TMD and a charge transfered hole in the inorganic layer of the 2D-perovskite. The observation of the same behaviour for both TMD intralayer and interlayer excitons in the heterostructure testifies to the succesful spin injection from TMD to the 2D-perovskite. These results have shown the importance of the Dexter-like coupling, which allows to tune the degree and sign of the valley polarization via excitation energy, thus becoming an additional control knob in tuning of the excitonic properties.

The studies presented in Chapter 5 concerned the tuning of the excitonic properties via application of electric field in natural bilayers of $MoSe_2$. An emergence of quadrupolar excitonic states, *i.e.* a superposition of anti-aligned dipolar states, was observed for the first time in a homobilayer structure. Aided by theoretical calculations, the probable mechanism for the formation of quadrupolar excitons was attributed to the dipolar exchange between spin-singlet dipolar interlayer excitons. Moreover, the complex interactions of the intralayer and interlayer excitons in the presence of electric field was revealed and attributed to hybridizations stemming from both the electron and the hole tunneling. Consequently, the spatial character of the excitons between the intralayer, hybrid and interlayer character was found to be a strongly electric-field tunable property. These results demonstrated the importance of taking into account different coupling mechanisms in the form of charge carrier tunneling and the dipolar exchange coupling in order to understand the excitonic landscape of the natural homobilayers of $MoSe_2$. The observed strong tunability of the excitonic properties signifies the potential of the TMD homobilayer systems as electric field tunable platform for investigations of many-body phenomena.

Overall, the results presented in this thesis add another important layer to understanding of the physical mechanisms governing the excitonic properties of transition metal dichalcogenides. Control of these properties via intrinsic and extrinsic factors has great potential for their future applications in both fundamental studies as well as realization of practical opto-electronic devices.

APPENDIX A

Publications and conferences

Publications based on the results presented in this thesis:

1. **J. Jasiński**, J. Hagel, S. Brem, E. Wietek, T. Taniguchi, K. Watanabe, A. Chernikov, N. Bruyant, M. Dyksik, A. Surrente, M. Baranowski, D. K. Maude, E. Malic and P. Płochocka
"Quadrupolar Excitons in Natural MoSe2 Bilayers"
arXiv:2407.18040 [cond-mat.mes-hall] (2024)

2. **J. Jasiński**, J. J. P. Thompson, S. Palai, M. Śmiertka, M. Dyksik, T. Taniguchi, K. Watanabe, M. Baranowski, D. K. Maude, A. Surrente, E. Malic and P. Płochocka
"Control of The Valley Polarization of Monolayer WSe_2 *by Dexter-like Coupling"*
2D Materials **11(2)**, 025007 (2024)

3. **J. Jasiński**, A. Balgarkashi, V. Piazza, D. Dede, A. Surrente, M. Baranowski, D. K. Maude, M. Banerjee, R. Frisenda, A. Castellanos-Gomez, A. Fontcuberta i Morral and P. Plochocka
"Strain induced lifting of the charged exciton degeneracy in monolayer MoS_2 *on a GaAs nanomembrane"*
2D Materials **9**, 045006 (2022)

Other publications:

1. M. Karpińska, **J. Jasiński**, R. Kempt, J. D. Ziegler, H. Sansom, T. Taniguchi, K. Watanabe, H. J. Snaith, A. Surrente, M. Dyksik, D. K. Maude, Ł. Kłopotowski, A. Chernikov, A. Kuc, M. Baranowski and P. Plochocka
"Interlayer excitons in MoSe2/2D perovskite hybrid heterostructures – the interplay between charge and energy transfer"
Nanoscale **14**, 8085-8095 (2022)

2. A. Balgarkashi, V. Piazza, **J. Jasiński**, R. Frisenda, A. Surrente, M. Baranowski, M. Dimitrievska, D. Dede, W. Kim, L. Güniat, J.-B. Leran, A. Castellanos-Gomez, P. Plochocka and A. Fontcuberta i Morral
"Spatial Modulation of Vibrational and Luminescence Properties of Monolayer MoS2 Using a GaAs Nanowire Array"
IEEE Journal of Quantum Electronics **8.4**, 1-8 (2022)

3. P. Holewa, **J. Jasiński**, A. Shikin, E. Lebedkina, A. Maryński, M. Syperek and E. Semenova
   "Optical Properties of Site-Selectively Grown InAs/InP Quantum Dots with Predefined Positioning by Block Copolymer Lithography"
   Materials **14(2)**, 391 (2021)

Scientific conferences:

1. **Flatlands - Beyond graphene 2024**
   9-13 September 2024, Wrocław, Poland
   Oral presentation: *"Quadrupolar Excitons in Natural MoSe2 bilayer"*
   J. Jasiński, J. Hagel, S. Brem, T. Taniguchi, K. Watanabe, A. Surrente, M. Baranowski, D. K. Maude, E. Malic, P. Płochocka.

2. **Flatlands - Beyond graphene 2023**
   25-29 September 2023, Prague, Czech Republic
   Oral presentation: *"Valley Polarisation in Monolayer TMDs and TMD/2D Perovskite Heterostructures"*
   J. Jasiński, S. Palai, J. Thompson, M. Śmiertka , J. D. Ziegler, K. Watanabe, T. Taniguchi, M. Baranowski, A. Surrente, E. Malic, A. Chernikov and P. Płochocka.

3. **Exciton Transport in 2D Materials**
   30 May- 2 June 2023, San Sebastián, Spain
   Poster presentation: *"Valley Polarisation in Monolayer TMDs and TMD/2D Perovskite Heterostructures"*
   J. Jasiński, S. Palai, J. Thompson, M. Śmiertka ,J. D. Ziegler, K. Watanabe, T. Taniguchi, M. Baranowski, A. Surrente, E. Malic, A. Chernikov and P. Płochocka.

4. **Workshop "MAGNETIC FIELDS IN MATERIALS RESEARCH"**
   22-24 May 2023, Wrocław, Poland
   Poster presentation: *"Valley Polarisation in Monolayer TMDs and TMD/2D Perovskite Heterostructures"*
   J. Jasiński, S. Palai, J. Thompson, M. Śmiertka , J. D. Ziegler, K. Watanabe, T. Taniguchi, M. Baranowski, A. Surrente, E. Malic, A. Chernikov and P. Płochocka.

5. **Mauterndorf Winterschool 2023**
   12-17 February 2023, Mauterndorf, Austria
   Poster presentation: *"Strain induced lifting of the charged exciton degeneracy in monolayer MoS_2 on GaAs nanomembranes"*
   J. Jasiński, A. Balgarkashi, V. Piazza, D. Dede, A. Surrente, M. Baranowski, D. K. Maude, M. Banerjee, R. Frisenda, A. Castellanos-Gomez, A. Fontcuberta i Morral and P. Płochocka.

6. **Flatlands - Beyond graphene 2022**
   28-30 September 2022, Lanzarote, Spain
   Oral presentation: *"Strain induced lifting of the charged exciton degeneracy in monolayer* MoS_2 *on GaAs nanomembranes"*
   J. Jasiński, A. Balgarkashi, V. Piazza, D. Dede, A. Surrente, M. Baranowski, D. K. Maude, M. Banerjee, R. Frisenda, A. Castellanos-Gomez, A. Fontcuberta i Morral and P. Płochocka.

7. **50th International School** & **Conference on the Physics of Semiconductors "Jaszowiec 2022"**
   4-10 June 2022, Szczyrk, Poland
   Oral presentation: *"Strain Engineering of the Polarization Properties of* MoS_2 *Monolayers via Integration on GaAs Nanomembranes"*
   J. Jasiński, A. Balgarkashi, V. Piazza, D. Dede, A. Surrente, M. Baranowski, D. K. Maude, M. Banerjee, R. Frisenda, A. Castellanos-Gomez, A. Fontcuberta i Morral and P. Płochocka.

8. **Optics of Excitons in Confined Systems OECS17**
   30 August-2 September 2021, Dortmund, Germany
   Poster presentation: *"Optical Properties of* MoS_2 *on GaAs nanomembranes"*
   J. Jasiński, A. Balgarkashi, D. Dede, A. Surrente, M. Baranowski, R. Frisenda, A. Castellanos-Gomez, A. Fontcuberta i Morral and P. Płochocka.

Bibliography

[Aras 2022] F Gonca Aras, Alp Yilmaz, H Gunalp Tasdelen, Ayberk Ozden, Feridun Ay, Nihan Kosku Perkgoz and Aydan Yeltik. *A review on recent advances of chemical vapor deposition technique for monolayer transition metal dichalcogenides (MX2: Mo, W; S, Se, Te)*. Materials Science in Semiconductor Processing, vol. 148, page 106829, 2022. (Cited on page 2.)

[Arora 2015] Ashish Arora, Maciej Koperski, Karol Nogajewski, Jacques Marcus, Clément Faugeras and Marek Potemski. *Excitonic resonances in thin films of WSe$_2$: from monolayer to bulk material*. Nanoscale, vol. 7, no. 23, pages 10421–10429, 2015. (Cited on page 12.)

[Arora 2017] Ashish Arora, Matthias Drüppel, Robert Schmidt, Thorsten Deilmann, Robert Schneider, Maciej R Molas, Philipp Marauhn, Steffen Michaelis de Vasconcellos, Marek Potemski, Michael Rohlfing*et al. Interlayer excitons in a bulk van der Waals semiconductor*. Nature communications, vol. 8, no. 1, page 639, 2017. (Cited on pages 15, 87 and 89.)

[Arora 2018] Ashish Arora, Thorsten Deilmann, Philipp Marauhn, Matthias Drüppel, Robert Schneider, Maciej R Molas, Diana Vaclavkova, Steffen Michaelis de Vasconcellos, Michael Rohlfing, Marek Potemski*et al. Valley-contrasting optics of interlayer excitons in Mo-and W-based bulk transition metal dichalcogenides*. Nanoscale, vol. 10, no. 33, pages 15571–15577, 2018. (Cited on page 87.)

[Astrakharchik 2021] GE Astrakharchik, IL Kurbakov, DV Sychev, AK Fedorov and Yu E Lozovik. *Quantum phase transition of a two-dimensional quadrupolar system*. Physical Review B, vol. 103, no. 14, page L140101, 2021. (Cited on page 89.)

[Baek 2023] Ji-Hwan Baek, Hyoung Gyun Kim, Soo Yeon Lim, Seong Chul Hong, Yunyeong Chang, Huije Ryu, Yeonjoon Jung, Hajung Jang, Jungcheol Kim, Yichao Zhang*et al. Thermally induced atomic reconstruction into fully commensurate structures of transition metal dichalcogenide layers*. Nature materials, vol. 22, no. 12, pages 1463–1469, 2023. (Cited on pages 15 and 87.)

[Bai 2023] Yusong Bai, Yiliu Li, Song Liu, Yinjie Guo, Jordan Pack, Jue Wang, Cory R Dean, James Hone and Xiaoyang Zhu. *Evidence for exciton crystals in a 2D semiconductor heterotrilayer*. Nano Letters, vol. 23, no. 24, pages 11621–11629, 2023. (Cited on page 89.)

[Baranowski 2017] Michał Baranowski, Alessandro Surrente, Duncan Kennedy Maude, M Ballottin, AA Mitioglu, PCM Christianen, YC Kung, D Dumcenco, A Kis and P Plochocka. *Dark excitons and the elusive valley polar-*

ization in transition metal dichalcogenides. 2D Materials, vol. 4, no. 2, page 025016, 2017. (Cited on pages 11 and 69.)

[Baranowski 2019] Michal Baranowski, Szymon J Zelewski, Mikael Kepenekian, Boubacar Traoré, Joanna M Urban, Alessandro Surrente, Krzysztof Galkowski, Duncan K Maude, Agnieszka Kuc, Edward P Booker *et al. Phase-transition-induced carrier mass enhancement in 2D Ruddlesden–Popper perovskites.* ACS Energy Letters, vol. 4, no. 10, pages 2386–2392, 2019. (Cited on pages 75 and 77.)

[Baranowski 2022a] Michał Baranowski, Mateusz Dyksik and Paulina Płochocka. *2d metal halide perovskites: A new fascinating playground for exciton fine structure investigations.* Scientiae Radices, vol. 1, 2022. (Cited on pages 74, 75 and 76.)

[Baranowski 2022b] Michal Baranowski, Alessandro Surrente and Paulina Plochocka. *Two Dimensional Perovskites/Transition Metal Dichalcogenides Heterostructures: Puzzles and Challenges.* Israel Journal of Chemistry, vol. 62, no. 3-4, page e202100120, 2022. (Cited on pages 63, 74, 75 and 76.)

[Barbone 2018] Matteo Barbone, Alejandro R-P Montblanch, Dhiren M Kara, Carmen Palacios-Berraquero, Alisson R Cadore, Domenico De Fazio, Benjamin Pingault, Elaheh Mostaani, Han Li, Bin Chen, Kenji Watanabe, Takashi Taniguchi, Sefaattin Tongay, Gang Wang, Andrea C Ferrari and Mete Atatüre. *Charge-tuneable biexciton complexes in monolayer* WSe_2. Nature Communications, vol. 9, no. 1, page 3721, 2018. (Cited on page 13.)

[Barré 2023] Elyse Barré, Medha Dandu and Archana Raja. *Quadrupolar excitons take the stage.* Nature Materials, vol. 22, no. 12, pages 1437–1438, 2023. (Cited on page 89.)

[Bayer 2002] M Bayer, G Ortner, O Stern, A Kuther, AA Gorbunov, A Forchel, Pawel Hawrylak, S Fafard, K Hinzer, TL Reinecke *et al. Fine structure of neutral and charged excitons in self-assembled In (Ga) As/(Al) GaAs quantum dots.* Physical Review B, vol. 65, no. 19, page 195315, 2002. (Cited on pages 57 and 58.)

[Berghäuser 2018] Gunnar Berghäuser, Ivan Bernal-Villamil, Robert Schmidt, Robert Schneider, Iris Niehues, Paul Erhart, Steffen Michaelis de Vasconcellos, Rudolf Bratschitsch, Andreas Knorr and Ermin Malic. *Inverted valley polarization in optically excited transition metal dichalcogenides.* Nature communications, vol. 9, no. 1, page 971, 2018. (Cited on pages 61, 62, 68 and 70.)

[Bernal-Villamil 2018] Ivan Bernal-Villamil, Gunnar Berghäuser, Malte Selig, Iris Niehues, Robert Schmidt, Robert Schneider, Philipp Tonndorf, Paul Erhart, Steffen Michaelis de Vasconcellos, Rudolf Bratschitsch*et al.* *Exciton broadening and band renormalization due to Dexter-like intervalley coupling.* 2D Materials, vol. 5, no. 2, page 025011, 2018. (Cited on pages 70, 72 and 73.)

[Bertolazzi 2011] Simone Bertolazzi, Jacopo Brivio and Andras Kis. *Stretching and breaking of ultrathin MoS_2.* ACS Nano, vol. 5, no. 12, pages 9703–9709, 2011. (Cited on pages 47 and 49.)

[Bhongale 2013] Satyan G Bhongale, Ludwig Mathey, Erhai Zhao, Susanne F Yelin and Mikhail Lemeshko. *Quantum phases of quadrupolar Fermi gases in optical lattices.* Physical Review Letters, vol. 110, no. 15, page 155301, 2013. (Cited on page 88.)

[Blancon 2017] J-C Blancon, Hsinhan Tsai, Wanyi Nie, Costas C Stoumpos, Laurent Pedesseau, Claudine Katan, Mikaël Kepenekian, Chan Myae Myae Soe, Kannatassen Appavoo, Matthew Y Sfeir*et al.* *Extremely efficient internal exciton dissociation through edge states in layered 2D perovskites.* Science, vol. 355, no. 6331, pages 1288–1292, 2017. (Cited on page 74.)

[Blatter 1996] Gianni Blatter and Vadim Geshkenbein. *Van der Waals attraction of vortices in anisotropic and layered superconductors.* Physical Review Letters, vol. 77, no. 24, page 4958, 1996. (Cited on page 1.)

[Branny 2017] Artur Branny, Santosh Kumar, Raphaël Proux and Brian D Gerardot. *Deterministic strain-induced arrays of quantum emitters in a two-dimensional semiconductor.* Nature communications, vol. 8, no. 1, page 15053, 2017. (Cited on page 47.)

[Brem 2020] Samuel Brem, Kai-Qiang Lin, Roland Gillen, Jonas M Bauer, Janina Maultzsch, John M Lupton and Ermin Malic. *Hybridized intervalley moiré excitons and flat bands in twisted WSe 2 bilayers.* Nanoscale, vol. 12, no. 20, pages 11088–11094, 2020. (Cited on pages 17 and 87.)

[Brem 2024] Samuel Brem and Ermin Malic. *Optical signatures of moiré trapped biexcitons.* 2D Materials, vol. 11, no. 2, page 025030, 2024. (Cited on page 88.)

[Bromley 1972] RA Bromley, Ray B Murray and Abe D Yoffe. *The band structures of some transition metal dichalcogenides. III. Group VIA: trigonal prism materials.* Journal of Physics C: Solid State Physics, vol. 5, no. 7, page 759, 1972. (Cited on page 2.)

[Butov 1999] LV Butov, AA Shashkin, VT Dolgopolov, KL Campman and AC Gossard. *Magneto-optics of the spatially separated electron and hole layers in G a A s/A l x Ga 1- x As coupled quantum wells.* Physical Review B, vol. 60, no. 12, page 8753, 1999. (Cited on page 80.)

[Cao 2015] Duyen H Cao, Constantinos C Stoumpos, Omar K Farha, Joseph T Hupp and Mercouri G Kanatzidis. *2D homologous perovskites as light-absorbing materials for solar cell applications.* Journal of the American Chemical Society, vol. 137, no. 24, pages 7843–7850, 2015. (Cited on page 74.)

[Castellanos-Gomez 2014] Andres Castellanos-Gomez, Michele Buscema, Rianda Molenaar, Vibhor Singh, Laurens Janssen, Herre SJ Van Der Zant and Gary A Steele. *Deterministic transfer of two-dimensional materials by all-dry viscoelastic stamping.* 2D Materials, vol. 1, no. 1, page 011002, 2014. (Cited on pages 2, 41, 43, 49 and 90.)

[Chen 2018a] Shao-Yu Chen, Thomas Goldstein, Takashi Taniguchi, Kenji Watanabe and Jun Yan. *Coulomb-bound four-and five-particle intervalley states in an atomically-thin semiconductor.* Nature Communications, vol. 9, no. 1, page 3717, 2018. (Cited on page 64.)

[Chen 2018b] Yani Chen, Yong Sun, Jiajun Peng, Junhui Tang, Kaibo Zheng and Ziqi Liang. *2D Ruddlesden–Popper perovskites for optoelectronics.* Advanced Materials, vol. 30, no. 2, page 1703487, 2018. (Cited on pages 1 and 74.)

[Chen 2019] Shao-Yu Chen, Zhengguang Lu, Thomas Goldstein, Jiayue Tong, Andrey Chaves, Jens Kunstmann, LSR Cavalcante, Tomasz Wozniak, Gotthard Seifert, DR Reichman, Takashi Taniguchi, Kenji Watanabe, Dmitry Smirnov and Jun Yan. *Luminescent emission of excited Rydberg excitons from monolayer* WSe_2. Nano Letters, vol. 19, no. 4, pages 2464–2471, 2019. (Cited on page 65.)

[Chen 2020a] Yingying Chen, Zeyi Liu, Junze Li, Xue Cheng, Jiaqi Ma, Haizhen Wang and Dehui Li. *Robust interlayer coupling in two-dimensional perovskite/monolayer transition metal dichalcogenide heterostructures.* ACS Nano, vol. 14, no. 8, pages 10258–10264, 2020. (Cited on pages 63, 76, 79 and 80.)

[Chen 2020b] Yingying Chen, Jiaqi Ma, Zeyi Liu, Junze Li, Xiangfeng Duan and Dehui Li. *Manipulation of valley pseudospin by selective spin injection in chiral two-dimensional perovskite/monolayer transition metal dichalcogenide heterostructures.* ACS Nano, vol. 14, no. 11, pages 15154–15160, 2020. (Cited on pages 63, 76 and 79.)

[Chen 2023] Jiajun Chen, Xiaofei Yue, Yabing Shan, Huishan Wang, Jinkun Han, Haomin Wang, Chenxu Sheng, Laigui Hu, Ran Liu, Weihuang Yang*et al.* *Twist-angle-dependent momentum-space direct and indirect interlayer excitons in WSe 2/WS 2 heterostructure.* RSC advances, vol. 13, no. 26, pages 18099–18107, 2023. (Cited on pages 15 and 87.)

[Chernikov 2014] Alexey Chernikov, Timothy C Berkelbach, Heather M Hill, Albert Rigosi, Yilei Li, Burak Aslan, David R Reichman, Mark S Hybertsen and Tony F Heinz. *Exciton binding energy and nonhydrogenic Rydberg series in monolayer WS 2.* Physical review letters, vol. 113, no. 7, page 076802, 2014. (Cited on pages 1, 7, 9, 10, 30, 61 and 87.)

[Chernikov 2015] Alexey Chernikov, Arend M Van Der Zande, Heather M Hill, Albert F Rigosi, Ajanth Velauthapillai, James Hone and Tony F Heinz. *Electrical tuning of exciton binding energies in monolayer WS 2.* Physical review letters, vol. 115, no. 12, page 126802, 2015. (Cited on page 18.)

[Cho 2021] Chullhee Cho, Joeson Wong, Amir Taqieddin, Souvik Biswas, Narayana R Aluru, SungWoo Nam and Harry A Atwater. *Highly strain-tunable interlayer excitons in MoS2/WSe2 heterobilayers.* Nano letters, vol. 21, no. 9, pages 3956–3964, 2021. (Cited on pages 15 and 87.)

[Choi 2021] Junho Choi, Matthias Florian, Alexander Steinhoff, Daniel Erben, Kha Tran, Dong Seob Kim, Liuyang Sun, Jiamin Quan, Robert Claassen, Somak Majumder*et al. Twist angle-dependent interlayer exciton lifetimes in van der Waals heterostructures.* Physical Review Letters, vol. 126, no. 4, page 047401, 2021. (Cited on pages 15 and 87.)

[Christopher 2019] Jason W Christopher, Mounika Vutukuru, David Lloyd, J Scott Bunch, Bennett B Goldberg, David J Bishop and Anna K Swan. *Monolayer MoS 2 strained to 1.3% with a microelectromechanical system.* Journal of Microelectromechanical Systems, vol. 28, no. 2, pages 254–263, 2019. (Cited on pages 47, 52, 54, 55 and 56.)

[Ciarrocchi 2022] Alberto Ciarrocchi, Fedele Tagarelli, Ahmet Avsar and Andras Kis. *Excitonic devices with van der Waals heterostructures: valleytronics meets twistronics.* Nature Reviews Materials, vol. 7, no. 6, pages 449–464, 2022. (Cited on pages 2, 11 and 87.)

[Conley 2013] Hiram J Conley, Bin Wang, Jed I Ziegler, Richard F Haglund Jr, Sokrates T Pantelides and Kirill I Bolotin. *Bandgap engineering of strained monolayer and bilayer MoS2.* Nano letters, vol. 13, no. 8, pages 3626–3630, 2013. (Cited on pages 34 and 35.)

[Conway 2022] MA Conway, JB Muir, SK Earl, Matthias Wurdack, Rishabh Mishra, JO Tollerud and JA Davis. *Direct measurement of biexcitons in monolayer WS2.* 2D Materials, vol. 9, no. 2, page 021001, 2022. (Cited on page 13.)

[Coogan 2021] Áine Coogan and Yurii K Gun'ko. *Solution-based "bottom-up" synthesis of group VI transition metal dichalcogenides and their applications.* Materials Advances, vol. 2, no. 1, pages 146–164, 2021. (Cited on pages 2 and 3.)

[Dadgar 2018] AM Dadgar, D Scullion, K Kang, D Esposito, EH Yang, IP Herman, MA Pimenta, E-JG Santos and AN Pasupathy. *Strain engineering and Raman spectroscopy of monolayer transition metal dichalcogenides.* Chemistry of Materials, vol. 30, no. 15, pages 5148–5155, 2018. (Cited on pages 35, 47 and 52.)

[Davila 2024] Yuset Guerra Davila, Francisco WN Silva, Maykol CD Oliveira, Zhuohang Yu, Thais CV Carvalho, Clenilton C dos Santos, Antonio G Souza Filho, Mauricio Terrones, Rafael S Alencar and Bartolomeu C Viana. *Temperature and power-dependent photoluminescence spectroscopy in suspended WSe2 monolayer.* Journal of Physics D: Applied Physics, vol. 57, no. 16, page 165304, 2024. (Cited on page 82.)

[Dean 2010] Cory R Dean, Andrea F Young, Inanc Meric, Chris Lee, Lei Wang, Sebastian Sorgenfrei, Kenji Watanabe, Takashi Taniguchi, Phillip Kim, Kenneth L Shepard and James Hone. *Boron nitride substrates for high-quality graphene electronics.* Nature Nanotechnology, vol. 5, no. 10, pages 722–726, 2010. (Cited on page 1.)

[DeCrescent 2020] Ryan A DeCrescent, Naveen R Venkatesan, Clayton J Dahlman, Rhys M Kennard, Xie Zhang, Wenhao Li, Xinhong Du, Michael L Chabinyc, Rashid Zia and Jon A Schuller. *Bright magnetic dipole radiation from two-dimensional lead-halide perovskites.* Science advances, vol. 6, no. 6, page eaay4900, 2020. (Cited on pages 75 and 76.)

[Deilmann 2017] Thorsten Deilmann and Kristian Sommer Thygesen. *Dark excitations in monolayer transition metal dichalcogenides.* Physical Review B, vol. 96, no. 20, page 201113, 2017. (Cited on page 11.)

[Deilmann 2024] Thorsten Deilmann and Kristian Sommer Thygesen. *Quadrupolar and dipolar excitons in symmetric trilayer heterostructures: Insights from first principles theory.* 2D Materials, 2024. (Cited on page 89.)

[Dery 2016] Hanan Dery. *Theory of intervalley Coulomb interactions in monolayer transition-metal dichalcogenides.* Physical Review B, vol. 94, no. 7, page 075421, 2016. (Cited on pages 11, 61 and 69.)

[Dey 2017] Prasenjit Dey, Luyi Yang, Cedric Robert, Gang Wang, Bernhard Urbaszek, Xavier Marie and Scott A Crooker. *Gate-controlled spin-valley locking of resident carriers in* WSe_2 *monolayers.* Physical Review Letters, vol. 119, no. 13, page 137401, 2017. (Cited on pages 11, 61 and 70.)

[Dirac 1926] Paul Adrien Maurice Dirac. *On the theory of quantum mechanics.* Proceedings of the Royal Society of London. Series A, Containing Papers of a Mathematical and Physical Character, vol. 112, no. 762, pages 661–677, 1926. (Cited on page 18.)

[Dou 2015] Letian Dou, Andrew B Wong, Yi Yu, Minliang Lai, Nikolay Kornienko, Samuel W Eaton, Anthony Fu, Connor G Bischak, Jie Ma, Tina Ding*et al.* *Atomically thin two-dimensional organic-inorganic hybrid perovskites.* Science, vol. 349, no. 6255, pages 1518–1521, 2015. (Cited on page 74.)

[Duan 2015] Xidong Duan, Chen Wang, Anlian Pan, Ruqin Yu and Xiangfeng Duan. *Two-dimensional transition metal dichalcogenides as atomically thin semiconductors: opportunities and challenges.* Chemical Society Reviews, vol. 44, no. 24, pages 8859–8876, 2015. (Cited on page 1.)

[Dufferwiel 2018] S Dufferwiel, TP Lyons, DD Solnyshkov, AAP Trichet, A Catanzaro, F Withers, Guillaume Malpuech, JM Smith, KS Novoselov, MS Skolnick*et al.* *Valley coherent exciton-polaritons in a monolayer semiconductor.* Nature communications, vol. 9, no. 1, page 4797, 2018. (Cited on page 33.)

[Dyksik 2021] Mateusz Dyksik, Herman Duim, Duncan K Maude, Michal Baranowski, Maria Antonietta Loi and Paulina Plochocka. *Brightening of dark excitons in 2D perovskites.* Science Advances, vol. 7, no. 46, page eabk0904, 2021. (Cited on page 76.)

[Dyksik 2024] Mateusz Dyksik, Dorian Beret, Michal Baranowski, Herman Duim, Sébastien Moyano, Katarzyna Posmyk, Adnen Mlayah, Sampson Adjokatse, Duncan K Maude, Maria Antonietta Loi*et al.* *Polaron vibronic progression shapes the optical response of 2D perovskites.* Advanced Science, vol. 11, no. 7, page 2305182, 2024. (Cited on page 74.)

[Echeverry 2016] JP Echeverry, Bernhard Urbaszek, Thierry Amand, Xavier Marie and Iann C Gerber. *Splitting between bright and dark excitons in transition metal dichalcogenide monolayers.* Physical Review B, vol. 93, no. 12, page 121107, 2016. (Cited on page 11.)

[Efimkin 2017] Dmitry K Efimkin and Allan H MacDonald. *Many-body theory of trion absorption features in two-dimensional semiconductors.* Physical Review B, vol. 95, no. 3, page 035417, 2017. (Cited on pages 20 and 21.)

[Eisenstein 2004] JP Eisenstein and Allan H MacDonald. *Bose–Einstein condensation of excitons in bilayer electron systems.* Nature, vol. 432, no. 7018, pages 691–694, 2004. (Cited on page 88.)

[Erkılıc 2019] Ufuk Erkılıc, Pablo Solís-Fernández, Hyun Goo Ji, Keisuke Shinokita, Yung-Chang Lin, Mina Maruyama, Kazu Suenaga, Susumu Okada, Kazunari Matsuda and Hiroki Ago. *Vapor phase selective growth of two-dimensional perovskite/WS2 heterostructures for optoelectronic applications.* ACS applied materials & interfaces, vol. 11, no. 43, pages 40503–40511, 2019. (Cited on page 63.)

[Even 2013] Jacky Even, Laurent Pedesseau, Jean-Marc Jancu and Claudine Katan. *Importance of spin–orbit coupling in hybrid organic/inorganic perovskites for* *photovoltaic applications.* The Journal of Physical Chemistry Letters, vol. 4, no. 17, pages 2999–3005, 2013. (Cited on page 75.)

[Feng 2024] Shun Feng, Aidan J Campbell, Mauro Brotons-Gisbert, Daniel Andres-Penares, Hyeonjun Baek, Takashi Taniguchi, Kenji Watanabe, Bernhard Urbaszek, Iann C Gerber and Brian D Gerardot. *Highly tunable ground and excited state excitonic dipoles in multilayer 2H-MoSe2.* Nature Communications, vol. 15, no. 1, page 4377, 2024. (Cited on pages 15, 17, 87 and 89.)

[Fogler 2014] MM Fogler, LV Butov and KS Novoselov. *High-temperature superfluidity with indirect excitons in van der Waals heterostructures.* Nature communications, vol. 5, no. 1, page 4555, 2014. (Cited on page 88.)

[Fox 2010] Mark Fox. Optical properties of solids, volume 3. Oxford university press, 2010. (Cited on pages 8, 23, 24 and 26.)

[Friedman 2017] Adam L Friedman, Aubrey T Hanbicki, F Keith Perkins, Glenn G Jernigan, James C Culbertson and Paul M Campbell. *Evidence for chemical vapor induced 2H to 1T phase transition in MoX2 (X= Se, S) transition metal dichalcogenide films.* Scientific reports, vol. 7, no. 1, page 3836, 2017. (Cited on page 3.)

[Frindt 1963] RF Frindt and AD Yoffe. *Physical properties of layer structures: optical properties and photoconductivity of thin crystals of molybdenum disulphide.* Proceedings of the Royal Society of London. Series A. Mathematical and Physical Sciences, vol. 273, no. 1352, pages 69–83, 1963. (Cited on page 1.)

[Frisenda 2017] Riccardo Frisenda, Yue Niu, Patricia Gant, Aday J Molina-Mendoza, Robert Schmidt, Rudolf Bratschitsch, Jinxin Liu, Lei Fu, Dumitru Dumcenco, Andras Kis, David Perez de Lara and Andres Castellanos-Gomez. *Micro-reflectance and transmittance spectroscopy: a versatile and powerful tool to characterize 2D materials.* Journal of Physics D: Applied Physics, vol. 50, no. 7, page 074002, 2017. (Cited on page 12.)

[Fu 2019] Qundong Fu, Xiaolei Wang, Fucai Liu, Yuxin Dong, Zirui Liu, Shoujun Zheng, Apoorva Chaturvedi, Jiadong Zhou, Peng Hu, Zhuqing Zhu, Fang Bo, Yi Long and Zheng Liu. *Ultrathin Ruddlesden–Popper perovskite heterojunction for sensitive photodetection.* Small, vol. 15, no. 39, page 1902890, 2019. (Cited on page 63.)

[Gan 2018] Xiaorong Gan, Lawrence Yoon Suk Lee, Kwok-yin Wong, Tsz Wing Lo, Kwun Hei Ho, Dang Yuan Lei and Huimin Zhao. *2H/1T phase transition of multilayer MoS2 by electrochemical incorporation of S vacancies.* ACS Applied Energy Materials, vol. 1, no. 9, pages 4754–4765, 2018. (Cited on page 3.)

[Geim 2007] Andre K Geim and Konstantin S Novoselov. *The rise of graphene.* Nature materials, vol. 6, no. 3, pages 183–191, 2007. (Cited on pages 1 and 2.)

[Geim 2013] Andre K Geim and Irina V Grigorieva. *Van der Waals heterostructures.* Nature, vol. 499, no. 7459, pages 419–425, 2013. (Cited on pages 1, 2 and 87.)

[Gerber 2019] Iann C. Gerber, Emmanuel Courtade, Shivangi Shree, Cedric Robert, Takashi Taniguchi, Kenji Watanabe, Andrea Balocchi, Pierre Renucci, Delphine Lagarde, Xavier Marie and Bernhard Urbaszek. *Interlayer excitons in bilayer* MoS_2 *with strong oscillator strength up to room temperature.* Phys. Rev. B, vol. 99, page 035443, Jan 2019. (Cited on pages 15, 87 and 89.)

[Glazov 2020] Mikhail M Glazov. *Optical properties of charged excitons in two-dimensional semiconductors.* The Journal of Chemical Physics, vol. 153, no. 3, 2020. (Cited on pages 20 and 21.)

[Glazov 2022] MM Glazov, Florian Dirnberger, Vinod M Menon, Takashi Taniguchi, Kenji Watanabe, Dominique Bougeard, Jonas D Ziegler and Alexey Chernikov. *Exciton fine structure splitting and linearly polarized emission in strained transition-metal dichalcogenide monolayers.* Physical Review B, vol. 106, no. 12, page 125303, 2022. (Cited on pages 33 and 59.)

[Gong 2011] Ming Gong, Weiwei Zhang, Guang-Can Guo and Lixin He. *Exciton polarization, fine-structure splitting, and the asymmetry of quantum dots under uniaxial stress.* Physical review letters, vol. 106, no. 22, page 227401, 2011. (Cited on page 57.)

[Gong 2018] Xiwen Gong, Oleksandr Voznyy, Ankit Jain, Wenjia Liu, Randy Sabatini, Zachary Piontkowski, Grant Walters, Golam Bappi, Sergiy Nokhrin, Oleksandr Bushuyev*et al. Electron–phonon interaction in efficient perovskite blue emitters.* Nature materials, vol. 17, no. 6, pages 550–556, 2018. (Cited on page 74.)

[Gong 2024] Yiyang Gong, Shuai Yue, Yin Liang, Wenna Du, Tieyuan Bian, Chuanxiu Jiang, Xiaotian Bao, Shuai Zhang, Mingzhu Long, Guofu Zhou, Jun Yin, Shibin Deng, Qing Zhang, Bo Wu and Xinfeng Liu. *Boosting exciton mobility approaching Mott-Ioffe-Regel limit in Ruddlesden- Popper perovskites by anchoring the organic cation.* Nature Communications, vol. 15, no. 1, page 1893, 2024. (Cited on page 81.)

[Grancini 2019] Giulia Grancini and Mohammad Khaja Nazeeruddin. *Dimensional tailoring of hybrid perovskites for photovoltaics.* Nature Reviews Materials, vol. 4, no. 1, pages 4–22, 2019. (Cited on page 1.)

[Gu 2022] Jie Gu, Liguo Ma, Song Liu, Kenji Watanabe, Takashi Taniguchi, James C Hone, Jie Shan and Kin Fai Mak. *Dipolar excitonic insulator in a* *moiré lattice.* Nature physics, vol. 18, no. 4, pages 395–400, 2022. (Cited on page 88.)

[Gupta 2019] Garima Gupta and Kausik Majumdar. *Fundamental exciton linewidth broadening in monolayer transition metal dichalcogenides.* Physical Review B, vol. 99, no. 8, page 085412, 2019. (Cited on page 64.)

[Hagel 2021] Joakim Hagel, Samuel Brem, Christopher Linderälv, Paul Erhart and Ermin Malic. *Exciton landscape in van der Waals heterostructures.* Physical Review Research, vol. 3, no. 4, page 043217, 2021. (Cited on pages 15, 87 and 103.)

[Hagel 2022] Joakim Hagel, Samuel Brem and Ermin Malic. *Electrical tuning of moiré excitons in MoSe2 bilayers.* 2D Materials, vol. 10, no. 1, page 014013, 2022. (Cited on pages 15, 87 and 89.)

[Hanbicki 2015] AT Hanbicki, M Currie, G Kioseoglou, AL Friedman and BT Jonker. *Measurement of high exciton binding energy in the monolayer transition-metal dichalcogenides WS_2 and WSe_2.* Solid State Communications, vol. 203, pages 16–20, 2015. (Cited on pages 1, 7, 10, 12, 61 and 87.)

[Hao 2016] Kai Hao, Galan Moody, Fengcheng Wu, Chandriker Kavir Dass, Lixiang Xu, Chang-Hsiao Chen, Liuyang Sun, Ming-Yang Li, Lain-Jong Li, Allan H MacDonald*et al. Direct measurement of exciton valley coherence in monolayer WSe2.* Nature Physics, vol. 12, no. 7, pages 677–682, 2016. (Cited on page 33.)

[Hao 2017] Kai Hao, Judith F Specht, Philipp Nagler, Lixiang Xu, Kha Tran, Akshay Singh, Chandriker Kavir Dass, Christian Schüller, Tobias Korn, Marten Richter, Andreas Knorr, Xiaolin Li and Galan Moody. *Neutral and charged inter-valley biexcitons in monolayer $MoSe_2$.* Nature Communications, vol. 8, no. 1, page 15552, 2017. (Cited on pages 11, 15, 61 and 69.)

[He 2014] Keliang He, Nardeep Kumar, Liang Zhao, Zefang Wang, Kin Fai Mak, Hui Zhao and Jie Shan. *Tightly bound excitons in monolayer WSe_2.* Physical Review Letters, vol. 113, no. 2, page 026803, 2014. (Cited on pages 1, 7, 10, 61 and 87.)

[Hecht 2012] Eugene Hecht. Optics. Pearson Education India, 2012. (Cited on page 25.)

[Höfer 2019] Bianca Höfer, Fabian Olbrich, Jan Kettler, Matthias Paul, Jonathan Höschele, Michael Jetter, Simone L Portalupi, Fei Ding, Peter Michler and Oliver G Schmidt. *Tuning emission energy and fine structure splitting in quantum dots emitting in the telecom O-band.* AIP Advances, vol. 9, no. 8, 2019. (Cited on page 57.)

[Hsu 2014] Wei-Ting Hsu, Zi-Ang Zhao, Lain-Jong Li, Chang-Hsiao Chen, Ming-Hui Chiu, Pi-Shan Chang, Yi-Chia Chou and Wen-Hao Chang. *Second harmonic generation from artificially stacked transition metal dichalcogenide twisted bilayers.* ACS nano, vol. 8, no. 3, pages 2951–2958, 2014. (Cited on pages 4 and 5.)

[Hsu 2019] Wei-Ting Hsu, Bo-Han Lin, Li-Syuan Lu, Ming-Hao Lee, Ming-Wen Chu, Lain-Jong Li, Wang Yao, Wen-Hao Chang and Chih-Kang Shih. *Tailoring excitonic states of van der Waals bilayers through stacking configuration, band alignment, and valley spin.* Science advances, vol. 5, no. 12, page eaax7407, 2019. (Cited on page 89.)

[Hu 2001] Jiangtao Hu, Liang-shi Li, Weidong Yang, Liberato Manna, Lin-wang Wang and A Paul Alivisatos. *Linearly polarized emission from colloidal semiconductor quantum rods.* Science, vol. 292, no. 5524, pages 2060–2063, 2001. (Cited on page 32.)

[Hu 2020] Chaowei Hu, Kyle N Gordon, Pengfei Liu, Jinyu Liu, Xiaoqing Zhou, Peipei Hao, Dushyant Narayan, Eve Emmanouilidou, Hongyi Sun, Yuntian Liu, Harlan Brawer, Arthur P Ramirez, Lei Ding, Huibo Cao, Qihang Liu, Dan Dessau and Li Li. *A van der Waals antiferromagnetic topological insulator with weak interlayer magnetic coupling.* Nature Communications, vol. 11, no. 1, page 97, 2020. (Cited on page 1.)

[Huang 2016] Jiani Huang, Thang B Hoang and Maiken H Mikkelsen. *Probing the origin of excitonic states in monolayer WSe 2.* Scientific reports, vol. 6, no. 1, page 22414, 2016. (Cited on pages 80, 81 and 82.)

[Huang 2021] Xiong Huang, Tianmeng Wang, Shengnan Miao, Chong Wang, Zhipeng Li, Zhen Lian, Takashi Taniguchi, Kenji Watanabe, Satoshi Okamoto, Di Xiao*et al.* *Correlated insulating states at fractional fillings of the WS2/WSe2 moiré lattice.* Nature Physics, vol. 17, no. 6, pages 715–719, 2021. (Cited on page 88.)

[Huang 2022a] Di Huang, Junho Choi, Chih-Kang Shih and Xiaoqin Li. *Excitons in semiconductor moiré superlattices.* Nature nanotechnology, vol. 17, no. 3, pages 227–238, 2022. (Cited on pages 2 and 87.)

[Huang 2022b] Zhiheng Huang, Yanchong Zhao, Tao Bo, Yanbang Chu, Jinpeng Tian, Le Liu, Yalong Yuan, Fanfan Wu, Jiaojiao Zhao, Lede Xian*et al.* *Spatially indirect intervalley excitons in bilayer W Se 2.* Physical Review B, vol. 105, no. 4, page L041409, 2022. (Cited on pages 17 and 87.)

[Huang 2023] Di Huang, Kevin Sampson, Yue Ni, Zhida Liu, Danfu Liang, Kenji Watanabe, Takashi Taniguchi, Hebin Li, Eric Martin, Jesper Levinsen*et al.* *Quantum dynamics of attractive and repulsive polarons in a doped MoSe 2* *monolayer.* Physical Review X, vol. 13, no. 1, page 011029, 2023. (Cited on pages 20, 21 and 93.)

[Huard 2000] V Huard, RT Cox, K Saminadayar, A Arnoult and S Tatarenko. *Bound states in optical absorption of semiconductor quantum wells containing a two-dimensional electron gas.* Physical review letters, vol. 84, no. 1, page 187, 2000. (Cited on page 19.)

[Hui 2013] Yeung Yu Hui, Xiaofei Liu, Wenjing Jie, Ngai Yui Chan, Jianhua Hao, Yu-Te Hsu, Lain-Jong Li, Wanlin Guo and Shu Ping Lau. *Exceptional tunability of band energy in a compressively strained trilayer MoS2 sheet.* ACS nano, vol. 7, no. 8, pages 7126–7131, 2013. (Cited on pages 35, 47 and 52.)

[Hurtado Parra 2022] Sebastian Hurtado Parra, Daniel B Straus, Bryan T Fichera, Natasha Iotov, Cherie R Kagan and James M Kikkawa. *Large exciton polaron formation in 2D hybrid perovskites via time-resolved photoluminescence.* ACS nano, vol. 16, no. 12, pages 21259–21265, 2022. (Cited on page 74.)

[Iakovlev 2023] ZA Iakovlev and MM Glazov. *Fermi polaron fine structure in strained van der Waals heterostructures.* 2D Materials, vol. 10, no. 3, page 035034, 2023. (Cited on pages 21 and 59.)

[Iff 2017] Oliver Iff, Yu-Ming He, Nils Lundt, Sebastian Stoll, Vasilij Baumann, Sven Höfling and Christian Schneider. *Substrate engineering for high-quality emission of free and localized excitons from atomic monolayers in hybrid architectures.* Optica, vol. 4, no. 6, pages 669–673, 2017. (Cited on page 56.)

[Jadczak 2023] Joanna Jadczak, Joerg Debus, Justyna Olejnik, Ching-Hwa Ho, Kenji Watanabe, Takashi Taniguchi and Leszek Bryja. *Biexciton and Singlet Trion Upconvert Exciton Photoluminescence in a MoSe2 Monolayer Supported by Acoustic and Optical K-Valley Phonons.* The Journal of Physical Chemistry Letters, vol. 14, no. 39, pages 8702–8708, 2023. (Cited on page 15.)

[Jasiński 2022] Jakub Jasiński, Akshay Balgarkashi, Valerio Piazza, Didem Dede, Alessandro Surrente, Michał Baranowski, Duncan K Maude, Mitali Banerjee, Riccardo Frisenda, Andres Castellanos-Gomez*et al.* *Strain induced lifting of the charged exciton degeneracy in monolayer MoS2 on a GaAs nanomembrane.* 2D Materials, vol. 9, no. 4, page 045006, 2022. (Cited on pages 33 and 60.)

[Jasiński 2024a] Jakub Jasiński, Joakim Hagel, Samuel Brem, Edith Wietek, Takashi Taniguchi, Kenji Watanabe, Alexey Chernikov, Nicolas Bruyant, Mateusz Dyksik, Alessandro Surrente*et al.* *Quadrupolar Excitons in MoSe2 Bilayers.* arXiv preprint arXiv:2407.18040, 2024. (Cited on page 108.)

[Jasiński 2024b] Jakub Jasiński, Joshua JP Thompson, Swaroop Palai, Maciej Śmiertka, Mateusz Dyksik, Takashi Taniguchi, Kenji Watanabe, Michał Baranowski, Duncan K Maude, Alessandro Surrente*et al.* *Control of the valley polarization of monolayer WSe2 by Dexter-like coupling.* 2D Materials, vol. 11, no. 2, page 025007, 2024. (Cited on pages 69, 70 and 86.)

[Jauregui 2019] Luis A Jauregui, Andrew Y Joe, Kateryna Pistunova, Dominik S Wild, Alexander A High, You Zhou, Giovanni Scuri, Kristiaan De Greve, Andrey Sushko, Che-Hang Yu*et al.* *Electrical control of interlayer exciton dynamics in atomically thin heterostructures.* Science, vol. 366, no. 6467, pages 870–875, 2019. (Cited on pages 15, 17 and 87.)

[Ji 2023] Jongho Ji, Hoe-Min Kwak, Jimyeong Yu, Sangwoo Park, Jeong-Hwan Park, Hyunsoo Kim, Seokgi Kim, Sungkyu Kim, Dong-Seon Lee and Hyun S Kum. *Understanding the 2D-material and substrate interaction during epitaxial growth towards successful remote epitaxy: a review.* Nano Convergence, vol. 10, no. 1, page 19, 2023. (Cited on page 47.)

[Jiang 2021] Ying Jiang, Shula Chen, Weihao Zheng, Biyuan Zheng and Anlian Pan. *Interlayer exciton formation, relaxation, and transport in TMD van der Waals heterostructures.* Light: Science & Applications, vol. 10, no. 1, page 72, 2021. (Cited on page 87.)

[Jones 2013] Aaron M Jones, Hongyi Yu, Nirmal J Ghimire, Sanfeng Wu, Grant Aivazian, Jason S Ross, Bo Zhao, Jiaqiang Yan, David G Mandrus, Di Xiao*et al.* *Optical generation of excitonic valley coherence in monolayer WSe2.* Nature nanotechnology, vol. 8, no. 9, pages 634–638, 2013. (Cited on page 33.)

[Kapuściński 2021] Piotr Kapuściński, Alex Delhomme, Diana Vaclavkova, Artur O Slobodeniuk, Magdalena Grzeszczyk, Miroslav Bartos, Kenji Watanabe, Takashi Taniguchi, Clément Faugeras and Marek Potemski. *Rydberg series of dark excitons and the conduction band spin-orbit splitting in monolayer WSe2.* Communications Physics, vol. 4, no. 1, page 186, 2021. (Cited on page 82.)

[Karpinska 2021] Miriam Karpinska, Minpeng Liang, Roman Kempt, Kati Finzel, Machteld Kamminga, Mateusz Dyksik, Nan Zhang, Catherine Knodlseder, Duncan K Maude, Michał Baranowski, Łukasz Kłoptowski, Jianting Ye, Agnieszka Kuc and Paulina Plochocka. *Nonradiative Energy Transfer and Selective Charge Transfer in a $WS_2/(PEA)_2PbI_4$ Heterostructure.* ACS Applied Materials & Interfaces, vol. 13, no. 28, pages 33677–33684, 2021. (Cited on pages 32, 63 and 79.)

[Karpińska 2022] M Karpińska, J Jasiński, R Kempt, JD Ziegler, H Sansom, T Taniguchi, K Watanabe, HJ Snaith, A Surrente, M Dyksik, DK Maude, Ł Kłoptowski, A Chernikov, A Kuc, M Baranowski and P Plochocka. *Interlayer excitons in MoSe$_2$/2D perovskite hybrid heterostructures–the interplay between charge and energy transfer.* Nanoscale, vol. 14, no. 22, pages 8085–8095, 2022. (Cited on pages 32, 63, 76 and 79.)

[Keldysh 1979] LV Keldysh. *Coulomb interaction in thin semiconductor and semimetal films.* Soviet Journal of Experimental and Theoretical Physics Letters, vol. 29, page 658, 1979. (Cited on page 10.)

[Khestanova 2023] Ekaterina Khestanova, Tatyana Ivanova, Roland Gillen, Alessandro D'Elia, Oliver Nicholas Gallego Lacey, Lena Wysocki, Alexander Gruneis, Vasily Kravtsov, Wlodek Strupinski, Janina Maultzsch*et al.* *Robustness of momentum-indirect interlayer excitons in MoS2/WSe2 heterostructure against charge carrier doping.* ACS Photonics, vol. 10, no. 4, pages 1159–1168, 2023. (Cited on pages 15 and 87.)

[Kim 2017] Jonghwan Kim, Chenhao Jin, Bin Chen, Hui Cai, Tao Zhao, Puiyee Lee, Salman Kahn, Kenji Watanabe, Takashi Taniguchi, Sefaattin Tongay, Michael F Crommie and Feng Wang. *Observation of ultralong valley lifetime in WSe$_2$/MoS$_2$ heterostructures.* Science Advances, vol. 3, no. 7, page e1700518, 2017. (Cited on pages 11, 61 and 70.)

[Klein 2018] Dahlia R Klein, David MacNeill, Jose L Lado, David Soriano, Efrén Navarro-Moratalla, Kenji Watanabe, Takashi Taniguchi, Soham Manni, Paul Canfield, Joaquín Fernández-Rossier and Pablo Jarillo-Herrero. *Probing magnetism in 2D van der Waals crystalline insulators via electron tunneling.* Science, vol. 360, no. 6394, pages 1218–1222, 2018. (Cited on page 1.)

[Koperski 2015] Maciej Koperski, K Nogajewski, Ashish Arora, V Cherkez, Paul Mallet, J-Y Veuillen, J Marcus, Piotr Kossacki and M Potemski. *Single photon emitters in exfoliated WSe2 structures.* Nature nanotechnology, vol. 10, no. 6, pages 503–506, 2015. (Cited on page 47.)

[Kormányos 2015] Andor Kormányos, Guido Burkard, Martin Gmitra, Jaroslav Fabian, Viktor Zólyomi, Neil D Drummond and Vladimir Fal'ko. *$k\cdot p$ theory for two-dimensional transition metal dichalcogenide semiconductors.* 2D Materials, vol. 2, no. 2, page 022001, 2015. (Cited on pages 21, 82 and 101.)

[Kośmider 2013] K Kośmider, Jhon W González and Joaquın Fernández-Rossier. *Large spin splitting in the conduction band of transition metal dichalcogenide monolayers.* Physical Review B, vol. 88, no. 24, page 245436, 2013. (Cited on pages 6, 61 and 82.)

[Kou 2017] Liangzhi Kou, Yandong Ma, Ziqi Sun, Thomas Heine and Changfeng Chen. *Two-dimensional topological insulators: Progress and prospects.* The Journal of Physical Chemistry Letters, vol. 8, no. 8, pages 1905–1919, 2017. (Cited on page 1.)

[Kovalchuk 2023] S Kovalchuk, K Greben, A Kumar, S Pessel, K Watanabe, T Taniguchi, D Christiansen, M Selig, A Knorr and KI Bolotin. *Interlayer excitons in semiconductor bilayers under a strong electric field.* arXiv preprint arXiv:2303.09931, 2023. (Cited on pages 17, 87, 92 and 107.)

[Kozawa 2016] Daichi Kozawa, Alexandra Carvalho, Ivan Verzhbitskiy, Francesco Giustiniano, Yuhei Miyauchi, Shinichiro Mouri, AH Castro Neto, Kazunari Matsuda and Goki Eda. *Evidence for fast interlayer energy transfer in MoSe2/WS2 heterostructures.* Nano letters, vol. 16, no. 7, pages 4087–4093, 2016. (Cited on page 32.)

[Kumar 2006] Jitendra Kumar, Sheetal Kapoor, Saral K Gupta and Pranay K Sen. *Theoretical investigation of the effect of asymmetry on optical anisotropy and electronic structure of Stranski-Krastanov quantum dots.* Physical Review B—Condensed Matter and Materials Physics, vol. 74, no. 11, page 115326, 2006. (Cited on page 32.)

[Kumar 2012] Ashok Kumar and PK Ahluwalia. *Electronic structure of transition metal dichalcogenides monolayers 1H-MX 2 (M= Mo, W; X= S, Se, Te) from ab-initio theory: new direct band gap semiconductors.* The European Physical Journal B, vol. 85, pages 1–7, 2012. (Cited on page 5.)

[Kumar 2015] Santosh Kumar, Artur Kaczmarczyk and Brian D Gerardot. *Strain-induced spatial and spectral isolation of quantum emitters in mono-and bilayer WSe2.* Nano letters, vol. 15, no. 11, pages 7567–7573, 2015. (Cited on page 47.)

[Kundu 2022] Sudipta Kundu, Mit H Naik, HR Krishnamurthy and Manish Jain. *Moiré induced topology and flat bands in twisted bilayer WSe 2: A first-principles study.* Physical Review B, vol. 105, no. 8, page L081108, 2022. (Cited on page 88.)

[Lahrz 2014] Martin Lahrz, Mikhail Lemeshko, Klaus Sengstock, Christoph Becker and Ludwig Mathey. *Detecting quadrupole interactions in ultracold Fermi gases.* Physical Review A, vol. 89, no. 4, page 043616, 2014. (Cited on page 88.)

[Lahrz 2015] Martin Lahrz, Mikhail Lemeshko and Ludwig Mathey. *Exotic roton excitations in quadrupolar Bose–Einstein condensates.* New Journal of Physics, vol. 17, no. 4, page 045005, 2015. (Cited on page 88.)

[Laikhtman 2009] B Laikhtman and Ronen Rapaport. *Exciton correlations in coupled quantum wells and their luminescence blue shift.* Physical Review B, vol. 80, no. 19, page 195313, 2009. (Cited on page 80.)

[Larkin 2017] Peter Larkin. Infrared and raman spectroscopy: principles and spectral interpretation. Elsevier, 2017. (Cited on page 33.)

[Laturia 2018] Akash Laturia, Maarten L Van de Put and William G Vandenberghe. *Dielectric properties of hexagonal boron nitride and transition metal dichalcogenides: from monolayer to bulk*. npj 2D Materials and Applications, vol. 2, no. 1, page 6, 2018. (Cited on page 104.)

[Lee 2010] Changgu Lee, Hugen Yan, Louis E Brus, Tony F Heinz, James Hone and Sunmin Ryu. *Anomalous lattice vibrations of single-and few-layer MoS2*. ACS nano, vol. 4, no. 5, pages 2695–2700, 2010. (Cited on pages 34, 35 and 53.)

[Lee 2014] Chul-Ho Lee, Gwan-Hyoung Lee, Arend M Van Der Zande, Wenchao Chen, Yilei Li, Minyong Han, Xu Cui, Ghidewon Arefe, Colin Nuckolls, Tony F Heinz*et al.* *Atomically thin p–n junctions with van der Waals heterointerfaces*. Nature nanotechnology, vol. 9, no. 9, pages 676–681, 2014. (Cited on page 87.)

[Leisgang 2020] Nadine Leisgang, Shivangi Shree, Ioannis Paradisanos, Lukas Sponfeldner, Cedric Robert, Delphine Lagarde, Andrea Balocchi, Kenji Watanabe, Takashi Taniguchi, Xavier Marie*et al.* *Giant Stark splitting of an exciton in bilayer MoS2*. Nature nanotechnology, vol. 15, no. 11, pages 901–907, 2020. (Cited on pages 17, 42 and 87.)

[Li 2012] Sheng S Li. Semiconductor physical electronics. Springer Science & Business Media, 2012. (Cited on page 26.)

[Li 2018] Zhipeng Li, Tianmeng Wang, Zhengguang Lu, Chenhao Jin, Yanwen Chen, Yuze Meng, Zhen Lian, Takashi Taniguchi, Kenji Watanabe, Shengbai Zhang, Dmitry Smirnov and Su-Fei Shi. *Revealing the biexciton and trion-exciton complexes in BN encapsulated* WSe_2. Nature Communications, vol. 9, no. 1, page 3719, 2018. (Cited on pages 12 and 64.)

[Li 2020a] Lihui Li, Weihao Zheng, Chao Ma, Hepeng Zhao, Feng Jiang, Yu Ouyang, Biyuan Zheng, Xianwei Fu, Peng Fan, Min Zheng*et al.* *Wavelength-tunable interlayer exciton emission at the near-infrared region in van der Waals semiconductor heterostructures*. Nano letters, vol. 20, no. 5, pages 3361–3368, 2020. (Cited on pages 15 and 87.)

[Li 2020b] Zhipeng Li, Tianmeng Wang, Shengnan Miao, Zhen Lian and Su-Fei Shi. *Fine structures of valley-polarized excitonic states in monolayer transitional metal dichalcogenides*. Nanophotonics, vol. 9, no. 7, pages 1811–1829, 2020. (Cited on page 64.)

[Li 2021] En Li, Jin-Xin Hu, Xuemeng Feng, Zishu Zhou, Liheng An, Kam Tuen Law, Ning Wang and Nian Lin. *Lattice reconstruction induced multiple ultra-flat bands in twisted bilayer WSe2*. Nature communications, vol. 12, no. 1, page 5601, 2021. (Cited on page 88.)

[Li 2022] Yangang Li, Guizhi Kuang, Zhongjie Jiao, Lin Yao and Ruihuan Duan. *Recent progress on the mechanical exfoliation of 2D transition metal dichalcogenides*. Materials Research Express, vol. 9, no. 12, page 122001, 2022. (Cited on page 2.)

[Li 2023a] Weijie Li, Zach Hadjri, Luka M Devenica, Jin Zhang, Song Liu, James Hone, Kenji Watanabe, Takashi Taniguchi, Angel Rubio and Ajit Srivastava. *Quadrupolar–dipolar excitonic transition in a tunnel-coupled van der Waals heterotrilayer*. Nature Materials, vol. 22, no. 12, pages 1478–1484, 2023. (Cited on pages 89 and 98.)

[Li 2023b] Xuefei Li, Xinhang Shi, Damiano Marian, David Soriano, Teresa Cusati, Giuseppe Iannaccone, Gianluca Fiori, Qi Guo, Wenjie Zhao and Yanqing Wu. *Rhombohedral-stacked bilayer transition metal dichalcogenides for high-performance atomically thin CMOS devices*. Science Advances, vol. 9, no. 7, page eade5706, 2023. (Cited on page 3.)

[Li 2024] Xiangdong Li, Tong Tong, Xiaopeng Fan, Minru Qi, Shen Wang, Guofeng Zhang, Ruiyun Chen, Jianyong Hu, Zhichun Yang, Ganying Zeng*et al. Robust Layer-Dependent Valley Polarization and Valley Coherence in Spiral WS2 at Room Temperature*. Advanced Photonics Research, page 2400014, 2024. (Cited on page 33.)

[Lian 2023] Zhen Lian, Dongxue Chen, Lei Ma, Yuze Meng, Ying Su, Li Yan, Xiong Huang, Qiran Wu, Xinyue Chen, Mark Blei*et al. Quadrupolar excitons and hybridized interlayer Mott insulator in a trilayer moiré superlattice*. Nature communications, vol. 14, no. 1, page 4604, 2023. (Cited on page 89.)

[Lin 2022] Kai-Qiang Lin, Jonas D Ziegler, Marina A Semina, Javid V Mamedov, Kenji Watanabe, Takashi Taniguchi, Sebastian Bange, Alexey Chernikov, Mikhail M Glazov and John M Lupton. *High-lying valley-polarized trions in 2D semiconductors*. Nature Communications, vol. 13, no. 1, page 6980, 2022. (Cited on pages 18 and 19.)

[Liu 2013] Gui-Bin Liu, Wen-Yu Shan, Yugui Yao, Wang Yao and Di Xiao. *Three-band tight-binding model for monolayers of group-VIB transition metal dichalcogenides*. Physical Review B, vol. 88, no. 8, page 085433, 2013. (Cited on pages 6 and 82.)

[Liu 2014] Kaihui Liu, Liming Zhang, Ting Cao, Chenhao Jin, Diana Qiu, Qin Zhou, Alex Zettl, Peidong Yang, Steve G Louie and Feng Wang. *Evolution of interlayer coupling in twisted molybdenum disulfide bilayers*. Nature communications, vol. 5, no. 1, page 4966, 2014. (Cited on page 87.)

[Liu 2019a] Erfu Liu, Jeremiah van Baren, Takashi Taniguchi, Kenji Watanabe, Yia-Chung Chang and Chun Hung Lui. *Magnetophotoluminescence of exciton Rydberg states in monolayer* WSe_2. Physical Review B, vol. 99, no. 20, page 205420, 2019. (Cited on page 65.)

[Liu 2019b] Yanping Liu, Yuanji Gao, Siyu Zhang, Jun He, Juan Yu and Zongwen Liu. *Valleytronics in transition metal dichalcogenides materials.* Nano Research, vol. 12, pages 2695–2711, 2019. (Cited on page 11.)

[Liu 2020a] Hsiang-Lin Liu, Teng Yang, Jyun-Han Chen, Hsiao-Wen Chen, Huaihong Guo, Riichiro Saito, Ming-Yang Li and Lain-Jong Li. *Temperature-dependent optical constants of monolayer MoS 2, MoSe 2, WS 2, and WSe 2: spectroscopic ellipsometry and first-principles calculations.* Scientific reports, vol. 10, no. 1, page 15282, 2020. (Cited on page 81.)

[Liu 2020b] Yuanda Liu, Kévin Dini, Qinghai Tan, Timothy Liew, Kostya S Novoselov and Weibo Gao. *Electrically controllable router of interlayer excitons.* Science advances, vol. 6, no. 41, page eaba1830, 2020. (Cited on pages 17 and 87.)

[Liu 2021] Erfu Liu, Jeremiah van Baren, Zhengguang Lu, Takashi Taniguchi, Kenji Watanabe, Dmitry Smirnov, Yia-Chung Chang and Chun Hung Lui. *Exciton-polaron Rydberg states in monolayer MoSe2 and WSe2.* Nature communications, vol. 12, no. 1, page 6131, 2021. (Cited on page 20.)

[Lloyd 2016] David Lloyd, Xinghui Liu, Jason W Christopher, Lauren Cantley, Anubhav Wadehra, Brian L Kim, Bennett B Goldberg, Anna K Swan and J Scott Bunch. *Band gap engineering with ultralarge biaxial strains in suspended monolayer MoS2.* Nano letters, vol. 16, no. 9, pages 5836–5841, 2016. (Cited on page 35.)

[Lorchat 2021] Etienne Lorchat, Malte Selig, Florian Katsch, Kentaro Yumigeta, Sefaattin Tongay, Andreas Knorr, Christian Schneider and Sven Höfling. *Excitons in bilayer mos 2 displaying a colossal electric field splitting and tunable magnetic response.* Physical Review Letters, vol. 126, no. 3, page 037401, 2021. (Cited on pages 17 and 87.)

[Lu 2013] Hai-Zhou Lu, Wang Yao, Di Xiao and Shun-Qing Shen. *Intervalley scattering and localization behaviors of spin-valley coupled dirac fermions.* Physical Review Letters, vol. 110, no. 1, page 016806, 2013. (Cited on pages 11, 61 and 70.)

[Lundskog 2014] Anders Lundskog, Chih-Wei Hsu, K Fredrik Karlsson, Supaluck Amloy, Daniel Nilsson, Urban Forsberg, Per Olof Holtz and Erik Janzén. *Direct generation of linearly polarized photon emission with designated orientations from site-controlled InGaN quantum dots.* Light: Science & Applications, vol. 3, no. 1, pages e139–e139, 2014. (Cited on page 32.)

[Lundt 2018] N Lundt, E Cherotchenko, O Iff, X Fan, Y Shen, Pierre Bigenwald, AV Kavokin, Sven Höfling and C Schneider. *The interplay between excitons and trions in a monolayer of MoSe2.* Applied Physics Letters, vol. 112, no. 3, 2018. (Cited on page 18.)

[Luong 2017] Dinh Hoa Luong, Hyun Seok Lee, Guru Prakash Neupane, Shrawan Roy, Ganesh Ghimire, Jin Hee Lee, Quoc An Vu and Young Hee Lee. *Tunneling Photocurrent Assisted by Interlayer Excitons in Staggered van der Waals Hetero-Bilayers.* Advanced Materials, vol. 29, no. 33, page 1701512, 2017. (Cited on pages 15 and 87.)

[Lyons 2019] Thomas P Lyons, Scott Dufferwiel, Matthew Brooks, Freddie Withers, T Taniguchi, Kenji Watanabe, KS Novoselov, Guido Burkard and Alexander I Tartakovskii. *The valley Zeeman effect in inter-and intra-valley trions in monolayer WSe2.* Nature communications, vol. 10, no. 1, page 2330, 2019. (Cited on page 13.)

[Ma 2021] Xiaoli Ma, Shaohua Fu, Jianwei Ding, Meng Liu, Ang Bian, Fang Hong, Jiatao Sun, Xiaoxian Zhang, Xiaohui Yu and Dawei He. *Robust interlayer exciton in WS2/MoSe2 van der Waals heterostructure under high pressure.* Nano Letters, vol. 21, no. 19, pages 8035–8042, 2021. (Cited on pages 15 and 87.)

[Mak 2010] Kin Fai Mak, Changgu Lee, James Hone, Jie Shan and Tony F Heinz. *Atomically thin MoS 2: a new direct-gap semiconductor.* Physical review letters, vol. 105, no. 13, page 136805, 2010. (Cited on page 1.)

[Mak 2013] Kin Fai Mak, Keliang He, Changgu Lee, Gwan Hyoung Lee, James Hone, Tony F Heinz and Jie Shan. *Tightly bound trions in monolayer MoS2.* Nature materials, vol. 12, no. 3, pages 207–211, 2013. (Cited on pages 18, 19 and 56.)

[Malic 2018] Ermin Malic, Malte Selig, Maja Feierabend, Samuel Brem, Dominik Christiansen, Florian Wendler, Andreas Knorr and Gunnar Berghäuser. *Dark excitons in transition metal dichalcogenides.* Physical Review Materials, vol. 2, no. 1, page 014002, 2018. (Cited on page 11.)

[Manca 2017] Marco Manca, Mikhail M Glazov, Cédric Robert, Fabian Cadiz, Takashi Taniguchi, Kenji Watanabe, Emmanuel Courtade, Thierry Amand, Pierre Renucci, Xavier Marie, Gang Wang and Bernhard Urbaszek. *Enabling valley selective exciton scattering in monolayer* WSe_2 *through upconversion.* Nature Communications, vol. 8, no. 1, page 14927, 2017. (Cited on page 62.)

[Manzeli 2017] Sajedeh Manzeli, Dmitry Ovchinnikov, Diego Pasquier, Oleg V Yazyev and Andras Kis. *2D transition metal dichalcogenides.* Nature Reviews Materials, vol. 2, no. 8, pages 1–15, 2017. (Cited on pages 2 and 3.)

[Mao 2018] Lingling Mao, Weijun Ke, Laurent Pedesseau, Yilei Wu, Claudine Katan, Jacky Even, Michael R Wasielewski, Constantinos C Stoumpos and Mercouri G Kanatzidis. *Hybrid Dion–Jacobson 2D lead iodide perovskites.* Journal of the American Chemical Society, vol. 140, no. 10, pages 3775–3783, 2018. (Cited on page 74.)

[Martín-Sánchez 2017] Javier Martín-Sánchez, Rinaldo Trotta, Antonio Mariscal, Rosalía Serna, Giovanni Piredda, Sandra Stroj, Johannes Edlinger, Christian Schimpf, Johannes Aberl, Thomas Lettner, Johannes Wildmann, Huiying Huang, Xueyong Yuan, Dorian Ziss, Julian Stangl and Armando Rastelli. *Strain-tuning of the optical properties of semiconductor nanomaterials by integration onto piezoelectric actuators.* Semiconductor Science and Technology, vol. 33, no. 1, page 013001, 2017. (Cited on page 47.)

[McIntyre 1971] JDE McIntyre and David E Aspnes. *Differential reflection spectroscopy of very thin surface films.* Surface Science, vol. 24, no. 2, pages 417–434, 1971. (Cited on page 25.)

[Merkl 2019] Philipp Merkl, Fabian Mooshammer, Philipp Steinleitner, Anna Girnghuber, K-Q Lin, Philipp Nagler, Johannes Holler, Christian Schüller, John M Lupton, Tobias Korn*et al. Ultrafast transition between exciton phases in van der Waals heterostructures.* Nature materials, vol. 18, no. 7, pages 691–696, 2019. (Cited on page 87.)

[Michail 2023] Antonios Michail, Dimitris Anestopoulos, Nikos Delikoukos, Spyridon Grammatikopoulos, Sotirios A Tsirkas, Nektarios N Lathiotakis, Otakar Frank, Kyriakos Filintoglou, John Parthenios and Konstantinos Papagelis. *Tuning the Photoluminescence and Raman Response of Single-Layer WS2 Crystals Using Biaxial Strain.* The Journal of Physical Chemistry C, vol. 127, no. 7, pages 3506–3515, 2023. (Cited on page 35.)

[Miller 1984] David AB Miller, DS Chemla, TC Damen, AC Gossard, W Wiegmann, TH Wood and CA Burrus. *Band-edge electroabsorption in quantum well structures: The quantum-confined Stark effect.* Physical Review Letters, vol. 53, no. 22, page 2173, 1984. (Cited on page 17.)

[Mitioglu 2018] Anatolie Mitioglu, Jonathan Buhot, MV Ballottin, Sergiu Anghel, Konstantin Sushkevich, Leonid Kulyuk and Peter CM Christianen. *Observation of bright exciton splitting in strained WSe 2 monolayers.* Physical Review B, vol. 98, no. 23, page 235429, 2018. (Cited on pages 33, 57 and 59.)

[Molina-Sanchez 2011] Alejandro Molina-Sanchez and Ludger Wirtz. *Phonons in single-layer and few-layer MoS 2 and WS 2.* Physical Review B, vol. 84, no. 15, page 155413, 2011. (Cited on page 52.)

[Montblanch 2021] Alejandro R-P Montblanch, Dhiren M Kara, Ioannis Paradisanos, Carola M Purser, Matthew SG Feuer, Evgeny M Alexeev, Lucio Stefan, Ying Qin, Mark Blei, Gang Wang*et al. Confinement of long-lived interlayer excitons in WS2/WSe2 heterostructures.* Communications Physics, vol. 4, no. 1, page 119, 2021. (Cited on pages 15 and 87.)

[Mueller 2018] Thomas Mueller and Ermin Malic. *Exciton physics and device application of two-dimensional transition metal dichalcogenide semiconductors.*

npj 2D Materials and Applications, vol. 2, no. 1, page 29, 2018. (Cited on pages 1, 10 and 87.)

[Muir 2022] Jack B Muir, Jesper Levinsen, Stuart K Earl, Mitchell A Conway, Jared H Cole, Matthias Wurdack, Rishabh Mishra, David J Ing, Eliezer Estrecho, Yuerui Lu*et al.* *Interactions between Fermi polarons in monolayer WS2*. Nature Communications, vol. 13, no. 1, page 6164, 2022. (Cited on page 20.)

[Nayak 2017] Pramoda K Nayak, Yevhen Horbatenko, Seongjoon Ahn, Gwangwoo Kim, Jae-Ung Lee, Kyung Yeol Ma, A-Rang Jang, Hyunseob Lim, Dogyeong Kim, Sunmin Ryu*et al.* *Probing evolution of twist-angle-dependent interlayer excitons in MoSe2/WSe2 van der Waals heterostructures*. ACS nano, vol. 11, no. 4, pages 4041–4050, 2017. (Cited on pages 15 and 87.)

[Novoselov 2016] KS Novoselov, o A Mishchenko, o A Carvalho and AH Castro Neto. *2D materials and van der Waals heterostructures*. Science, vol. 353, no. 6298, page aac9439, 2016. (Cited on pages 2 and 87.)

[Ochoa 2013] Héctor Ochoa and Rafael Roldán. *Spin-orbit-mediated spin relaxation in monolayer* MoS_2. Physical Review B, vol. 87, no. 24, page 245421, 2013. (Cited on pages 11, 61 and 70.)

[Okada 2018] Mitsuhiro Okada, Alex Kutana, Yusuke Kureishi, Yu Kobayashi, Yuika Saito, Tetsuki Saito, Kenji Watanabe, Takashi Taniguchi, Sunny Gupta, Yasumitsu Miyata*et al.* *Direct and indirect interlayer excitons in a van der Waals heterostructure of hBN/WS2/MoS2/hBN*. ACS nano, vol. 12, no. 3, pages 2498–2505, 2018. (Cited on pages 15 and 87.)

[Ovesen 2019] Simon Ovesen, Samuel Brem, Christopher Linderälv, Mikael Kuisma, Tobias Korn, Paul Erhart, Malte Selig and Ermin Malic. *Interlayer exciton dynamics in van der Waals heterostructures*. Communications Physics, vol. 2, no. 1, page 23, 2019. (Cited on page 97.)

[Palacios-Berraquero 2017] Carmen Palacios-Berraquero, Dhiren M Kara, Alejandro R-P Montblanch, Matteo Barbone, Pawel Latawiec, Duhee Yoon, Anna K Ott, Marko Loncar, Andrea C Ferrari and Mete Atatüre. *Large-scale quantum-emitter arrays in atomically thin semiconductors*. Nature communications, vol. 8, no. 1, page 15093, 2017. (Cited on page 47.)

[Palummo 2015] Maurizia Palummo, Marco Bernardi and Jeffrey C Grossman. *Exciton radiative lifetimes in two-dimensional transition metal dichalcogenides*. Nano letters, vol. 15, no. 5, pages 2794–2800, 2015. (Cited on page 26.)

[Paradisanos 2020] Ioannis Paradisanos, Shivangi Shree, Antony George, Nadine Leisgang, Cedric Robert, Kenji Watanabe, Takashi Taniguchi, Richard J Warburton, Andrey Turchanin, Xavier Marie*et al.* *Controlling interlayer* *excitons in MoS2 layers grown by chemical vapor deposition.* Nature communications, vol. 11, no. 1, page 2391, 2020. (Cited on page 15.)

[Peimyoo 2021] Namphung Peimyoo, Thorsten Deilmann, Freddie Withers, Janire Escolar, Darren Nutting, Takashi Taniguchi, Kenji Watanabe, Alireza Taghizadeh, Monica Felicia Craciun, Kristian Sommer Thygesen*et al.* *Electrical tuning of optically active interlayer excitons in bilayer MoS2.* Nature Nanotechnology, vol. 16, no. 8, pages 888–893, 2021. (Cited on pages 16, 17 and 87.)

[Pelant 2012] Ivan Pelant and Jan Valenta. Luminescence spectroscopy of semiconductors. OUP Oxford, 2012. (Cited on pages 26, 28 and 31.)

[Perea-Causin 2022] Raul Perea-Causin, Daniel Erkensten, Jamie M Fitzgerald, Joshua JP Thompson, Roberto Rosati, Samuel Brem and Ermin Malic. *Exciton optics, dynamics, and transport in atomically thin semiconductors.* APL Materials, vol. 10, no. 10, 2022. (Cited on pages 10 and 87.)

[Peter 2010] YU Peter and Manuel Cardona. Fundamentals of semiconductors: physics and materials properties. Springer Science & Business Media, 2010. (Cited on pages 7 and 33.)

[Plechinger 2016] Gerd Plechinger, Philipp Nagler, Ashish Arora, Robert Schmidt, Alexey Chernikov, Andrés Granados Del Águila, Peter CM Christianen, Rudolf Bratschitsch, Christian Schüller and Tobias Korn. *Trion fine structure and coupled spin–valley dynamics in monolayer tungsten disulfide.* Nature Communications, vol. 7, no. 1, page 12715, 2016. (Cited on pages 11, 13, 61 and 69.)

[Posmyk 2024a] Katarzyna Posmyk, Mateusz Dyksik, Alessandro Surrente, Duncan K Maude, Natalia Zawadzka, Adam Babiński, Maciej R Molas, Watcharaphol Paritmongkol, Mirosław Mączka, William A Tisdale*et al.* *Exciton Fine Structure in 2D Perovskites: The Out-of-Plane Excitonic State.* Advanced Optical Materials, vol. 12, no. 8, page 2300877, 2024. (Cited on pages 32 and 76.)

[Posmyk 2024b] Katarzyna Posmyk, Natalia Zawadzka, Łucja Kipczak, Mateusz Dyksik, Alessandro Surrente, Duncan K Maude, Tomasz Kazimierczuk, Adam Babinski, Maciej R Molas, Wakul Bumrungsan*et al.* *Bright Excitonic Fine Structure in Metal-Halide Perovskites: From Two-Dimensional to Bulk.* Journal of the American Chemical Society, 2024. (Cited on pages 32, 57 and 76.)

[Qiu 2015] Diana Y Qiu, Ting Cao and Steven G Louie. *Nonanalyticity, valley quantum phases, and lightlike exciton dispersion in monolayer transition metal dichalcogenides: Theory and first-principles calculations.* Physical review letters, vol. 115, no. 17, page 176801, 2015. (Cited on pages 11 and 102.)

[Qiu 2021] Dong Qiu, Chuanhui Gong, SiShuang Wang, Miao Zhang, Chao Yang, Xianfu Wang and Jie Xiong. *Recent advances in 2D superconductors.* Advanced Materials, vol. 33, no. 18, page 2006124, 2021. (Cited on page 1.)

[Regan 2020] Emma C Regan, Danqing Wang, Chenhao Jin, M Iqbal Bakti Utama, Beini Gao, Xin Wei, Sihan Zhao, Wenyu Zhao, Zuocheng Zhang, Kentaro Yumigeta*et al.* *Mott and generalized Wigner crystal states in WSe2/WS2 moiré superlattices.* Nature, vol. 579, no. 7799, pages 359–363, 2020. (Cited on page 88.)

[Rice 2013] Caitlin Rice, RJ Young, R Zan, U Bangert, Daniel Wolverson, T Georgiou, R Jalil and KS Novoselov. *Raman-scattering measurements and first-principles calculations of strain-induced phonon shifts in monolayer MoS 2.* Physical Review B, vol. 87, no. 8, page 081307, 2013. (Cited on pages 47 and 52.)

[Rivera 2015] Pasqual Rivera, John R Schaibley, Aaron M Jones, Jason S Ross, Sanfeng Wu, Grant Aivazian, Philip Klement, Kyle Seyler, Genevieve Clark, Nirmal J Ghimire*et al.* *Observation of long-lived interlayer excitons in monolayer MoSe2–WSe2 heterostructures.* Nature communications, vol. 6, no. 1, page 6242, 2015. (Cited on pages 80 and 87.)

[Rivera 2018] Pasqual Rivera, Hongyi Yu, Kyle L Seyler, Nathan P Wilson, Wang Yao and Xiaodong Xu. *Interlayer valley excitons in heterobilayers of transition metal dichalcogenides.* Nature nanotechnology, vol. 13, no. 11, pages 1004–1015, 2018. (Cited on page 87.)

[Robert 2016] Cédric Robert, David Lagarde, Fabian Cadiz, Gang Wang, Benjamin Lassagne, Thierry Amand, Andrea Balocchi, Pierre Renucci, Seffattin Tongay, Bernhard Urbaszek*et al.* *Exciton radiative lifetime in transition metal dichalcogenide monolayers.* Physical review B, vol. 93, no. 20, page 205423, 2016. (Cited on page 26.)

[Robert 2018] Cédric Robert, MA Semina, Fabian Cadiz, Marco Manca, Emmanuel Courtade, T Taniguchi, K Watanabe, H Cai, Sefaattin Tongay, Benjamin Lassagne*et al.* *Optical spectroscopy of excited exciton states in MoS 2 monolayers in van der Waals heterostructures.* Physical Review Materials, vol. 2, no. 1, page 011001, 2018. (Cited on pages 25 and 57.)

[Robert 2020] Cédric Robert, Bo Han, Piotr Kapuscinski, Alex Delhomme, Clément Faugeras, Thierry Amand, Maciej R Molas, Miroslav Bartos, Kenji Watanabe, Takashi Taniguchi*et al.* *Measurement of the spin-forbidden dark excitons in MoS2 and MoSe2 monolayers.* Nature communications, vol. 11, no. 1, page 4037, 2020. (Cited on page 11.)

[Rojas-Lopez 2021] Rafael R Rojas-Lopez, Juliana C Brant, Maíra SO Ramos, Túlio HLG Castro, Marcos HD Guimarães, Bernardo RA Neves and

Paulo SS Guimarães. *Photoluminescence and charge transfer in the prototypical 2D/3D semiconductor heterostructure MoS2/GaAs.* Applied Physics Letters, vol. 119, no. 23, 2021. (Cited on page 56.)

[Ross 2013] Jason S Ross, Sanfeng Wu, Hongyi Yu, Nirmal J Ghimire, Aaron M Jones, Grant Aivazian, Jiaqiang Yan, David G Mandrus, Di Xiao, Wang Yao*et al.* *Electrical control of neutral and charged excitons in a monolayer semiconductor.* Nature communications, vol. 4, no. 1, page 1474, 2013. (Cited on page 15.)

[Rytova 2018] Natalia S Rytova. *Screened potential of a point charge in a thin film.* arXiv preprint arXiv:1806.00976, 2018. (Cited on page 10.)

[Samarth 2017] Nitin Samarth. *Magnetism in flatland.* Nature, vol. 546, no. 7657, pages 216–217, 2017. (Cited on page 1.)

[Schaibley 2016] John R Schaibley, Hongyi Yu, Genevieve Clark, Pasqual Rivera, Jason S Ross, Kyle L Seyler, Wang Yao and Xiaodong Xu. *Valleytronics in 2D materials.* Nature Reviews Materials, vol. 1, no. 11, pages 1–15, 2016. (Cited on page 11.)

[Schmidt 2016a] H Schmidt, I Yudhistira, L Chu, AH Castro Neto, B Özyilmaz, S Adam and G Eda. *Quantum transport and observation of Dyakonov-Perel spin-orbit scattering in monolayer* MoS_2. Physical Review Letters, vol. 116, no. 4, page 046803, 2016. (Cited on pages 11, 61 and 70.)

[Schmidt 2016b] Robert Schmidt, Gunnar Berghauser, Robert Schneider, Malte Selig, Philipp Tonndorf, Ermin Malic, Andreas Knorr, Steffen Michaelis de Vasconcellos and Rudolf Bratschitsch. *Ultrafast coulomb-induced intervalley coupling in atomically thin* WS_2. Nano Letters, vol. 16, no. 5, pages 2945–2950, 2016. (Cited on pages 11, 61 and 69.)

[Sell 2022] JC Sell, JR Vannucci, DG Suárez-Forero, B Cao, DW Session, H-J Chuang, KM McCreary, MR Rosenberger, BT Jonker, S Mittal*et al.* *Magneto-optical measurements of the negatively charged 2 s exciton in WSe 2.* Physical Review B, vol. 106, no. 8, page L081409, 2022. (Cited on page 107.)

[Shepard 2017] Gabriella D Shepard, Jenny V Ardelean, Obafunso A Ajayi, Daniel Rhodes, Xiaoyang Zhu, James C Hone and Stefan Strauf. *Trion-species-resolved quantum beats in MoSe2.* ACS nano, vol. 11, no. 11, pages 11550–11558, 2017. (Cited on pages 15 and 43.)

[Shimazaki 2020] Yuya Shimazaki, Ido Schwartz, Kenji Watanabe, Takashi Taniguchi, Martin Kroner and Ataç Imamoğlu. *Strongly correlated electrons and hybrid excitons in a moiré heterostructure.* Nature, vol. 580, no. 7804, pages 472–477, 2020. (Cited on pages 17 and 87.)

[Shin 2024] Heechang Shin, Ajit Kumar Katiyar, Anh Tuan Hoang, Seok Min Yun, Beom Jin Kim, Gwanjin Lee, Youngjae Kim, JaeDong Lee, Hyunmin Kim and Jong-Hyun Ahn. *Nonconventional Strain Engineering for Uniform Biaxial Tensile Strain in MoS2 Thin Film Transistors.* ACS nano, vol. 18, no. 5, pages 4414–4423, 2024. (Cited on page 35.)

[Sidler 2017] Meinrad Sidler, Patrick Back, Ovidiu Cotlet, Ajit Srivastava, Thomas Fink, Martin Kroner, Eugene Demler and Atac Imamoglu. *Fermi polaron-polaritons in charge-tunable atomically thin semiconductors.* Nature Physics, vol. 13, no. 3, pages 255–261, 2017. (Cited on pages 20, 59, 92 and 94.)

[Sigl 2020] Lukas Sigl, Florian Sigger, Fabian Kronowetter, Jonas Kiemle, Julian Klein, Kenji Watanabe, Takashi Taniguchi, Jonathan J Finley, Ursula Wurstbauer and Alexander W Holleitner. *Signatures of a degenerate many-body state of interlayer excitons in a van der Waals heterostack.* Physical Review Research, vol. 2, no. 4, page 042044, 2020. (Cited on page 88.)

[Singh 2016] Akshay Singh, Kha Tran, Mirco Kolarczik, Joe Seifert, Yiping Wang, Kai Hao, Dennis Pleskot, Nathaniel M Gabor, Sophia Helmrich, Nina Owschimikow, Ulrike Woggon and Xiaoqin Li. *Long-lived valley polarization of intravalley trions in monolayer* WSe_2. Physical Review Letters, vol. 117, no. 25, page 257402, 2016. (Cited on page 70.)

[Singh 2023] Simrjit Singh, Weiyi Gong, Christopher E Stevens, Jin Hou, Aditya Singh, Huiqin Zhang, Surendra B Anantharaman, Aditya D Mohite, Joshua R Hendrickson, Qimin Yan and Deep Jariwala. *Valley-Polarized Interlayer Excitons in 2D Chalcogenide–Halide Perovskite–van der Waals Heterostructures.* ACS Nano, vol. 17, no. 8, pages 7487–7497, 2023. (Cited on page 63.)

[Slobodkin 2020] Yevgeny Slobodkin, Yotam Mazuz-Harpaz, Sivan Refaely-Abramson, Snir Gazit, Hadar Steinberg and Ronen Rapaport. *Quantum phase transitions of trilayer excitons in atomically thin heterostructures.* Physical Review Letters, vol. 125, no. 25, page 255301, 2020. (Cited on pages 88 and 89.)

[Smith 2018] Matthew D Smith and Hemamala I Karunadasa. *White-light emission from layered halide perovskites.* Accounts of chemical research, vol. 51, no. 3, pages 619–627, 2018. (Cited on page 74.)

[Sokolowski 2023] Nikodem Sokolowski, Swaroop Palai, Mateusz Dyksik, Katarzyna Posmyk, Michał Baranowski, Alessandro Surrente, Duncan Maude, Felix Carrascoso, Onur Cakiroglu, Estrella Sanchez*et al. Twist-angle dependent dehybridization of momentum-indirect excitons in MoSe2/MoS2 heterostructures.* 2D Materials, vol. 10, no. 3, page 034003, 2023. (Cited on pages 15 and 87.)

[Song 2013] Yang Song and Hanan Dery. *Transport theory of monolayer transition-metal dichalcogenides through symmetry.* Physical Review Letters, vol. 111, no. 2, page 026601, 2013. (Cited on pages 11, 61 and 70.)

[Splendiani 2010] Andrea Splendiani, Liang Sun, Yuanbo Zhang, Tianshu Li, Jonghwan Kim, Chi-Yung Chim, Giulia Galli and Feng Wang. *Emerging photoluminescence in monolayer MoS2.* Nano letters, vol. 10, no. 4, pages 1271–1275, 2010. (Cited on pages 5, 6 and 93.)

[Stier 2016] Andreas V Stier, Kathleen M McCreary, Berend T Jonker, Junichiro Kono and Scott A Crooker. *Exciton diamagnetic shifts and valley Zeeman effects in monolayer* WS_2 *and* MoS_2 *to 65 Tesla.* Nature Communications, vol. 7, no. 1, page 10643, 2016. (Cited on pages 1, 6, 7, 11, 32 and 61.)

[Stoumpos 2016] Constantinos C Stoumpos, Duyen H Cao, Daniel J Clark, Joshua Young, James M Rondinelli, Joon I Jang, Joseph T Hupp and Mercouri G Kanatzidis. *Ruddlesden–Popper hybrid lead iodide perovskite 2D homologous semiconductors.* Chemistry of Materials, vol. 28, no. 8, pages 2852–2867, 2016. (Cited on page 62.)

[Straus 2018] Daniel B Straus and Cherie R Kagan. *Electrons, excitons, and phonons in two-dimensional hybrid perovskites: connecting structural, optical, and electronic properties.* The Journal of Physical Chemistry Letters, vol. 9, no. 6, pages 1434–1447, 2018. (Cited on pages 1 and 74.)

[Sung 2020] Jiho Sung, You Zhou, Giovanni Scuri, Viktor Zólyomi, Trond I Andersen, Hyobin Yoo, Dominik S Wild, Andrew Y Joe, Ryan J Gelly, Hoseok Heo*et al.* *Broken mirror symmetry in excitonic response of reconstructed domains in twisted MoSe2/MoSe2 bilayers.* Nature nanotechnology, vol. 15, no. 9, pages 750–754, 2020. (Cited on pages 16, 17, 18, 87, 92 and 107.)

[Tagarelli 2023] Fedele Tagarelli, Edoardo Lopriore, Daniel Erkensten, Raül Perea-Causín, Samuel Brem, Joakim Hagel, Zhe Sun, Gabriele Pasquale, Kenji Watanabe, Takashi Taniguchi*et al.* *Electrical control of hybrid exciton transport in a van der Waals heterostructure.* Nature Photonics, vol. 17, no. 7, pages 615–621, 2023. (Cited on pages 17 and 87.)

[Takeoka 2006] Yuko Takeoka, Keisuke Asai, Masahiro Rikukawa and Kohei Sanui. *Systematic studies on chain lengths, halide species, and well thicknesses for lead halide layered perovskite thin films.* Bulletin of the Chemical Society of Japan, vol. 79, no. 10, pages 1607–1613, 2006. (Cited on page 74.)

[Tan 2019] Qing-Hai Tan, Shu-Liang Ren, Tao Shen, Xue-Lu Liu, Wei Shi, Yu-Jia Sun, Hui-Xiong Deng, Ping-Heng Tan and Jun Zhang. *Unraveling the defect emission and exciton–lattice interaction in bilayer WS2.* The Journal of Physical Chemistry C, vol. 123, no. 7, pages 4433–4440, 2019. (Cited on pages 17 and 87.)

[Tang 2020] Yanhao Tang, Lizhong Li, Tingxin Li, Yang Xu, Song Liu, Katayun Barmak, Kenji Watanabe, Takashi Taniguchi, Allan H MacDonald, Jie Shan*et al.* *Simulation of Hubbard model physics in WSe2/WS2 moiré superlattices.* Nature, vol. 579, no. 7799, pages 353–358, 2020. (Cited on page 88.)

[Tang 2021] Ming-Chun Tang, Siyuan Zhang, Timothy J Magnanelli, Nhan V Nguyen, Edwin J Heilweil, Thomas D Anthopoulos and Christina A Hacker. *Unraveling the compositional heterogeneity and carrier dynamics of alkali cation doped 3D/2D perovskites with improved stability.* Materials Advances, vol. 2, no. 4, pages 1253–1262, 2021. (Cited on page 75.)

[Tanoh 2020] Arelo OA Tanoh, Nicolas Gauriot, Geraud Delport, James Xiao, Raj Pandya, Jooyoung Sung, Jesse Allardice, Zhaojun Li, Cyan A Williams, Alan Baldwin*et al.* *Directed energy transfer from monolayer WS2 to near-infrared emitting PbS–CdS quantum dots.* ACS nano, vol. 14, no. 11, pages 15374–15384, 2020. (Cited on page 32.)

[Tebyetekerwa 2021] Mike Tebyetekerwa, Jian Zhang, Sandra Elizabeth Saji, Ary Anggara Wibowo, Sharidya Rahman, Thien N Truong, Yuerui Lu, Zongyou Yin, Daniel Macdonald and Hieu T Nguyen. *Twist-driven wide freedom of indirect interlayer exciton emission in MoS2/WS2 heterobilayers.* Cell Reports Physical Science, vol. 2, no. 8, 2021. (Cited on pages 15 and 87.)

[Tempelaar 2019] Roel Tempelaar and Timothy C Berkelbach. *Many-body simulation of two-dimensional electronic spectroscopy of excitons and trions in monolayer transition metal dichalcogenides.* Nature communications, vol. 10, no. 1, page 3419, 2019. (Cited on page 14.)

[Thomas 2021] SE Thomas, M Billard, N Coste, SC Wein, Priya, H Ollivier, Olivier Krebs, L Tazaïrt, A Harouri, A Lemaitre*et al.* *Bright polarized single-photon source based on a linear dipole.* Physical review letters, vol. 126, no. 23, page 233601, 2021. (Cited on page 32.)

[Toh 2017] Rou Jun Toh, Zdeněk Sofer, Jan Luxa, David Sedmidubskỳ and Martin Pumera. *3R phase of MoS 2 and WS 2 outperforms the corresponding 2H phase for hydrogen evolution.* Chemical Communications, vol. 53, no. 21, pages 3054–3057, 2017. (Cited on page 2.)

[Toporski 2018] Jan Toporski, Thomas Dieing and Olaf Hollricher. Confocal raman microscopy, volume 66. Springer, 2018. (Cited on page 33.)

[Tornatzky 2018] Hans Tornatzky, Anne-Marie Kaulitz and Janina Maultzsch. *Resonance profiles of valley polarization in single-layer* MoS_2 *and* $MoSe_2$. Physical Review Letters, vol. 121, no. 16, page 167401, 2018. (Cited on page 11.)

[Tran 2019] Kha Tran, Galan Moody, Fengcheng Wu, Xiaobo Lu, Junho Choi, Kyounghwan Kim, Amritesh Rai, Daniel A Sanchez, Jiamin Quan, Akshay

Singh*et al.* *Evidence for moiré excitons in van der Waals heterostructures.* Nature, vol. 567, no. 7746, pages 71–75, 2019. (Cited on pages 15 and 87.)

[Tsai 2016] Hsinhan Tsai, Wanyi Nie, Jean-Christophe Blancon, Constantinos C Stoumpos, Reza Asadpour, Boris Harutyunyan, Amanda J Neukirch, Rafael Verduzco, Jared J Crochet, Sergei Tretiak*et al.* *High-efficiency two-dimensional Ruddlesden–Popper perovskite solar cells.* Nature, vol. 536, no. 7616, pages 312–316, 2016. (Cited on page 74.)

[Tutuncuoglu 2015] Gozde Tutuncuoglu, M de La Mata, D Deiana, Heidi Potts, Federico Matteini, Jordi Arbiol and A Fontcuberta i Morral. *Towards defect-free 1-D GaAs/AlGaAs heterostructures based on GaAs nanomembranes.* Nanoscale, vol. 7, no. 46, pages 19453–19460, 2015. (Cited on page 48.)

[Ugeda 2014] Miguel M Ugeda, Aaron J Bradley, Su-Fei Shi, Felipe H Da Jornada, Yi Zhang, Diana Y Qiu, Wei Ruan, Sung-Kwan Mo, Zahid Hussain, Zhi-Xun Shen, Feng Wang, Steven G Louie and Michael F Crommie. *Giant bandgap renormalization and excitonic effects in a monolayer transition metal dichalcogenide semiconductor.* Nature Materials, vol. 13, no. 12, pages 1091–1095, 2014. (Cited on pages 1, 7 and 61.)

[Vaclavkova 2018] D Vaclavkova, J Wyzula, K Nogajewski, M Bartos, AO Slobodeniuk, C Faugeras, M Potemski and MR Molas. *Singlet and triplet trions in WS2 monolayer encapsulated in hexagonal boron nitride.* Nanotechnology, vol. 29, no. 32, page 325705, 2018. (Cited on page 13.)

[Van Der Zande 2014] Arend M Van Der Zande, Jens Kunstmann, Alexey Chernikov, Daniel A Chenet, YuMeng You, XiaoXiao Zhang, Pinshane Y Huang, Timothy C Berkelbach, Lei Wang, Fan Zhang*et al.* *Tailoring the electronic structure in bilayer molybdenum disulfide via interlayer twist.* Nano letters, vol. 14, no. 7, pages 3869–3875, 2014. (Cited on page 87.)

[Villafañe 2023] Viviana Villafañe, Malte Kremser, Ruven Hübner, Marko M Petrić, Nathan P Wilson, Andreas V Stier, Kai Müller, Matthias Florian, Alexander Steinhoff and Jonathan J Finley. *Twist-Dependent Intra-and Interlayer Excitons in Moiré MoSe 2 Homobilayers.* Physical Review Letters, vol. 130, no. 2, page 026901, 2023. (Cited on pages 87, 92 and 107.)

[Wagner 2020] Koloman Wagner, Edith Wietek, Jonas D Ziegler, Marina A Semina, Takashi Taniguchi, Kenji Watanabe, Jonas Zipfel, Mikhail M Glazov and Alexey Chernikov. *Autoionization and dressing of excited excitons by free carriers in monolayer WSe 2.* Physical review letters, vol. 125, no. 26, page 267401, 2020. (Cited on page 20.)

[Wang 2014] L Wang and MW Wu. *Electron spin relaxation due to D'yakonov-Perel'and Elliot-Yafet mechanisms in monolayer* MoS_2*: role of intravalley* *and intervalley processes.* Physical Review B, vol. 89, no. 11, page 115302, 2014. (Cited on pages 11, 61 and 70.)

[Wang 2015a] Gang Wang, Xavier Marie, I Gerber, Thierry Amand, Delphine Lagarde, Louis Bouet, M Vidal, Andrea Balocchi and Bernhard Urbaszek. *Giant enhancement of the optical second-harmonic emission of WSe 2 monolayers by laser excitation at exciton resonances.* Physical review letters, vol. 114, no. 9, page 097403, 2015. (Cited on page 33.)

[Wang 2015b] Gang Wang, Cédric Robert, Aslihan Suslu, Bin Chen, Sijie Yang, Sarah Alamdari, Iann C Gerber, Thierry Amand, Xavier Marie, Sefaattin Tongay and Bernhard Urbaszek. *Spin-orbit engineering in transition metal dichalcogenide alloy monolayers.* Nature Communications, vol. 6, no. 1, page 10110, 2015. (Cited on pages 70 and 72.)

[Wang 2015c] Yu-Ting Wang, Chih-Wei Luo, Atsushi Yabushita, Kaung-Hsiung Wu, Takayoshi Kobayashi, Chang-Hsiao Chen and Lain-Jong Li. *Ultrafast multi-level logic gates with spin-valley coupled polarization anisotropy in monolayer* MoS_2. Scientific Reports, vol. 5, no. 1, page 8289, 2015. (Cited on pages 11, 61 and 69.)

[Wang 2017a] Gang Wang, Cédric Robert, Mikhail M Glazov, Fabian Cadiz, Emmanuel Courtade, Thierry Amand, Delphine Lagarde, Takashi Taniguchi, Kenji Watanabe, Bernhard Urbaszek*et al. In-plane propagation of light in transition metal dichalcogenide monolayers: optical selection rules.* Physical review letters, vol. 119, no. 4, page 047401, 2017. (Cited on page 11.)

[Wang 2017b] Yong Wang, Zhan Wang, Wang Yao, Gui-Bin Liu and Hongyi Yu. *Interlayer coupling in commensurate and incommensurate bilayer structures of transition-metal dichalcogenides.* Physical Review B, vol. 95, no. 11, page 115429, 2017. (Cited on page 102.)

[Wang 2018a] Gang Wang, Alexey Chernikov, Mikhail M Glazov, Tony F Heinz, Xavier Marie, Thierry Amand and Bernhard Urbaszek. *Colloquium: Excitons in atomically thin transition metal dichalcogenides.* Reviews of Modern Physics, vol. 90, no. 2, page 021001, 2018. (Cited on pages 1, 7, 10, 61 and 87.)

[Wang 2018b] Zefang Wang, Yi-Hsin Chiu, Kevin Honz, Kin Fai Mak and Jie Shan. *Electrical tuning of interlayer exciton gases in WSe2 bilayers.* Nano letters, vol. 18, no. 1, pages 137–143, 2018. (Cited on pages 17 and 87.)

[Wang 2019] Zefang Wang, Daniel A Rhodes, Kenji Watanabe, Takashi Taniguchi, James C Hone, Jie Shan and Kin Fai Mak. *Evidence of high-temperature exciton condensation in two-dimensional atomic double layers.* Nature, vol. 574, no. 7776, pages 76–80, 2019. (Cited on page 88.)

[Wang 2020a] Qixing Wang, Qi Zhang, Xin Luo, Junyong Wang, Rui Zhu, Qijie Liang, Lei Zhang, Justin Zhou Yong, Calvin Pei Yu Wong, Goki Eda, Juergen H Smet and Andrew T Wee. *Optoelectronic properties of a van der Waals WS_2 monolayer/2D perovskite vertical heterostructure.* ACS Applied Materials & Interfaces, vol. 12, no. 40, pages 45235–45242, 2020. (Cited on page 63.)

[Wang 2020b] Tianmeng Wang, Zhipeng Li, Yunmei Li, Zhengguang Lu, Shengnan Miao, Zhen Lian, Yuze Meng, Mark Blei, Takashi Taniguchi, Kenji Watanabe, Sefaattin Tongay, Dmitry Smirnov, Chuanwei Zhang and Su-Fei Shi. *Giant valley-polarized Rydberg excitons in monolayer WSe_2 revealed by magneto-photocurrent spectroscopy.* Nano Letters, vol. 20, no. 10, pages 7635–7641, 2020. (Cited on page 65.)

[Wang 2021a] Haizhen Wang, Jiaqi Ma and Dehui Li. *Two-dimensional hybrid perovskite-based van der Waals heterostructures.* The Journal of Physical Chemistry Letters, vol. 12, no. 34, pages 8178–8187, 2021. (Cited on page 63.)

[Wang 2021b] Qixing Wang, Julian Maisch, Fangdong Tang, Dong Zhao, Sheng Yang, Raphael Joos, Simone Luca Portalupi, Peter Michler and Jurgen H Smet. *Highly polarized single photons from strain-induced quasi-1D localized excitons in WSe2.* Nano letters, vol. 21, no. 17, pages 7175–7182, 2021. (Cited on page 47.)

[Wang 2021c] Qixing Wang and Andrew TS Wee. *Upconversion photovoltaic effect of WS2/2D perovskite heterostructures by two-photon absorption.* ACS nano, vol. 15, no. 6, pages 10437–10443, 2021. (Cited on page 63.)

[Wannier 1937] Gregory H Wannier. *The structure of electronic excitation levels in insulating crystals.* Physical Review, vol. 52, no. 3, page 191, 1937. (Cited on page 7.)

[Weber 2003] Tino Weber, Jens Herbig, Michael Mark, Hanns-Christoph Nagerl and Rudolf Grimm. *Bose-Einstein condensation of cesium.* Science, vol. 299, no. 5604, pages 232–235, 2003. (Cited on page 88.)

[Wilson 2017] Neil R Wilson, Paul V Nguyen, Kyle Seyler, Pasqual Rivera, Alexander J Marsden, Zachary PL Laker, Gabriel C Constantinescu, Viktor Kandyba, Alexei Barinov, Nicholas DM Hine*et al. Determination of band offsets, hybridization, and exciton binding in 2D semiconductor heterostructures.* Science advances, vol. 3, no. 2, page e1601832, 2017. (Cited on page 15.)

[Wu 2017] Fengcheng Wu, Timothy Lovorn and Allan H MacDonald. *Topological exciton bands in moiré heterojunctions.* Physical review letters, vol. 118, no. 14, page 147401, 2017. (Cited on page 88.)

[Wu 2019] Lingling Wu, Yuzhong Chen, Hongzhi Zhou and Haiming Zhu. *Ultrafast energy transfer of both bright and dark excitons in 2D van der Waals heterostructures beyond dipolar coupling.* ACS Nano, vol. 13, no. 2, pages 2341–2348, 2019. (Cited on page 77.)

[Xiao 2012] Di Xiao, Gui-Bin Liu, Wanxiang Feng, Xiaodong Xu and Wang Yao. *Coupled spin and valley physics in monolayers of* MoS_2 *and other group-VI dichalcogenides.* Physical Review Letters, vol. 108, no. 19, page 196802, 2012. (Cited on pages 1, 6, 7, 10, 11, 32, 61, 69 and 87.)

[Xie 2023] Yongzhi Xie, Yuchen Gao, Fengyu Chen, Yunkun Wang, Jun Mao, Qinyun Liu, Saisai Chu, Hong Yang, Yu Ye, Qihuang Gong*et al. Bright and dark quadrupolar excitons in the WSe 2/MoSe 2/WSe 2 heterotrilayer.* Physical Review Letters, vol. 131, no. 18, page 186901, 2023. (Cited on pages 89 and 98.)

[Xiong 2023] Richen Xiong, Jacob H Nie, Samuel L Brantly, Patrick Hays, Renee Sailus, Kenji Watanabe, Takashi Taniguchi, Sefaattin Tongay and Chenhao Jin. *Correlated insulator of excitons in WSe2/WS2 moiré superlattices.* Science, vol. 380, no. 6647, pages 860–864, 2023. (Cited on page 88.)

[Xu 2014] Xiaodong Xu, Wang Yao, Di Xiao and Tony F Heinz. *Spin and pseudospins in layered transition metal dichalcogenides.* Nature Physics, vol. 10, no. 5, pages 343–350, 2014. (Cited on pages 1, 6, 7, 11, 32 and 61.)

[Xu 2020] Yang Xu, Song Liu, Daniel A Rhodes, Kenji Watanabe, Takashi Taniguchi, James Hone, Veit Elser, Kin Fai Mak and Jie Shan. *Correlated insulating states at fractional fillings of moiré superlattices.* Nature, vol. 587, no. 7833, pages 214–218, 2020. (Cited on page 88.)

[Yan 2015] Tengfei Yan, Xiaofen Qiao, Pingheng Tan and Xinhui Zhang. *Valley depolarization in monolayer* WSe_2. Scientific Reports, vol. 5, no. 1, page 15625, 2015. (Cited on pages 11, 61 and 69.)

[Yan 2019] Wei Yan, Lan Meng, Zhaoshun Meng, Yakui Weng, Lulu Kang and Xing-ao Li. *Probing angle-dependent interlayer coupling in twisted bilayer WS2.* The Journal of Physical Chemistry C, vol. 123, no. 50, pages 30684–30688, 2019. (Cited on pages 17 and 87.)

[Yang 1991] XL Yang, SH Guo, FT Chan, KW Wong and WY Ching. *Analytic solution of a two-dimensional hydrogen atom. I. Nonrelativistic theory.* Physical Review A, vol. 43, no. 3, page 1186, 1991. (Cited on page 9.)

[Yang 2019] Arky Yang, Jean-Christophe Blancon, Wei Jiang, Hao Zhang, Joeson Wong, Ellen Yan, Yi-Rung Lin, Jared Crochet, Mercouri G Kanatzidis, Deep Jariwala, Tony Low, Adhita D Mohite and Harry A Atwater. *Giant enhancement of photoluminescence emission in* WS_2*-two-dimensional* *perovskite heterostructures.* Nano Letters, vol. 19, no. 8, pages 4852–4860, 2019. (Cited on page 63.)

[Yao 2008] Wang Yao, Di Xiao and Qian Niu. *Valley-dependent optoelectronics from inversion symmetry breaking.* Physical Review B, vol. 77, no. 23, page 235406, 2008. (Cited on pages 1, 6, 7, 11, 32 and 61.)

[Yao 2022] Wendian Yao, Dong Yang, Yingying Chen, Junchao Hu, Junze Li and Dehui Li. *Layer-number engineered momentum-indirect interlayer excitons with large spectral tunability.* Nano Letters, vol. 22, no. 17, pages 7230–7237, 2022. (Cited on pages 63, 76 and 80.)

[Ye 2018a] Jialiang Ye, Tengfei Yan, Binghui Niu, Ying Li and Xinhui Zhang. *Nonlinear dynamics of trions under strong optical excitation in monolayer MoSe2.* Scientific reports, vol. 8, no. 1, page 2389, 2018. (Cited on page 15.)

[Ye 2018b] Ziliang Ye, Lutz Waldecker, Eric Yue Ma, Daniel Rhodes, Abhinandan Antony, Bumho Kim, Xiao-Xiao Zhang, Minda Deng, Yuxuan Jiang, Zhengguang Lu, Dmitry Smirnov, Kenji Watanabe, Takashi Taniguchi, James Hone and Tony F Heinz. *Efficient generation of neutral and charged biexcitons in encapsulated WSe2 monolayers.* Nature Communications, vol. 9, no. 1, page 3718, 2018. (Cited on pages 13 and 64.)

[Yu 2014a] Hongyi Yu, Gui-Bin Liu, Pu Gong, Xiaodong Xu and Wang Yao. *Dirac cones and Dirac saddle points of bright excitons in monolayer transition metal dichalcogenides.* Nature Communications, vol. 5, no. 1, page 3876, 2014. (Cited on pages 11, 61, 69 and 100.)

[Yu 2014b] Tao Yu and MW Wu. *Valley depolarization due to intervalley and intravalley electron-hole exchange interactions in monolayer* MoS_2. Physical Review B, vol. 89, no. 20, page 205303, 2014. (Cited on pages 11, 61 and 69.)

[Yu 2015] Hongyi Yu, Xiaodong Cui, Xiaodong Xu and Wang Yao. *Valley excitons in two-dimensional semiconductors.* National Science Review, vol. 2, no. 1, pages 57–70, 2015. (Cited on pages 1, 6, 7, 11, 32, 33, 57 and 61.)

[Yu 2017] Hongyi Yu, Gui-Bin Liu, Jianju Tang, Xiaodong Xu and Wang Yao. *Moiré excitons: From programmable quantum emitter arrays to spin-orbit–coupled artificial lattices.* Science advances, vol. 3, no. 11, page e1701696, 2017. (Cited on page 88.)

[Yu 2018] Hongyi Yu, Gui-Bin Liu and Wang Yao. *Brightened spin-triplet interlayer excitons and optical selection rules in van der Waals heterobilayers.* 2D Materials, vol. 5, no. 3, page 035021, 2018. (Cited on page 101.)

[Yu 2020] Juan Yu, Xiaofei Kuang, Jiahong Zhong, Lingkai Cao, Cheng Zeng, Junnan Ding, Chunxiao Cong, Shenghao Wang, Pengfei Dai, Xiaofei Yue*et al.*

Observation of double indirect interlayer exciton in WSe 2/WS 2 heterostructure. Optics express, vol. 28, no. 9, pages 13260–13268, 2020. (Cited on pages 15 and 87.)

[Yu 2023] Leo Yu, Kateryna Pistunova, Jenny Hu, Kenji Watanabe, Takashi Taniguchi and Tony F Heinz. *Observation of quadrupolar and dipolar excitons in a semiconductor heterotrilayer.* Nature materials, vol. 22, no. 12, pages 1485–1491, 2023. (Cited on pages 89 and 98.)

[Yuan 2020] Long Yuan, Biyuan Zheng, Jens Kunstmann, Thomas Brumme, Agnieszka Beata Kuc, Chao Ma, Shibin Deng, Daria Blach, Anlian Pan and Libai Huang. *Twist-angle-dependent interlayer exciton diffusion in WS2–WSe2 heterobilayers.* Nature materials, vol. 19, no. 6, pages 617–623, 2020. (Cited on pages 15 and 87.)

[Zannoni 1999] Alberto Zannoni. *On the quantization of the monoatomic ideal gas.* arXiv preprint cond-mat/9912229, 1999. (Cited on page 18.)

[Zeng 2012] Hualing Zeng, Junfeng Dai, Wang Yao, Di Xiao and Xiaodong Cui. *Valley polarization in MoS_2 monolayers by optical pumping.* Nature Nanotechnology, vol. 7, no. 8, pages 490–493, 2012. (Cited on pages 11, 61 and 69.)

[Zhang 2015] Xiao-Xiao Zhang, Yumeng You, Shu Yang Frank Zhao and Tony F Heinz. *Experimental evidence for dark excitons in monolayer WSe_2.* Physical Review Letters, vol. 115, no. 25, page 257403, 2015. (Cited on page 82.)

[Zhang 2019] Xiaowei Zhang, Ruowang Chen, Pengjun Wang, Zhixing Gan, Yuejun Zhang, Han Jin, Jiawen Jian and Jun Xu. *Investigation of energy transfer mechanisms in rare-earth doped amorphous silica films embedded with tin oxide nanocrystals.* Optics Express, vol. 27, no. 3, pages 2783–2791, 2019. (Cited on page 32.)

[Zhang 2020a] Long Zhang, Zhe Zhang, Fengcheng Wu, Danqing Wang, Rahul Gogna, Shaocong Hou, Kenji Watanabe, Takashi Taniguchi, Krishnamurthy Kulkarni, Thomas Kuo*et al.* *Twist-angle dependence of moiré excitons in WS2/MoSe2 heterobilayers.* Nature communications, vol. 11, no. 1, page 5888, 2020. (Cited on pages 15 and 87.)

[Zhang 2020b] Qi Zhang, Eric Linardy, Xinyun Wang and Goki Eda. *Excitonic energy transfer in heterostructures of quasi-2D perovskite and monolayer WS_2.* ACS Nano, vol. 14, no. 9, pages 11482–11489, 2020. (Cited on page 63.)

[Zhang 2020c] Zhiming Zhang, Yimeng Wang, Kenji Watanabe, Takashi Taniguchi, Keiji Ueno, Emanuel Tutuc and Brian J LeRoy. *Flat bands in twisted bilayer transition metal dichalcogenides.* Nature Physics, vol. 16, no. 11, pages 1093–1096, 2020. (Cited on page 88.)

[Zhao 2020] Peiliang Zhao, Jin Yu, H Zhong, Malte Rösner, Mikhail I Katsnelson and Shengjun Yuan. *Electronic and optical properties of transition metal dichalcogenides under symmetric and asymmetric field-effect doping.* New Journal of Physics, vol. 22, no. 8, page 083072, 2020. (Cited on page 18.)

[Zhou 2020] Hongzhi Zhou, Yida Zhao, Weijian Tao, Yujie Li, Qiaohui Zhou and Haiming Zhu. *Controlling exciton and valley dynamics in two-dimensional heterostructures with atomically precise interlayer proximity.* ACS Nano, vol. 14, no. 4, pages 4618–4625, 2020. (Cited on page 77.)

[Zhou 2021] You Zhou, Jiho Sung, Elise Brutschea, Ilya Esterlis, Yao Wang, Giovanni Scuri, Ryan J Gelly, Hoseok Heo, Takashi Taniguchi, Kenji Watanabe*et al. Bilayer Wigner crystals in a transition metal dichalcogenide heterostructure.* Nature, vol. 595, no. 7865, pages 48–52, 2021. (Cited on page 88.)

[Zhou 2022] Huabin Zhou, Haojie Lai, Xiao Sun, Ning Zhang, Yuee Wang, Pengyi Liu, Yang Zhou and Weiguang Xie. *Van der Waals MoS2/two-dimensional perovskite heterostructure for sensitive and ultrafast sub-band-gap photodetection.* ACS Applied Materials & Interfaces, vol. 14, no. 2, pages 3356–3362, 2022. (Cited on page 63.)

[Zhu 2011] Zhiyong Y Zhu, Yingchun C Cheng and Udo Schwingenschlögl. *Giant spin-orbit-induced spin splitting in two-dimensional transition-metal dichalcogenide semiconductors.* Physical Review B, vol. 84, no. 15, page 153402, 2011. (Cited on pages 1, 6, 7, 32 and 61.)

[Zhu 2013] CR Zhu, Gang Wang, BL Liu, Xavier Marie, XF Qiao, X Zhang, XX Wu, H Fan, PH Tan, Thierry Amand*et al. Strain tuning of optical emission energy and polarization in monolayer and bilayer MoS 2.* Physical Review B, vol. 88, no. 12, page 121301, 2013. (Cited on pages 47 and 52.)

[Zhu 2014a] Bairen Zhu, Hualing Zeng, Junfeng Dai, Zhirui Gong and Xiaodong Cui. *Anomalously robust valley polarization and valley coherence in bilayer WS2.* Proceedings of the National Academy of Sciences, vol. 111, no. 32, pages 11606–11611, 2014. (Cited on pages 17, 33 and 87.)

[Zhu 2014b] CR Zhu, K Zhang, M Glazov, B Urbaszek, Thierry Amand, ZW Ji, BL Liu and Xavier Marie. *Exciton valley dynamics probed by Kerr rotation in* WSe_2 *monolayers.* Physical Review B, vol. 90, no. 16, page 161302, 2014. (Cited on pages 11, 61 and 69.)

[Zhu 2023] Bairen Zhu, Ke Xiao, Siyuan Yang, Kenji Watanabe, Takashi Taniguchi and Xiaodong Cui. *In-Plane Electric-Field-Induced Orbital Hybridization of Excitonic States in Monolayer WSe 2.* Physical Review Letters, vol. 131, no. 3, page 036901, 2023. (Cited on page 65.)

[Ziegler 2022] Jonas D Ziegler, Kai-Qiang Lin, Barbara Meisinger, Xiangzhou Zhu, Manuel Kober-Czerny, Pabitra K Nayak, Cecilia Vona, Takashi Taniguchi, Kenji Watanabe, Claudia Draxl*et al.* *Excitons at the phase transition of 2D hybrid perovskites.* ACS Photonics, vol. 9, no. 11, pages 3609–3616, 2022. (Cited on page 77.)